Heavy to light meson decay form factors

Logan Sean Roberts

Supervised by Dr. Chris Bouchard

Submitted in fulfillment of the requirements for the Degree of Doctor of Philosophy

School of Physics and Astronomy

College of Science and Engineering

May 2026

Abstract

This thesis presents our progress on using lattice Quantum Chromodynamics to calculate scalar, vector, and tensor kinematic form factors for the following semileptonic meson decays: $B \to \pi$, $B_s \to K$, $D \to \pi$ and $D_s \to K$. These meson decays include the quark transitions $b \to u$ or $c \to d$, whose amplitudes are parameterized by elements of the Cabibbo-Kobayashi-Maskawa (CKM) matrix. Calculating scalar and vector form factors for these decays can, alongside experimentally determined differential decay rates, be used to make precise determinations of the CKM matrix elements V_{ub} and V_{cd}. More precise CKM matrix elements have broad implications for Standard Model flavor physics, such as enabling better tests of CKM matrix unitarity. Moreover, calculating tensor form factors has implications for Standard Model-suppressed and beyond Standard Model physics. This line of lattice calculations uses the Highly Improved Staggered Quark (HISQ) formalism, and $n_f = 2+1+1$ MILC-HISQ gluon field ensembles. Using a modified z-expansion, we succeed in calculating scalar, vector, and tensor kinematic form factors in the continuum limit for all four meson decays of interest to this work. Finally we compare our $q^2 = 0$ and $q^2 = q^2_{\mathrm{max}}$ form factor results to those of other relevant works.

Acknowledgements

I would first like to thank my supervisor Chris Bouchard for his teaching, guidance, and support throughout all stages of my time as a Ph.D. student. I would also like to thank Will Parrott, Judd Harrison, Brian Colquhoun, and Kerr Miller for helping me with these lattice calculations. I wish to give a special thanks to the artist *Macroblank*, whose compositions were the soundtrack to my writing of this thesis, and I thank my parents for encouraging me to pursue my education in a far away land. Finally, I wish to thank my darling bride Olivia, whose love and support made this work possible.

Declaration of originality and AI usage

Besides the standard introductory physics of Chapters 2 and 3, the work I present here is my own, working in collaboration with others in the HPQCD collaboration. I am the primary contributor to this work, whose status was previously given in [1], to which I am also the primary contributor. My use of generative AI in this work was limited to finding credible sources for research, and making minor grammatical checks. Besides these sparse instances, no materials within this work were created/written by generative AI.

Contents

List of Figures

List of Tables

Chapter 1

Introduction

The primary aim of this work is to calculate the hadronic form factors across the physical kinematic range of the following semileptonic meson decays: $D \to \pi$, $B \to \pi$, $D_s \to K$, and $B_s \to K$. These meson decays may all be described as *heavy-light*, which means there is certain shared physics which characterizes heavy mesons (D, D_s, B, B_s) undergoing semileptonic decays into light mesons (π, K). This shared physics permits a certain degree of efficiency in achieving our aim, where the work needed to calculate the form factors of one meson decay is largely reusable or applicable to the calculation of another. These form factor calculations make use of the Highly Improved Staggered Quark (HISQ) action [12], and likewise fall in line with other HPQCD form factor calculations involving heavy meson decays and the HISQ action [13, 14, 15, 16, 17, 18].

The motivation for this work primarily lies in high-precision Standard Model flavor physics. By calculating more accurate form factors, we are able to place tighter constraints on the Standard Model expectations of particle physics experiments. To be more specific, we can use scalar and vector form factor results alongside experimentally determined differential decay rates to calculate CKM matrix elements: V_{cd} for the $D \to \pi$ and $D_s \to K$ decays, and V_{ub} for the $B \to \pi$ and $B_s \to K$ decays. The value of V_{ub} is of particular interest to this work and particle physicists more broadly: there is an approximately 2-3 σ discrepancy in its value determined by either *inclusive* or *exclusive* semileptonic meson decays. In this work we deal only in exclusive decays, and so a more precise exclusive determination of V_{ub} has obvious implications on that discrepancy.

Besides the issue of inclusive/exclusive determinations, the precision of CKM matrix elements has significant implications to the phenomenology of flavor physics in the Standard Model, and perhaps beyond Standard Model (BSM) physics as well. Should the 3×3 CKM matrix be shown to be non-unitary, we would have evidence of BSM physics. Having precise determinations of CKM matrix elements is therefore essential to proving or disproving the unitary structure of the CKM matrix, and in making accurate Standard Model predictions. The current averages of the CKM matrix elements are given by the particle data group (PDG) in [19].

The Flavor Lattice Averaging Group (FLAG) provides current global averages for many of the form factors we examine in this work [7]. The FLAG average takes into account form factor calculations which use different lattice data and vary in methodology. We aim to publish the finalized results of this work to improve the FLAG averages. We expect improvement in this regard due to our use of the fully relativistic HISQ action across a broad kinematic range, and our use of the Heavy-HISQ method of extrapolating to the physical bottom quark mass (which we discuss in section 3.4).

Moving on from scalar and vector form factors, the tensor form factors of these heavy-light meson decays are a somewhat unexplored domain of lattice QCD. There are currently no published results for physical continuous $D \to \pi$, $D_s \to K$, and $B_s \to K$ tensor form factors as determined by lattice QCD. The tensor form factors of these meson decays uniquely probe Standard Model-suppressed behavior, such as flavor changing neutral currents (FCNCs). The very recent publication by the LHCb collaboration [20] finds the first experimental evidence of the $B^+ \to \pi^+ e^+ e^-$ decay, which involves the FCNC of a b quark decaying into a d quark. This result makes Standard Model comparisons to the $B \to \pi$ tensor form factor results given in [6]. For the same reasons we discuss above, we intend to improve upon those results and offer more precise Standard Model predictions of FCNC behavior.

The outline of this thesis is as follows: in chapter 2 we take an overview of Standard Model physics, with a focus on the particle physics and field theory which form the basis of our four meson decays of interest. In chapter 3 we explore the theory of lattice QCD, which allows us to apply numerical methods to solving and calculating relevant quantities, such as path integral and correlation functions. These correlation functions encode the physics of the meson decays whose form factors we wish to eventually calculate. In chapter 4 we fully detail the methodology we employ to fit those correlation functions to the appropriate fit forms. In doing so we extract sets of energies and amplitudes which characterize the meson decays we have simulated on the lattice. In chapter 5 we describe our general methodology of transforming the outputs of fitting correlation functions into physical continuum form factor results. In chapter 6 we then apply the methodologies of chapters 4 and 5 to arrive at the current status of our $D \to \pi$ and $B \to \pi$ form factor results. In chapter 7 we likewise do the same for our $D_s \to K$ and $B_s \to K$ form factor results. Finally in chapter 8 we summarize and provide an outlook for HPQCD's future calculation of these form factors

Chapter 2

The Standard Model of Particle Physics

In this chapter we provide a brief summary of Standard Model physics, beginning with the Standard Model Lagrangian. We move on to discuss fermions and gauge field theories, with a focus on the electroweak sector. We then take a closer look at the weak interaction in the context of meson decays and their form factors, and finish with a discussion of path integrals and correlation functions. Much of the Standard Model content in this chapter is drawn from [21, 22, 23].

2.1 The Standard Model in a nutshell

To begin our overview of the Standard Model, let us examine a simplified version of the Standard Model Lagrangian, given by

$$\begin{aligned}\mathscr{L}_{\mathrm{SM}} = &-\frac{1}{4}F_{\mu\nu}F^{\mu\nu} \\ &+ i\overline{\psi}\not{D}\psi + \text{h.c.} \\ &+ \overline{\psi}_i y_{ij}\psi_j\phi + \text{h.c.} \\ &+ |D_\mu\phi|^2 - V(\phi)\end{aligned} \tag{2.1}$$

The first line in equation 2.1 describes the fundamental forces of the universe, these being the strong force, and the electroweak interaction[1]. These forces are mediated by spin-1 gauge fields, the excitations of which are the gauge boson particles. The second line then describes the interaction of those fundamental forces with one-half spin matter fields, whose particles are the fermions. The third line describes how fermions interact with the zero-spin scalar Higgs field, and the fourth line describes the nature of the Higgs field itself.

The tidy description of the Standard Model in 2.1 blends together the separate but related theories into which the Standard Model can be decomposed. These theories originate from the fundamental symmetries of the Standard Model, whose combined field representation is given by the gauge group

$$SU(3)_c \times SU(2)_L \times U(1)_Y . \tag{2.2}$$

The gauge symmetry $SU(3)_c$ describes the color charge of the strong force, whose gauge bosons are the gluons. The electroweak interaction, the $SU(2)_L \times U(1)_Y$ component of equation 2.2, is more complicated however. Above the electroweak energy scale (about 246 GeV), this combined symmetry group remains intact. In this unbroken symmetry group, $SU(2)_L$ describes how the left-handed components of fermions transform as doublets whereas the right-handed components transform as singlets, and $U(1)_Y$ describes hypercharge. Below that energy scale those symmetries spontaneously break, the phenomena of which we call electroweak symmetry breaking (EWSB). The consequences of EWSB lead to the physics we are familiar with today. These include massive fermions and the massive scalar Higgs boson of the Higgs interaction. The remnants of that broken symmetry group also give us the weak interaction, whose force is mediated by massive $W^{\pm}/Z^0$ bosons, and electromagnetism, a force which follows an unbroken $U(1)$ symmetry and is mediated by a massless gauge boson: the photon γ. Therefore after EWSB, the fundamental forces of the universe are the strong force, the weak force, and electromagnetism. Quantum Chromodynamics (QCD) is the quantum theory which describes the strong force, and Quantum Electrodynamics (QED) is the quantum theory which describes electromagnetism.

---

1. After electroweak symmetry breaking this is no longer true, more on this in the next paragraph.

We can further break down fermions into quarks and leptons. There are six flavors of quark (u, d, s, c, b, t), which we can organize into three generations. Quarks have mass and interact with all three fundamental forces. Similarly, there are six leptons, three charged and three neutral. The charged leptons (e, μ, τ) have mass and experience the weak force and electromagnetism. Meanwhile the neutral leptons (ν_e, ν_μ, ν_τ) are treated as being massless in the Standard Model and only experience the weak force. Like the quarks, we can similarly organize the leptons into three generations. In the rest of this chapter we more fully explore the intricacies of the Standard Model, with a focus on the components most relevant to the interest of this work: Lattice QCD and the kinematic form factors of heavy meson decays.

2.2 Fermions

The physics of fermions in the Standard Model originates from the interaction between space-time and local gauge symmetries. We can model fermions ψ as a representation of the Lorentz group $SO(1,3)$, from which we get the Dirac spinor $\psi(x)$. For this fermion to undergo a Lorentz transformation Λ we get

$$\psi(x) \to S[\Lambda]\psi(\Lambda^{-1}x). \tag{2.3}$$

Here $S[\Lambda]$ is a 4×4 matrix which satisfies the equation

$$S^{-1}(\Lambda)\gamma^\mu S(\Lambda) = \Lambda^\mu_\nu \gamma^\nu, \tag{2.4}$$

where γ^μ are the Dirac gamma matrices. Under the Minkowski spacetime metric $\eta = \mathrm{diag}(-1,1,1,1)$ the gamma matrices encode the Clifford algebra $\{\gamma^\mu, \gamma^\nu\} = 2\eta^{\mu\nu}$. The dynamics of free fermions are characterized by the Lorentz invariant Dirac equation

$$(i\gamma^\mu \partial_\mu - m)\psi = 0. \tag{2.5}$$

When such a fermion experiences an interaction with a gauge field, the partial derivative in equation 2.5 becomes a covariant derivative D_μ. We can write D_μ as

$$D_\mu = \partial_\mu + igA_\mu, \tag{2.6}$$

where g is the coupling strength of the interaction, and A is the vector gauge field of the interaction.

2.3 Gauge field theories

In the Standard Model, we can say that gauge theories arise out of local symmetries, where gauge fields transform under some Lie group G. The differences in a Lie algebra's structure determine if the corresponding gauge theory is Abelian or non-Abelian. In Abelian theories like QED, the gauge field does not experience self-interaction. This is not the case for non-Abelian theories like QCD, where gauge fields experience self-interaction and gauge bosons likewise experience self-coupling. We explore the properties of Standard Model gauge theories in more depth throughout the remainder of this section.

2.3.1 Quantum Electrodynamics

Quantum electrodynamics is the most simple of the gauge theories present in the Standard Model. As discussed before, QED is experienced by (electrically) charged particles and is mediated by photons. The charged particles we can write as Dirac fields $\psi(x)$, and the photon is a quantized excitation of the vector field A. We suppress any spacetime arguments x when dealing with gauge fields for the purpose of reducing notation; it should be understood that all gauge fields have spacetime dependency. Under a local gauge symmetry these two fields transform under QED as

$$\begin{aligned} \psi(x) &\to e^{ie\alpha(x)}\psi(x), \\ A^\mu &\to A^\mu - \partial^\mu \alpha, \end{aligned} \tag{2.7}$$

where e is the gauge coupling constant and $\alpha(x)$ is some spacetime-dependent gauge parameter. The vector field A with components A_μ helps us define the field strength tensor $F_{\mu\nu}$ and the covariant derivative D_μ in QED, which are given by

$$\begin{aligned} F_{\mu\nu} &= \partial_\mu A_\nu - \partial_\nu A_\mu, \\ D_\mu &= \partial_\mu - ieQA_\mu, \end{aligned} \tag{2.8}$$

where Q is the charge of the field or particle under QED. Putting these equations together, we may write the QED Lagrangian as

$$\mathscr{L}_{\text{QED}} = \overline{\psi}(i\not{D} - m)\psi - \frac{1}{4}F_{\mu\nu}F^{\mu\nu}, \tag{2.9}$$

where $\overline{\psi} \equiv \psi^\dagger\gamma^0$, and $\not{D} \equiv \gamma_\mu D^\mu$. Considering equations 2.7 and 2.9, we can see that $U = e^{ie\alpha}$ is unitary and of rank 1. In other words, U is just a number, and therefore QED is a $U(1)$ Abelian gauge theory.

2.3.2 Quantum Chromodynamics

Let us now move on to discuss a non-Abelian gauge theory: QCD [24, 25]. QCD is a non-Abelian gauge theory whose gauge field transforms under the Lie group G. The generators T^a of QCD satisfy the relation $[T^a, T^b] = if^{abc}T^c$. Under the local G transformation the Dirac field $\psi(x)$ and the vector field A transform as

$$\begin{aligned} \psi(x) &\to U(x)\psi(x), \\ &\equiv e^{ig_s\alpha^a(x)T^a}\psi(x), \\ A_\mu &\to UA_\mu U^\dagger - \frac{i}{g_s}(\partial_\mu U)U^\dagger. \end{aligned} \tag{2.10}$$

Here we have suppressed spinor indices, g_s is the strong coupling constant, and $\alpha^a(x)$ are some real functions which parameterize the transformation. The associated covariant derivative D_μ and field strength tensor $F^a_{\mu\nu}$ of QCD are likewise given by

$$\begin{aligned} D_\mu &= \partial_\mu + ig_s A^a_\mu T^a, \\ F^a_{\mu\nu} &= \partial_\mu A^a_\nu - \partial_\nu A^a_\mu - g_s f^{abc} A^b_\mu A^c_\nu, \end{aligned} \tag{2.11}$$

where we use $A_\mu = A^a_\mu T^a$. This means that A_μ is a component of a spacetime four-vector, and a vector in the eight-dimensional vector space of the Lie algebra $SU(3)$, with components A^a_μ and unit vectors T^a. Unlike QED, here we see the presence of a nonlinear term in the equation of the field strength tensor. It is in this term that the self interacting, non-Abelian structure of QCD manifests. We would recover an Abelian gauge theory if $f^{abc} = 0$. If we write the compact form of the field strength tensor $F_{\mu\nu} = \frac{i}{g_s}[D_\mu, D_\nu]$, we can see that $F_{\mu\nu}$ transforms covariantly under a local G transformation, rather than remaining invariant:

$$F_{\mu\nu} \to U F_{\mu\nu} U^{-1}. \tag{2.12}$$

While the field strength tensor is not Lorentz invariant, we can obtain the required term in the QCD Lagrangian by defining the gauge invariant term

$$\frac{1}{4} F^a_{\mu\nu} F^{a\mu\nu} = \frac{1}{2g_s^2} \operatorname*{Tr}_{\text{color}} \left([D_\mu, D_\nu][D^\mu, D^\nu] \right). \tag{2.13}$$

As an $SU(3)$ gauge theory, the $N^2 - 1 = 8$ gauge bosons of QCD (gluons) carry the QCD's color charge. The three color charges are red, blue, and green (r, b, g), and the eight gluons act as a color octet: $r\bar{g}$, $r\bar{b}$, $g\bar{r}$, $g\bar{b}$, $b\bar{r}$, $b\bar{g}$, $\frac{1}{\sqrt{2}}(r\bar{r} - g\bar{g})$, and $\frac{1}{\sqrt{3}}(r\bar{r} + g\bar{g} - 2b\bar{b})$. Gluons always couple to another gluon or one of the six flavors of quark, which transform as color triplets. We can say then that physical states in nature only exist as color neutral states, a phenomenon which is known as *confinement*. We can relate the gauge field theory generators of QCD to the Gell-Mann matrices

λ^a as $T^a = \frac{1}{2}\lambda^a$, where $a \in \{1,...,8\}$. Doing so, we arrive at the QCD Lagrangian, given by

$$\mathscr{L}_{\text{QCD}} = -\frac{1}{4}G^a_{\mu\nu}G^{a\mu\nu} + \sum_{q\in\{u,c,t,d,s,b\}} \overline{\psi}_q \left(i\not{\partial} - g_s \not{A}^a \frac{\lambda^a}{2} - m_q \right) \psi_q. \tag{2.14}$$

Here we differentiate from QED by now writing the field strength tensor as $G^a_{\mu\nu}$ to denote that gluons are the force carrying boson in QCD. We also see the same slashed notation where for some vector X, $\not{X} \equiv \gamma_\mu X^\mu$.

2.3.3 The Electroweak sector

While the lattice simulations to come are performed in pure QCD, the meson decays in which we are interested are fundamentally electroweak processes. As far as gauge theories go, the peculiarities of the electroweak sector [26, 27] warrant some extra discussion.

While QCD's $SU(3)$ symmetries remain unbroken after EWSB, the same cannot be said for the originally unbroken symmetries of the electroweak interaction. The electroweak symmetry group $SU(2)_L \times U(1)_Y$ mixes Abelian and non-Abelian gauge theories which couple to fermions differently. From the non-Abelian $SU(2)_L$ component we have three gauge fields W^i_μ for $i \in \{1,2,3\}$, and the generators $T^i = \frac{\sigma^i}{2}$, where σ^i are the Pauli matrices. Meanwhile from the Abelian $U(1)_Y$ component we have one gauge field B_μ, and its scalar generator Y: hypercharge. The combined covariant derivative under these gauge theories is then given by

$$D_\mu = \partial_\mu + igW^i_\mu T^i + ig'YB_\mu, \tag{2.15}$$

where g and g' are the associated coupling constants of either gauge field. The field strength tensors of these gauge fields are likewise given by

$$\begin{aligned} W^i_{\mu\nu} &= \partial_\mu W^i_\nu - \partial_\nu W^i_\mu + g\varepsilon^{ijk}W^j_\mu W^k_\nu, \\ B_{\mu\nu} &= \partial_\mu B_\nu - \partial_\nu B_\mu, \end{aligned} \tag{2.16}$$

where ε^{ijk} is the structure constant of $SU(2)_L$.

The key distinction which separates the electroweak interaction from QCD and QED is that $SU(2)_L$ is *chiral.* As such, left-handed fermions ψ_L transform as doublets under $SU(2)_L$, while right-handed fermions ψ_R are singlets under $SU(2)_L$. For each fermion generation, We can define the left-handed quark and lepton doublets as

$$Q_L = \begin{pmatrix} u_L \\ d_L \end{pmatrix}, \quad L_L = \begin{pmatrix} \nu_L \\ e_L \end{pmatrix}. \tag{2.17}$$

Meanwhile u_R, d_R, e_R, and ν_R are right handed singlets. We note that ν_R does not interact with any gauge theory in the Standard Model, and so it is often not part of the minimal Standard Model field content. Unlike QCD or QED, the gauge couplings in the electroweak interaction are not symmetric between ψ_L and ψ_R, and so we can say that $SU(2)_L$ does not preserve parity symmetry.

After EWSB [28, 27, 29], these gauge fields mix together with the scalar Higgs field ϕ. In doing so, they form the physically observable charged gauge fields $W^{\pm}_{\mu}$ and neutral gauge fields Z^0_{μ}, A_{μ}. The post-EWSB gauge field degrees of freedom are related to the pre-EWSB degrees of freedom by

$$\begin{aligned} W^{\pm}_{\mu} &= \frac{1}{\sqrt{2}}(W^1_{\mu} \pm iW^2_{\mu}), \\ Z^0_{\mu} &= \cos\theta_W W^3_{\mu} - \sin\theta_W B_{\mu}, \\ A_{\mu} &= \sin\theta_W W^3_{\mu} + \cos\theta_W B_{\mu}, \end{aligned} \tag{2.18}$$

where $\theta_W = \frac{g'}{\sqrt{g^2+g'^2}}$ is the *weak mixing angle.* We can write the masses of the corresponding gauge bosons as

$$M_{W^{\pm}} = \frac{vg}{2}, \quad M_{Z^0} = \frac{v\sqrt{g^2+g'^2}}{2} = \frac{M_{W^{\pm}}}{\cos\theta_W}, \quad M_{\gamma} = 0, \tag{2.19}$$

where v is the vacuum expectation value of the Higgs potential. Here we may also acknowledge that A_μ is the very same Abelian gauge field we see in our discussion of QED (section 2.3.1), and as such its gauge boson is the photon γ. After EWSB, it is accurate to say that the fields $W_\mu^\pm$ and Z_μ^0 now characterize the weak interaction. The corresponding Lagrangian of the weak interaction can be separated into distinct parts: charged currents (coupled to the $W^\pm$) which change quark flavor within flavor doublets, neutral currents (coupled to the Z^0) which have chiral structure and preserve flavor, and triple and quartic couplings from gauge boson self-interaction. We take a closer look at charged and neutral currents in the context of meson decays in the following section.

The electroweak interaction is also the context in which quarks and charged leptons acquire mass in the Standard Model, this being in the form of Yukawa couplings [27, 30]. If we remain in a mass eigenstate basis (ignoring flavor changing for now) we can write the Yukawa couplings for an up-type quark, down-type quark, and charged lepton as y^u, y^d, and y^e respectively. The couplings appear in the Yukawa portion of the Standard Model Lagrangian $\mathscr{L}_Y$ as

$$\mathscr{L}_Y = \overline{Q}_L y^d \phi d_R - \overline{Q}_L y^u \tilde{\phi} u_R - \overline{L}_L y^e \phi e_R + \text{h.c.}, \tag{2.20}$$

where the Higgs field conjugate $\tilde{\phi} = i\sigma^2\phi^*$. In this mass eigenstate basis, the Yukawa couplings are scalars, which permit us to simply write those fermion masses as

$$m_u = \frac{vy^u}{\sqrt{2}}, \quad m_d = \frac{vy^d}{\sqrt{2}}, \quad m_e = \frac{vy^e}{\sqrt{2}}, \quad m_\nu = 0. \tag{2.21}$$

By rotating into the weak eigenstate basis, we introduce flavor mixing into the Yukawa Lagrangian, and as such the Yukawa couplings now become complex 3×3 matrices Y_{ij}^u, Y_{ij}^d, and Y_{ij}^e, where the indices $i, j \in \{1,2,3\}$ label fermion generation. In the weak eigenstate bases the Yukawa Lagrangian is instead given by

$$\mathscr{L}_Y = \overline{Q}_L^i Y_{ij}^d \phi d_R^j - \overline{Q}_L^i Y_{ij}^u \tilde{\phi} u_R^j - \overline{L}_L^i Y_{ij}^e \phi e_R^j + h.c., \tag{2.22}$$

where the flavor doublets and singlets pick up flavor indices as well.

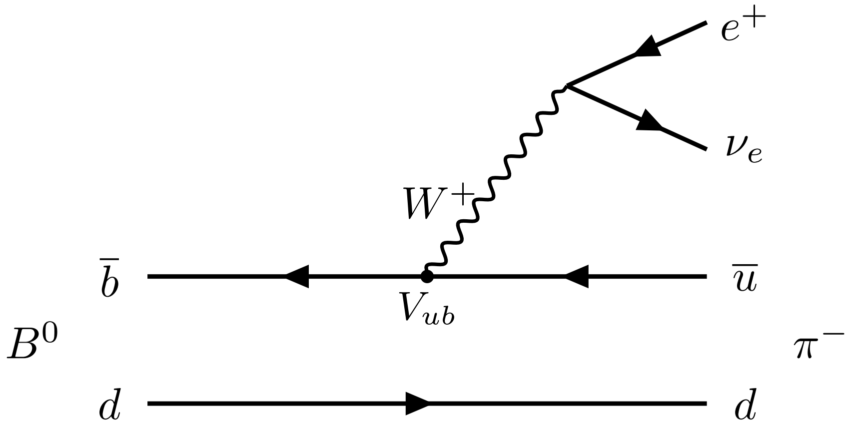

Figure 2.1: Diagram for the semileptonic $B^0 \to \pi^- e^+ \nu$ meson decay, the amplitude of which contains the CKM matrix element V_{ub}.

2.4 Meson decays

In this section we more fully explore the physics of the weak interaction, with a focus on meson decays. We do so in the context of flavor changing charged and neutral currents, which ultimately lead us to the kinematic form factors we aim to calculate.

2.4.1 Flavor changing charged currents

At tree level, the Standard Model meson decays of interest to this work ($B \to \pi$, $D \to \pi$, $B_s \to K$, $D_s \to K$) all involve flavor changing weak decays via charged currents. This is to say, some valence bottom/charm quark within a meson weakly decays, emitting a charged $W^\pm$ boson and changing flavor to an up/down quark. We call such an interaction a flavor changing charged current (FCCC). Figure 2.1 shows the Feynman diagram of a semileptonic $B \to \pi$ meson decay, which contains a FCCC.

In the weak eigenstate basis, we can write the Lagrangian of a FCCC as

$$\mathscr{L}_{\text{FCCC}} = -\frac{g}{2}\overline{u}^i_L \gamma^\mu d^i_L W^+_\mu + \text{h.c.}, \tag{2.23}$$

where u^i_L and d^i_L denote up and down-type left-handed quark fields of generation i. If we wish to rotate into a mass eigenstate basis, we arrive at a problem in the Yukawa sector. The up and down-type quark mass matrices arise from the independent complex Yukawa matrices Y^u and Y^d. These matrices can be diagonalized by different unitary transformations, but not simultaneously. In other words, weak interaction eigenstates are not aligned with their mass eigenstates. We can parameterize this misalignment with the introduction of the Cabibbo-Kobayashi-Maskawa (CKM) matrix [31, 32], a unitary 3×3 matrix with matrix elements V_{ij}. Doing so, we can write the Lagrangian of a FCCC in the mass eigenstate basis as

$$\mathscr{L}_{\text{FCCC}} = -\frac{g}{2}\overline{u}^i_L \gamma^\mu V_{ij} d^j_L W^+_\mu + \text{h.c.}, \tag{2.24}$$

With this formulation, we can say that the $W^\pm$ bosons mediate transitions between different quark generations ($u \to d, s, b$ for example), with amplitudes weighted by the corresponding CKM matrix elements.

2.4.2 The CKM Matrix

As we have seen, the CKM matrix V_{CKM} parametrizes the relative strength of flavor changing weak interactions of quarks. We can likewise say that a given CKM matrix element represents the probability for an up or down-type quark to decay into an opposite-type quark of a certain generation. Thankfully, we can probe the values of the CKM matrix by studying hadronic transitions arising from quark flavor-changing interactions, as V_{CKM} elements are present in the decay amplitudes. The PDG gives a current global average of the CKM matrix as [19]

$$V_{\text{CKM}} \equiv \begin{pmatrix} |V_{ud}| & |V_{us}| & |V_{ub}| \\ |V_{cd}| & |V_{cs}| & |V_{cb}| \\ |V_{td}| & |V_{ts}| & |V_{tb}| \end{pmatrix} = \begin{pmatrix} 0.97367(32) & 0.22431(85) & 0.00382(20) \\ 0.221(4) & 0.975(6) & 0.0411(12) \\ 0.0086(2) & 0.0415(9) & 1.010(27) \end{pmatrix} \tag{2.25}$$

Considering the unitary nature of this matrix, we can construct a *unitary triangle* whose angles $\phi_{1,2,3}$ are determined from the elements of V_{CKM}. By imposing the unitary constraint where $V_{ud}V^*_{ub} + V_{cd}V^*_{cb} + V_{td}V^*_{tb} = 0$, we can write

$$\phi_1 = \arg\left(\frac{V_{cd}V^*_{cb}}{V_{td}V^*_{tb}}\right), \quad \phi_2 = \arg\left(\frac{V_{td}V^*_{tb}}{V_{ud}V^*_{ub}}\right), \quad \phi_3 = \arg\left(\frac{V_{ud}V^*_{ub}}{V_{cd}V^*_{cb}}\right). \tag{2.26}$$

Figure 2.2 provides a visual representation of these angles in the context of the experimental constraints imposed upon them. This figure follows the Wolfenstein parameterization [33] of the unitarity triangle, which is one of several possible methods to impose unitary constraints. In this parameterization, we reduce the number of free parameters in the CKM matrix from nine to four by redefining the appropriate relative phase terms. These parameters λ, A, and ρ are related to the mixing angles of the different quark generations, and η corresponds to a CP-violating phase term. To order λ^3, we can write the Wolfenstein parametrization of the CKM matrix as

$$\begin{pmatrix} 1-\frac{1}{2}\lambda^2 & \lambda & A\lambda^3(\rho - i\eta) \\ -\lambda & 1-\frac{1}{2}\lambda^2 & A\lambda^2 \\ A\lambda^3(1-\rho-i\eta) & -A\lambda^2 & 1 \end{pmatrix} + \mathscr{O}(\lambda^4). \tag{2.27}$$

The triangle constructed from equation 2.26 and under this parameterization happens to have three sides which are the same order of magnitude. This makes it easier to probe CKM matrix elements experimentally at similar levels of precision.

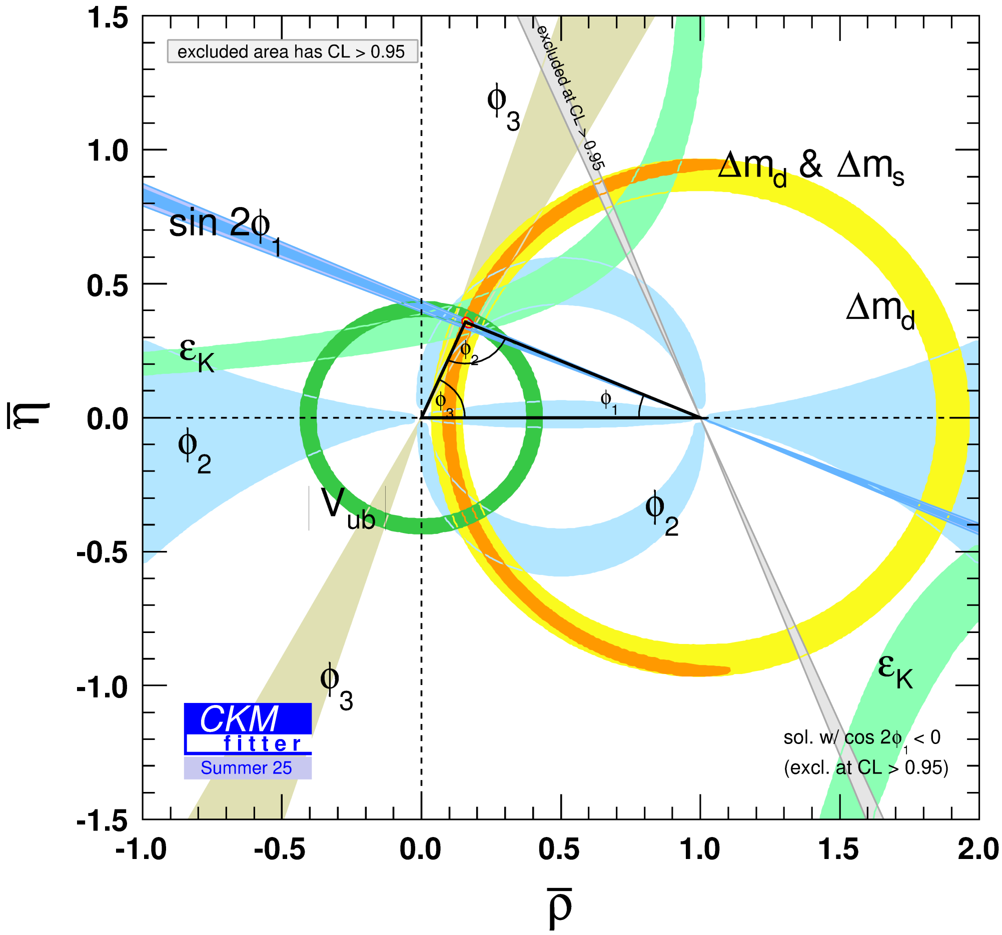

Figure 2.2: The CKM matrix represented as the Unitary Triangle, whose angles are defined in equation 2.26. Image created by the CKMfitter group [2].

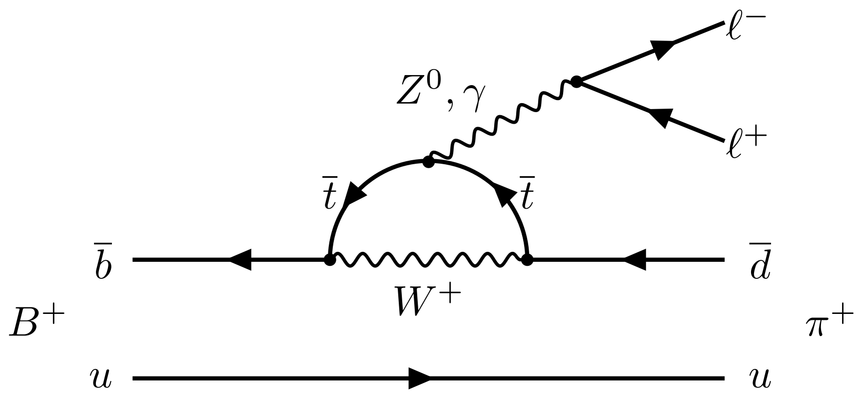

Figure 2.3: Sample $B^+ \to \pi^+\ell^+\ell^-$ Feynman diagram, which contains a Standard Model-suppressed flavor changing neutral current.

2.4.3 Flavor changing neutral currents

At the beginning of section 2.4.1, we were careful with our language in specifying that tree level and Standard Model meson decays are characterized by FCCCs. If we push past tree level and consider meson decays at the level of one-loop interactions, we can encounter a Standard Model-suppressed [34] flavor changing neutral current (FCNC). Meson decays like the one shown in figure 2.3 contain FCNCs, wherein top quark loops facilitate the emission of a (neutrally charged) Z^0 or γ boson. In this example, the initial and final quark states involved in the decay are of the same type: either both up-type or both down-type.

In addition to one-loop level Standard Model physics, FCNCs are also relevant to beyond Standard Model (BSM) physics. The rare nature of FCNCs makes them highly sensitive to new physics, as even small contributions from BSM particles might significantly modify FCNC decay rates or angular distributions in collider experiments.

2.4.4 Kinematic Form Factors

The core aim of this work is to calculate the kinematic form factors of various heavy meson decays, the theory of which ties together the weak interaction, flavor changing currents, the CKM matrix, and semileptonic decays. Let us begin by considering the semileptonic decay of some meson M_1 to another meson M_2, and a lepton pair $\ell\nu$. In such a decay, the valence quark q_1 in M_1 weakly decays into the valence quark q_2 in M_2 via a FCCC. We can write the amplitude $\mathscr{A}$ of this meson decay as

$$\mathscr{A} = \left(\frac{ie}{\sqrt{2}\sin\theta_W}\right)^2 V_{q_1q_2} \langle M_2, \ell\nu| J_\mu^{q_1q_2} \left(\frac{g^{\mu\nu}}{p^2 - M_W^2}\right) L_\nu^{\ell\nu} |M_1\rangle \,. \tag{2.28}$$

Here we define p to be the four-momentum carried off by the W boson, and we also introduce the hadronic current J_μ^{ij} and the leptonic current L_μ^{ij}. We define these currents as

$$\begin{aligned} J_\mu^{ij} &\equiv \frac{1}{2}(\overline{u}^i\gamma_\mu d^j - \overline{u}^i\gamma_5\gamma_\mu d^j), \\ L_\mu^{ij} &\equiv \frac{1}{2}(\overline{\nu}^i\gamma_\mu e^j - \overline{\nu}^i\gamma_5\gamma_\mu e^j). \end{aligned} \tag{2.29}$$

Both these currents contain terms of the form $\overline{\psi}\gamma_\mu\psi$ and $\overline{\psi}\gamma_\mu\gamma_5\psi$, which we can refer to as a vector current V_μ^{ij} and an axial-vector current A_μ^{ij} respectively. We can make a few approximations and substitutions to simplify equation 2.28 into a more useful form. First, we can introduce the Fermi constant $G_F = \frac{g^2\sqrt{2}}{8m_W^2}$, which links the strength of the weak interaction to the $W^\pm$ mass. Furthermore, so long as the W boson's four-momentum is much less than its mass, we can make the approximation $(p^2 - M_W^2)^{-1} \approx -M_W^{-2}$. With these steps we can now write the decay amplitude as

$$\begin{aligned} \mathscr{A} &= 2\sqrt{2}G_f V_{q_1q_2} \langle M_2, \ell\nu| J_\mu^{q_1q_2} g^{\mu\nu} L_\nu^{\ell\nu} |M_1\rangle \,, \\ &= 2\sqrt{2}G_f V_{q_1q_2} \langle \ell\nu| L_\mu^{\ell\nu} |\Omega\rangle \langle M_2| J_\mu^{q_1q_2} |M_1\rangle \,, \end{aligned} \tag{2.30}$$

where $|\Omega\rangle$ is the state of the vacuum. In the second line of equation 2.30 we have factorized the leptonic and hadronic matrix elements[2], the latter of which is of particular interest to this work. As we will discuss in the following chapter, calculating $\langle M_2|J_\mu^{q_1q_2}|M_1\rangle$ at low energies (where the strong coupling constant of QCD is large) requires a non-perturbative approach such as Lattice QCD.

Putting the actual calculation of the hadronic matrix element aside, we may parameterize the hadronic matrix element in terms of meson masses m_M, meson momentum p_μ^M, leptonic current momentum q^μ, and the scalar and vector form factors: $f_0(q^2)$ and $f_+(q^2)$. In this context the current's momentum $q \equiv (p_{M_1} - p_{M_2})$, and the q^2 dependency is why we call them *kinematic* form factors. While the current $J_\mu^{q_1q_2}$ has both a vector and axial-vector component, only the vector component contributes to hadronic current in the case where M_1 and M_2 are pseudoscalar mesons. QCD is a parity conserving interaction, and any axial-vector contribution would violate the parity invariance of QCD. As such, the current insertion $J_\mu^{q_1q_2} \to V_\mu^{q_1q_2}$, and so from [35] we have the general form

$$\langle M_2|V_\mu^{q_1q_2}|M_1\rangle = f_+(q^2)\left(p_\mu^{M_1} + p_\mu^{M_2} - \frac{m_{M_1}^2 - m_{M_2}^2}{q^2}q^\mu\right) + f_0(q^2)\frac{m_{M_1}^2 - m_{M_2}^2}{q^2}q^\mu. \tag{2.31}$$

We can similarly define hadronic matrix elements for scalar and tensor current insertions as well. The hadronic matrix elements with a scalar current insertion, or *scalar matrix element* for short, has no dependence on $f_+(q^2)$, which allows us to isolate $f_0(q^2)$ from $f_+(q^2)$. The *tensor matrix element* meanwhile is parameterized by a tensor from factor $f_T(q^2,\mu)$, which also has dependency on an energy scale μ. We more fully discuss these matrix elements in chapter 5.

For a semileptonic meson decay mediated by a FCCC, it is possible to relate that meson's experimentally-determined differential decay rate $\frac{d\Gamma}{dq^2}$ to the corresponding scalar and vector form factor and CKM matrix element. While there are four meson decays of interest to this work ($B \to \pi$, $D \to \pi$, $B_s \to K$, $D_s \to K$), we can describe them all as heavy-to-light meson decays, where B, B_s, D, and D_s are all *heavy*, while the π and K are *light*. In any case, we can generalize all four

2. We can do this because the leptonic and hadronic currents do not interact in pure QCD.

meson decays as a heavy meson H decaying to a light meson L, some charged lepton ℓ, and a neutrino ν. We therefore write the differential decay rate of $H \to L\ell\nu$ as

$$\begin{aligned}\frac{d\Gamma}{dq^2}(H \to L\ell\nu) = \frac{G_F^2}{24\pi^3}|V_{q_1q_2}|^2 \left(1 - \frac{m_\ell^2}{q^2}\right)^2 |p_L| \\ \times \left[\left(1 + \frac{m_\ell^2}{2q^2}\right)|p_L|^2|f_+(q^2)|^2 + \frac{3m_\ell^2}{8q^2}\frac{(m_H^2 - m_L^2)^2}{m_H^2}|f_0(q^2)|^2\right].\end{aligned} \tag{2.32}$$

Here, the momentum of the light meson p_L is presented in the rest frame of the heavy meson. In these cases where $H \in \{B, B_s\}$, $V_{q_1q_2} = V_{ub}$. Meanwhile if $H \in \{D, D_s\}$, then $V_{q_1q_2} = V_{cd}$. In the limit where $m_\ell \to 0$, equation 2.32 simplifies to

$$\frac{d\Gamma}{dq^2}(H \to L) = \frac{G_F^2}{24\pi^3}|V_{q_1q_2}|^2 \times |p_L|^3 \times |f_+(q^2)|^2. \tag{2.33}$$

Herein lies the physics which serves as the core motivation for this work: we can use lattice QCD as the theoretical framework in which we can calculate more accurate kinematic form factors. These can be used alongside experimentally determined differential decay rates to solve for $V_{q_1q_2}$ in equation 2.33, giving us more precise CKM matrix elements.

While more precise vector form factors lead to more precise determinations of CKM matrix elements, more precise tensor form factors lead to better constraints on Standard Model-suppressed and BSM physics. We do not delve into the rich phenomenology of such physics in this work, but such considerations should find a place in future publications based on this work's line of lattice calculations (the status of which we cover in chapters 6 and 7).

2.5 The path integral and correlation functions

In the following chapter we explore how the methods of Lattice QCD discretize standard model physics, such that we can use numerical methods to make calculations and solve problems which cannot be achieved analytically. The basis of those methods requires the discretization of path integrals and correlation functions. In this section we aim to briefly cover these topics in the context of the physical continuum, which is to say, not in any discretized lattice theory.

We may begin this discussion by considering the time-ordered product of n scalar fields $\phi(x_n)$, which we can write as $T\{\phi_H(x_1)...\phi_H(x_n)\}$. We add notation here to denote that the fields are defined in the Heisenberg picture, which is to say that the state vectors are fixed in time, and the field operators carry all time dependence. By taking the expectation value of this time ordered product of fields, we obtain its Green's function, which we can alternatively refer to as an n-point *correlation function*. This function is given by

$$C_n(x_1,...,x_n) = \langle\Omega| T\{\phi_H(x_1)...\phi_H(x_n)\} |\Omega\rangle \,, \tag{2.34}$$

where $|\Omega\rangle$ is the vacuum in the interaction picture. In the interaction picture, we decompose some interacting Hamiltonian H into some non-interacting free theory piece H_0 and an interacting piece H_{int}. In this picture we can then write free theory vacuum as $H_0|\Omega\rangle = 0$, and the energy of the vacuum state is given by $\langle\Omega| H |\Omega\rangle = E_0$. Putting this together we can write the full Hamiltonian in the interaction picture H_I as

$$H_I(t) = e^{iH_0t} H_{\text{int}} e^{-iH_0t}. \tag{2.35}$$

Since H_I represents only a weak perturbation to the free theory, the vacuum state of the interacting theory should retain a non-zero projection onto the free theory vacuum, which gives us $\langle \Omega | 0 \rangle \neq 0$. As a result, the time evolution T of the free theory vacuum can be modeled by the insertion of the states $e^{-iHT} |0\rangle$, which we define as

$$\begin{aligned} e^{-iHT} |0\rangle &= \sum_n e^{-iE_nT} |n\rangle \langle n|0\rangle \\ &= e^{-iE_0T} |\Omega\rangle \langle \Omega|0\rangle + \sum_{n\neq 0} e^{-iE_nT} |n\rangle \langle n|0\rangle \end{aligned} \tag{2.36}$$

All we have effectively done here is separated the $n = 0$ ground state from the $n \neq 0$ states, which we can call *excited* states, as $E_0 < E_n$ for all $n \neq 0$. This also means that taking the limit $T \to \infty(1 - i\varepsilon)$ suppresses the contributions from the excited states more rapidly than the ground state contribution. Physically, this reflects the assumption that the fields behave as (non-interacting) free fields in the asymptotic past (T) and asymptotic future $(+T)$ of the interaction.

If we implement this method of relating the interacting ground state to the vacuum of the free theory, we may write for our n-point correlation function that

$$\begin{aligned} C_n(x_1, ..., x_n) &= \langle \Omega | T\{\phi_H(x_1)...\phi_H(x_n)\} |\Omega\rangle , \\ &= \lim_{T\to\infty(1-i\varepsilon)} \frac{\langle 0| T\{\phi(x_1)...\phi(x_n)\} e^{-i\int_{-T}^{T} dt H_I(t)} |0\rangle}{\langle 0| e^{-i\int_{-T}^{T} dt H_I(t)} |0\rangle}. \end{aligned} \tag{2.37}$$

The complete derivation of equation 2.37 is provided by [21], but for our purposes the key takeaway is that this equation leads us nicely into discussing the path integral. We can define the path integral as the integral over all potential field configurations. As such we can equate the n-point correlation function to the path integral:

$$C_n(x_1, ..., x_n) = \frac{1}{Z} \int D\phi \;\; \phi(x_1)...\phi(x_n) e^{i\int d^4x \mathscr{L}[\phi]}, \tag{2.38}$$

where we have defined the partition function Z as the path integral without any field insertions. If we consider the path integral in the context of QCD, the strong coupling constant being large at low energies (the same energy scales of the semileptonic meson decays of interest to this work) is problematic. This large coupling prevents the perturbative expansion of the integral in equation 2.38, which is the analytical method by which we might normally calculate the path integral. This once again leads us into the numerical methods of lattice QCD, which we discuss in chapter 3.

Having explored the equations of an n-point correlation function, let us narrow our scope to only two and three-point correlation functions, which form the basis of our work going forward. Doing so requires us to make a Wick rotation [36], where we transform from Minkowski spacetime to Euclidean spacetime, such that $(t \to -it)$. This also implies that our infinite time limit $T \to -i\infty(1-i\varepsilon)$. With the Wick rotation, the $i = \sqrt{-1}$ terms which appear in the path integral (equation 2.38) instead become -1.

Let us begin with the two-point correlation function $C_2(x_2, x_1)$. Consider that for a free Hamiltonian in the interaction picture we can write the interaction picture field as

$$\phi_I = e^{H_0(t-t_0)}\phi(t_0, \vec{x})e^{-H_0(t-t_0)}, \tag{2.39}$$

where we have decomposed the spacetime coordinate $x_0 \to (t_0, \vec{x})$. With equations 2.37 and 2.39, we can impose that $t_2 > t_1$ and derive a more useful equation for a two point correlation function:

$$\begin{aligned}
C_2(x_2, x_1) &= \lim_{T \to (1-i\varepsilon)} \frac{\langle 0|\, \phi_I(x_2)\phi_I(x_1) e^{-\int_{-T}^{T} dt H_I(t)}\, |0\rangle}{\langle 0|\, e^{-\int_{-T}^{T} dt H_I(t)}\, |0\rangle}, \\
&= \frac{\langle 0|\, \phi_I(x_2)\phi_I(x_1)\, |0\rangle}{\langle 0|0\rangle}, \\
&= \sum_n \frac{\langle 0|\, \phi_I(x_2)\, |n\rangle \langle n|\, \phi_I(x_1)\, |0\rangle}{2(E_n - E_0)}, \\
&= \sum_n \frac{\langle 0|\, e^{H_0(t_2-t_0)}\phi(t_0, \vec{x}_2)e^{-H_0(t_2-t_0)}\, |n\rangle \langle n|\, e^{H_0(t_1-t_0)}\phi(t_0, \vec{x}_1)e^{-H_0(t_1-t_0)}\, |0\rangle}{2(E_n - E_0)}, \\
&= \sum_n e^{-(E_n-E_0)(t_2-t_1)} \frac{\langle 0|\, \phi(t_0, \vec{x}_2)\, |n\rangle \langle n|\, \phi(t_0, \vec{x}_1)\, |0\rangle}{2(E_n - E_0)}.
\end{aligned} \tag{2.40}$$

If we now make a few definitions, we can arrive at an equation for a two-point correlation function which will prove to be incredibly useful. First, we redefine E_n as an energy relative to vacuum: $E_n \to E_n - E_0$. Furthermore, in the context of correlation functions it is common to refer to any $\phi(x_n)$ as a *current insertion.* If we then define the new quantity $t = t_2 - t_1$, we can finally write

$$C_2(x_2, x_1) = \sum_n e^{-E_n t} \frac{\langle 0| \phi(\vec{x}_2) |n\rangle \langle n| \phi(\vec{x}_1) |0\rangle}{2E_n}. \tag{2.41}$$

In this formulation, the two-point correlation function can be characterized as having two distinct parts. The first of these is an exponential term with dependence on energy (relative to the vacuum) and the difference in time between current insertions. The second of these are amplitude terms, which take the form of current insertion matrix elements divided by $2E_n$. In the following chapters of this thesis, it will be commonplace to describe correlation functions in terms of energy and amplitude terms.

Expanding our scope now to three-point correlation functions $C_3(x_3, x_2, x_1)$, we can perform similar substitutions and redefinitions as before. If we define the quantities $t = t_2 - t_1$ and $T = t_3 - t_1$, and keep the convention of defining energies relative to vacuum, we can write

$$C_3(x_3, x_2, x_1) = \sum_{m,n} e^{E_m(T-t)} e^{-E_n t} \frac{\langle 0| \phi(\vec{x}_3) |m\rangle \langle m| \phi(\vec{x}_2) |n\rangle \langle n| \phi(\vec{x}_1) |0\rangle}{4E_m E_n}. \tag{2.42}$$

Together, equations 2.41 and 2.42 constitute the fit equations we will utilize to great effect in chapter 4.

Chapter 3

Lattice Quantum Chromodynamics

In this chapter we establish the foundational principles of lattice QCD. We discuss the motivation for developing a discretized theory, and how we discretize the path integral. We review various gluon and quark actions, arriving at the improved action we use in the work: the HISQ action. We end this chapter with an in-depth exploration of quark propagators and correlation functions on the lattice.

3.1 The motivation for Lattice QCD

The motivation to put QCD on the lattice originates from the problem of energy scales and perturbativity. The strong coupling constant $\alpha_s = \frac{g_s^2}{4\pi}$ has energy scale dependency, and at low energies the strong coupling constant becomes large. The result of a large α_s is that quarks and gluons do not exist as free particles, but are instead confined within the composite structure of hadrons [37]. Furthermore, perturbation theory requires coupling constants to be small, and so an analytical perturbative approach to QCD breaks down at low energies where the coupling constant is large. The methods of lattice QCD therefore involve using a numerical approach to solve the path integral, which can be managed by computers with the introduction of a discretized version of the theory.

3.2 The fundamentals of Lattice QCD

In this section, we explore the basic principles of Lattice QCD. These fundamentals cover path integral discretization, lattice actions, and the description of particles on the lattice. Much of the content and notation in this section is based on [38].

3.2.1 Path integral discretization

In section 2.5 we discussed the path integral and correlation functions in the context of the physical continuum, which is to say, not on the lattice. Let us begin building a discretized theory with the equation for the path integral (equation 2.38) and some real scalar field ϕ. We first move from a Minkowski metric to a Euclidean metric via Wick rotation, such that time $t \rightarrow -it$, and likewise for a four-vector x we have $x \rightarrow (-ix^0, \vec{x})$. We can then denote the action of the scalar field ϕ in terms of its Euclidean action $S_E[\phi]$. With these terms we can write the associated partition function Z in a Euclidean spacetime as

$$Z = \int D\phi e^{-S_E[\phi]}, \tag{3.1}$$

which is equivalent to the path integral without any operator insertion. We can arrive at some n-point correlation function by inserting an operator which is a function of the scalar field. If we insert such an operator $\Gamma[\phi]$, which has contains n instances of ϕ, our n-point correlation function is then

$$C_n(x) = \frac{1}{Z} \int D\phi \Gamma[\phi] e^{-S_E[\phi]}. \tag{3.2}$$

By rotating from a Minkowski metric to a Euclidean metric, we have replaced the oscillating phase term which appears in the equation of the path integral (equation 2.38) with an exponential decaying term.

Let us now introduce the lattice into this theory. We formally discretize our four-dimensional (Euclidean) space time, upon which we impose periodic boundary conditions. The resulting spacetime structure is a four-dimensional torus. This spacetime has coordinates $x = (x^0, x^1, x^2, x^3)$, where adjacent coordinates are separated by a constant *lattice spacing* a, which is sometimes referred to as the *lattice constant*. In this work we often mix notation for our spacetime dimensions where the dimension $\mu \in \{0,1,2,3\} \equiv \{t,x,y,z\}$. Each spacetime dimension has a number of coordinates, or *lattice sites* N_μ. The length of lattice in the μ direction is therefore aN_μ. Throughout this work we will often encounter quantities given in *lattice units*, where the necessary factors of a are implied such that the quantity is dimensionless. For example, we can simply say that a given lattice dimension is of length N_μ in lattice units. Similarly, in lattice units the four-dimensional torus has a volume $\mathrm{Vol} = N_t N_x N_y N_z$.

This discretization gives us the benefit of having a model with finite degrees of freedom. Within this model we can simulate standard model physics numerically with computers. This naturally introduces *discretization errors* that separate this theory from an infinite volume, physical continuum theory. However, having a non-infinite volume and non-zero lattice spacing prevents *infrared* and *ultra-violet* divergences in the theory. This is to say, we have removed very low energy/long distance effects, and we have removed very high energy/short distance effects

Under this scheme where we have discretized spacetime, we can treat continuous integrals over spacetime as finite sums over some number of lattice sites. Likewise, we can treat derivatives as finite differences. Recalling equation 3.2, we can write the infinite dimensional measure $D\phi$ as

$$D\phi = \prod_{x \in \text{lattice}} d\phi(x). \tag{3.3}$$

With the now discretized integral measure defined, we can address defining the discretized path integral itself. We do so via the methods of Monte Carlo integration [39, 40, 41, 42], which we will summarize here. Suppose we generate a number N_{cfg} of field configurations $\phi^{(\alpha)}$ for $\alpha \in \{1,2,...,N_{\text{cfg}}\}$; this gives us

$$\phi^{(\alpha)} = \{\phi^{(\alpha)}(x)\}. \tag{3.4}$$

Suppose now that we select some number of configurations from the probability distribution $P[\phi^{(\alpha)}]$, where $P[\phi^{(\alpha)}] \propto e^{-S_E[\phi^{(\alpha)}]}$. If that number of configurations is sufficiently high, we can approximate the n-point correlation function (equation 3.2) as

$$C_n[\phi] \approx \frac{1}{N_{\text{cfg}}} \sum_{\alpha=1}^{N_{\text{cfg}}} \Gamma[\phi^{(\alpha)}]. \tag{3.5}$$

This Monte Carlo approach allows us to apply statistical methods to our lattice simulation. To summarize: the action $S[\phi^{(\alpha)}]$ determines the probability distribution $P[\phi^{(\alpha)}]$, from which some number N_{cfg} of field configurations $\phi^{(\alpha)}$ are generated. The path integral is then calculated as the average over those field configurations. Configuration generation is carried out via a Markov Chain process, for which the Metropolis algorithm in good illustrative example [39]. This algorithm begins by selecting some initial $\phi(x_j)$. Some random number δ is then drawn from a uniform distribution with range $(-r, r)$, where then $\phi(x_j)$ is updated such that $\phi(x_j) \to \phi(x_j) + \delta$. This update precipitates some measurable change in the action ΔS. In the case where $\Delta S < 0$, then the update is kept and the algorithm moves on to $\phi(x_{j+1})$. Meanwhile if $\Delta S \geq 0$, we accept the update only if $e^{-\Delta S} > u$, where u is a random number in the range $(0,1)$. If $e^{-\Delta S} \leq u$ then the update is rejected and the algorithm proceeds to $\phi(x_{j+1})$. The last step in this algorithm is key to avoiding unwanted behavior in the Markov Chain. Namely, without allowing some random instances of positive ΔS, the algorithm might stabilize at what is only a local minimum, or simply find a state which minimizes the action. Allowing only negative instances of ΔS would drive our simulation towards a classical trajectory, and would not permit any quantum behavior in our configurations.

3.2.2 Gluon actions and improvements

Let us move on to discuss how we implement various actions on the lattice. Ultimately we seek to have both quark fields ψ and gluon fields A_μ in our discretized path integral, where the action in that integral ought to be guided by a Euclidean and discretized version of the QCD Lagrangian (equation 2.14). Putting quarks aside for now, let us first explore how we model gluons on the lattice. Rather than placing gluons at actual lattice sites $A_\mu(x)$, we instead model gluons as links between lattice sites $U_\mu(x)$. For a lattice spacing a, a direction along a lattice dimension μ, and the unit vector in that direction $\hat{\mu}$, we can define the path ordered (denoted by $\mathscr{P}$) gluon field *link* as

$$\begin{aligned} U_\mu(x) &= \mathscr{P} e^{-i\int_x^{x+a\hat{\mu}} g_s A\cdot dx} \\ &\approx e^{-iag_sA_\mu} \end{aligned} \tag{3.6}$$

With this approximation, we can maintain gauge invariance in our discretized theory. For example, if we apply the $SU(3)$ gauge transformation $G(x)$ on a gluon field link $U_\mu(x)$ we have

$$U_\mu(x) \to G(x)U_\mu(x)G^\dagger(x+a\hat{\mu}). \tag{3.7}$$

Here we can see that $U_\mu(x)$ transforms covariantly, and acts as a *gauge link* between lattice sites x and $x+a\hat{\mu}$. Given that gluons are the gauge bosons of QCD, we might also refer to the gauge link as a *gluon link*. We can also define the hermitian conjugate $U_\mu^\dagger(x) = U_{-\mu}(x+a\hat{\mu})$, which describes a gluon link in the inverse direction from $x+a\hat{\mu}$ to x. Because the $SU(3)$ gauge transformation is unitary ($GG^\dagger = 1$), connected loops of (gauge covariant) gluon links are necessarily gauge invariant.

The most basic gauge invariant quantity we can build with gluon links is an $a\times a$ loop, known widely in lattice theory as the *plaquette* [37, 43]. Tracing over color, we can define the plaquette $P_{\mu\nu}(x)$ as

$$P_{\mu\nu}(x) = \frac{1}{3}\mathrm{ReTr}\left[U_\mu(x)U_\nu(x+a\hat{\mu})U_\mu^\dagger(x+a\hat{\nu})U_\nu^\dagger(x)\right] \tag{3.8}$$

Defining the plaquette is a powerful tool on the lattice; we can see why when we expand the plaquette about the lattice site x_0. Expanding in powers of $-iag_sA$ we get

$$P_{\mu\nu}(x) = \frac{1}{3}\mathrm{ReTr}\left[1 - i\oint g_sA\cdot dx - \frac{1}{2}\left(\oint g_sA\cdot dx\right)^2 \ldots\right]. \tag{3.9}$$

If for now we only worry about first order terms, we can use Green's theorem to write the loop integral which appears in equation 3.9 as

$$\begin{aligned}\oint A\cdot dx &= \int_{-a/2}^{a/2} dx_\mu dx_\nu \left[\partial_\mu A_\nu(x_0+x) - \partial_\nu A_\mu(x_0+x)\right] \\ &= \int_{-a/2}^{a/2} dx_\mu dx_\nu \left[F_{\mu\nu}(x_0) + (x_\mu D_\mu + x_\nu D_\nu)F_{\mu\nu}(x_0) + \frac{1}{2}(x_\mu^2 D_\mu^2 + x_\nu^2 D_\nu^2)F_{\mu\nu}(x_0)\right] \\ &= a^2 F_{\mu\nu}(x_0) + \frac{a^4}{24}(D_\mu^2 + D_\nu^2)F_{\mu\nu}(x_0) + \ldots \quad ,\end{aligned} \tag{3.10}$$

where $F_{\mu\nu}$ is the QCD field strength tensor. Substituting the right hand side of the last line of equation 3.10 into equation 3.9 we arrive at

$$P_{\mu\nu}(x) = \frac{1}{3}\mathrm{Tr}\left[1 - \frac{a^4}{2}F_{\mu\nu}^2 - \frac{g_s^2 a^6}{24}F_{\mu\nu}(D_\mu^2 + D_\nu^2)F_{\mu\nu} + \ldots\right]\Bigg|_{x_0} . \tag{3.11}$$

We can use this formulation of the plaquette to define the Wilson Action S_{W} [37]. Truncating S_{W} to only $\mathscr{O}(a^2)$ terms we get

$$\begin{aligned}S_{\mathrm{W}} &= \frac{6}{g_s^2}\sum_{x,\mu>\nu}(1 - P_{\mu\nu}) \\ &= \int d^4x \sum_{\mu\nu}\frac{1}{2}\mathrm{Tr}\left[F_{\mu\nu}^2 + \frac{a^2}{12}F_{\mu\nu}(x_0)(D_\mu^2 + D_\nu^2)F_{\mu\nu}(x_0) + \ldots\right].\end{aligned} \tag{3.12}$$

With the Wilson action, we can define the scale of the lattice via the coupling strength term g_s. In common lattice QCD notation we often use the term $\beta = \frac{6}{g_s^2}$. In this context, we can refer to the Wilson action the first order gluon action: the action succeeds at describing gluon links on the lattice, but it does introduce certain discretization errors beginning at order a^2. From equation 3.12 we can see that the Wilson action differs from the continuum gluon action $\mathscr{L}_{\mathrm{glue}} = \frac{1}{2}\mathrm{Tr}F_{\mu\nu}F^{\mu\nu}$ by increasing powers of lattice spacing a. To address this problem we can implement the methods of Symanzik improvement [44], whereby the appropriate combination of various gluon loops removes certain terms of order a^2 or higher [45].

For the sake of completeness, it is worth mentioning the problem of *tadpoles* which can appear even in improved gluon actions. In lattice QCD, tadpoles are plaquettes with only one vertex. They effectively act as self-interaction loops which artificially inflate quantum corrections on the lattice. These higher order terms appear in the expansion of $e^{-iag_s A_\mu}$ in the gluon link operator U_μ. We can make our gluon action *tadpole improved* [46] by taking $U_\mu \to u_0 U_\mu$, where $u_0 = \langle 0| P_{\mu\nu} |0\rangle^{-1/4}$.

3.3 The Highly Improved Staggered Quark formalism

In the previous section, we described how to model gluons on the lattice as links between lattice sites, and used plaquettes to describe a Symanzik improved Wilson action. Plenty of lattice QCD research can be carried out by only considering gluons in this discretized theory. However because the interest of this work is ultimately related to the decays of heavy mesons, we seek to add the description of quarks to our action. We do so via the HISQ formalism [12], the construction of which we fully explore in this section.

3.3.1 Addressing quark masses on the lattice

Before we arrive at discretizing quarks on the lattice, let us first address the issue of dealing with quark masses on the lattice, which appear in the lattice QCD Lagrangian (given in equation 2.14). If we define the matrix $M = (\not{D} + m)$, where $\not{D}$ is a covariant finite difference operator, then we can succinctly define the action of QCD as

$$\begin{aligned} S_{\text{QCD}} &= S_{\text{glue}} + \sum_x \overline{\psi}(\not{D} + m)\psi, \\ &= S_{\text{glue}} + \sum_x \overline{\psi} M \psi. \end{aligned} \tag{3.13}$$

We can therefore define the quark portion of the QCD action as $S_{\text{quark}} \equiv \sum_x \overline{\psi} M \psi$. The matrix M appears in the path integral's partition function Z, which we can rearrange as:

$$\begin{aligned} Z &= \int \mathscr{D}U \mathscr{D}\psi \mathscr{D}\overline{\psi} e^{-(S_{\text{glue}}+\overline{\psi}M\psi)} \\ &= \int \mathscr{D}U \text{Det}(M) e^{-S_{\text{glue}}} \\ &= \int \mathscr{D}U e^{-S_{\text{glue}}+\log(\text{Det}(M))} \end{aligned} \tag{3.14}$$

The presence of $\text{Det}(M)$ in this equation poses a challenge to any line of lattice QCD research: calculating $\text{Det}(M)$ is prohibitively demanding of computer resources. So much so, that many lattice calculations are carried out in the *quenched approximation*, where sea quark self-interacting loops are removed from the action via the removal of the $\log(\text{Det}(M))$ term in equations 3.14. Our lattice calculations do not follow the quenched approximation, and so we still need a solution to calculating this term.

The challenge of calculating $\text{Det}(M)$ is not only reserved to the partition function: the term can also appear in the correlation function of a meson. Suppose we wish to simulate some generic meson H, with quark composition q_1 and q_2, traveling along the lattice. Inserting a creation operator for this meson at some initial time t_0, and then inserting an annihilation operator at some later time t_0+t, we can write its two-point correlation function[1] as

$$\langle 0 | H^\dagger(t_0+t) H(t_0) | 0 \rangle = \frac{1}{Z} \int \mathscr{D}U \underset{\text{spin}}{\text{Tr}} \underset{\text{color}}{\text{Tr}} \underset{\vec{x}}{\text{Tr}} \left[M_{q_1}^{-1} \gamma_5 M_{q_2}^{-1} \gamma_5 \right] e^{-S_{\text{glue}}+\log(\text{Det}(M))}. \tag{3.15}$$

In this equation γ_5 is some local operator which creates the pseudoscalar meson H with the appropriate quantum numbers, and within the integral we take the trace over spin, color, and the three lattice spatial dimensions $\vec{x}$. In equation 3.15 we can again spot the $\text{Det}(M)$ term.

1. We explore correlation functions on the lattice in great detail in section 3.5. We discuss them here only to prove the point that we cannot ignore the need to calculate $\text{Det}(M)$.

We can approximately calculate $\mathrm{Det}(M)$ if we make a slight detour and address the problem of calculating M^{-1} first. This inverse mass matrix also appears in equation 3.15, and though is not as expensive to calculate as $\mathrm{Det}(M)$, it too is prohibitively demanding of computer resources. Therefore we instead take advantage of the Hermitian positive definite properties of the mass matrix:

$$M^{\dagger}(M^{\dagger}M)^{-1} = M(M^2)^{-1} = MM^{-2} = M^{-1}. \tag{3.16}$$

Therefore instead of directly calculating M^{-1} we can instead place our interest in $(M^{\dagger}M)^{-1}$. For the propagator source[2] ξ we can write that $\xi = M^{\dagger}Mx$. This then implies that $x = (M^{\dagger}M)^{-1}\xi$. To solve for x here, we can employ the conjugate gradient algorithm [47]. As a prerequisite to using this algorithm, we can first identify that minimizing $f(x)$ where

$$f(x) = \frac{1}{2}x^T M^{\dagger}Mx - \xi^T x, \tag{3.17}$$

is equivalent to solving for x. We will not go into full detail, but we will summarize the technique here. The conjugate gradient algorithm minimizes $f(x)$ by iteratively moving along directions which are *conjugate* (independent with respect to the function's curvature), rather than simply moving along the direction of steepest descent. Each step n chooses an optimal step size along the current direction. That optimal step size is determined by the residual r_n, for which

$$-r_n = \nabla f(x_n) = M^{\dagger}Mx_n - \xi. \tag{3.18}$$

Iterating upon these steps guarantees that the largest reduction in $f(x)$ occurs along that line. By constructing mutually conjugate directions, the algorithm converges to the minimum of $f(x)$ in at most n steps for an n-dimensional quadratic function.

Once we have minimized $f(x)$, we have equivalently solved for $x = (M^{\dagger}M)^{-1}\xi$. Using then the relations in equation 3.16 we can more easily arrive at an approximate value of M^{-1} and save computation time. Recall however that our initial motivation for calculating M^{-1} was that it would help us calculate $\mathrm{Det}(M)$. Having already calculated the inversion of $(M^{\dagger}M)^{-1}$ in the previous step,

2. See section 3.5.5 for how we implement random wall sources.

we can utilize another algorithmic technique: the Φ algorithm [48]. With this technique we modify the determinant term like $\text{Det}(M) \to \text{Det}(M^\dagger M)$. Introducing an arbitrary scalar field Φ, we can write the heuristic equation

$$\text{Det}(M^\dagger M) = \int \mathscr{D}\Phi^\dagger \mathscr{D}\Phi e^{-\Phi^\dagger (M^\dagger M)^{-1}\Phi}. \tag{3.19}$$

We do not attempt to solve this equation analytically, we instead utilize numerical Monte Carlo techniques. We find this technique to be successful in determining $\text{Det}(M^\dagger M)$, which leaves us with one final hurdle: for each quark flavor we would now have two factors of the mass matrix. In fact, as a result of the doubling symmetry and our staggered quarks (which we discuss in the following sections), we actually are left with eight factors of M. Fortunately for us, taking the eighth root of the determinant is sufficient to recover an acceptable determination of $\text{Det}(M)$.

In both the cases of calculating M^{-1} and $\text{Det}(M)$, even with these algorithmic techniques, the computation time needed remains burdensome. Suppose we want to include sea quarks in our action. At the low energy scale of lattice QCD, sea quark effects are dominated by up, down, and strange quarks [49]. This worsens the problem of calculating M^{-1} and $\text{Det}(M)$, because these quantities must be calculated for every quark flavor. Problematically, doing so is more expensive for lighter quark flavors. We can somewhat suppress this problem by simulating two degenerate light quarks l such that $m_l = m_u = m_d$, rather than calculating M^{-1} and $\text{Det}(M)$ separately for an up quark and down quark of non-degenerate masses. Additionally, we can set the light quark mass to be non-physically large, closer to the mass of the strange quark. We do this explicitly on some of our gluon field ensembles (see section 3.4.3). The lattice spacing in this work are fine enough that we can justify adding charm quarks to the sea as well. However the ultra-violet cutoff effect from these lattice spacings rules out the need to add bottom and top quarks to the sea.

3.3.2 The naive quark action and the doubling problem

Recall that we can separate the QCD action S_{QCD} into a gluon portion S_{glue} and a quark portion $S_q = \sum_x \overline{\psi} M \psi$, where the quark mass matrix $M = (\not{D} + m)$. Under the same $SU(3)$ gauge transformation we applied to gluon links, we expect $\psi(x) \to G(x)\psi(x)$. We can identify that the matrix M in S_{quark} contains a covariant derivative term. In the interest of discretization, let us introduce the discrete derivative Δ_μ where

$$\Delta_\mu \psi(x) = \frac{1}{2a}\left[U_\mu(x)\psi(x+a\hat{\mu}) - U^\dagger_\mu(x-a\hat{\mu})\psi(x-a\hat{\mu})\right]. \tag{3.20}$$

Discretizing the quark action in this naive way does get us closer to a full description of fermions on the lattice, however it does introduce the problem of *doubling symmetry* [50, 51]. This symmetry occurs where, for every quark we instantiate on the lattice, we indirectly create 15 other quarks of equivalent flavor at different lattice sites. To explain this phenomenon, let us first consider the qualities of gamma matrices γ_μ in a Euclidean metric. In such a case, the gamma matrices have the following relevant properties: $\{\gamma_\mu, \gamma_\nu\} = 2\delta_{\mu\nu}$, $\gamma^\dagger_\mu = \gamma_\mu$, and $\gamma^2_\mu = 1$. With these matrices we can define complete set of 16 spinor matrices γ_n as

$$\gamma_n = \prod_{\mu=0}^{3} (\gamma_\mu)^{n_\mu}, \tag{3.21}$$

where n is a four-vector whose components $n_\mu \in \{0,1\}$. Suppose now that the naive quark action is symmetric about the transformation $\psi \to \tilde{\psi}$ where

$$\begin{aligned} \tilde{\psi} &\equiv \gamma_5\gamma_\mu(-1)^{\frac{x_\mu}{a}}\psi(x), \\ &= \gamma_5\gamma_\mu e^{\frac{i\pi x_\mu}{a}}\psi(x). \end{aligned} \tag{3.22}$$

As a result of the $\frac{\pi}{a}$ term which appears in this equation, there will be an equivalent mode with momentum $p_\mu \approx \frac{\pi}{a}$ for every low momentum mode $\psi(x)$. Here we can also note that we can make this transformation in one lattice dimension independently of any other. As such, we can characterize the behavior of this general transformation as

$$\begin{aligned} \psi(x) &\to B_\zeta(x)\psi(x), \\ \overline{\psi}(x) &\to \overline{\psi}(x)B_\zeta^\dagger(x). \end{aligned} \tag{3.23}$$

We can define this general transformation operator $B_\zeta(x)$ for $\zeta_\mu \in \{0,1\}$ as

$$\begin{aligned} B_\zeta(x) &\equiv \gamma_{\overline{\zeta}}(-1)^{\frac{\zeta\cdot x}{a}} \propto \prod_\mu (\gamma_5\gamma_\mu)^{\zeta_\mu} e^{\frac{ix\cdot\zeta\pi}{a}}, \\ \overline{\zeta}_\mu &\equiv \sum_{\mu\neq\nu} \zeta_\nu \mathrm{mod} 2. \end{aligned} \tag{3.24}$$

Though the notation here is dense, the key take away is that we have a total of 16 ζ_μs, 15 *doublers* and one real $\zeta_0 = (0,0,0,0)$ mode. From now on we will refer to these extra fermion doublers as *tastes* rather than flavors, to avoid the obvious confusion with physical quark flavors.

If these various quark tastes were identical and did not interact with each other, then a simple insertion of $\frac{1}{16}$ into $\mathrm{Det}(M)$ would solve the problem of this doubling symmetry. Unfortunately, the existence of *taste exchange* interaction prevents such a simple solution; the various tastes do in fact interact with each other. For example, a quark can emit a gluon with momentum $p \approx \frac{\zeta\pi}{a}$, which can then be absorbed by another low momentum quark of another taste. Such quarks would remain mostly on-shell, and as a result they would both experience taste change. This form of taste change is present on the lattice as another discretization error, and is suppressed by the scale of a^2. Various other quark actions attempt to resolve the problem of doubling symmetry by giving mass to the doublers. Such a change causes the tastes to decouple as $a \to 0$. Among such actions are the well known Wilson quark action [37] and Clover quark action [52]. The Wilson quark action however has fermions which break chiral symmetry, resulting in additional $\mathcal{O}(a)$ errors. The Clover quark action improves on the Wilson quark action, but only order-by-order in perturbation theory. In this work, we use the HISQ action [12], which we develop further in the following sections.

3.3.3 Staggered quarks

Let us now address the namesake *staggered quarks* [53] which will appear in HISQ action. Staggered quarks are functionally equivalent to naive quarks, however the introduction of quark staggering greatly reduces computation time. We begin our investigation of staggered quarks by transforming the naive quark fields as

$$\begin{aligned} \psi(x) &\to \Omega(x)\chi(x), \\ \overline{\psi}(x) &\to \overline{\chi}(x)\Omega^{\dagger}(x). \end{aligned} \tag{3.25}$$

Here we introduce another set of 16 spinor matrices $\Omega(x)$, which we define as

$$\Omega(x) \equiv \prod_{\mu=0}^{3} \gamma_{\mu}^{(x_{\mu})}. \tag{3.26}$$

These matrices have the properties that $\Omega^{\dagger}(x)\Omega(x) = 1$, and $\Omega(x) = \gamma_n$ for $n_{\mu} = x_{\mu}\text{mod}2$. With these spinor matrices we can define the spinor matrix term $\alpha_{\mu}(x)$ as

$$\alpha_{\mu}(x) = \Omega^{\dagger}(x)\gamma_{\mu}\Omega(x+\hat{\mu}). \tag{3.27}$$

Using this definition of $\alpha_{\mu}(x)$, and the discretized covariant derivative Δ from the naive quark action, we can define the staggered quark action S_{sq} as

$$\begin{aligned} S_{\text{sq}} &= \overline{\psi}(x)(\gamma\cdot\Delta+m)\psi(x), \\ &= \overline{\chi}(x)(\alpha(x)\cdot\Delta+m)\chi(x). \end{aligned} \tag{3.28}$$

One benefit of this action is that it is diagonal in spinor space. As a result, we only need one component of the staggered quark field χ: the various components of χ are identical. We can utilize this quality of staggered quark fields to construct the observable

$$\langle\chi(x)\overline{\chi}(y)\rangle = g(x,y)\mathbf{1}_{\text{spinor}}. \tag{3.29}$$

Here we introduce the staggered quark propagator $g(x,y)$, which has one only spinor component. Fortunately for us, having only one spinor component effectively reduces the number of quark tastes present on the lattice from 16 to four, and computation time is likewise reduced by that same factor of four.

3.3.4 Symanzik improved quark actions

We can begin working towards the final form of the HISQ action by first tackling leading order taste exchange discretization errors. We do this through the introduction of the form factor $f_\mu(p)$ to the gluon quark vertex $\overline{\psi}\gamma_\mu U_\mu \psi$. This form factor has the quality $f_\mu(p) = 0$ for $p \to \frac{\zeta\pi}{a}$, $\zeta^2 \neq 0$, and $\zeta_\mu = 0$. In the case of $\zeta_\mu = 1$, the interaction vanishes. Alternatively, $f_\mu(p) = 1$ for $p \to 0$. This formulation is facilitated on the lattice by the smearing operator $\mathscr{F}_\mu$, which acts on our gluon gauge links like $U_\mu(x) \to \mathscr{F}_\mu U_\mu(x)$. Symmetrizing over all possible operator orderings [54], we can define the smearing operator as

$$\mathscr{F}_\mu \equiv \prod_{\mu \neq \nu} \left(1 + \frac{a^2 \delta_\nu^{(2)}}{4} \right) \Bigg|_{\text{symm}} . \tag{3.30}$$

Here we use the special operator $\delta_\nu^{(2)}$, where the (2) notation indicates that the operator acts like a covariant second derivative when acting on the gauge link $U_\mu(x)$:

$$\begin{aligned} \delta_\nu^{(2)} U_\mu(x) \equiv \frac{1}{a^2} \Big[& U_\nu(x) U_\mu(x + a\hat{\nu}) U_\nu^\dagger(x + a\hat{\mu}) \\ & + U_\nu^\dagger(x - a\hat{\nu}) U_\mu(x - a\hat{\nu}) U_\nu(x - a\hat{\nu} + a\hat{\mu}) - 2U_\mu(x) \Big]. \end{aligned} \tag{3.31}$$

With this definition we can see that when $p \to \frac{\pi}{a}$ the smearing operator $\mathscr{F}$ vanishes as $\delta_\nu^{(2)} U_\mu \to \frac{-4}{a^2} U_\mu$.

Unfortunately, $\mathscr{O}(a^2)$ errors are introduced in equation 3.30. These errors however are addressed by the Symanzik-improved ASQTAD action [54]. Implementing the ASQTAD action begins with amending the smearing operator such that

$$\mathscr{F}_\mu^{\text{ASQTAD}} = \mathscr{F}_\mu - \sum_{\nu\neq\mu} \frac{a^2(\delta_\nu)^2}{4}. \tag{3.32}$$

Here we once again have a special operator δ_ν, which acts as a covariant first derivative on the gauge link:

$$\begin{aligned}\delta_\nu U_\mu(x) \equiv \frac{1}{a}\Big[&U_\nu(x)U_\mu(x+a\hat{\nu})U_\nu^\dagger(x+a\hat{\mu}) \\ &- U_\nu^\dagger(x-a\hat{\nu})U_\mu(x-a\hat{\nu})U_\nu(x-a\hat{\nu}+a\hat{\mu})\Big].\end{aligned} \tag{3.33}$$

Before arriving at the final form of the ASQTAD action, we need to also address the naive discrete derivative operator Δ_μ (see equation 3.40), which also has $\mathscr{O}(a^2)$ errors. We do so by the inclusion of a *Naik* term [55], such that the discrete derivative $\Delta_\mu \to \Delta_\mu - \frac{a^2}{6}\Delta_\mu^3$. Putting this all together we arrive at the equation for the ASQTAD action:

$$S_{\text{ASQTAD}} = \sum_x \overline{\psi}(x)\left[\sum_\mu \gamma_\mu\left(\Delta_\mu(V) - \frac{a^2}{6}\Delta_\mu^3(U) + m_0\right)\right], \tag{3.34}$$

where m_0 is the bare lattice mass and $V_\mu = \mathscr{F}_\mu^{\text{ASQTAD}} U_\mu(x)$.

At this point our Symanzik-improved action serves us well at tree level. The smearing in the ASQTAD action however introduces a problem at one loop. This is to say, when we smear gauge links in one direction under the ASQTAD action, we are left with non-smeared gauge links in all orthogonal directions. The presence of these non-smeared gauge links allows for the persistence of taste exchange errors in our quark action at one loop. Addressing this problem within the ASQTAD action directly leads us to the HISQ action [12], which implements the technique of repeated smearing. We define the HISQ action as

$$S_{\text{HISQ}} = \sum_x \overline{\psi}(x)(\cancel{D}^{\text{HISQ}} + m)\psi. \tag{3.35}$$

Furthermore we define the HISQ covariant derivative D_μ^{HISQ} and the HISQ smearing operator $\mathscr{F}_\mu^{\text{HISQ}}$ as

$$D_\mu^{\text{HISQ}} \equiv \Delta_\mu(W) - \frac{a^2}{6}\left(1+\varepsilon_{\text{tree}}(m)\right)\Delta_\mu^3(X) \tag{3.36}$$

$$\mathscr{F}_\mu^{\text{HISQ}} \equiv \left(\mathscr{F}_\mu - \sum_{\nu\neq\mu}\frac{a^2(\delta_\nu)^2}{4}\right)\mathscr{U}\mathscr{F}_\mu. \tag{3.37}$$

Let us break down the various terms which appear in equations 3.35 and 3.36. First, in equation 3.36 we find a different Naik term which contains $\varepsilon_{\text{tree}}$, which is a function of the tree level pole mass m_{tree}. In the HISQ action we can define m_{tree} as

$$m_{\text{tree}}(m) = m\left(1 - \frac{3}{80}m^4 + \frac{23}{2240}m^6 + \frac{1783}{537600}m^{10} + \mathscr{O}(m^{12})\right). \tag{3.38}$$

Furthermore if we require that the tree level pole mass is equal to the tree level kinematic mass [56], we can define the Naik Epsilon term [55] at tree level as

$$\varepsilon_{\text{tree}}(m) = -1 + \frac{1}{\sinh^2(m_{\text{tree}})} \times \left(4 - \sqrt{4 + \frac{12m_{\text{tree}}}{\cosh(m_{\text{tree}})\sinh(m_{\text{tree}})}},\right) \tag{3.39}$$

where we have suppressed m arguments in m_{tree}. Furthermore in equation 3.36 we introduce the difference operators W and X, where

$$\begin{aligned} W_\mu(X) &\equiv \mathscr{F}_\mu^{\text{HISQ}} U_\mu(x), \\ X_\mu(x) &\equiv \mathscr{U}\mathscr{F}_\mu U_\mu(x). \end{aligned} \tag{3.40}$$

Finally then in equation 3.37 and 3.40 we implement the special operator $\mathscr{U}$, which make the operator it acts upon unitary. From this construction, we can say that the HISQ action taste exchange error is corrected at order $\alpha_s(am)^2$, which is a substantial advantage over the ASQTAD action.

3.3.5 Twisted boundary conditions

In the previous section we described the doubling symmetry problem, which is related to specific high momentum modes ($p \approx \frac{\pi}{a}$) on the lattice. It is worthwhile then to discuss how we actually impart momentum into quarks on the lattice. We elect to do this via twisted boundary conditions [57, 58, 59, 60], which we briefly go over here. For a quark of three-momentum $\vec{p}$, we can define the j-th component of its momentum p_j as

$$p_j = 2\pi \frac{\theta_j}{aN_j}, \tag{3.41}$$

where θ is the *twist angle* and aN_j is the length of the lattice in the j direction. We use the index j here rather than μ because twisted boundary conditions are limited to the three spatial dimensions on the lattice $j \in \{1,2,3\} \equiv \{x,y,z\}$. Using this definition, suppose we aim to impart momentum by transforming our quark fields as $\psi(x) \to e^{i\vec{p}\cdot\vec{x}}\psi(x)$. On the lattice, we can do this by multiplying gauge links by e^{iap_j}, giving us

$$\overline{\psi} e^{iap_j} U_j(x) \psi(x + a\hat{j}) = \overline{\psi} e^{i\vec{p}\cdot\vec{x}} U_j(x) e^{-i\vec{p}\cdot(\vec{x}+a\hat{j})} \psi(x + a\hat{j}). \tag{3.42}$$

Inserting momentum onto the quark field in this manner leads to periodic boundary conditions, such that

$$\psi(x + aN_j\hat{j}) = e^{2\pi i\theta_j}\psi(x). \tag{3.43}$$

The presence of the aN_j terms in these equations means that this method introduces twist angle dependent finite volume effects into our lattice simulation. We can minimize such effects if we avoid selecting values of $\theta \approx n\frac{2\pi}{N_j}$, where n is just some integer [61].

3.4 The heavy-HISQ method

Throughout this work, we will reference a generic heavy quark h. This heavy quark paired with a *spectator* light quark l or strange quark s constitutes a generic heavy meson H. When the flavor of the spectator quark is important we will use the notation $H_l \equiv H$ and H_s, but for much of this discussion H will suffice. In this section we outline how, by varying the mass of this heavy quark, we can model the four meson decays of interest to this work: $D \to \pi$, $B \to \pi$, $D_s \to K$, $B_s \to K$.

3.4.1 Varying the heavy quark mass

In this work, we simulate heavy quarks which have masses am_h that range from the physical charm quark mass up to the limit where $am_h = 0.8$. This somewhat arbitrary choice was made to avoid potential divergences which would appear in Taylor series or power series expansions of terms containing factors of am_h, equation 5.13 in chapter 5 for example. It has been recently shown that values of $am_h \geq 1$ (but not $am_h \gg 1$) do not necessarily jeopardize our lattice calculations[3], the small $\mathcal{O}(am_h)^2$ discretization errors of the HISQ action help in this regard. Besides our finest lattices however, the values of am_h required to meet the physical bottom quark mass lie well above the soft threshold where large values of am_h would jeopardize our lattice calculations.

Our solution to this problem is the heavy-HISQ method. In this method we simulate and perform calculations at many heavy quark masses, from the charm quark mass up to some percentage of the physical bottom quark mass. This provides us with enough data to extrapolate results to the physical bottom quark mass, provided we have accounted for heavy quark mass dependencies in that extrapolation. This quark mass extrapolation is analogous to a continuum limit extrapolation,

3. See appendix A in [62].

where we use gluon field ensembles of varying lattice spacing a such that we can model how results change as $a \to 0$. The heavy-HISQ method has been utilized successfully in previous lattice calculations involving D and B mesons [13, 14, 15, 16, 17, 18], and we likewise employ the method in this work as well.

3.4.2 Heavy Quark Effective Theory

As alluded to previously, extrapolating to the physical bottom quark mass only produces reliable results if we properly account for heavy quark mass dependencies. We do so through our implementation of Heavy Quark Effective Theory (HQET) [63, 64, 65]. This theory aims to construct an effective theory of heavy meson decays, which improves in quality as we approach the *heavy quark limit*, which is to say, as $m_h \to \infty$. This treatment is possible due to the significant energy splitting between the heavy quarks (charm and bottom) and the natural energy scale of lattice QCD $\Lambda_{\text{QCD}} = 0.5$ GeV. The energy scale Λ_{QCD} aligns well with the light and strange valence quarks in our simulations, which we can take to be the light degrees of freedom in this theory.

In the heavy quark limit, we can consider the heavy quark to be static in the rest frame of the heavy meson. As a result, the light and strange quarks only interact with the color field of the static heavy meson; they are impartial to any differences in the heavy meson's flavor or spin [66]. So long as the implications of the heavy quark limit are valid down to the energy scale of the charm quark, we can safely compare and interpolate the results of heavy mesons whose masses lie within the D to B mass range. That validity is ensured by various HQET-respecting terms which appear in the later stages (see chapter 5) of our form factor calculations.

3.4.3 HISQ ensembles

For this work, we have access to data generated from five different gluon field ensembles, and we are in the process of generating data from four more ensembles. Table 3.1 presents the specifications of the five ensembles we presently use in this work. We assign to each ensemble, or *set*, a label which denotes its relative lattice spacing a, and the ratio of the valence strange quark mass to the valence light quark mass. The lattice spacings include *fine* ($a \approx 0.09$fm), *superfine* ($a \approx 0.06$), and *ultrafine* ($a \approx 0.044$), which we can abbreviate as “f”, “sf”, and “uf” respectively. If for an ensemble the strange to light quark mass ratio $m_s/m_l \approx 5$, then a “5” is added to the set label. Meanwhile if that ratio on an ensemble instead matches the physical expectation [67] of $m_s/m_l = 27.18(10)$, then the suffix “phys” is added to the ensemble label.

The lattice spacing a is not something that we directly set for our gluon field ensembles, but is something we must derive. To do so, we first need to set the strong coupling constant strength g_s; by convention we do so indirectly by instead choosing a value of $\beta = 6/g_s^2$ (see equation 3.12). With β defined we can go on to calculate the ratio w_0/a, where w_0 is the Wilson flow parameter [68]. This calculation is carried out by smearing and integrating the Wilson flow [69] on the lattice until some dimensionless observable of our choice converges on a desired or expected value. The observables we use are the continuum mass ratios of the pion, kaon, and Ω baryon [68, 70]. In the context of this work, we arrive at a Wilson flow parameter value of $w_0 = 0.1715(9)$fm [71], from which we can then finally calculate lattice spacings.

The MILC collaboration generates all the HISQ ensembles we use in this work [72, 73, 74, 67]. These ensembles can all be described as $N_f = 2+1+1$ ensembles. This indicates that, in the sea, the ensembles have two degenerate light quarks, a strange quark, and a charm quark. The absence of bottom and top quarks in the sea does give rise to some systematic uncertainties. However at the low energy scale we use in this work, these uncertainties are small. The strange and charm quark masses in the sea are not exactly equal to the valence strange and charm quark masses

Table 3.1: Gluon field ensembles used in this work. The parameter $\beta = 6/g_s^2$ sets the strength of the strong coupling constant g_s^2. We discuss the ratio of the Wilson flow parameter w_0 divided by lattice spacing a in the text. The dimensions of the lattice on each ensemble in lattice units are given in column 4, where we have three spatial dimension of length N_x and one temporal dimension of length N_t. Finally, the masses of the various sea and valence quarks in each ensemble are given in columns 5-9

Set	β	w_0/a	$N_x^3 \times N_t$	$am_l^{\text{sea/val}}$	am_s^{sea}	am_c^{sea}	am_s^{val}	am_c^{val}
1 - f5	6.3	1.9006(20)	$32^3 \times 96$	0.0074	0.037	0.440	0.0376	0.449
2 - fphys	6.3	1.9518(7)	$64^3 \times 96$	0.00120	0.0363	0.432	0.036	0.433
3 - sf5	6.72	2.896(6)	$48^3 \times 144$	0.0048	0.024	0.286	0.0234	0.274
4- sfphys	6.72	3.0170(23)	$96^3 \times 192$	0.0008	0.022	0.260	0.0219	0.2585
5 - uf5	7.0	3.892(12)	$64^3 \times 192$	0.00316	0.0158	0.188	0.0165	0.194

on our ensembles. Following the tuning procedure seen in [75] we are able to tune those valence quark masses to be approximately equal to their physical values. Any remaining effect of quark mass mistuning (including that of the light quarks who have $am_l^{\text{sea}} = am_l^{\text{val}}$) is accounted for later in our form factor calculation chapter 5.

3.5 Correlation functions on the lattice

In section 2.5 we arrived at a description of continuum correlation functions expressed in terms of amplitudes and energies. In this section, we will formulate a description of correlation functions in terms of quark propagators on the lattice. It is these forms of correlations that we can actually instantiate on the lattice. These two descriptions are what allow us to fit the lattice correlation functions to the energy and amplitude fit forms we saw in the previous chapter. Moving forward in this effort, we will abide by the convention that lattice quantities be given in lattice units. Therefore the notation for quantities with units of energy $aE \to E$, units of length $aN_\mu \to N_\mu$, and units of time $at \to t$. In this scheme, lattice time corresponds to integer steps on the lattice, which we often refer to as lattice *time slices*.

We can begin our in-depth discussion of correlation functions by first examining two-point correlation functions. To construct such a function on the lattice, we insert the creation operator of a meson at some initial lattice site x_0. Breaking this lattice site into its temporal and spatial components we can say that $x_0 = (t_0, \vec{x}_0)$. We then allow the meson to propagate along the lattice until it reaches some lattice site $x_1 = (t_1, \vec{x}_1)$, where we insert the appropriate meson annihilation operator. Following the notation of equation 2.37 for $n = 2$ we can write the two point correlation function as

$$C_2(x_1, x_0) = \langle\Omega|\, \phi_H(x_1)\phi_H^\dagger(x_0)\,|\Omega\rangle\,, \tag{3.44}$$

where we have required $t_0 < t_1$, $|\Omega\rangle$ is the interacting theory ground state, and ϕ_H is a scalar field in the Heisenberg picture. If we impart three-momentum $\vec{p}$ onto the meson, take the Fourier transform of equation 3.44, and take the average over the three spatial dimensions $N_x \equiv N_y \equiv N_z$, we obtain a correlation function which only has dependency on the temporal dimension:

$$\tilde{C}_2^{\vec{p}}(t_0, t_1) = \frac{1}{N_x^3} \sum_{\vec{x}_1, \vec{x}_0} e^{-i\vec{p}\cdot(\vec{x}_0 - \vec{x}_1)} C_2(x_1, x_0). \tag{3.45}$$

Mapping the function in this way allows us to interpret the correlation function as a probability distribution whose amplitude corresponds to the likely presence of the meson propagator at some time t between t_0 and t_1.

Keeping this formulation in mind, let us move on to the $n = 3$ case: the three-point correlation function. In this scenario, the meson interacts with the current insertion J at some time slice t_1 in between its creation at t_0 and annihilation at t_2. We may then write the appropriate three-point correlation function as

$$C_3(x_2, x_1, x_0) = \langle\Omega|\, \phi_H(x_2) J(x_1) \phi_H^\dagger(x_0)\,|\Omega\rangle\,, \tag{3.46}$$

where we similarly require $t_0 < t_1 < t_2$. Following the same methods for the $n = 2$ case we can arrive at a three-point correlation function which only has time dependence by writing

$$\tilde{C}_3^{\vec{p}}(t_0, t_1, t_2) = \frac{1}{N_x^3} \sum_{\vec{x}_2, \vec{x}_1, \vec{x}_0} e^{-i\vec{p}\cdot(\vec{x}_0 - \vec{x}_1)} C_3(x_2, x_1, x_0). \tag{3.47}$$

Note that in the equation above we have only applied three-momentum to the meson propagating from $\vec{x}_0$ to $\vec{x}_1$. In this form we can interpret the three-point correlation function as the probability amplitude for a meson state created at t_0 to propagate in time, interact with the current insertion at t_1, and subsequently be projected onto the final meson state at t_2.

Only two and three-point correlation functions are of relevant interest to this work, and so we can condense the notation above which is contextualized for any n-point correlation function. First, moving forwards we will simplify the notation of our time-dependent correlation functions as $\tilde{C}_2^{\vec{p}}(t_0,t_1) \to C_2(t_0,t_1)$, and $\tilde{C}_3^{\vec{p}}(t_0,t_1,t_2) \to C_3(t_0,t_1,t_2)$. Second, while we insert creation operators at different source times t_0, the translational invariance of the lattice allow us to shift correlation functions as we please[4]. We always then work within the effective assumption that $t_0 = 0$. For a two-point function, we conventionally state that the matching annihilation operator is inserted at time $t_0 + t = t$. This single parameter t then parametrizes the separation of the creation and annihilation operators, and as such the correlation function only has t dependence: $C_2(t_0, t_0 + t) \to C_2(t)$. Meanwhile for three-point correlation functions, we maintain the convention that annihilation occurs at some time $t_0 + T = T$, while the current insertion occurs at time $t_0 + t = t$. Insisting that $t_0 < t < T$ ensures that the interaction on the lattice corresponds to the relevant equivalent physical phenomenon. We therefore have $C_3(t_0, t_0 + t, t_0 + T) \to C_3(t, T)$. In our simulations we therefore implement values of T which are much smaller than the temporal length of the lattice N_t. This avoids the effects which periodic boundary conditions might have on the otherwise clean physical ordering of creation, interaction, and then annihilation. This choice also justifies the assumption made we will make in equation 4.2 where we ignore the backwards propagating contribution in the three-point function fit form (see section 4.1.1).

---

4. In fact, we often fit multiple correlation functions with varying source times on the same configuration. By shifting the source time t_0 to the origin, we can take their average and improve their statistics

3.5.1 Staggered quark phases and spin-taste notation

As discussed throughout section 3.3, the staggered quarks we wish to simulate on the lattice vary in spinor and taste degrees of freedom. In this section and those following, we describe how we encode the composite *spin-taste* structure of a propagating quark as a general *phase term* in its corresponding correlation function.

We can begin by recalling the definition of the spinor matrices γ_n in equation 3.21, which are composed of multiplicative sums of the gamma matrices γ_μ raised to the power n_μ, where n is a four-vector whose components n_μ are either 0 or 1. In equation 3.26 we defined the related spinor matrices $\Omega(x)$ which are equal to the γ_n in the case that $n = (x)\text{mod}2$. The matrices $\Omega(x)$ facilitate the local field transformation of a naive quark $\psi(x)$ to a staggered quark $\chi(x)$ such that

$$\begin{aligned} \psi(x) &\to \Omega(x)\chi(x), \\ \overline{\psi} &\to \overline{\chi}(x)\Omega^\dagger(x). \end{aligned} \tag{3.48}$$

Finally then let us recall the spinor matrix term $\alpha_\mu(x)$ in equation 3.27. We can redefine $\alpha_\mu(x)$ as

$$\alpha_\mu(x) = \Omega^\dagger(x)\gamma_\mu\Omega(x+\hat{\mu}) = (-1)^{x_\mu^<}, \tag{3.49}$$

$$x_\mu^< = \sum_{\nu=0}^{\mu-1} x_\nu. \tag{3.50}$$

With this expanded definition we might better refer to $\alpha_\mu(x)$ as a lattice site-dependent phase term. We can see where such a term might appear when we see how the non-staggered Feynman quark propagator $S_F(a,b)$ relates to the staggered quark propagator $g(a,b)$:

$$\begin{aligned} S_F(a,b) &= \langle\psi(a)\overline{\psi}(b)\rangle \\ &= g(a,b)\Omega(a)\Omega^\dagger(b). \end{aligned} \tag{3.51}$$

This formulation of the Feynman propagators describes a quark that propagates from a point b to some point a. To describe the case for an antiquark propagating from b to a, we have

$$\begin{aligned}\gamma_5 S_F^\dagger(a,b)\gamma_5 &= \langle\psi(a)\overline{\psi}(b)\rangle,\\ &= \gamma_5\Omega(b)\Omega^\dagger(a)g^\dagger(a,b)\gamma_5.\end{aligned} \tag{3.52}$$

Here the “fifth” gamma matrix $\gamma_5 = \gamma_0\gamma_1\gamma_2\gamma_3$, and therefore $\gamma_5 = \gamma_n$ when $n = (1,1,1,1)$. The presence of γ_5 matrices in equation 3.52 is a result of reversing the argument ordering in the Feynman propagator: it preserves the hermitian symmetry of the action.

From equation 3.28 we know that the phase term $\alpha_\mu(x)$ appears in the staggered quark action. To complete our discussion of the HISQ method we ought to describe how the spin-taste structure of a propagator is encoded as a lattice site dependent phase. Recalling the doubling problem described in section 3.3.4, for every naive quark operator we are left with 16 different taste operators. These operators we can represent as four-dimensional vectors s whose components are either 1 or 0. These tastes have the identical structure to the spin matrices γ_n, and so we will differentiate between the two by denoting a taste matrix as ξ_s (not to be confused with the notation for the propagator source ξ). We can therefore denote a propagator's spin-taste structure as $\gamma_n\otimes\xi_s$. Recalling equation 3.27 we can write the spin-taste operator's action upon a quark field as

$$\gamma_n\otimes\xi_s\psi(x) = (-1)^{\bar{s}\cdot x}\gamma_s^\dagger\gamma_n\psi(x\oplus(s+n)) \tag{3.53}$$

Here we introduce the vector $\bar{s}$ where $\bar{s}_\mu = (\sum_{\mu\neq\nu}s_\nu)\mathrm{mod}2$. We also use the direct sum operator $\oplus$ to add $(s+n)$ to the lattice site x modulo the hypercube (ignoring the periodic boundary conditions for now) in which x lies. We can call this hypercube X, where $X_\mu\mathrm{mod}2 = 0$. As such we can write that if x lies in X, then

$$(x\oplus(s+n))_\mu \equiv X_\mu + (x_\mu - X_\mu + (s+n)_\mu)\mathrm{mod}2, \tag{3.54}$$

from which we get the useful property that $x_\mu - X_\mu \in \{0,1\}$. The possible results of $(x \oplus (s+n))_\mu$ are limited to three outcomes, which are dependent on whether or not $s_\mu = n_\mu$ and whether $x_\mu \text{mod}2 = 0$ or 1:

$$(x \oplus (s+n))_\mu = \begin{cases} x_\mu & (s_\mu = n_\mu), \\ x_{\mu+1} & (s_\mu \neq n_\mu, x_\mu \text{mod}2 = 0), \\ x_{\mu-1} & (s_\mu \neq n_\mu, x_\mu \text{mod}2 = 1). \end{cases} \tag{3.55}$$

In the cases where $s_\mu \neq n_\mu$, we are left with *point-split* fermion operators, an example of which is $\psi(x+\hat{\mu})$. Here and in equation 3.53 we suppress any gauge link operators to to keep the notation simple; a point-split operator of this kind should in full be written as $U_\mu(x)\psi(x+\hat{\mu})$. Moving forward we will continue to suppress gauge link operators in our notation.

Returning back now to equation 3.53, there are a few principles to keep in mind when inserting any given spin-taste operator into our quark propagators. First, the presence of point-split operators tends to make the corresponding correlation function noisier, and so local ($n_\mu = s_\mu$) spin-taste operators are preferred. Second, quark taste is ultimately an unphysical property. If any taste-pertaining terms in a correlation function do not cancel, that correlation function will reduce to zero plus any noise. Finally, we can remind ourselves that it is standard model physics we wish to simulate on our lattices; spin is a quantum number that should be preserved in a QCD interaction. The spin operator should therefore match that of the physical meson or current of interest to us. Fortunately, implementing a chosen spin-taste structure as phases with lattice site dependency is rather trivial: that functionality is built into the MILC code [72, 73] we use to generate correlation functions.

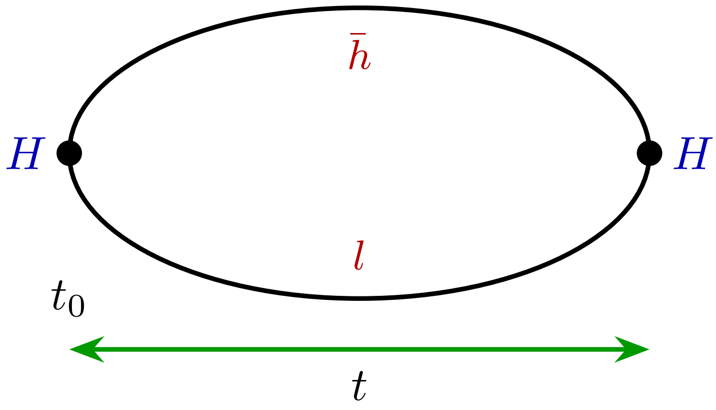

Figure 3.1: Sample diagram of a two-point correlation function. The meson H with quark content $\bar{h}l$ is created at time t_0. It propagates along the lattice, where it is then annihilated at time t_0+t.

Let us now summarize the general methodology we employ to generate our desired propagators and correlation functions on the lattice. We begin by using naive quarks to build a desired correlation function. We then transform that correlation function into staggered quark propagators and lattice site-dependent phases. For each configuration (see chapter 3.2.1), we then invert the Dirac matrix M off of the source of ξ to calculate those staggered quark propagators. Finally then we group appropriate propagators together as new correlation functions and take the average over the number of configurations.

3.5.2 Two-point correlation functions

Having established the theory of spin-taste structure and phases for our staggered quark propagators, let us take a closer look at how exactly we build the correlation functions we instantiate onto the lattice, beginning with two-point correlation functions. The example meson we will use for the following discussion is a generic pseudo-scalar heavy meson H, with heavy-light quark content $\bar{h}l$. The two-point diagram of such a meson is given in figure 3.1. Keep in mind however that swapping H for another meson with differing quark content is trivial in the upcoming suite of correlation function derivations: it is mostly a change in quark propagator labeling.

Moving forward, there are four different spin-taste structured correlation functions of interest to our work. The first of these is the meson current $H_5^5(x_t) = \overline{\psi}_h(x_t)\gamma_5 \otimes \xi_5 \psi_l(x_t)$, where the current's subscript and superscript notation indicates the n and s vectors in the spin-taste operator. The γ_5 and ξ_5 operators indicate that the vectors $n = s = \bar{s} = (1,1,1,1)$. Here the current $H_5^5(x_t)$ annihilates a local Goldstone heavy meson H with $\bar{h}l$ quark content at the lattice time slice x_t. With equation 3.53 we can write for this current that

$$\begin{aligned} H_5^5(x_t) &= \overline{\psi}_h(x_t)\xi_5 \otimes \gamma_5 \psi_l(x_t), \\ &= \overline{\psi}_h(x_t)(-1)^{x_t^0+x_t^1+x_t^2+x_t^3}\gamma_5^\dagger \psi_l(x_t), \\ &= (-1)^{\tilde{x}_t}\overline{\psi}_h(x_t)\psi_l(x_t). \end{aligned} \tag{3.56}$$

Here we see the components of $x_t = (x_t^0, x_t^1, x_t^2, x_t^3)$ appear in the phase term, and introduce $\tilde{x} = \sum_\mu x^\mu$. We can likewise create that same H meson at the lattice time slice x_0 using the meson current insertion

$$\begin{aligned} H_5^{5\dagger}(x_0) &= (-1)^{\tilde{x}_0}\left(\overline{\psi}_h(x_0)\psi_l(x_0)\right)^\dagger, \\ &= (-1)^{\tilde{x}_0}\left(\psi_h^\dagger(x_0)\gamma_0\psi_l(x_0)\right)^\dagger, \\ &= (-1)^{\tilde{x}_0}\psi_l^\dagger(x_0)\gamma_0^\dagger\psi_h(x_0), \\ &= (-1)^{\tilde{x}_0}\overline{\psi}_l(x_0)\psi_h(x_0). \end{aligned} \tag{3.57}$$

With these meson currents, we can construct the associated two-point correlation function using the time ordered field operator $T\{\}$:

$$\begin{aligned} \langle H_5^5(x_t)H_5^{5\dagger}(x_0)\rangle &= \langle 0|\, T\{H_5^5(x_t)H_5^{5\dagger}(x_0)\}\,|0\rangle\,, \\ &= (-1)^{\tilde{x}_0+\tilde{x}_t}\langle 0|\, T\{\overline{\psi}_h(x_t)\psi_l(x_t)\overline{\psi}_l(x_0)\psi_h(x_0)\}\,|0\rangle\,. \end{aligned} \tag{3.58}$$

From this point we can perform appropriate Wick contractions to rearrange the propagator terms in the correlation function. We ignore the global phase terms which might arise from rearranging the propagators in this way; we can correct for any final global phase term when we interface with the aforementioned MILC code. Implementing Wick contractions in this way means that this correlation function is equivalent to a light quark l propagating between its creation and annihilation points of x_0 and x_t, and likewise for an heavy antiquark $\bar{h}$. Writing out these Wick contractions and using equations 3.51 and 3.52 we can write the correlation function as

$$\begin{aligned}
\langle H_5^5(x_t) H_5^{5\dagger}(x_0)\rangle &= (-1)^{\tilde{x}_0+\tilde{x}_t} \langle 0|\, \overline{\psi}_h(x_t)\, \psi_l(x_t)\, \overline{\psi}_l(x_0)\, \psi_h(x_0)\, |0\rangle\,, \\
&= (-1)^{\tilde{x}_0+\tilde{x}_t} \langle 0|\, \psi_h(x_0)\, \overline{\psi}_h(x_t)\, \psi_l(x_t)\, \overline{\psi}_l(x_0)\, |0\rangle\,, \\
&= (-1)^{\tilde{x}_0+\tilde{x}_t} \operatorname*{Tr}_{\text{spin}} \left[\gamma_5 S_F^{h\dagger}(x_t,x_0) \gamma_5 S_F^{l}(x_t,x_0)\right], \\
&= (-1)^{\tilde{x}_0+\tilde{x}_t} \operatorname*{Tr}_{\text{spin}} \left[\gamma_5 \Omega(x_0)\Omega^\dagger(x_t) \operatorname*{Tr}_{\text{color}} \left(g^{h\dagger}(x_t,x_0)\right) \gamma_5 \operatorname*{Tr}_{\text{color}} \left(g^{l}(x_t,x_0)\right) \Omega(x_t)\Omega^\dagger(x_0)\right], \\
&= (-1)^{\tilde{x}_0+\tilde{x}_t} \operatorname*{Tr}_{\text{spin}} \left(\gamma_5 \Omega(x_0)\Omega^\dagger(x_t) \gamma_5 \Omega(x_t)\Omega^\dagger(x_0)\right) \operatorname*{Tr}_{\text{color}} \left(g^{h\dagger}(x_t,x_0) g^{l}(x_t,x_0)\right).
\end{aligned} \tag{3.59}$$

In this equation we see operators which trace over both color and spinor indices. We have thus far suppressed the implied spinor indices in the Feynman propagators and the γ_n matrices for the sake of limiting notation, but we include the necessary trace over spin operator here. We can further simplify the last line of equation 3.59 by considering how $\gamma_\mu \gamma_5 = -\gamma_5 \gamma_\mu$ and the definition of $\Omega(x)$ from equation 3.26. Doing so we can write that $\gamma_5 \Omega(x) = (-1)^{\tilde{x}} \Omega(x) \gamma_5$, and likewise we can write $\gamma_5 \Omega^\dagger(x) = (-1)^{\tilde{x}} \Omega^\dagger(x) \gamma_5$. Therefore we have

$$\begin{aligned}
\langle H_5^5(x_t) H_5^{5\dagger}(x_0)\rangle &= (-1)^{\tilde{x}_0+\tilde{x}_t} (-1)^{\tilde{x}_0+\tilde{x}_t} \operatorname*{Tr}_{\text{spinor}} \left(\gamma_5 \gamma_5 \Omega(x_0)\Omega^\dagger(x_t) \Omega(x_t)\Omega^\dagger(x_0)\right) \operatorname*{Tr}_{\text{color}} \left(g^{h\dagger}(x_t,x_0) g^{l}(x_t,x_0)\right), \\
&= 4 \operatorname*{Tr}_{\text{color}} \left(g^{h\dagger}(x_t,x_0) g^{l}(x_t,x_0)\right),
\end{aligned} \tag{3.60}$$

where the trace over the spinor matrices gives us the factor of 4. From this equation we can see that the two-point correlation function built from staggered quark propagators with $\xi_5 \otimes \gamma_5$ spin-taste structure has no phase term with lattice site dependency. This spin-taste structure describes the local (not point-split) Goldstone heavy and light mesons H, H_s, π, and K that we will encounter in this work. We will come to see however that, in order to eventually calculate vector and tensor form factors for various meson decays, we will need two-point correlation functions of non-Goldstone mesons.

The first two-point correlation function with non-Goldstone spin-taste structure we might discuss is built from the local current insertion $H^{5t}_{5t}(x_t) = \overline{\psi}_h(x_t)\gamma_5\gamma_0 \otimes \xi_5\xi_0\psi_l(x_t)$. The notation here indicates spin taste structure where, like before, γ_5 and ξ_5 are indicated by the number 5 in the superscript and subscript of the current insertion. We meanwhile follow the notation where for $\gamma_{n\neq 5}$ and $\xi_{s\neq 5}$, $n,s \in (0,1,2,3)$ are indicated by (t,x,y,z) respectively. This meson current, like before, annihilates a heavy meson at lattice time slice x_t, but this time that meson has non-Goldstone spin-taste structure.

To derive the phase dependency, we can use the relation that $\gamma_m\gamma_n \otimes \xi_r\xi_s = \gamma_m \otimes \xi_r\gamma_n \otimes \xi_s$. Additionally we can say for γ_0, ξ_0 that the spin-taste vectors $n = s = (1,0,0,0)$, $\bar{n} = \bar{s} = (0,1,1,1)$. Putting these relations together we arrive at

$$\begin{aligned} H^{5t}_{5t}(x_t) &= \overline{\psi}_h(x_t)\gamma_5\gamma_0 \otimes \xi_5\xi_0\psi_l(x_t), \\ &= \overline{\psi}_h(x_t)\gamma_5 \otimes \xi_5\gamma_0 \otimes \xi_0\psi_l(x_t), \\ &= \overline{\psi}_h(x_t)(-1)^{\tilde{x}_t}(-1)^{\tilde{x}_t - x^0_t}\psi_l(x_t), \\ &= (-1)^{x^0_t}\overline{\psi}_h(x_t)\psi_l(x_t). \end{aligned} \tag{3.61}$$

Following from this definition, we can find that the corresponding current $H^{5t\dagger}_{5t}(x_0) = (-1)^{\tilde{x}^0_0}\overline{\psi}_l(x_t)\psi_h(x_t)$ creates that same meson at x_0. Using the same techniques of Wick contractions and tracing over spinor matrices in equations 3.59 and 3.60, we can construct the two-point correlation function of the local non-Goldstone heavy meson H' as

$$\begin{aligned} \langle H^{5t}_{5t}(x_t)H^{5t\dagger}_{5t}(x_0)\rangle &= (-1)^{x^0_0+x^0_t}\langle 0|\,\psi_h(x_0)\,\overline{\psi}_h(x_t)\,\psi_l(x_t)\,\overline{\psi}_l(x_0)\,|0\rangle\,, \\ &= (-1)^{x^0_0+x^0_t}(-1)^{\tilde{x}_0+\tilde{x}_t}4\operatorname*{Tr}_{\text{color}}\left(g^{h\dagger}(x_t,x_0)g^{l}(x_t,x_0)\right), \\ &= (-1)^{\tilde{x}_0+\tilde{x}_t+x^0_0+x^0_t}4\operatorname*{Tr}_{\text{color}}\left(g^{h\dagger}(x_t,x_0)g^{l}(x_t,x_0)\right). \end{aligned} \tag{3.62}$$

We can see in this equation that this phase term encodes dependency on the lattice sites x_0 and x_t. While the meson corresponding to this correlation function is non-Goldstone, the spin-taste structure is still local. The next current insertion we can discuss is the non-local, point-split current $H^{5x}_{5}(x_t)$ which has spin-taste structure $\gamma_5 \otimes \xi_5\xi_1$. The implied identity spin matrix $\mathbb{1}$ has the vector $n = \bar{n} = (0,0,0,0)$, while the taste vector in ξ_1 is $s = (0,1,0,0)$, and $\bar{s} = (1,0,1,1)$. We can define

$H_5^{5x}(x_t) = \overline{\psi}_h \gamma_5 \otimes \xi_1 \xi_5 \psi_l$, having swapped the positions of $\xi_5\xi_1 \to \xi_1\xi_5$. Doing so precipitates an overall (not lattice site dependent) phase of -1, which we can promptly ignore. Implementing this swap, and inserting the implied identity spin matrix $\mathbb{1}$ we can write

$$\begin{aligned} H_5^{5x}(x_t) &= \overline{\psi}_h(x_t)\mathbb{1}\gamma_5 \otimes \xi_1\xi_5\psi_l(x_t), \\ &= \overline{\psi}_h(x_t)\mathbb{1} \otimes \xi_1\gamma_5 \otimes \xi_5\psi_l(x_t), \\ &= (-1)^{\tilde{x}_t}(-1)^{\tilde{x}_t - x_t^1}\overline{\psi}_h(x_t)\gamma_1^\dagger\psi_l(x_t \oplus (0,1,0,0)), \\ &= (-1)^{x_t^1}\overline{\psi}_h(x_t)\gamma_1^\dagger\psi_l(x_t \oplus \hat{1}). \end{aligned} \tag{3.63}$$

In this formulation, the point-split fermions are joined by the (implicit) gauge link operator $U_1(x_t)$ in the direction of x_t^1. The unit vector $\hat{1}$ likewise shares the x_t^1 direction. It is also important to note that we pick up and then ignore an additional global (-1) phase term from $\gamma_1^\dagger$ (see equation 3.53) in the third line of equation 3.63. For $H_5^{5x}(x_0)$ we likewise arrive at $H_5^{5x\dagger}(x_0) = (-1)^{x_0^1}\overline{\psi}_l(x_0 \oplus \hat{1})\gamma_1\psi_h(x_0)$.

Constructing a two-point function with $\langle H_5^{5x}(x_t)H_5^{5x}(x_0)\rangle$ allows us to describe the non-local, non-Goldstone heavy meson which we will denote as H''. We can do so utilizing equations 3.53 and 3.54, which implies the relations $\Omega(x \oplus \hat{1}) = (-1)^{x^0}\gamma_1\Omega(x)$ and likewise $\Omega^\dagger(x \oplus \hat{1}) = (-1)^{x^0}\Omega^\dagger(x)\gamma_1^\dagger$. Writing this out we get

$$\begin{aligned} \langle H_5^{5x}(x_t)H_5^{5x}(x_0)\rangle &= (-1)^{x_0^1 + x_t^1}\langle 0|\, \psi_h(x_0)\,\overline{\psi}_h(x_t)\,\gamma_1^\dagger\,\psi_l(x_t \oplus \hat{1})\,\overline{\psi}_l(x_0 \oplus \hat{1})\,|0\rangle, \\ &= (-1)^{x_0^1 + x_t^1}\operatorname*{Tr}_{\text{spin}}\left(\gamma_5\Omega(x_0)\Omega^\dagger(x_t)\gamma_5\gamma_1^\dagger\Omega(x_t \oplus \hat{1})\Omega^\dagger(x_0 \oplus \hat{1})\gamma_1\right) \\ &\times \operatorname*{Tr}_{\text{color}}\left(g^{h\dagger}(x_t, x_0)g^l(x_t \oplus \hat{1}, x_0 \oplus \hat{1})\right), \\ &= (-1)^{x_0^1 + x_t^1}(-1)^{\tilde{x}_0 + \tilde{x}_t}(-1)^{x_0^0 + x_t^0}\operatorname*{Tr}_{\text{spin}}\left(\Omega(x_0)\Omega^\dagger(x_t)\Omega(x_t \oplus \hat{1})\Omega^\dagger(x_0 \oplus \hat{1})\right) \\ &\times \operatorname*{Tr}_{\text{color}}\left(g^{h\dagger}(x_t, x_0)g^l(x_t \oplus \hat{1}, x_0 \oplus \hat{1})\right), \\ &= (-1)^{x_0^2 + x_t^2 + x_0^3 + x_t^3}\, 4\operatorname*{Tr}_{\text{color}}\left(g^{h\dagger}(x_t, x_0)g^l(x_t \oplus \hat{1}, x_0 \oplus \hat{1})\right). \end{aligned} \tag{3.64}$$

This correlation function contains a point-split quark propagator, and a lattice site-dependent phase term. Once again, we have suppressed the gluon link operators which are implied from the point splitting.

The final meson insertion we need is the non-local, non-Goldstone, point split $H_{5t}^{yz}(x_t) = \overline{\psi}_h \gamma_5 \gamma_0 \otimes \xi_2 \xi_3 \psi_l(x_t)$. The corresponding meson with $\gamma_5\gamma_0 \otimes \xi_2\xi_3$ spin-taste structure we can denote as H'''. Here we have two instances of point-splitting, and so we will try be clear in our derivation where terms cancel. We can write this meson current insertion as

$$\begin{aligned}
H_{5t}^{yz}(x_t) &= \overline{\psi}_h(x_t)\gamma_5\gamma_0 \otimes \xi_2\xi_3 \psi_l(x_t), \\
&= \overline{\psi}_h(x_t)\gamma_5 \otimes \xi_2 \gamma_0 \otimes \xi_3 \psi_l(x_t), \\
&= (-1)^{\tilde{x}_t - x_t^3} \overline{\psi}_h \gamma_5 \otimes \xi_2 \gamma_3^\dagger \gamma_0 \psi_l(x_t \oplus (1,0,0,1)), \\
&= (-1)^{\tilde{x}_t - x_t^3} (-1)^{\tilde{x}_t - x_t^2} \overline{\psi}_h(x_t) \gamma_2^\dagger \gamma_5 \gamma_3^\dagger \gamma_0 \psi_l(x_t \oplus \hat{1}), \\
&= (-1)^{-(x_t^2 + x_t^3)} \overline{\psi}_h(x_t) \gamma_2^\dagger \gamma_5 \gamma_3^\dagger \gamma_0 \psi_l(x_t \oplus \hat{1}), \\
&= (-1)^{x_t^2 + x_t^3} \overline{\psi}_h(x_t) \gamma_1^\dagger \psi_l(x_t \oplus \hat{1}), \\
\implies H_{5t}^{yz\dagger}(x_0) &= (-1)^{x_0^2 + x_0^3} \overline{\psi}_l(x_0 \oplus \hat{1}) \gamma_1 \psi_h(x_0).
\end{aligned} \tag{3.65}$$

Once again we take advantage of ignoring overall (-1) global phase terms, which in this case arise from shifting the positions of gamma matrices and using $\gamma_5 = \gamma_0\gamma_1\gamma_2\gamma_3$. The Euclidean metric gives us some leniency as the matrices γ_μ are hermitian ($\gamma_\mu^\dagger = \gamma_\mu$). Finally then the two-point correlation function for H''' can be constructed as

$$\begin{aligned}
\langle H_{5t}^{yz}(x_t) H_{5t}^{yz\dagger}(x_0)\rangle &= (-1)^{x_0^2+x_0^3}(-1)^{x_t^2+x_t^3} \langle 0|\, \psi_h(x_0)\, \overline{\psi}_h(x_t)\, \gamma_1^\dagger\, \psi_l(x_t \oplus \hat{1})\, \overline{\psi}_l(x_0 \oplus \hat{1}) \gamma_1\, |0\rangle \\
&= (-1)^{x_0^2+x_0^3+x_t^2+x_t^3} \operatorname*{Tr}_{\text{spin}} \left(\gamma_5 \Omega(x_0) \Omega^\dagger(x_t) \gamma_5 \gamma_1^\dagger \Omega(x_t \oplus \hat{1}) \Omega^\dagger(x_0 \oplus \hat{1}) \gamma_1 \right) \\
&\times \operatorname*{Tr}_{\text{color}} \left(g^{h\dagger}(x_t, x_0) g^l(x_t \oplus \hat{1}, x_0 \oplus \hat{1}) \right) \\
&= (-1)^{x_0^2+x_0^3+x_t^2+x_t^3} (-1)^{x_0^0+x_t^0} \operatorname*{Tr}_{\text{spin}} \left(\gamma_5 \Omega(x_0) \Omega^\dagger(x_t) \gamma_5 \gamma_1^\dagger \gamma_1 \Omega(x_t) \Omega^\dagger(x_0) \gamma_1^\dagger \gamma_1 \right) \\
&\times \operatorname*{Tr}_{\text{color}} \left(g^{h\dagger}(x_t, x_0) g^l(x_t \oplus \hat{1}, x_0 \oplus \hat{1}) \right) \\
&= (-1)^{\tilde{x}_0 - x_0^1 + \tilde{x}_t - x_t^1} (-1)^{\tilde{x}_0 + \tilde{x}_t} \operatorname*{Tr}_{\text{spin}} \left(\Omega(x_0) \Omega^\dagger(x_t) \Omega(x_t) \Omega^\dagger(x_0) \right) \\
&\times \operatorname*{Tr}_{\text{color}} \left(g^{h\dagger}(x_t, x_0) g^l(x_t \oplus \hat{1}, x_0 \oplus \hat{1}) \right) \\
&= (-1)^{x_0^1 + x_t^1} 4 \operatorname*{Tr}_{\text{color}} \left(g^{h\dagger}(x_t, x_0) g^l(x_t \oplus \hat{1}, x_0 \oplus \hat{1}) \right)
\end{aligned} \tag{3.66}$$

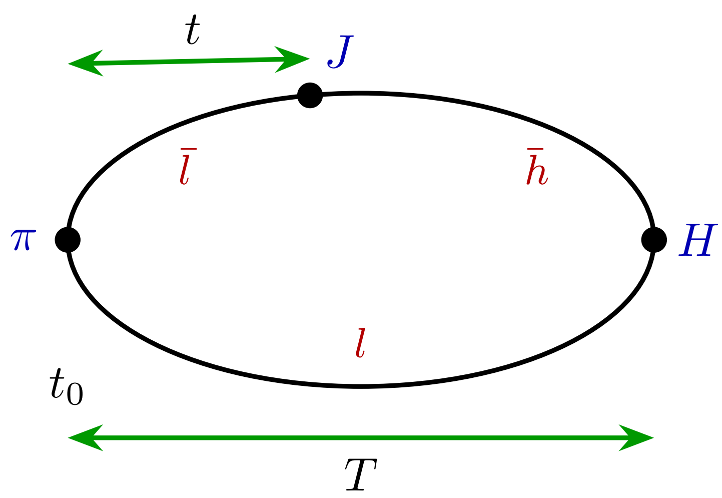

Figure 3.2: Sample diagram of a three-point correlation function. A pion is created at time t_0. Some current insertion J is inserted at time t_0+t, which annihilates $\bar{l}$ and creates $\bar{h}$. A heavy meson is then annihilated at time t_0+T.

3.5.3 Three-point correlation functions

In the previous section, we explored the current insertions which acted as meson operators in two-point correlation functions. The meson operators of interest to us in this work are $J \in \{H_{(s)}, H'_{(s)}, H''_{(s)}, H'''_{(s)}, \pi, K\}$. Moving forward, we will refer to these current insertions strictly as *meson operators*, and reserve the term *current insertion* to the scalar, vector, and tensor current insertions ($J \in \{S, V, T\}$) which we will construct in this section.

Figure 3.2 gives a sample diagram of a three point correlation function for a heavy meson H, a light meson π, and some current insertion J. The mesons are separated on the lattice by some length T, while the source meson and current insertion are separated by some smaller length t such that $t < T$. The implied time reversal in this figure ($\pi \to H$ rather than $H \to \pi$) is explained in section 3.5.5. For now, we may trust the fact that QCD is symmetric under time reversal and so none of the corresponding physics should meaningfully change.

The first current insertion we can discuss in this context is the most simple: the scalar current insertion $S(x_t) = \overline{\psi}_l(x_t)\psi_h(x_t)$, where we do not include the implied $\mathbb{1}\otimes\mathbb{1}$ spin-taste structure. We can say for this scalar current insertion that, at x_t, a light antiquark is annihilated and a heavy antiquark is created. To construct a three-point correlation function, we follow a similar procedure as before using Wick contractions and spin-taste identities. We also choose the meson operators H_5^5 and π_5^5 which both have Goldstone spin-taste structure $\gamma_5\otimes\xi_5$. If we wish to insert a pion at x_0, a scalar current at x_t, and a heavy meson at x_T, we can construct the namesake *scalar* three-point correlation function as

$$\begin{aligned}
\langle H_5^5(x_T)S(x_t)\pi_5^{5\dagger}(x_0)\rangle &= (-1)^{\tilde{x}_0+\tilde{x}_T}\,\langle 0|\,\overline{\psi}_h(x_T)\,\psi_l(x_T)\,\overline{\psi}_l(x_t)\,\psi_h(x_t)\,\overline{\psi}_l(x_0)\,\psi_l(x_0)\,|0\rangle \\
&= (-1)^{\tilde{x}_0+\tilde{x}_T}\,\langle 0|\,\psi_h(x_t)\,\overline{\psi}_h(x_T)\,\psi_l(x_t)\,\overline{\psi}_l(x_0)\,\psi_l(x_0)\,\overline{\psi}_l(x_t)\,|0\rangle \\
&= (-1)^{\tilde{x}_0+\tilde{x}_T}\operatorname*{Tr}_{\text{spin}}\left(\gamma_5 S_F^{h\dagger}(x_T,x_t)\gamma_5 S_F^{l}(x_T,x_0)\gamma_5 S_F^{l\dagger}(x_t,x_0)\gamma_5\right), \\
&= (-1)^{\tilde{x}_0+\tilde{x}_T}\operatorname*{Tr}_{\text{spin}}\left(\gamma_5\Omega(x_t)\Omega^\dagger(x_T)\gamma_5\Omega(x_T)\Omega^\dagger(x_0)\gamma_5\Omega(x_0)\Omega^\dagger(x_t)\gamma_5\right) \\
&\times \operatorname*{Tr}_{\text{color}}\left(g^{h\dagger}(x_T,x_t)g^{l}(x_T,x_0)g^{l\dagger}(x_t,x_0)\right), \\
&= (-1)^{\tilde{x}_0+\tilde{x}_T}(-1)^{\tilde{x}_0+\tilde{x}_T}\operatorname*{Tr}_{\text{spin}}\left(\Omega(x_t)\Omega^\dagger(x_T)\Omega(x_T)\Omega^\dagger(x_0)\Omega(x_0)\Omega^\dagger(x_t)\right) \\
&\times \operatorname*{Tr}_{\text{color}}\left(g^{h\dagger}(x_T,x_t)g^{l}(x_T,x_0)g^{l\dagger}(x_t,x_0)\right), \\
&= 4\operatorname*{Tr}_{\text{color}}\left(g^{h\dagger}(x_T,x_t)g^{l}(x_T,x_0)g^{l\dagger}(x_t,x_0)\right).
\end{aligned} \tag{3.67}$$

Like in the case of two-point correlation functions, we can shift the position of spinor components and only pick up global phase terms, which we again ignore. Like the meson operators with $\gamma_5\otimes\xi_5$ spin-taste structures, we can see that the scalar three-point correlation function also has no lattice site dependent phase term.

The next current insertion we can examine is the *temporal* vector current insertion $V^0(x_t) = \overline{\psi}_l(x_t)\gamma_0\otimes\xi_0\psi_h(x_t)$. We stress the term "temporal" here because the raised index 0 denotes the x^0 direction on the lattice, which we call the temporal dimension. The spin and taste vectors in this case are then $n = s = (1,0,0,0)$, $\overline{n} = \overline{s} = (0,1,1,1)$. We can likewise define a *spatial* vector current insertion as $V^1(x_t) = \overline{\psi}_l(x_t)\gamma_1\otimes\xi_1\psi_h(x_t)$, with spin and taste vectors $n = s = (0,1,0,0)$ and $\overline{n} = \overline{s} = (1,0,1,1)$. We treat the three spatial dimensions of lattice identically, and so any correlation function built from the current insertions $V^2(x_t)$ and $V^3(x_t)$ would be equivalent to those we build from $V^1(x_t)$. Following the same techniques as before, we can convert spin-taste operators into relative phase terms for both vector currents and write that

$$\begin{aligned} V^0(x_t) &= \overline{\psi}_l(x_t)\gamma_0 \otimes \xi_0 \psi_h(x_t), \\ &= (-1)^{\tilde{x}_t - x_t^0}\overline{\psi}_l(x_t)\psi_h(x_t), \\ V^1(x_t) &= \overline{\psi}_l(x_t)\gamma_1 \otimes \xi_1 \psi_h(x_t), \\ &= (-1)^{\tilde{x}_t - x_t^1}\overline{\psi}_l(x_t)\psi_h(x_t). \end{aligned} \tag{3.68}$$

Focusing first now on the temporal vector three-point correlation function, we may use the same pion as the scalar case with $\gamma_5 \otimes \xi_5$ spin-taste structure. However, to ensure the conservation of quantum numbers and canceling of taste terms, we use the H' heavy meson with $\gamma_0 \otimes \xi_0$ spin taste structure to build the temporal vector three-point correlation function. Doing so, we arrive at

$$\begin{aligned} \langle H_{5t}^{5t}(x_T)V^0(x_t)\pi_5^{5\dagger}(x_0)\rangle &= (-1)^{x_T^0 + \tilde{x}_t - x_t^0 + \tilde{x}_0} \langle 0|\, \psi_h(x_t)\,\overline{\psi}_h(x_T)\,\psi_l(x_T)\,\overline{\psi}_l(x_0)\,\psi_l(x_0)\,\overline{\psi}_l(x_t)\,|0\rangle\,, \\ &= (-1)^{x_T^0 + \tilde{x}_t - x_t^0 + \tilde{x}_0}(-1)^{\tilde{x}_T + \tilde{x}_0} 4 \operatorname*{Tr}_{\text{color}}\left(g^{h\dagger}(x_T,x_t)g^l(x_T,x_0)g^{l\dagger}(x_t,x_0)\right), \\ &= (-1)^{\tilde{x}_t + \tilde{x}_T - x_t^0 - x_T^0} 4 \operatorname*{Tr}_{\text{color}}\left(g^{h\dagger}(x_T,x_t)g^l(x_T,x_0)g^{l\dagger}(x_t,x_0)\right). \end{aligned} \tag{3.69}$$

Intuitively, the temporal vector three-point correlation function has phase dependency in the temporal dimension lattice sites.

Deriving the right equation for the spatial vector three-point correlation function is not as simple, and so we show the steps more thoroughly. While we can still use the Goldstone pion as before, we need the non-Goldstone point-split heavy meson $H'' \equiv H_5^{5x}(x_T)$ to use in tandem with $V^1(x_t)$. Putting these operators together we have

$$
\begin{aligned}
\langle H_5^{5x}(x_T)V^1(x_t)\pi_5^{5\dagger}(x_0)\rangle &= (-1)^{x_T^1+\tilde{x}_t-x_t^1+\tilde{x}_0}\,\langle 0|\,\overline{\psi}_h(x_T)\,\gamma_1^\dagger\,\psi_l(x_T\oplus\hat{1})\,\overline{\psi}_l(x_t)\,\psi_h(x_t)\,\overline{\psi}_l(x_0)\,\psi_l(x_0)\,|0\rangle \\
&= (-1)^{\tilde{x}_0+\tilde{x}_t+x_T^1-x_t^1}\,\langle 0|\,\psi_h(x_t)\,\overline{\psi}_h(x_T)\,\gamma_1^\dagger\,\psi_l(x_T\oplus\hat{1})\,\overline{\psi}_l(x_0)\,\psi_l(x_0)\,\overline{\psi}_l(x_t)\,|0\rangle \\
&= (-1)^{\tilde{x}_0+\tilde{x}_t+x_T^1-x_t^1}\,\underset{\text{spin}}{\mathrm{Tr}}\Big(\gamma_5\Omega(x_t)\Omega^\dagger(x_T)\gamma_5\gamma_1^\dagger\Omega(x_T\oplus\hat{1})\Omega^\dagger(x_0)\gamma_5\Omega(x_0)\Omega^\dagger(x_t)\gamma_5\Big) \\
&\times \underset{\text{color}}{\mathrm{Tr}}\Big(g^{h\dagger}(x_T,x_t)g^l(x_T\oplus\hat{1},x_0)g^{l\dagger}(x_t,x_0)\Big) \\
&= (-1)^{\tilde{x}_0+\tilde{x}_t+x_T^0+x_T^1-x_t^1}\,\underset{\text{spin}}{\mathrm{Tr}}\Big(\gamma_5\Omega(x_t)\Omega^\dagger(x_T)\gamma_5\Omega(x_T)\Omega^\dagger(x_0)\gamma_5\Omega(x_0)\Omega^\dagger(x_t)\gamma_5\Big) \\
&\times \underset{\text{color}}{\mathrm{Tr}}\Big(g^{h\dagger}(x_T,x_t)g^l(x_T\oplus\hat{1},x_0)g^{l\dagger}(x_t,x_0)\Big) \\
&= (-1)^{\tilde{x}_0+\tilde{x}_t+x_T^0+x_T^1-x_t^1}(-1)^{\tilde{x}_0+\tilde{x}_T}\,\underset{\text{spin}}{\mathrm{Tr}}\Big(\Omega(x_t)\Omega^\dagger(x_T)\Omega(x_T)\Omega^\dagger(x_0)\Omega(x_0)\Omega^\dagger(x_t)\Big) \\
&\times \underset{\text{color}}{\mathrm{Tr}}\Big(g^{h\dagger}(x_T,x_t)g^l(x_T\oplus\hat{1},x_0)g^{l\dagger}(x_t,x_0)\Big) \\
&= (-1)^{\tilde{x}_t-x_t^1+x_T^2+x_T^3}4\,\underset{\text{color}}{\mathrm{Tr}}\Big(g^{h\dagger}(x_T,x_t)g^l(x_T\oplus\hat{1},x_0)g^{l\dagger}(x_t,x_0)\Big)
\end{aligned}
\tag{3.70}
$$

Like the temporal case, we can see here in the phase term that the spatial vector three-point correlation function has dependency on spatial dimension lattice sites. Both the temporal and spatial vector three-point functions here can be used to eventually calculate vector form factors; in chapters 4 and 5 we discuss cases where either or both are useful.

Finally then, with the aim of calculating tensor form factors, we need a three-point correlation function which contains a tensor current insertion T^{0k}. The tensor current insertion can have different spin-taste structures $\gamma_0\gamma_k \otimes \xi_0\xi_k$ where $k \in \{1,2,3\}$. A value of $k=1$ is the only option we use in this work, and so we shorten our notation such that $T^{01} \equiv T$. We can therefore write

$$
\begin{aligned}
T(x_t) &= \overline{\psi}_l(x_t)\gamma_0\gamma_1 \otimes \xi_0\xi_1\,\psi_h(x_t), \\
&= \overline{\psi}_l(x_t)\gamma_0 \otimes \xi_0\gamma_1 \otimes \xi_1\,\psi_h(x_t), \\
&= (-1)^{x_t^0+x_t^1}\overline{\psi}_l(x_t)\psi_h(x_t).
\end{aligned}
\tag{3.71}
$$

As alluded to before, we need the H''' meson with $\gamma_5\gamma_0 \otimes \xi_2\xi_3$ spin-taste structure to construct a correlation function with the same Goldstone pion and tensor current insertion. Doing so we get

$$\begin{aligned}
\langle H_{5t}^{yz}(x_T)T(x_t)\pi_5^{5\dagger}(x_0)\rangle &= (-1)^{\tilde{x}_0+x_t^0+x_t^1+x_T^2+x_T^3} \langle 0|\, \overbrace{\psi_h(x_t)\,\overline{\psi}_h(x_T)}\,\gamma_1^\dagger\, \overbrace{\psi_l(x_T\oplus\hat{1})\,\overline{\psi}_l(x_0)}\, \overbrace{\psi_l(x_0)\,\overline{\psi}_l(x_t)}\, |0\rangle\,, \\
&= (-1)^{\tilde{x}_0+x_t^0+x_t^1+x_T^2+x_T^3} \operatorname*{Tr}_{\text{spin}}\Big(\gamma_5\Omega(x_t)\Omega_h^\dagger(x_T)\gamma_5\gamma_1^\dagger\Omega(x_T\oplus\hat{1})\Omega^\dagger(x_0)\gamma_5\Omega(x_0)\Omega^\dagger(x_t)\gamma_5\Big) \\
&\times \operatorname*{Tr}_{\text{color}}\Big(g^{h\dagger}(x_T,x_t)g^l(x_T\oplus\hat{1},x_0)g^{l\dagger}(x_t,x_0)\Big)\,, \\
&= (-1)^{\tilde{x}_T-x_T^1+x_t^0+x_t^1} \operatorname*{Tr}_{\text{spin}}\Big(\Omega(x_t)\Omega_h^\dagger(x_T)\Omega(x_T)\Omega^\dagger(x_0)\Omega(x_0)\Omega^\dagger(x_t)\Big) \\
&\times \operatorname*{Tr}_{\text{color}}\Big(g^{h\dagger}(x_T,x_t)g^l(x_T\oplus\hat{1},x_0)g^{l\dagger}(x_t,x_0)\Big)\,, \\
&= (-1)^{\tilde{x}_T-x_T^1+x_t^0+x_t^1} 4 \operatorname*{Tr}_{\text{color}}\Big(g^{h\dagger}(x_T,x_t)g^l(x_T\oplus\hat{1},x_0)g^{l\dagger}(x_t,x_0)\Big)\,.
\end{aligned} \tag{3.72}$$

Here and in the spatial vector case, we again note that we have suppressed the gauge link terms $U_1(x_T)$ which would appear with the point-split staggered quark propagator.

3.5.4 Spin-taste structure summary

In this section we provide a condensed summary of the spin-taste structures and correlation functions discussed in the previous sections. We include notation here to indicate where we might swap a light quark propagator for a strange quark propagator. To begin, the meson operators and current insertions (which we might also call HISQ quark bilinears) in this work are as follows:

$$
\begin{aligned}
H_{(s)} &: H^{5}_{(s),5} = \overline{\psi}_h(\gamma_5 \otimes \xi_5)\psi_{l(s)}, \\
H'_{(s)} &: H^{5t}_{(s),5t} = \overline{\psi}_h(\gamma_5\gamma_0 \otimes \xi_5\xi_0)\psi_{l(s)}, \\
H''_{(s)} &: H^{5x}_{(s),5} = \overline{\psi}_h(\gamma_5 \otimes \xi_5\xi_1)\psi_{l(s)}, \\
H'''_{(s)} &: H^{yz}_{(s),5t} = \overline{\psi}_h(\gamma_5\gamma_0 \otimes \xi_2\xi_3)\psi_{l(s)}, \\
\pi(K) &: \pi(K)^{5}_{5} = \overline{\psi}_l(\gamma_5 \otimes \xi_5)\psi_{l(s)}, \\
S &= \overline{\psi}_h\psi_l, \\
V^0 &= \overline{\psi}_h(\gamma_0 \otimes \xi_0)\psi_l, \\
V^1 &= \overline{\psi}_h(\gamma_1 \otimes \xi_1)\psi_l, \\
T &= \overline{\psi}_h(\gamma_1\gamma_0 \otimes \xi_1\xi_0)\psi_l.
\end{aligned}
\tag{3.73}
$$

For any meson operator, its corresponding two point correlation functions are constructed identically: using H^5_5 for example we have $\langle H^5_5(x_t)H^{5\dagger}_5(x_0)\rangle$. Moving on, the ordering of quark bilinears in three-point correlation functions is important, so we will not generalize. We label our required three-point correlation functions by their current insertion $J \in \{S, V^0, V^1, T\}$. Their forms for $H \to \pi$ are given by[5]

$$
\begin{aligned}
\text{Scalar:} &\quad \langle H^5_5(x_T)S(x_t)\pi^{5\dagger}_5(x_0)\rangle, \\
\text{Temporal Vector:} &\quad \langle H^{5t}_{5t}(x_T)V^0(x_t)\pi^{5\dagger}_5(x_0)\rangle, \\
\text{Spatial Vector:} &\quad \langle H^{5x}_5(x_T)V^1(x_t)\pi^{5\dagger}_5(x_0)\rangle, \\
\text{Tensor:} &\quad \langle H^{yz}_{5t}(x_T)T(x_t)\pi^{5\dagger}_5(x_0)\rangle.
\end{aligned}
\tag{3.74}
$$

5. Technically these functions describe $\pi \to H$, but the symmetries of QCD make correcting this difference trivial.

The strange spectator quark equivalent of the above functions are made simply by swapping $H \to H_s$ and $\pi \to K$. In the next section it will be useful to generalize two and three-point correlation functions as

$$C_2(x_t, x_0) = (-1)^{\phi_2(x_0,x_t)} \operatorname*{Tr}_{\text{color}} \left(g^{h\dagger}(x_t, x_0) g^l(x_t, x_0) \right), \tag{3.75}$$

$$C_3(x_T, x_t, x_0) = (-1)^{\phi_3(x_0,x_t,x_T)} \operatorname*{Tr}_{\text{color}} \left(g^{h\dagger}(x_t, x_T) g^l(x_T, x_0) g^{l\dagger}(x_t, x_0) \right). \tag{3.76}$$

Here $(-1)^{\phi_2(x_0,x_t)}$ and $(-1)^{\phi_3(x_0,x_t,x_T)}$ are the specific lattice site dependent phase terms which encode the spin-taste structure of a specified two or three-point correlation function. Equation 3.75 describes a heavy meson with heavy-light valence quark content, and equation 3.76 describes the $H \to \pi$. We will stick with these general forms of equations 3.75 and 3.76 for now, but again note that changing the flavor of the spectator quark from $l \to s$ precipitates functions which describe H_s, K, and $H_s \to K$.

3.5.5 Random wall sources

Seeing as kinematic form factors are of interest to this work, we must have a robust methodology for imparting momentum into our lattice simulations. We have already discussed twisted boundary conditions [57] in section 3.3.5, but it is useful to develop those ideas further in the context of our staggered quark propagators and their corresponding correlation functions. Through a Fourier transform, we can recover mesons in momentum eigenstates which have three-momentum $\vec{p}$. Using the technique of twisted boundary conditions we can impart momentum onto a single quark. Therefore the Fourier transform of the generic two point function (equation 3.75) can be written as

$$\tilde{C}_2^{\vec{p}}(t_0, t_0 + t) = \frac{1}{N_x^3} \sum_{\vec{x}_t, \vec{x}_0} e^{-i\vec{p}\cdot(\vec{x}_0 - \vec{x}_t)} C_2(x_t, x_0), \tag{3.77}$$

where we have slightly altered our notation such that $x_0^0 \equiv t_0$, and $x_t^0 \equiv t_0 + t$. Solving this equation requires staggered quark propagators for all x_0 and x_t options on the lattice. Unfortunately, this leads to increases in computation time proportional to two times the volume of the lattice squared. We address this problem through the implementation of random wall sources. Doing so introduces random noise into our correlation functions, but it does significantly reduce computation time. We implement random wall sources by first introducing the following new propagators:

$$P^{l,\vec{p}}(x_t,t_0) \equiv \frac{1}{\sqrt{N_x^3}} \sum_{\vec{x}_0} e^{i\vec{p}\cdot(\vec{x}_0-\vec{x}_t)}(-1)^{\phi_2(x_0,0)}\Phi(\vec{x}_0)g^l(x_t,x_0), \tag{3.78}$$

$$P^{h,\vec{p}\dagger}(x_t,t_0) \equiv \frac{1}{\sqrt{N_x^3}} \sum_{\vec{x}_0} e^{-i\vec{p}\cdot(\vec{x}_0-\vec{x}_t)} g^{h\dagger}(x_t,x_0)\Phi^\dagger(\vec{x}_0). \tag{3.79}$$

Here we include the term $\Phi(\vec{x}_0)$, which is a field of random complex color vectors that act on the spatial components of t_0 [76, 77]; different choices of $\Phi(\vec{x}_0)$ are made for each gauge field configuration. For some function $f(\vec{x},\vec{x}')$, this random color field has the property

$$\langle f(\vec{x},\vec{x}')\Phi^\dagger(\vec{x}')\Phi(\vec{x})\rangle = \delta_{\vec{x}',\vec{x}} f(\vec{x},\vec{x}'). \tag{3.80}$$

We also note that the source's spin-taste phase term only needs to be applied to one quark propagator. With these new random color wall propagators, we can define a new construction ρ_2 as

$$\rho_2 = \sum_{\vec{x}_t} (-1)^{\phi_2(0,x_t)} \operatorname*{Tr}_{\text{color}} \left(P^{h,\vec{p}\dagger}(x_t,t_0) P^{l,\vec{p}}(x_t,t_0) \right). \tag{3.81}$$

Expanding the random color wall propagators in this equation and giving momentum only to the light quark, we can see that this construction is equal to the Fourier transform of a two-point correlation function:

$$\begin{aligned}
\rho_2 &= \frac{1}{N_x^3} \sum_{\vec{x}_t} (-1)^{\phi_2(0,x_t)} \operatorname*{Tr}_{\text{color}} \left(\sum_{\vec{x}'_0} e^{-i\vec{p}\cdot(\vec{x}'_0-\vec{x}_t)} (-1)^{\phi_2(x'_0,0)} g^{h\dagger}(x_t,x'_0)\Phi^\dagger(\vec{x}'_0) \sum_{\vec{x}_0} \Phi(\vec{x}_0) g^l(x_t,x_0) \right), \\
&= \frac{1}{N_x^3} \sum_{\vec{x}_t} (-1)^{\phi_2(0,x_t)} \sum_{\vec{x}'_0,\vec{x}_0} e^{-i\vec{p}\cdot(\vec{x}'_0-\vec{x}_t)} (-1)^{\phi_2(x'_0,0)} \operatorname*{Tr}_{\text{color}} \left(g^{h\dagger}(x_t,x'_0)\Phi^\dagger(\vec{x}'_0)\Phi(\vec{x}_0) g^l(x_t,x_0) \right), \\
&= \frac{1}{N_x^3} \sum_{\vec{x}_t,\vec{x}_0} (-1)^{\phi_2(x_0,x_t)} e^{-i\vec{p}\cdot(\vec{x}_0-\vec{x}_t)} \operatorname*{Tr}_{\text{color}} \left(g^{h\dagger}(x_t,x'_0) g^l(x_t,x_0) \right), \\
&= \tilde{C}_2^{\vec{p}}(t_0,t_0+t).
\end{aligned} \tag{3.82}$$

We have made two substitutions in this derivation. First, we note that $(-1)^{\phi_2(a,b)} = (-1)^{\phi_2(a,0)} \times (-1)^{\phi_2(0,b)}$. Second, we implement the two-component dummy variable $x_0' = (x_0^0, \vec{x}_0')$, where only the second component is also a dummy variable. Arriving at $\rho_2 = \tilde{C}_2^{\vec{p}}(t_0, t_0+t)$ means that we can produce quark propagators on random color walls $\Phi(x)$, impart momentum and a lattice site dependent phase to a single quark at the source, and then destroy those quark propagators while inserting the relative phase at the sink. Importantly, these quark propagators can all be grouped together at the source by taking the average over the random color walls.

Tying propagators together in this way is less resource-demanding than calculating $g(x,y)$, which is an *all-to-all* propagator. That calculation would require us to solve an equation of the form

$$\begin{aligned} g(x^0,\vec{x},y^0,\vec{y}) &= \sum_{z^0,\vec{z}} D^{-1}(x^0,\vec{x},z^0,\vec{z})\delta^3(\vec{y}-\vec{z})\delta(y^0-z^0) \\ &= \sum_{\vec{z}} D^{-1}(x^0,\vec{x},y^0,\vec{z})\delta^3(\vec{y}-\vec{z}) \end{aligned} \tag{3.83}$$

The problem becomes clear when we assign indices a, b, c to the three spatial coordinates. In doing so, equation 3.83 implies that

$$g_{ac}(x^0,y^0) = D^{-1}_{ab}(x^0,y^0)\delta_{bc} \tag{3.84}$$

Here, we need to invert the matrix D off of the source vector for every choice of index c, of which there are N_x^3 permutations. This inversion of D is made difficult because, besides the 1 in the c position, all of the source vector's elements equal 0. We are spared this challenge however by the insertion of random color walls: the propagator instead becomes

$$\begin{aligned} P(x^0,\vec{x},y^0) &= \sum_{\vec{y}} \left(\sum_{z^0,\vec{z}} D^{-1}(x^0,\vec{x},z^0,\vec{z})\delta^3(\vec{y}-\vec{z})\delta(y^0-z^0)\Phi(\vec{y}) \right) \\ &= \sum_{\vec{z}} D^{-1}(x^0,\vec{x},y^0,\vec{z})\Phi(\vec{z}) \end{aligned} \tag{3.85}$$

Reintroducing the spatial coordinate indices, equation 3.85 likewise implies that

$$P_a(x^0,y^0) = D^{-1}_{ab}(x^0,y^0)\Phi_b \tag{3.86}$$

where Φ_b is a random wall vector, the inclusion of which in this equation merges the many N_x^3 inversions we see in equation 3.84 into just a single inversion. This significantly reduces computation time, with the trade off of introducing random noise.

Having tackled two-point correlation functions, let us now address three-point correlation functions. Now source phase and momentum is instead given to the light antiquark $\bar{l}$. Meanwhile the light spectator quark l propagator acts as an *extended source* for the $\bar{h}$ propagator. That is to say, the l serves as a source to generate the $\bar{h}$. Taking the Fourier transform of the generic three-point correlation function (equation 3.76) we get

$$\tilde{C}_3^{\vec{p}}(t_0, t_0+t, t_0+T) = \frac{1}{N_x^3} \sum_{\vec{x}_T, \vec{x}_t, \vec{x}_0} e^{-i\vec{p}\cdot(\vec{x}_0 - \vec{x}_t)} C_3(x_T, x_t, x_0). \tag{3.87}$$

Because we only apply momentum to the light antiquark, which propagates from t_0+t to t_0, x_T only appears in the Fourier transform as an argument in $C_3(x_T, x_t, x_0)$. In the context of a three-point correlation function, we can define the random color wall propagators for the light quark and light antiquark propagators as

$$P^{l,\vec{p}}(x_T, t_0) \equiv \frac{1}{\sqrt{N_x^3}} \sum_{\vec{x}_0} e^{i\vec{p}\cdot(\vec{x}_0 - \vec{x}_T)} (-1)^{\phi_3(x_0,0,0)} \Phi(\vec{x}_0) g^l(x_T, x_0), \tag{3.88}$$

$$P^{l,\vec{p}\dagger}(x_t, t_0) \equiv \frac{1}{\sqrt{N_x^3}} \sum_{\vec{x}_0} e^{-i\vec{p}\cdot(\vec{x}_0 - \vec{x}_t)} g^{l\dagger}(x_t, x_0) \Phi^\dagger(\vec{x}_0). \tag{3.89}$$

For our extended source $\bar{h}$, we can likewise define its random color wall propagator as

$$P_{\text{ext.}}^{h,\vec{p}_h\vec{p}_l\dagger}(x_t, t_0, t_0+T) \equiv \sum_{\vec{x}_T} e^{-i\vec{p}\cdot(\vec{x}_t - \vec{x}_T)} (-1)^{\phi_3(0,0,x_T)} g^{h\dagger}(x_t, x_T) P^{l,\vec{p}_l}(x_T, t_0). \tag{3.90}$$

Like the two-point correlator case, we can propose a construction ρ_3 comprised of random color wall propagators which equals the Fourier transform of the generic three-point correlation function, giving source phase and momentum to the light spectator quark:

$$
\begin{aligned}
\rho_3 &= \sum_{\vec{x}_t} (-1)^{\phi_3(0,x_t,0)} \operatorname*{Tr}_{\text{color}} \left(P^{h,\vec{0},\vec{0}\dagger}_{\text{ext.}}(x_t,t_0,t_0+T) P^{l,\vec{p}\dagger}(x_t,t_0) \right), \\
&= \frac{1}{N_x^3} \sum_{\vec{x}_t} (-1)^{\phi_3(0,x_t,0)} \operatorname*{Tr}_{\text{color}} \Bigg((-1)^{\phi_3(0,0,x_T)} g^{h\dagger}(x_t,x_T) \\
&\times \sum_{\vec{x}'_0,\vec{x}_0} e^{-i\vec{p}\cdot(\vec{x}_0-\vec{x}_t)} (-1)^{\phi_3(x_0,0,0)} \Phi(\vec{x}'_0) g^l(x_T,x'_0) g^{l\dagger}(x_t,x_0) \Phi^\dagger(\vec{x}_0) \Bigg), \\
&= \frac{1}{N_x^3} \sum_{\vec{x}_T,\vec{x}_t,\vec{x}_0} (-1)^{\phi_3(x_0,x_t,x_T)} e^{-i\vec{p}\cdot(\vec{x}_0-\vec{x}_t)} \operatorname*{Tr}_{\text{color}} \left(g^{h\dagger}(x_t,x_T) g^l(x_T,x_0) g^{l\dagger}(x_t,x_0) \right), \\
&= \tilde{C}_3^{\vec{p}}(t_0,t_0+t,t_0+T).
\end{aligned}
\tag{3.91}
$$

From this equation we can see how its possible to take the same heavy and light propagators from our two-point correlation functions and reuse them in the corresponding three-point function. We still however need the extended source generated propagator for the case of the three-point function. Because it is cheaper to generate heavier quarks on the lattice than light quarks, we only regenerate $\overline{h}$ off of the extended source l. The ability to reuse quark propagators in this way is actually the reason why we construct our three-point correlators "backwards". Notice from figure 3.2 that we do not place the heavy meson at t_0 and the pion at t_0+T to intuitively match the meson decay of interest: $H \to \pi$. Instead we swap their positions, such that the spectator light quark acts as an extended source in generating the heavy antiquark. Fortunately, QCD is symmetrical in time; and so performing the time reversal whenever it is necessary is trivial on our pure QCD lattices.

3.5.6 Opposite parity states

As a final note to end this chapter, it is worth noting a peculiar phenomenon which emerges from the HISQ action. We have already seen how the doubling problem and spin-taste structure manifests as phase terms in the equations of correlation functions. As a consequence, we expect our lattice correlation function to have an oscillating phase term $(-1)^t$. Recall that it is not just the lattice equivalent of a *ground state* physical pion which couples to the correlation function, but all states with matching quantum numbers (see equations 2.41 and 2.42). With no oscillating phase term, the coupled states would include some ground state meson and a theoretically infinite tower of radially excited states, all with otherwise identical quantum numbers. With the inclusion of this oscillating phase term however, we now also expect states which differ in having opposite parity to couple to the given correlation function [78]. For this reason, we might refer to these opposite parity states as *oscillating states*.

We can expect oscillating states to couple to all of our lattice two and three-point correlation functions, with one exception. Appendix D in [12] discusses how there is no oscillating term in the correlation function of an at rest meson composed of a light quark and an antiquark with degenerate masses. The quark and antiquark are created by the same field, and the only means by which they would have an interaction (which would have an amplitude), would be from annihilation or the emission of a highly off shell gluon. Such gluons are removed by the contact terms in the HISQ action. Therefore we do not expect any oscillating states to couple to the correlation function for a pion with zero three-momentum.

Chapter 4

Fitting Correlation Functions

In this chapter, we cover the fundamentals and methodology of fitting correlation functions. It is through fitting correlation functions that we extract the ground state energies and amplitudes which are required for form factor calculation, which we explore in chapter 5. The methods we describe here apply, unless otherwise noted, for both the $H \to \pi$ and $H_s \to K$ meson decays. The meson decay-specific materials which relate to fitting correlation functions, such as tables of decay-specific priors, are given in chapters 6 and 7.

4.1 The fundamentals of correlator fitting

4.1.1 Fit equations

From the previous chapter we now have explored two different descriptions of correlation functions. The first of these defines the correlation function of some meson M in terms of a number of exponential N_{exp} which we can label as $i \in [0, N_{\mathrm{exp}})$, energies E_i^M, and amplitudes A_i^M. The second description defined the correlation function in terms of quark propagators, and phases which relate to a meson's spin-taste structure. The form our generated correlator data takes is the latter of these two, and by equating the two definitions of the correlation function we can fit this correlator data to the fit form prescribed by the former. Equations 4.1 and 4.2 give the expected fit forms for our two and three-point correlation functions. We can first explore the fit form for the two-point correlation function, which following from equation 2.41 is given by

$$C_2^M(t) = \sum_{i=0}^{N_{\text{exp}}-1} \left(|A_i^{M,\text{n}}|^2 (e^{-E_i^{M,\text{n}} t} + e^{-E_i^{M,\text{n}}(N_t - t)}) - (-1)^t |A_i^{M,\text{o}}|^2 (e^{-E_i^{M,\text{o}} t} + e^{-E_i^{M,\text{o}}(N_t - t)}) \right) \tag{4.1}$$

Here we can discuss the various terms that appear in these fit forms. First we again note that the lattice operators used to generate the correlator data couple not only to some ground state of energy $E_{i=0}^M$, but to an infinite tower of excited energy states E_i^M for all $i \geq 0$. In our correlator fitting we limit the number of exponentials to some number N_{exp}, hence the sum over some number of states $i \in [0, N_{\text{exp}})$. In section 4.7.1 we discuss how we determine an appropriate value for N_{exp}. We have also defined the amplitude term A_i^M equal to the matrix element divided by $2E_i^M$ (see equation 2.41). For a lattice with finite dimensions, we must also consider the periodic boundary conditions we impose on that lattice. Such conditions necessitate the presence of some meson at the temporal end of the lattice N_t moving backwards (decreasing t) towards the opposite end t_0. The forwards and backwards propagating states are physically equivalent, and likewise share the same amplitudes and energies. Therefore in equation 4.1 exponentials with powers $-E_i t$ correspond to forward propagating states, while those with powers $-E_i(N_t - t)$ correspond to backwards propagating states. Finally, as discussed in section 3.5.6, meson states with opposite parity manifest in the correlation function as states whose phases oscillate in time t/a (or simply t in equations 4.1 and 4.2 where the factor of the unit lattice length a is implied). Energies and amplitudes that correspond to such oscillating states have superscripts o, while negative parity, non-oscillating states have superscripts n. A sample two-point correlator plot is given in figure 4.1, where we plot the log of the correlator and find the expected exponential behavior.

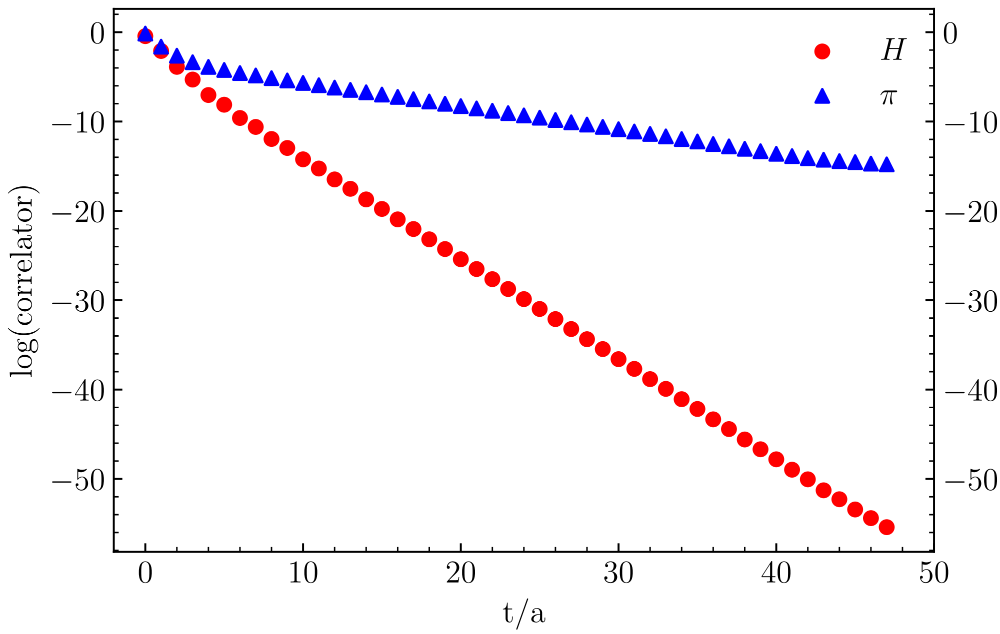

Figure 4.1: Sample H and π $\log(C_2^M)$ plot on the f5 ensemble. Data shown for $t/a \in [0, N_t/2]$ for $N_t/2 = 48$. Error bars are too small to be visible. Both the heavy meson H and light meson π have Goldstone pseudoscalar spin taste structure $\gamma_5 \otimes \xi_5$. The heavy quark in H has mass $am_h = 0.675$, and the light meson has twist $\theta = 1.282$, which is related to momentum via equation 4.10.

We can now go on to discuss the fit form of the three-point correlation function given by

$$
\begin{aligned}
C_3^{M_1,M_2}(t,T) = \sum_{i,j=0}^{N_{\mathrm{exp}}-1} \Big(& A_i^{M_1,\mathrm{n}} J_{ij}^{\mathrm{nn}} A_j^{M_2,\mathrm{n}} e^{-E_i^{M_1,\mathrm{n}} t} e^{-E_j^{M_2,\mathrm{n}}(T-t)} \\
& - (-1)^{(T-t)} A_i^{M_1,\mathrm{n}} J_{ij}^{\mathrm{no}} A_j^{M_2,\mathrm{o}} e^{-E_i^{M_1,\mathrm{n}} t} e^{-E_j^{M_2,\mathrm{o}}(T-t)} \\
& - (-1)^{t} A_i^{M_1,\mathrm{o}} J_{ij}^{\mathrm{on}} A_j^{M_2,\mathrm{n}} e^{-E_i^{M_1,\mathrm{o}} t} e^{-E_j^{M_2,\mathrm{n}}(T-t)} \\
& + (-1)^{T} A_i^{M_1,\mathrm{o}} J_{ij}^{\mathrm{oo}} A_j^{M_2,\mathrm{o}} e^{-E_i^{M_1,\mathrm{o}} t} e^{-E_j^{M_2,\mathrm{o}}(T-t)} \Big).
\end{aligned}
\tag{4.2}
$$

In a three-point correlation function we have two mesons M_1 and M_2 which propagate (both forward and backwards) from t_0 or T respectively, where T is the source-sink separation of the meson propagators (sometimes called the *width* of a three-point correlator), and at each t we insert the current J. The temporal region $t_0 \leq t \leq T$ corresponds to the physical meson decay in which we are interested. The signal within that region will be dominated by M_1 propagating forwards from t_0, and M_2 propagating backwards from T. For a small enough width T and large enough temporal lattice length N_t, any signal arising from periodic boundary conditions will have decayed before it

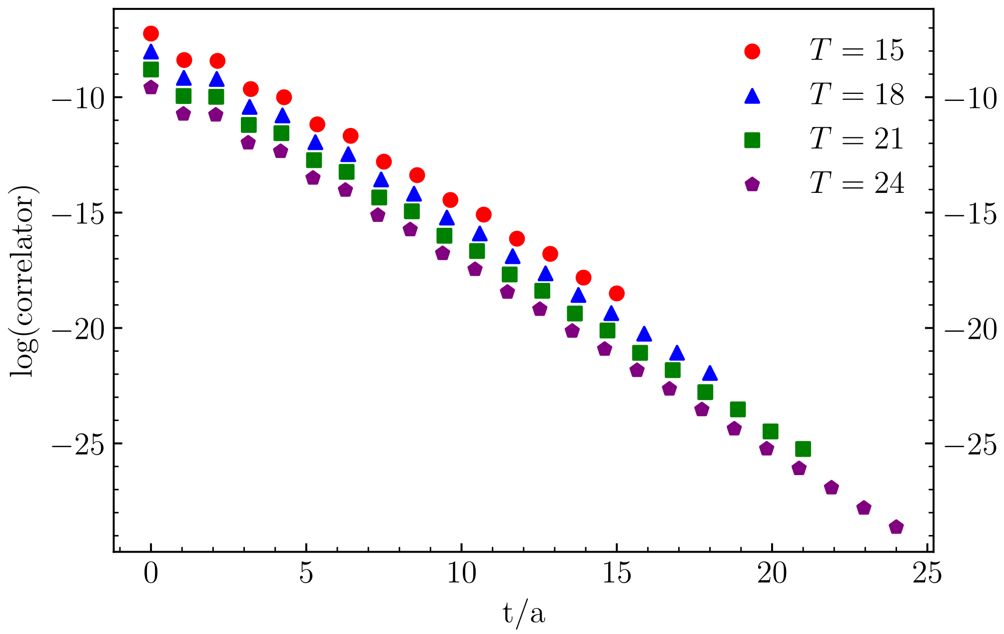

Figure 4.2: Sample $H \to \pi$, $\log(C_3^S)$ plot on the f5 ensemble. Error bars are too small to be visible. These three point correlators correspond to a scalar current insertion, a heavy quark mass $am_h = 0.675$, and a light meson with twist $\theta = 1.282$, which is related to momentum via equation 4.10. Four correlators with different values of source-sink separation T are shown.

contaminates the $t_0 \leq t \leq T$ region. Figure 4.2 provides a sample three-point log-correlator plot, which likewise shows the expected exponential behavior. The fit forms (equations 4.1 and 4.2) act as the model correlation functions C_2^{fit} and C_3^{fit} which we utilize in our augmented least squares fitting approach, which we discuss in the following subsection.

4.1.2 Bayesian fitting

For this research, we utilize a Bayesian fitting approach [79], where we effectively increase the sum of data we fit with the inclusion of *a priori* estimates of all fit parameters. We are motivated to take such an approach because we have some physics knowledge, to which we expect the data to adhere, that we wish to include in our analysis. In this procedure we augment the normal χ^2 equation one might expect to minimize in least squares fitting such that $\chi^2 \to \chi^2_{\text{aug}} = \chi^2 + \chi^2_{\text{prior}}$. The priors we insert into correlator fitting are gaussian variables, such that for some parameter X we write that its prior $P[X] = \tilde{X} \pm \tilde{\sigma}_X$, where $\tilde{X}$ is the prior's central value and $\tilde{\sigma}_X$ is its gaussian standard deviation (or uncertainty, which we colloquially use interchangeably). We utilize the *gvar* package [80] throughout this work to manage these priors. Among other things, this package allows the user to store and operate with gaussian random variables, and preserves the statistical correlations among such variables.

The application of this approach to correlator fitting specifically is well demonstrated in [81], whose notation we also follow. Considering a generic two-point correlator fit, we can then write the equation for χ^2_{aug} as

$$\chi^2_{\text{aug}}(E_i, A_i) = \sum_{t,t'} \Delta C_2(t) \sigma^{-2}_{t,t'} \Delta C_2(t') + \sum_i \frac{(E_i - \tilde{E}_i)^2}{(\tilde{\sigma}_{E_i})^2} + \sum_i \frac{(A_i - \tilde{A}_i)^2}{(\tilde{\sigma}_{A_i})^2}. \tag{4.3}$$

Here the second and third terms constitute χ^2_{prior}, while the first term in equation 4.3 is the standard term one might expect in least squares fitting. To simplify the equation we define

$$\Delta C_2(t) = \overline{C_2^{\text{data}}(t)} - C_2^{\text{model}}(t, E_i, A_i), \tag{4.4}$$

where $\overline{C_2^{\text{data}}(t)}$ is the averaged value of a Monte Carlo correlation function (the data) at t, and $C_2^{\text{model}}(t, E_i, A_i)$ is the value of the model correlation function as defined by 4.1 at t. It is the parameters in the model correlation function that are iterated upon by the fitter such that χ^2 is minimized. In the first term of equation 4.3 we also find the normalized covariance matrix[1] $\sigma_{t,t'}$, which we define as

$$\sigma^2_{t,t'} = \overline{C_2^{\text{data}}(t) C_2^{\text{data}}(t')} - \overline{C_2^{\text{data}}(t)}\; \overline{C_2^{\text{data}}(t')}. \tag{4.5}$$

1. Another name for the normalized covariance matrix is the *correlation* matrix. For the sake of not adding another “correlate”-containing phrase to this work (correlation function, correlator data, statistical correlations) we prefer the more clear, if somewhat clunky, ”normalized covariance matrix”.

From the construction of χ^2_{prior} we can predict how the assignment of priors might affect the minimization of χ^2_{aug}. For smaller, or more *narrow* prior uncertainties, the fitter is more strongly penalized when the fit parameter differs from the central value of its matching prior. Meanwhile, if a prior's uncertainty is relatively large, then the minimization of χ^2_{aug} will be relatively less sensitive to that prior's central value. Sections 4.3, 4.4, and 4.5 discuss our methods of prior determination extensively. Implementing priors in this way also prevents cases where the data alone would not prevent unbounded uncertainties on fit posteriors.

All of our correlator fitting is handled using the *corrfitter* package [82]. This package integrates our Bayesian fitting approach to correlator fitting, and encompasses/is a wrapper for the *lsqfit* package [83]. Both these packages utilize the *gvar* package such that fit parameter uncertainties and correlations are accounted for during the fitting process.

4.2 Partitioning the correlator fit

4.2.1 Motivation

While the computational resources we have access to for this research are generous, they are not sufficient to fit the sum of our correlator data simultaneously. Increasing the size of correlator data included in a fit will non-linearly increase the computing time of a fit. For this work, attempts to simply fit all $H \to \pi$ (or $H_s \to K$) correlator data simultaneously exceeded the allowed clock-time per job submitted to the Cambridge/DiRAC computer cluster we use. Perhaps the most significant contributor to correlator fit computation time is the inversion of the data covariance matrix (recall the term $\sigma^2_{t,t'}$ in equation 4.3), especially when data is both highly precise and correlated [84, 85, 86, 87]. There are a number of techniques we can utilize that can reduce the resources needed to calculate $\sigma^{-2}_{t,t'}$ [88], the testing and implementation of which we discuss here and in the following sections.

Perhaps the most direct approach we can take to reduce the computation time needed to invert the covariance matrix is to separate the fitting routine into distinct parts. This is to say, to not fit all Monte Carlo correlator data simultaneously, but to partition the fit such that the absolute size of the covariance matrix is reduced. This approach is analogous to the diagonal approximation discussed in [88, 89], where off diagonal elements in the covariance matrix are set equal to zero. In either case, the time needed to invert the covariance matrix is reduced. Naturally, a partitioned fit approach will not account for any statistical correlations among separately fit data. However if the statistical correlations among separately fit data are relatively large, we could jeopardize the validity of our fit results; the χ^2s of the separate fits would be underestimated. Therefore if we can determine which groupings of correlator data have relatively small statistical correlations with other grouping of correlator data, we can partition our fit routine along the lines that differentiate those groupings.

From this point onward, it will be useful to talk about statistical correlations among the fit parameters (energies and amplitudes) rather than our Monte Carlo correlator data. These parameters, as determined by the augmented least squares fit, acquire statistical correlations from the correlator data input into equation 4.3. These fit parameters are therefore useful proxies we can use to investigate covariance matrices. It is also important to note that, for this discussion, we only investigate the correlations among the ground state ($i = 0$) parameters, and do not analyze correlations among non-ground state ($i > 0$) parameters.

Per meson decay (two: $H \to \pi$, $H_s \to K$), per ensemble (five: f5, fphys, sf5, sfphys, uf5), we can categorize fit parameters by heavy quark mass am_h, twist angle θ (related to meson three-momentum $\vec{p}$ via equation 4.10), and meson or current insertion spin-taste structure (equation 3.73). Our three-point correlator data does also vary by source-sink separation T. We do not however consider source-sink separation as a dimension though which to partition our fit routine. This is because, for a constant heavy quark mass, twist, and current insertion, varying T does not change which current insertions $J_{ij}^{kl}(am_h, \theta)$ are determined by the fitter.

4.2.2 Analyzing normalized covariance matrices

Let us now explore some test fits and their resultant normalized covariance matrices to determine where it might be best to partition our fitting routine. Consider the matrix presented in figure 4.3. Here we present a normalized covariance matrix as a stylized heatmap, which makes it easier to visually spot clusters of inter-correlating parameters. In this figure we can see the relative correlations among heavy mesons energies E_H of two different spin-taste structures[2], and the matching[3] scalar and temporal vector current insertion amplitudes S, V^0. While the twist angle $\theta = 0.0$ is constant for all parameters, the mass of the heavy quark is varied.

In figure 4.3 we can immediately spot the pattern of 3×3 squares which correspond to the three different heavy quark masses present in the test fit. The four 3×3 blocks along the diagonal show the extent of relative correlations among parameters of matching meson spin-taste or current insertion. These statistical correlations are relatively higher than elsewhere in the sample matrix. Should heavy quark mass be the candidate dimension along which to partition the fit function, these statistical correlations would be lost, and we might invalidate the results of our least squares fit. In this test fit and in others across all ensembles and both meson decays, we see this consistent relationship among fit parameters of shared twist and spin-taste structure, but varying heavy quark mass. This observation rules out partitioning our final fit routine along the lines of heavy quark mass.

Next we can examine twist angle as a possible means by which to partition our fit function. Like before, we can perform a small test fit where, while keeping heavy quark mass constant, we vary twist angle and observe the clusters of statistical correlations. Figure 4.4 presents the normalized covariance matrix of a test fit that follows these constraints. In this matrix we can see that, other than the diagonal of self-correlations equal to 1.0, the highest relative correlations are among

2. Notice here we have dropped the notation for exponential order i for E_H; we are only discussing ground state $i = 0$ parameters. In doing so we also use subscripts and superscripts interchangeably for the notation of corresponding mesons.
3. Here we say "matching" to refer to their shared presence in three-point correlator construction (equation 3.74).

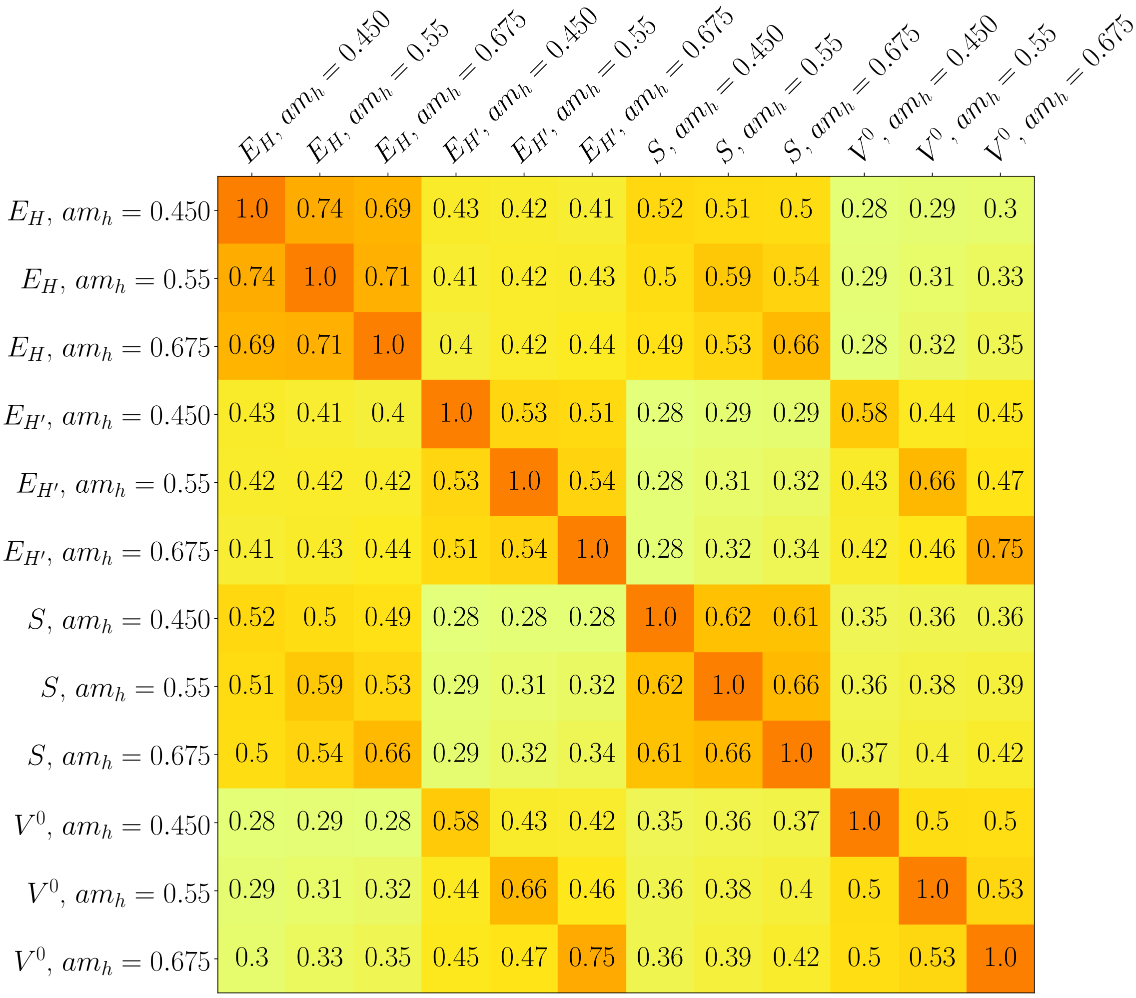

Figure 4.3: Sample normalized covariance matrix of correlator fit posteriors. Results are shown for the $H \to \pi$ meson decay on the f5 ensemble. The sample fit covers a subset of available correlator data. Fit parameters correspond to a range of heavy quark masses am_h, light meson twist $\theta = 0.0$, and source-sink separation (in lattice units) $T = 24$. Parameters shown are either heavy meson energies E_H, $E_{H'}$, or current insertion amplitudes $J \in \{S, V^0\}$. The heavy mesons H and H' differ only in spin-taste structure, which is given in 3.73, and are otherwise equivalent in quark composition and heavy quark mass.

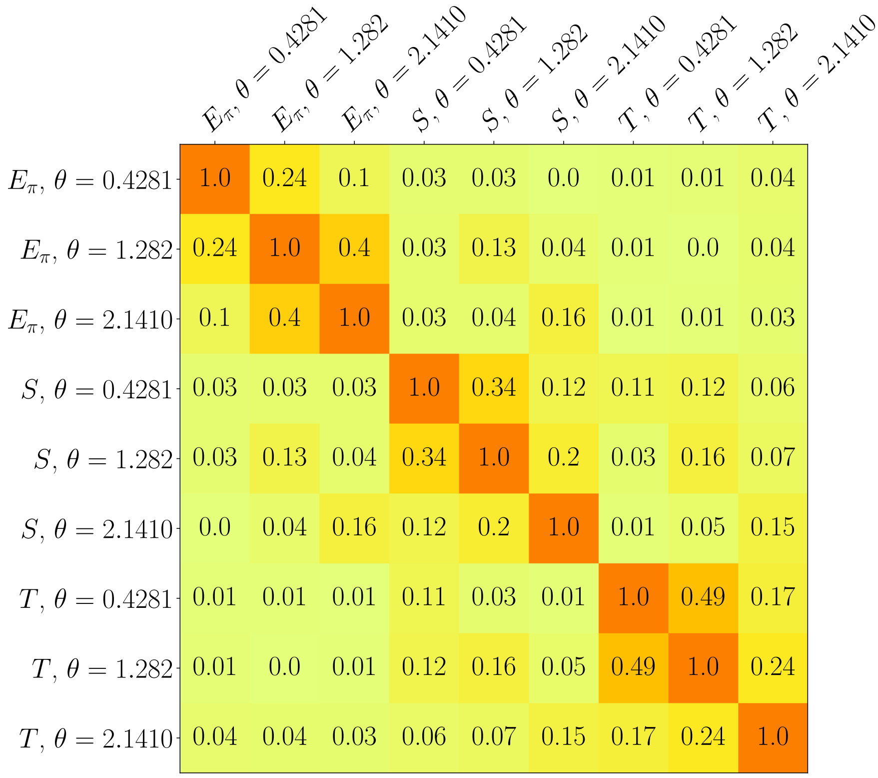

Figure 4.4: Sample normalized covariance matrix of correlator fit posteriors. Results are shown for the $H \to \pi$ meson decay on the f5 ensemble. The sample fit covers a subset of available correlator data. Fit parameters correspond to a heavy quark mass $am_h = 0.450$, a range of light meson twist θ, and source-sink separation (in lattice units) $T = 24$. Parameters shown are either light meson energies E_π or current insertion amplitudes $J \in \{S, T\}$, whose spin-taste structures are presented in equation 3.73.

groups of parameters of matching spin-taste but differing twist angle: the three 3×3 blocks along the diagonal of the matrix. Like before, this pattern suggests that twist angle is also not the best dimension along which to partition our fit routine. Across many test fits for all ensembles and both meson decays, we observe a similar pattern where parameters of matching spin-taste but varying twist angles have higher relative statistical correlations than those among parameters of matching twist but differing spin-taste.

These first two matrices point us in the direction of the final option we have to partition the fit function: to separate the fit along the lines of spin-taste construction. Figure 4.5 shows a normalized covariance matrix for a test fit of this type. The parameters shown all correspond to the same heavy quark mass (except for the pion which do not contain a heavy quark) and the same twist angle (except for the heavy mesons which all have twist $\theta = 0$). The first observation we can make is that the presented pion energy correlates relatively little with any other parameter. Furthermore, regardless of spin-taste construction, the heavy meson energies have relatively high correlations among themselves. These same heavy meson energies are then also highly correlated with the amplitudes of the scalar and temporal vector currents, but not the spatial vector or tensor currents. Counterintuitively, the energies of the heavy mesons H'' and H''' are not highly correlated with the amplitudes V^1 and T, even though they share the same three-point functions respectively. Figure 4.6 presents a normalized covariance matrix from the same test fit, but presents the amplitudes of heavy and light mesons instead of their energies. We can observe the same patterns of correlations here match those of the matrix in figure 4.5.

We find similar patterns of correlations among all $H \to \pi$ ensembles: figure 4.7 shows a similar normalized covariance matrix for the uf5 ensemble instead of the f5 ensemble. We do however observe a slight difference in examining a similar set of parameters from a test fit for $H_s \to K$. Consider the matrix in figure 4.8: here the light meson energy does have somewhat higher statistical correlations with the heavy meson energies. Additionally, the heavy meson energies are all highly correlated with each other, but not the amplitudes of the scalar or temporal vector currents they way they are in the case for $H \to \pi$. We observe that these observations for either $H \to \pi$ and $H_s \to K$ are consistent across all ensembles.

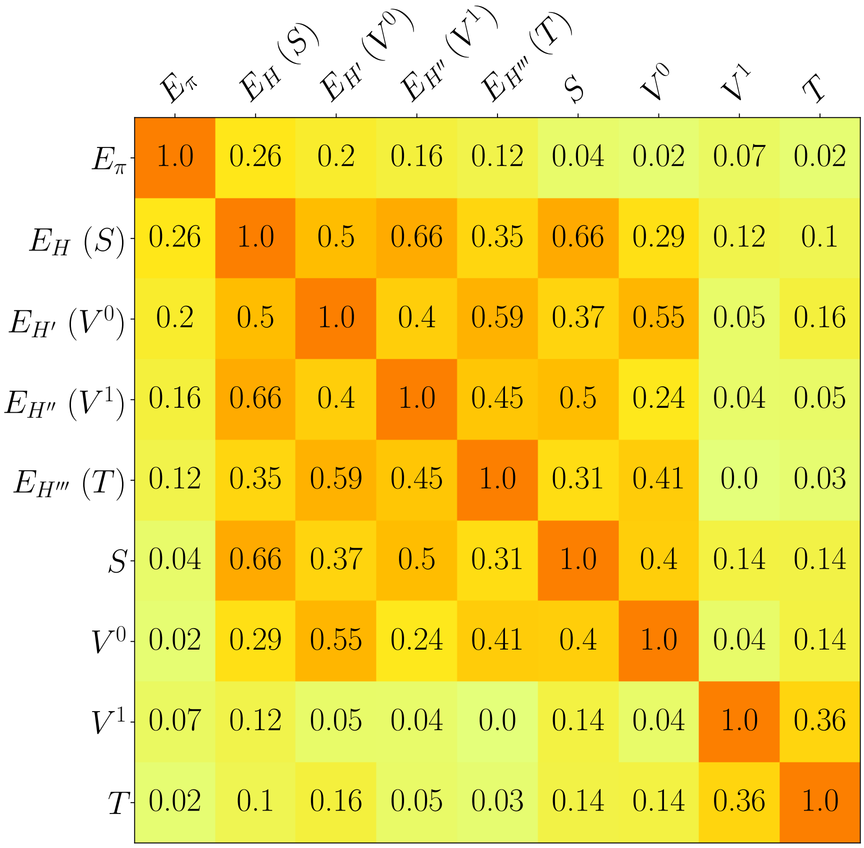

Figure 4.5: Sample normalized covariance matrix of correlator fit posteriors. Results are shown for the $H \to \pi$ meson decay on the f5 ensemble. The sample fit covers a subset of available correlator data. Fit parameters correspond to a heavy quark mass $am_h = 0.450$, light meson twist $\theta = 0.4281$, and source-sink separation (in lattice units) $T = 24$. Parameters shown are either meson energies E_M or current insertion amplitudes $J \in \{S, V, T\}$, whose spin-taste structures are presented in equation 3.73. Labels for heavy meson energies also indicate which current insertion J is present in its appropriate three point function (equation 3.74).

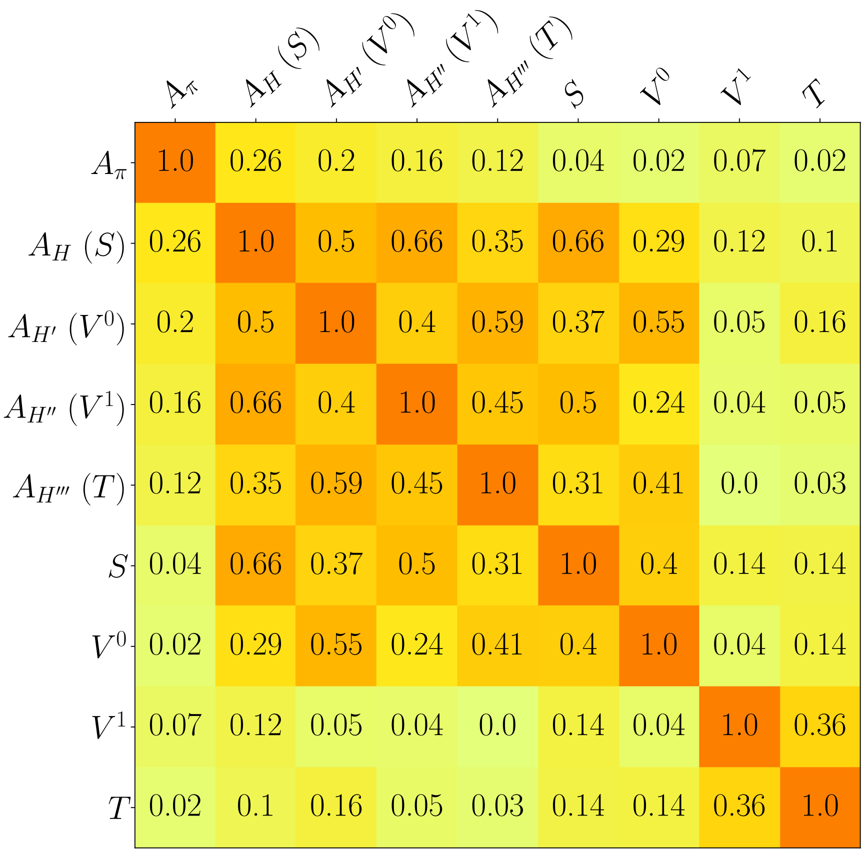

Figure 4.6: Sample normalized covariance matrix of correlator fit posteriors. Results are shown for the $H \to \pi$ meson decay on the f5 ensemble. The sample fit covers a subset of available correlator data. Fit parameters correspond to a heavy quark mass $am_h = 0.450$, light meson twist $\theta = 0.4281$, and source-sink separation (in lattice units) $T = 24$. Parameters shown are either meson amplitudes A_M or current insertion amplitudes $J \in \{S, V, T\}$, whose spin-taste structures are presented in equation 3.73. Labels for heavy meson amplitudes also indicate which current insertion J is present in its appropriate three point function (equation 3.74).

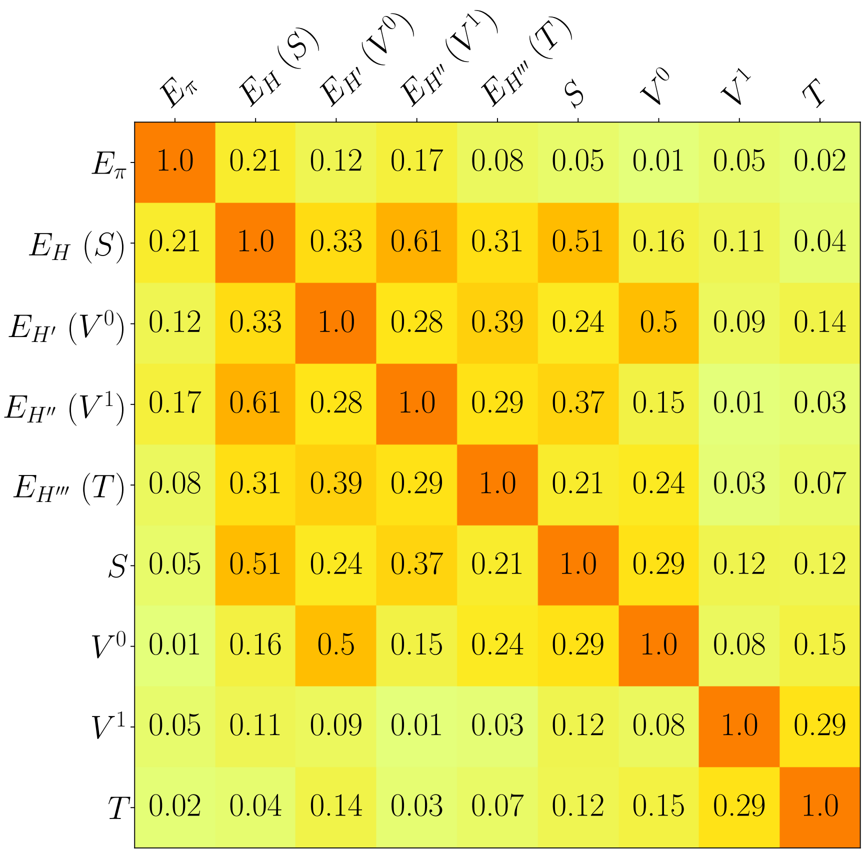

Figure 4.7: Sample normalized covariance matrix of correlator fit posteriors. Results are shown for the $H \to \pi$ meson decay on the uf5 ensemble. The sample fit covers a subset of available correlator data. Fit parameters correspond to a heavy quark mass $am_h = 0.194$, light meson twist $\theta = 0.706$, and source-sink separation (in lattice units) $T = 44$. Parameters shown are either meson energies E_M or current insertion amplitudes $J \in \{S, V, T\}$, whose spin-taste structures are presented in equation 3.73. Labels for heavy meson energies also indicate which current insertion J is present in its appropriate three point function (equation 3.74).

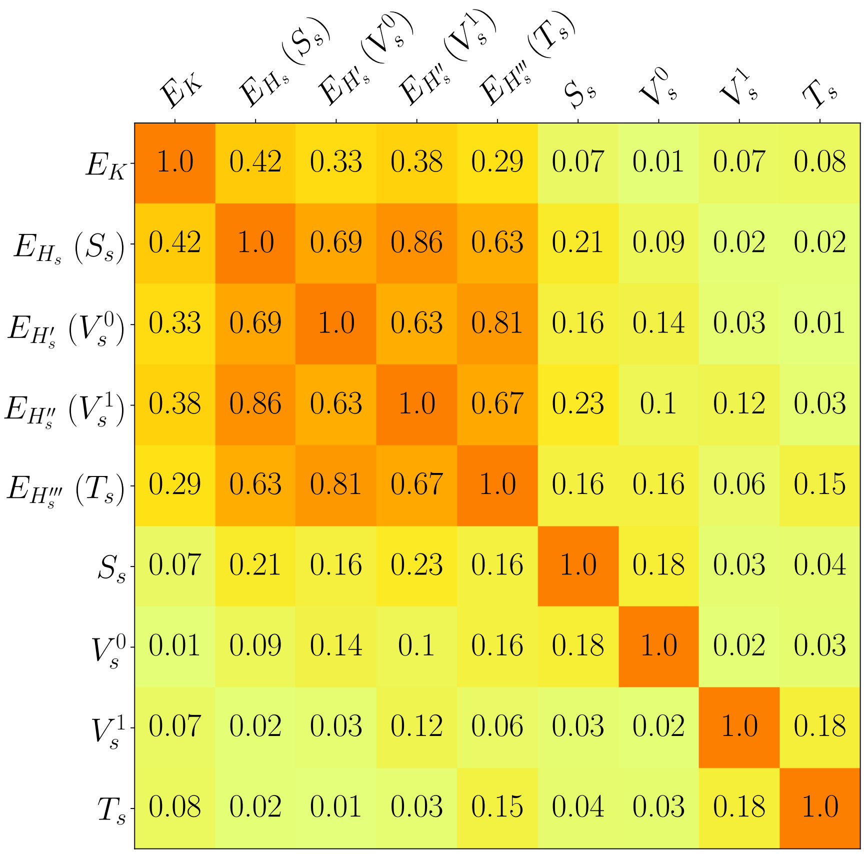

Figure 4.8: Sample normalized covariance matrix of correlator fit posteriors. Results are shown for the $H_s \to K$ meson decay on the f5 ensemble. The sample fit covers a subset of available correlator data. Fit parameters correspond to a heavy quark mass $am_h = 0.450$, light meson twist $\theta = 0.4281$, and source-sink separation (in lattice units) $T = 24$. Parameters shown are either meson energies E_M or current insertion amplitudes $J \in \{S_s, V_s, T_s\}$, whose spin-taste structures are presented in equation 3.73. Labels for heavy meson energies also indicate which current insertion J is present in its appropriate three point function (equation 3.74).

Focusing now on three-point amplitudes, we find that across all ensembles and both meson decays, the amplitudes of scalar and temporal vector currents are relatively more correlated with each other than either of them are with the amplitudes of spatial vector or tensor currents. The reverse of this also appears to be true. Figure 4.9 gives a clear example of this phenomenon. In this figure we see varying heavy quark mass and twist angle options, as well as the four different current insertions; the S and V^0 amplitudes correlate more with each other than with V^1 or T, and vice versa.

The consistency of this behavior across our entire data set then forms the basis of our finalized correlator fit routine. The majority of the Monte Carlo correlator data we are fitting correspond to three-point functions, which we can separate into two similarly sized categories: $J \in \{S, V^0\}$, and $J \in \{V^1, T\}$. Our fit method is then as follows: we fit all two-point correlators with the S, V^0 three-point correlators. Then, in the same fitting script, we fit all two-point correlators again with all V^1, T three point correlators. Having fit all two point correlators twice, we then calculate a weighted average of all doubly-fit parameters, the exact methodology of which we describe in the following section. Finally, all fit outputs are saved using the *gvar* package function which preserves the statistical correlations among those fit outputs.

4.2.3 Weighted average of fit parameters

In the previous section, we settled on a correlator fitting method where, for a given meson decay and ensemble, the $J \in \{S, V^0\}$ and $J \in \{V^1, T\}$ halves of the three-point correlator data are fit separately. To ensure that the statistical correlations between the two-point data and either half of the three point data are conserved, the two-point data is fit twice: once with either half of the three-point data. We are then left with the question of how to properly address the meson energy and amplitude fit posterior copies we obtain from both halves of the fit. Ideally, we want to take an average of the two copies such that we preserve statistical correlations. Not only should this average account for the high correlation between the two copies, but this new average should still preserve its correlations with all the other fit posteriors in either half of the fit. Thankfully, the

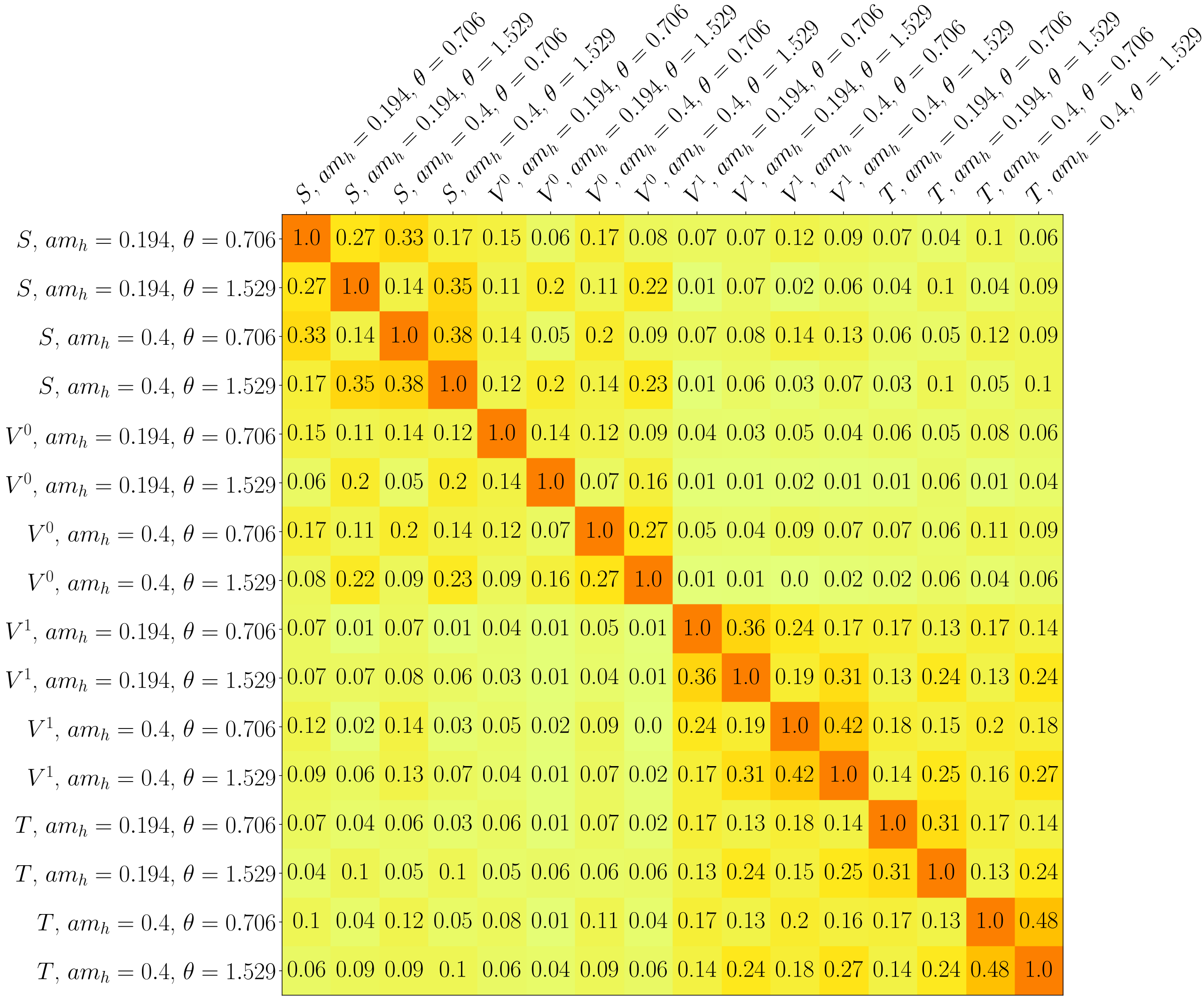

Figure 4.9: Sample normalized covariance matrix of correlator fit posteriors. Results are shown for the $H \to \pi$ meson decay on the uf5 ensemble. The sample fit covers a subset of available correlator data. Fit parameters correspond to a range of heavy quark masses and light meson twists, and source-sink separation (in lattice units) $T = 44$. Parameters shown are current insertion amplitudes $J \in \{S, V, T\}$, whose spin-taste structures are presented in equation 3.73.

lsqfit package contains a *weighted average* function that preserves these correlations, and accounts for the relative uncertainties of either `gvar` object (the gaussian random variable *object*, not the *gvar* package itself) in the weighted average. This new `gvar` is then a weighted average of the copies from both halves of the fit, which we can easily save for future use in form factor calculations. Each new, weighted average `gvar` however is a statistical least-squares fit in its own right, and carries its own χ^2 per degrees of freedom (χ^2/d.o.f.).

In correlator fit testing, it became clear that in the minority of cases, some weighted average `gvars` had $\chi^2/\text{d.o.f.} > 1$. Such instances corresponded to the doubly-fit posteriors from both halves of the partitioned fit not being within one standard deviation of the other. In these cases we can follow the guidelines given in the PDG [19] on how to scale the uncertainty of a weighted average to account for this phenomenon. To do so for some mean value g, we can multiply its standard deviation σ_g by some scaling factor λ, where

$$\lambda = \sqrt{\chi^2/(\text{d.o.f.} - 1)}. \tag{4.6}$$

Given that we are managing `gvars`, we want to use an indirect method to scale uncertainty without directly assigning a new uncertainty, and thereby removing the existing correlations. Suppose we label the final, scaled `gvar` we want to save for future calculations as $z \pm \sigma_z$. We then wish to create some uncorrelated `gvar` $y \pm \sigma_y$ which, when multiplied by the original unscaled weighted average `gvar` $x \pm \sigma_x$ gives a final scaled `gvar` $z \pm \sigma_z$ where $z = x$, $\sigma_z = \lambda \times \sigma_x$. Let us begin with the standard error propagation formula for this scenario:

$$\left(\frac{\sigma_z}{z}\right)^2 = \left(\frac{\sigma_x}{x}\right)^2 + \left(\frac{\sigma_y}{y}\right)^2. \tag{4.7}$$

For our desired case of scaling the uncertainty of the original weighted average σ_x by λ, we set $z = x$, $\sigma_z = \lambda\sigma_x$, and $y = 1$. We then have

$$\begin{aligned}\left(\frac{\lambda\sigma_x}{x}\right)^2 &= \left(\frac{\sigma_x}{x}\right)^2 + \sigma_y^2,\\ \sigma_y^2 &= \left(\frac{\lambda\sigma_x}{x}\right)^2 - \left(\frac{\sigma_x}{x}\right)^2\\ &= \frac{\sigma_x^2(\lambda^2-1)}{x^2},\\ \sigma_y &= \frac{\sigma_x\sqrt{\lambda^2-1}}{x}.\end{aligned} \tag{4.8}$$

With this formulation established, we can easily alter the fitting script to calculate weighted averages of meson energies and amplitudes that respect all statistical correlations in our fit. These new averages are then saved alongside the three-point parameters, the amplitudes of the current insertions, which we then use further in the process of form factor calculation. Across our current working set of correlator fits, wherever weighted average scaling is required, more often than not we calculate the scaling term to be in the range of $1 < \lambda < 2$, and very rarely do we see $\lambda > 3.5$.

4.2.4 Chained and marginalized fits

There are two more methods for reducing correlator fit computation time which we explored for this research, but ultimately did not implement in our final fit routine. These methods are *chained* fits, and *marginalized* fits. Both of these methods (detailed in the documentation for the *lsqfit* package [83]) entail truncating or modifying the default *lsqfit* routine of fitting all parameters simultaneously. Both these methods manage the correlator fitting in a somewhat more streamlined manner, as compared to the full partitioned fit routine we finally settled on. So while we do not include them in our final fit, it is worth exploring what they are and describing how we came to the decision to not utilize them.

In a chained fit, one chooses a subset of parameters to be fit first: meson energies and amplitudes for example. The fit posteriors of this first fit are then used as the (ideally very precise) priors for those same parameters in the next step in a chained fit. In this next step, or link, a new subset of parameters (some current insertion amplitudes for example) is fit alongside the posteriors from in the previous link. It is important to note that correlator data fit in one link is not fit again in subsequent links: only the fit posteriors are carried forward. This process continues for a number of user designated links until all parameters have been fit, where perhaps most of those parameters are given (very) narrow priors equal to the outputs from previous links. This method can, among other things, reduce the number of iterations the fitter takes to minimize the χ^2_{aug} function. Additionally, it does not remove statistical correlations among fit parameters. In testing however it was often the case that excluding three-point correlators in a two-point correlator only fit (the first link) would meaningfully affect the fitter's determination of a mesons energy or amplitude. Furthermore, we found that link composition and ordering significantly influenced final fit posteriors. Finally, even with a chained fit of all correlator data on a given ensemble and meson decay, we still hit the computation time limit. For these reasons we did not utilize a chained fit in our finalized fitting routine.

Where a chained fit partially separates the fitting of certain parameters, a marginalized fit entails removing some parameters from the fit more directly. Most of the parameters in our fit forms (equations 4.1 and 4.2) do not appear in the equations needed to calculate lattice form factors (see chapter 5). Such parameters include all excited state ($i > 0$) and oscillating terms which appear in the fit forms. In a marginalized fit we then use priors of these select parameters to model their respective parts of the fit function, which are then subtracted from the input data. This technique can be used to effectively prioritize the ground state parameters for which we have the most interest. Selecting which higher order and or oscillating parameters to marginalize requires a study of test fits to determine which are appropriate. We wish to avoid the case where marginalizing a certain set of non-ground state parameters significantly influences the fitter's determination of their ground state counterparts. In test fitting we found that across all ensembles there was no consistent set of parameters which, when marginalized, sped up the fitting process without significantly influencing the ground state parameters. For this reason we do not marginalize any parameters in our finalized fit technique.

4.3 Prior determination methodology

In this section we describe the general methods we use to determine the priors for the fit parameters which appear in equations 4.1 and 4.2. In general, we prefer automated methods of prior determination, with the interest of saving time. For example, cases where a ground state plateau is distinct enough from non-ground state signal, a function can take the rolling average of adjacent and consecutive data values. The central value of the ground state energy or amplitude can then be determined from where the change in this rolling average is minimized. Figure 4.10 shows an example of this automated approach. In most cases however, a clear ground state plateau is not apparent in the effective plot, which prevents a simple algorithm like the one described previously from determining an appropriate prior. In such cases, we assign prior manually by visually assessing effective energy and amplitude plots.

Irrespective of methodology, with prior determination we always aim to set conservative priors, avoiding cases where priors impose strict constraints on their matching posteriors. In test fitting, we ensure that prior absolute uncertainties are no smaller than at least ten times their matching posteriors. We take exception to this principle when we have additional physics information to which we expect the standard model-derived correlator data to adhere. Sections 4.4.3 and 4.4.4 detail examples of this in relation to the dispersion relation and excited state meson energies respectively. In such cases, physics based algorithms are used to automatically assign values to these priors, where the $10:1$ prior to posterior uncertainty rule is sometimes violated.

Finally, in the cases where we cannot use effective energy or amplitude plots, nor physics based preconceptions to determine priors, we utilize Gaussian Bayes Factor (GBF) optimization. Much more information on the Bayes factor can be found in [90, 91] and in section 4.8, but to effectively summarize its use here: prior tuning that maximizes a fit's GBF indicates that the prior neither over-constrains nor under-constrains the fit [92]. For priors indeterminable by the previously noted methods, such as oscillating excited three-point current insertion amplitudes, we opt to use this method. A prior is GBF optimized by performing a test fit, and recording the fit's GBF, or more often $\log(\mathrm{GBF})$. Then, the prior's mean or standard deviation is slightly adjusted. The fit is performed once more and the subsequent change (if any) of the $\log(\mathrm{GBF})$ is recorded. This process is repeated until a clear maximum is resolvable. The GBF optimization of a prior's uncertainty is aborted however if maximizing a fit's GBF violates the 10:1 prior to posterior uncertainty principle. In such cases, more conservative (larger standard deviation) priors are chosen over more precise, GBF-preferred priors.

4.4 Two-point correlation function priors

In the following subsections, we discuss how we determine priors on meson energies E_i^M and amplitudes A_i^M, which appear in both the two and three-point correlator fit forms (equations 4.1 and 4.18). We do however at times refer to meson energy and amplitude priors as *two-point priors* for conciseness. The full set of two-point priors includes the ground state and higher order energies and amplitudes of: mother mesons with varying masses and spin-taste structures, daughter mesons of varying momentum, and the negative parity/oscillating meson counterparts.

Before we delve into two-point priors, we note that in equation 4.1 the amplitude terms always appear as $|A_i|^2$. As such we can always parameterize amplitude terms as being positive. We likewise expect energy terms to be positive. To enforce positive valued energy and amplitude fit posteriors, we perform two-point correlators fits in $\log$-space. This is to say, we take the $\log$ of all assigned two-point priors before fitting. We then use these $\log$-priors as inputs when fitting the $\log$ of two-point correlation functions. Transforming out of log-space is as simple as taking the exponential of the returned fit posteriors. For the remainder of this section, we do not discuss priors in the context of log-space, though the transformation into log-space before and after fitting should always be implied.

4.4.1 Meson rest masses

The first set of priors we can discuss are the priors for the rest masses of the heavy and light mesons. By construction, the heavy mother mesons in this work (H, H_s) are always in the rest frame of the lattice, and so their energies are equivalent to their masses. In other words, they have no three-momentum $\vec{p}$. The lighter daughter mesons (π, K) however are simulated at varying three-momenta, whose priors we discuss in 4.4.3. In the context of three-point functions, a daughter meson of zero three-momentum corresponds to a $q^2_{\max}$ current insertion; the daughter meson remains at rest in the lattice frame and its energy equals its rest mass.

For a two-point correlator $C_2^M(t)$ of some meson M, we can define a function of its effective mass $aM_{\text{eff}}(t)$ as.

$$aM_{\text{eff}}(t) = \frac{1}{2}\cosh^{-1}\left(\frac{C_2(t-2)+C_2(t+2)}{2C_2(t)}\right). \tag{4.9}$$

For a well behaved two-point correlation function, it is possible to determine a prior for the meson's ground $i=0$ state mass from its effective mass plot. In this context "well behaved" simply means that the energy of higher order $i>1$ exponentials are much larger and therefore decay quickly in equation 4.1.

Figure 4.10 shows sample effective mass plots for $H \to \pi$ on the f5 and uf5 ensembles. From this figure we can see that the effective mass function follow a trend where, after t_{min}, the higher order states decay quickly. Then, the data stabilizes with relatively small uncertainty and minimal central value fluctuations. This is the signal for the ground state rest mass. Then, the uncertainty and the size of central value fluctuations grows towards the middle of the lattice length (The range of the x-axis is truncated in these figures, so they do not show this phenomena as clearly).

This consistent behavior, a steady region or plateau of stable ground state signal, in the effective mass plot permits the use of an automated prior determination method. We utilize a simple custom `python` function which takes a rolling average over sets of 4 adjacent effective mass values (that is to say: at 4 consecutive lattice time slices t/a) and finds where this rolling average changes the least. The central value of the rest mass's prior is then assigned to be equal to the change-minimized, rolling averaged $aM_{\text{eff}}(t)$. Figure 4.10 also gives a visual example on how this minimum change in the rolling average is related to the effective mass of a two-point correlation function.

Observing effective mass plots like 4.10 also enables us to assign fractional uncertainties to the priors for ground state meson rest masses. In this figure we can see that the two point pion correlator C_2^{π} effective mass data $aM_{\text{eff}}(t)$ remains within the bounds of $\pm 5\%$ of the change-minimized rolling average on the f5 ensemble, as opposed to about $\pm 30\%$ on the uf5 ensemble. Tables 6.3 and 6.3 gives the complete list of the fractional uncertainties we use in our correlator fits. In all cases, we confirm in test fitting that the standard deviations of meson mass fit posteriors are at least ten times smaller than the standard deviations of their matching fit prior. In many cases, the prior to posterior standard deviation ratio is much greater: on the order 100:1 or greater. This is an assuring sign that the priors we have chosen are not constricting to the fit. It is important to note that, after spotting such large prior to posterior ratios in test fitting, we do not then adjust priors to move closer to the ratio 10:1. Even in cases where such a change would increase the $\log(\text{GBF})$ of a fit, we would be violating the justification for using priors in the first place. We wish to maintain physics and or data backed reasons for prior choices, otherwise the priors lose their *a priori* nature.

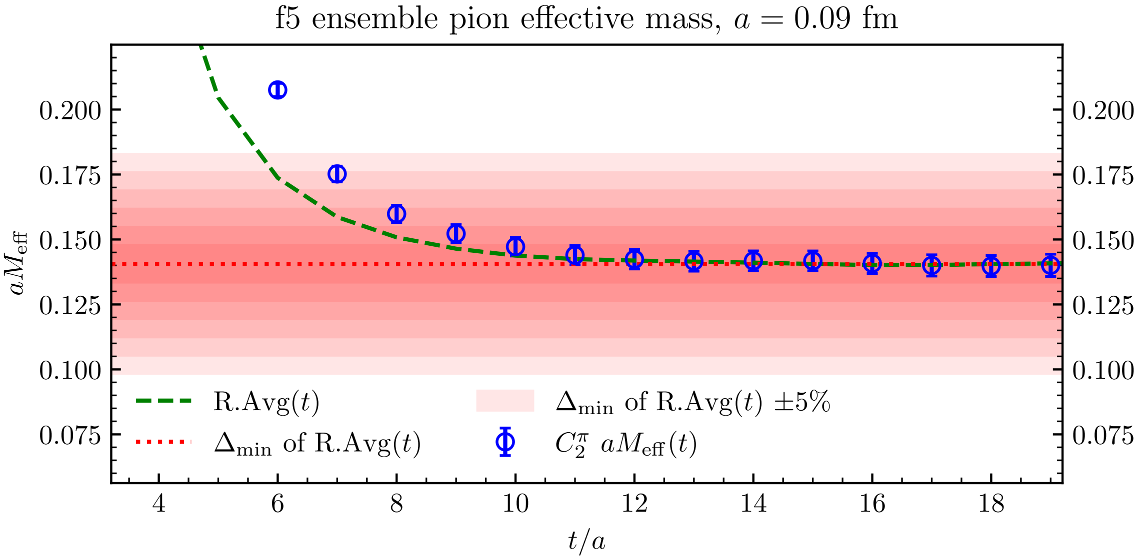

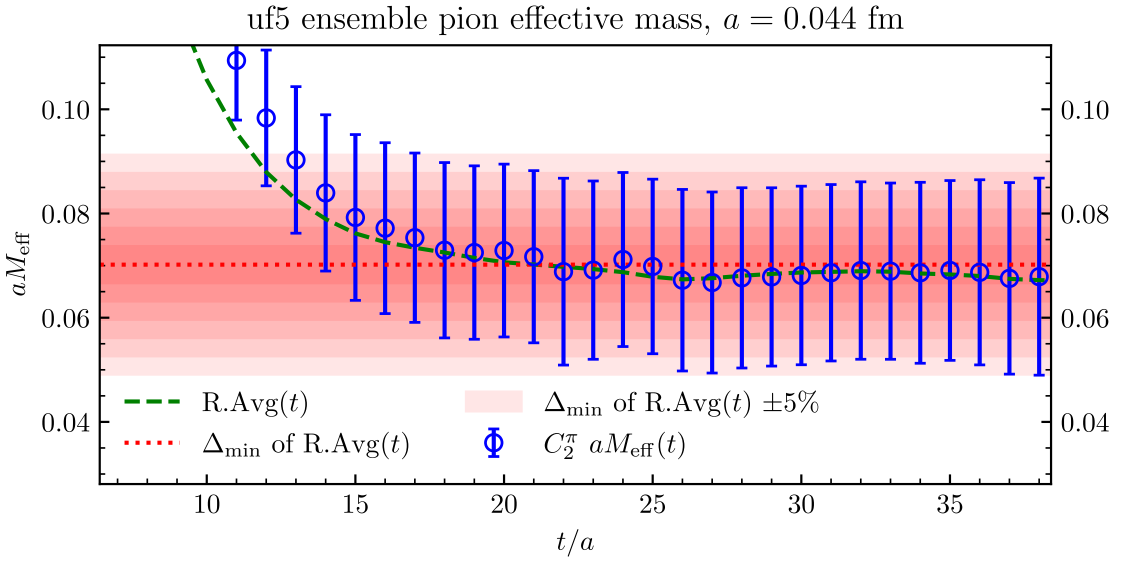

Figure 4.10: Sample pion effective mass plots on the f5 and uf5 ensembles. The effective mass $aM\mathrm{eff}(t)$, which is calculated from equation 4.9 and its respective two point correlation function C_2^{π}, is shown in blue. The rolling average of the effective mass R.Avg(t) is shown in dashed green. Where the change in this rolling average is minimized Δ_{min} of R.Avg(t) is shown in dotted red. Consecutive red bands show regions of $\pm 5\%$, out to $\pm 30\%$, of Δ_{min} of R.Avg(t).

4.4.2 Zero-momentum oscillating meson masses

Having established the methodology for determining priors on our ground state, zero-twist, non-oscillating meson energies (masses), we can now move on to determine priors for their $i = 0$, zero-twist, *oscillating* counterparts. The ground state mesons have angular momentum and parity quantum numbers of $J^P = 0^-$. The meson states with quantum numbers $J^P = 0^+$ however also couple to the correlation functions. As discussed in section 3.5.6, our use of the HISQ action [12] leads to opposite parity states manifesting as oscillating propagators on the lattice. We therefore call the lowest energy meson state with quantum numbers $J^P = 0^+$ the *lowest lying oscillating* state of that meson. These are the states which have energies and amplitudes $E_0^{M,o}$ and $A_0^{M,o}$ in equation 4.1. We discuss the amplitudes of these states later in section 4.4.6. As noted in section 3.5.6, the zero-momentum oscillating pion does not appear in its respective two-point correlator. However an estimate for its energy will be used later in section 4.4.3 to set priors non-zero-momentum oscillating pion energies. For this reason we still take care to determine reasonable priors for $E_0^{\pi,o}$.

Unfortunately, priors for these lowest lying oscillating states cannot be determined using the same methodology as before; we can not visually determine a lowest lying oscillating state's contribution to an effective mass plot. Instead, we can be guided by the known energy difference, or splitting, between the masses of physical negative and positive parity particles given by the Particle Data Group (PDG) [19]. For example, the ground state pion has a rest mass of about 140 MeV, while the next lowest energy pion state with opposite parity, the $f_0(500)$ has a rest has a mass of roughly 500 MeV. The energy splitting between the two is about 360 MeV, or roughly $0.7 \times \Lambda_{\mathrm{QCD}}$. This state however does not have the same isospin quantum number as the ground state pion, and so we do not expect it to couple to our pion propagators [93, 94]. Instead we must look to the $a_0(980)$ particle, which shares the same isospin quantum number as the ground state pion. The energy difference between those two particles is then 840 MeV, or $1.68 \times \Lambda_{\mathrm{QCD}}$. Knowing this energy difference allows us to set the central values of the priors for the lowest lying oscillating state energies $P[E_0^{\pi,o}] = P[E_0^{\pi,n}] + 1.68 \times \Lambda_{\text{QCD}}$. This works across all ensembles because we define the central value of $P[E_0^{\pi,o}]$ relative to the central value of the ground state pion on a given ensemble, and some scalar times Λ_{QCD}.

Setting the uncertainty for $P[E_0^{\pi,o}]$ is not a trivial task meanwhile. The known energy splitting for the physical continuum pion and $a_0(980)$ is not necessarily equal to the energy splitting between those equivalent states on the lattice. For finite lattice spacing, order $\mathcal{O}(a^2)$ taste symmetry breaking leads to non-degenerate quark masses of different tastes [12, 95]. This effect is larger for the positive parity pion state we are trying to identify in our correlator fitting.[96, 97]. Additionally, this a_0 resonance is strongly coupled to certain multi-particle channels of matching quantum numbers [98]. These factors combined means that the lowest lying oscillating state we extract from our correlator fitting may differ from the physical a_0 by hundreds of MeV. For this reason, we assign a large uncertainty to the priors $P[E_0^{\pi,o}]$ equal to $\pm(0.5 \times \Lambda_{\text{QCD}})$.

For the kaon in our $H_s \to K$ fitting, we see similar roadblocks to pinning down the lowest lying oscillating state. Our candidate oscillating state particle with quantum numbers $I(J^p) = \frac{1}{2}(0^+)$ is the $K_0^*(700)$. This state however is both very broad, and also strongly coupled to multi-particle states of matching quantum numbers [99], πK scattering in particular [100]. For these reasons and the taste splitting effects mentioned previously, we can expect that the $\frac{1}{2}(0^+)$ state our fitter will identify has an energy splitting closer to $\Lambda_{\text{QCD}} = 500$ MeV rather than 200 MeV. For this reason, we set the central values of $P[E_0^{K,o}] = P[E_0^{K,n}] + \Lambda_{\text{QCD}}$. We then likewise assign those priors an uncertainty equal to $\pm(0.5 \times \Lambda_{\text{QCD}})$.

Thankfully, determining the priors for the masses of the lowest lying oscillating H and H_s states is more simple. From Heavy Quark Effective Theory (HQET) we expect the splitting to not be significantly dependent on the heavy quark mass, and instead expect a consistent splitting of $\mathcal{O}(\Lambda_{\text{QCD}})$ [101, 102]. Considering the discretization effects inherent to our HISQ ensembles, and $1/m_b$ corrections more specifically [103], we expect to see a mass splitting closer to 400 MeV, or

$0.8 \times \Lambda_{\text{QCD}}$[104]. Across all ensembles and heavy quark masses we therefore give the priors central values equal to the ground state central value plus $0.8 \times \Lambda_{\text{QCD}}$. Meanwhile, because of this more defined mass splitting, we can select a small fractional uncertainty of 0.2 for these priors. This fractional uncertainty approaches Λ_{QCD} at the heavier end of our heavy quark options.

Finally, for all these oscillating meson states, in test fitting we check that the standard deviations of the fit posteriors are not overly constrained by the standard deviations of their matching priors. That is to say, we once again check that the $10:1$ prior to posterior uncertainty principle is not violated. Across all ensembles and in both $H \to \pi$ and $H_s \to K$ we find this to be the case.

4.4.3 Non-zero-momentum meson energies: the dispersion relation

Having established our methodology for assigning priors to zero-momentum meson energies, we can now move on to discuss how to assign priors for non-zero-momentum meson energies. Across all ensembles, the heavy mother meson is placed in the rest frame of the lattice, and so we need only consider the light daughter mesons (pions and kaons) in this regard.

As discussed in section 3.3.5, we impart momentum to the light mesons via twisted boundary conditions. We can describe a meson's three-momentum $\vec{p}$ in terms of a twist angle θ, where

$$\theta = |a\vec{p}| \times \frac{N_x}{\sqrt{3}\pi}, \tag{4.10}$$

and N_x is the spatial length of the lattice in lattice units. Equation 4.9 provides a template for how we *could* determine the priors for these light meson energies. In fact the equation is valid for any meson effective energy $aE_{\text{eff}}(t)$ of any momentum in our case, so in this context we can rewrite 4.9 as

$$aE_{\text{eff}}(t) = \frac{1}{2}\cosh^{-1}\left(\frac{C_2(t-2)+C_2(t+2)}{2C_2(t)}\right). \tag{4.11}$$

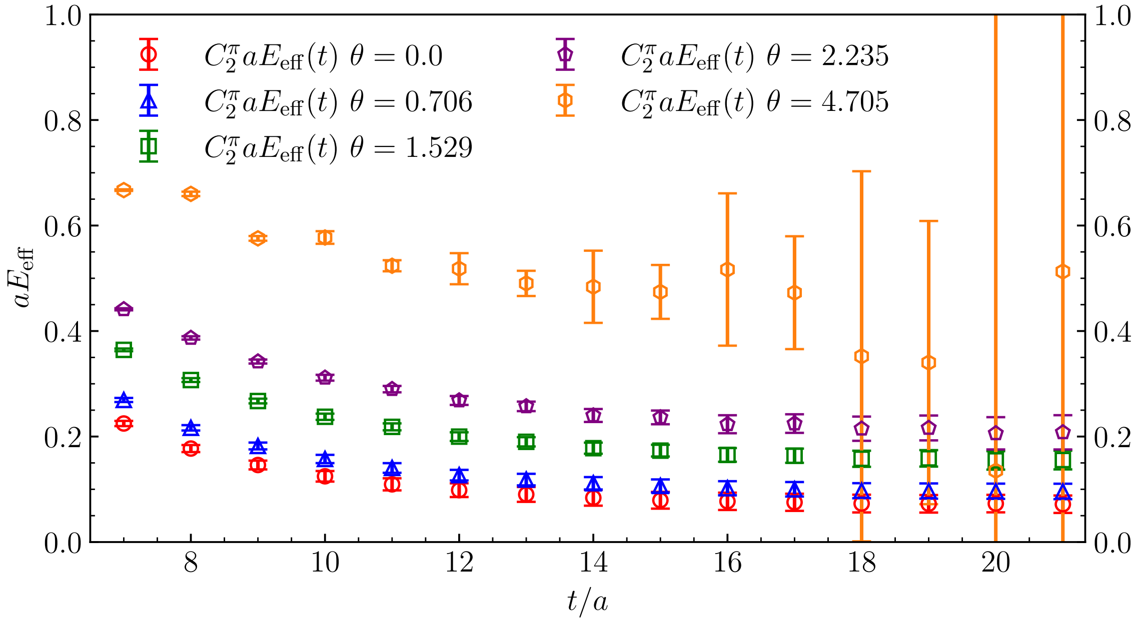

Figure 4.11: The full range of pion effective energies of varying twists on the uf5 ensemble. Light meson correlators C_2^π of twist θ are used in equation 4.11 to calculate effective energies $aE_{\rm eff}(t)$. The meson's twist is related to its lattice momentum via equation 4.10.

Following from equation 4.11 we can plot meson effective energies as we did effective masses. Figure 4.11 shows the range of pion effective energies of varying twists on the uf5 ensemble.

In assigning priors for non-zero-twist meson energies however, we can employ some *a priori* physics knowledge to move beyond simply observing effective energy plots. We can instead employ an energy dispersion relation which we expect the non-zero-twist mesons to follow, which at the continuum limit and in natural units is $E = \sqrt{M^2 + p^2}$. On the lattice, we modify the traditional, continuum limit dispersion relation with a term that accounts for discretization effects. With the HISQ action [12], the lowest order discretization effects we expect in this dispersion relation are of the order $(a\vec{p})^2$. Using the dispersion relation we can assign the priors of non-zero-twist meson energies $P[aE^M_{\vec{p}}]$[4] as

$$P[aE^M_{\vec{p}}] = \sqrt{P[aE^M_{\vec{0}}]^2 + (a\vec{p})^2} \times \left[1 + P[\varepsilon^M]\left(\frac{a\vec{p}}{\pi}\right)^2\right], \tag{4.12}$$

4. Note that we are still only discussing $i = 0$ parameters here. We therefore drop any i-indicating notation

where $P[aE^M_{\vec{0}}]$ is the prior of the meson's energy at zero-twist (its rest mass). Here we also introduce the discretization parameters ε^M, which scales the relative size of discretization effects on the dispersion relation. A given ε^M is specific to the light meson being fit (pion or kaon in our case) on a given ensemble. For two light mesons and five ensembles, we introduce ten new parameters into our correlator fitting routine, which therefore need priors as well. Following the findings from comparable HISQ-action fits [105, 16, 106, 17], the priors for ε^M were set as $P[\varepsilon^M] = 0 \pm 1$ throughout much of this project's timeline. In various test fits for this work, the posteriors for ε^π, ε^K fell within the bounds of these priors. In chapters 6 and 7 we test the dispersion relation with the current working set of correlator fits, with added discussion of the cases where we set $P[\varepsilon^M] \neq 0 \pm 1$.

In addition to the ground state pion and kaons, we can use the dispersion relation to assign priors for the non-zero-twist lowest lying oscillating pion and kaon energies as well. In fact, we can use the same equation as before, equation 4.12, with one minor change. That change is to introduce additional notation (which been otherwise ignored up until this point) to differentiate between oscillating and non-oscillating energies. This change applies to energies: $E^{M,n}_{\vec{p}}$, $E^{M,o}_{\vec{p}}$, and the discretization parameter as well: $\varepsilon^{M,n}$, $\varepsilon^{M,o}$. It is here where all the work we have done to determine the prior of $E^{\pi,o}_{\vec{0}}$ becomes useful. Even though the zero-momentum oscillating pion state does not contribute to the pion correlator, we can still us if to determine the priors of non-zero-momentum oscillating pion states, which do contribute to their correlators.

For various reasons, we can expect that the discretization parameter $\varepsilon^{M,o}$ will be weakly determined in correlator fitting. The first of these is that that the uncertainties for $P[E^{M,o}_{\vec{0}}]$ are already quite large: $\pm 0.5 \times \Lambda_{QCD}$. This means that the contribution to the high momentum $P[E^{M,o}_{\vec{p}}]$ uncertainties coming from the uncertainty of $P[E^{M,o}_{\vec{0}}]$ will still be relatively large. This is in contrast to the ground state light mesons with small $P[E^{M,n}_{\vec{0}}]$ uncertainties, where at high momentum the uncertainty assigned to $P[E^{M,n}_{\vec{p}}]$ via equation 4.12 is dominated by the uncertainty of $P[\varepsilon^{M,n}]$. The second reason we might expect a weak determination of $\varepsilon^{M,o}$ is that the oscillating contribution to the two point correlator decays quickly with time, making it more difficult for the fitter to determine a precise value for $\varepsilon^{M,o}$. For these reasons, for both $H \to \pi$ and $H_s \to K$, across all ensembles, we set all $P[\varepsilon^{M,0}] = 0.0 \pm 1.0$. We find in test fitting that fit posteriors of $P[\varepsilon^{M,o}]$ are consistent with their priors, having central values close to zero, with standard deviations less than or near order one.

It is important to note that ε's use in this fitting procedure is limited only to the construction of non-zero-twist meson energy priors. In other words, ε does not *directly* constrain a fit's posterior value for any $aE^{M}_{0,\vec{p}}$. In the two and three-point fit forms, various $aE^{\pi,K}_{0,\vec{p}}$ are fit no differently than any other fit parameter.

In the later stages of this project, we observed in test fitting consistent disagreement between the fit posteriors of non-zero-twist meson energies and their matching priors in some select cases. In an attempt to reconcile this disagreement, we revisited our use of the dispersion relation. Ignoring the discretization parameter contribution $1 \pm \varepsilon(a\vec{p}/\pi)^2$, the dispersion relation of the form $aE = \sqrt{(aM)^2 + (a\vec{p})^2}$ is a truncated version of what we would expect on the lattice. Because the light mesons are bosons, we can follow from equation 6.39 in [107] and write their full, non-truncated energy dispersion relation on the lattice as

$$aE^{M}_{\vec{p}} = \cosh^{-1}\left[1 + \frac{1}{2}aE^{M}_{\vec{0}} + 3\left(1 - \cos\left(\frac{a\vec{p}}{\sqrt{3}}\right)\right)\right]. \tag{4.13}$$

With this formulation, we can use equation 4.10 to write a better function which assigns priors to all non-zero-momentum energy priors:

$$P[aE^{M}_{\vec{p}}] = \cosh^{-1}\left[1 + \frac{1}{2}P[aE^{M}_{\vec{0}}] + 3\left(1 - \cos\left(\frac{a\vec{p}}{\sqrt{3}}\right)\right)\right] \times \left[1 + P[\varepsilon^{M}]\left(\frac{a\vec{p}}{\pi}\right)^2\right]. \tag{4.14}$$

Implementing this change to our fitting routine did not remedy the disagreeing meson energy priors we encountered in test fitting. We discuss these issues in chapters 6 and 7. In test fitting we found that meson energy priors assigned via equation 4.12 and those assigned via equation 4.14 were consistent with each other, as were the fit posteriors in either case. Our final decision in this matter was to use the non-truncated dispersion relation (equation 4.14) as part of our finalized fitting methodology.

4.4.4 Excited state meson energies

Up until this point, the meson energies we have discussed has remained limited to those whose exponential order $i = 0$ in equation 4.1. Having done so, we are now positioned to discuss all meson energy states, oscillating or otherwise, which have an exponential order $i > 0$, up to $i = N_{\text{exp}} - 1$, where N_{exp} is maximum number of exponentials for which we model in our correlator fitting routine.

From equation we 2.41 can see there are in theory an infinite number of higher order states which can contribute to a correlation function. Fortunately, these higher order states are constructed such that they are well behaved: their amplitudes and energies are such that their contributions to the correlation function decay much more quickly along the temporal length of the lattice. The effective mass plots in figure 4.10 show this behavior: the higher order states decay and the data is dominated by the $i = 0$ ground state after some time t/a. This well behaved ordering allows us to constrain the number of exponentials we fit to a manageable number. We do this by determining a point along the temporal length of the lattice t_{min}, such that any correlator data $C_2^M(t < t_{\text{min}})$ is ignored by the fitter. With an appropriate value for t_{min}, we can estimate that the signal of all higher order states $i \geq N_{\text{exp}}$ is negligible for any $t > t_{\text{min}}$. These states can be either ignored, or be thought of as "folded into" the signal of the $i = N_{\text{exp}} - 1$ state. Implementing a data cut off up to t_{min} is what allows us to fit to only some small number of exponentials N_{exp} in equations 4.1. We discuss our method of selecting appropriate values of N_{exp} and t_{min} later in section 4.7.1.

Let us first consider the energy of the $i=1$ states for the pion and the kaon. Following the similar rationale of determining the energy difference between the ground state and lowest lying oscillating state of these mesons, we can utilize the expected energy splittings between the non-oscillating $i=0$ and $i=1$ states, which we can write as ΔE_1^M. In the physical continuum, the particles which are comparable to the $i=1$ states on the lattice are those with a greater energy but the same quantum numbers as their ground state counterparts ($J^p=0^-$ for the ground state psuedoscalar pion and kaon). From the PDG, the first radial excitation of the ground state pion we might associate with the lattice $E^\pi_{i=1}$ state is the $\pi(1300)$. Similarly, the candidate particle for $E^K_{i=1}$ on the lattice would be the $K(1460)$. Following these values we might expect an energy difference between the $i=0$ and $i=1$ states to be $\Delta E_1^\pi \approx 1160$ MeV and $\Delta E_1^K \approx 965$ MeV. The experimental decay widths of these radially excited states are broad relative to their ground state counterparts, and again, are not necessarily the $i=1$ states that appear in our pion and kaon correlation functions. The effects of chiral symmetry breaking in relation to our physical and nonphysical light quarks on the lattice can also affect an expected mass splitting. Conservatively, we can say that we might expect the mass splitting between the $i=1$ and $i=0$ states for both the pion and kaon to be of the order of $2\times\Lambda_{\text{QCD}}$. We thereforeassign the central values for $P[E^{\pi(K)}_{i=1}]$ equal to the central value of $P[E^{\pi(K)}_{i=0}]+(2\times\Lambda_{\text{QCD}})$. We then assign an appropriately broad prior uncertainty of $\pm 0.5\times\Lambda_{\text{QCD}}$. For $i=1$ light meson energies with non-zero-momentum, we can once again utilize the dispersion relation discussed in the previous section. In test fitting we find that these priors do not overly constrain the posterior fit results for the $i=1$ light meson energies, which often have standard deviations of order ten times smaller than their matching priors.

Unlike the light mesons, the heavy mesons H, H_s don't have as clear of an expected energy splitting between the $i=0$ and $i=1$ states. We have some theoretical continuum expectations at both the charm and bottom ends of the heavy quark spectrum: $\Delta E_1^D \approx 710$ MeV, $\Delta E_1^{D_s} \approx 720$ MeV, $\Delta E_1^B \approx 610$ MeV, and $\Delta E_1^{B_s} \approx 610$ MeV [108]. Of these four, only the D meson has strong enough experimental evidence for a well defined first radial excitation, $D_0(2550)^0$. This suggests a value for $\Delta E_1^D \approx 680$ MeV. Regardless, these values are given in the continuum for physical heavy meson, and are not necessarily the exact energy splittings we might expect in our heavy meson correlation functions. Given this lack of clarity we resort to using the natural energy scale of QCD,

$\Lambda_{\text{QCD}} = 500$ MeV as the expected mass splitting. Like with the light mesons, we define $P[E^{H}_{i=1}]$, $P[E^{H_s}_{i=1}]$ relative to their $i=0$ counterparts, such that the central value of $P[E^{H_{(s)}}_{i=1}]$ is equal to the central value of $P[E^{H_{(s)}}_{i=0}] + \Lambda_{\text{QCD}}$. We likewise assign a broad prior uncertainty of $\pm 0.5 \times \Lambda_{\text{QCD}}$. In test fitting we find this prior assignment does not overly constrain our fit results, which often have standard deviations of order ten times smaller than their matching priors.

For all other higher order energy states, which included non-oscillating $i > 1$ and oscillating $i > 0$ states, we default to using the natural energy scale of Λ_{QCD} to assign priors for energy splittings. This, in conjunction with prior uncertainties of $\pm 0.5 \times \Lambda_{\text{QCD}}$ leads to priors with large uncertainties that cover the whole upper range of possible exited state energies.

4.4.5 Ground state meson amplitudes

Having discussed meson energies and their priors at length, we can now move on to discuss the other parameters that appear in our two-point correlator fit function: the amplitudes $A^{M,n}_i$, $A^{M,o}_i$. To determine the priors we assign to meson masses (which equals their energy in the case of zero momentum) we use a custom function to find where the change in a correlation function's effective mass was minimized. We can utilize an analogous function for a zero-momentum meson correlator whose effective amplitude $A_{\text{eff}}(t)$ can be written as

$$A_{\text{eff}}(t) = \sqrt{\frac{C_2(t)}{e^{-M_{\text{eff}}t} + e^{-M_{\text{eff}}(N_t - t)}}}. \tag{4.15}$$

Here N_t is the temporal length of the lattice in lattice units, and M_{eff} is the effective mass at lattice time slice t. We have dropped the implied notation that the masses, amplitudes, and correlators have matching meson superscripts M, and that the effective masses are also functions of time. Figure 4.12 shows a similar picture to what we see in effective energy plots, the signal from the higher order states die out after a certain t/a, and a stable ground state plateau is resolvable. The second (bottom) plot in figure 4.12 also demonstrates well how the uncertainty of correlator data grows larger towards the midpoint of the lattice.

Like before, we assign central values to the priors $P[A^M_{i=0}]$ equal to the value of $A^M_{\text{eff}}(t)$ where the change in its rolling average is minimized. Similarly we then assign fractional uncertainties to these priors appropriate to the relative size of the standard deviations of the plateau-region data in the effective amplitude plots. Tables 6.3 and 7.1 give the fractional uncertainties we assign priors to the ground state, zero-momentum meson amplitudes across all ensembles for either decay channel.

With four different heavy quark options for each heavy meson, we opt to not assign separate priors for each option. We noticed upon examination of their effective amplitude plots that the relative uncertainty of $A^M_{\text{eff}}(t)$ grew as the mass of heavy quark in the meson grew. We instead determine a fractional uncertainty from the effective amplitude plot of the lightest heavy meson, and scale that uncertainty up according to the ratio of the given heavy quark mass to the lightest mass option. This amplitude scaling is defined via equation 4.16:

$$\Delta(A_{m_j}) = \Delta(A_{m_0}) \left[\frac{(R-1)(\frac{m_j}{m_0}-1)}{(\frac{m_3}{m_0}-1)} + 1 \right]. \tag{4.16}$$

Here m_j for index $j \in \{0,1,2,3\}$ corresponds to the lightest to heaviest heavy quark mass on any ensemble, where m_0 is the lightest and m_3 is the heaviest. $\Delta(A_{m_j})$ is the fractional uncertainty assigned to the prior for the amplitude of the heavy meson which contains the heavy quark of mass m_j. The desired ensemble specific ratio R is selected to be equal to the desired ratio of $\Delta(A_{m_3})/\Delta(A_{m_0})$. For example, if $\Delta(A_{m_0})$ is determined to be 0.10 and the desired value of $\Delta(A_{m_3})$ is to be $4 \times \Delta(A_{m_0}) = 0.40$, then we set $R = 4$. The fractional uncertainties of $\Delta(A_{m_1})$ and $\Delta(A_{m_2})$ meanwhile will land somewhere between 0.10 and 0.40, scaled in relation to the ratio of their heavy quark mass $m_{1,2}$ to m_0. In test fitting we find that this method of prior uncertainty assignment produces broad, conservative priors which avoid violating the 10:1 prior to posterior uncertainty ratio benchmark.

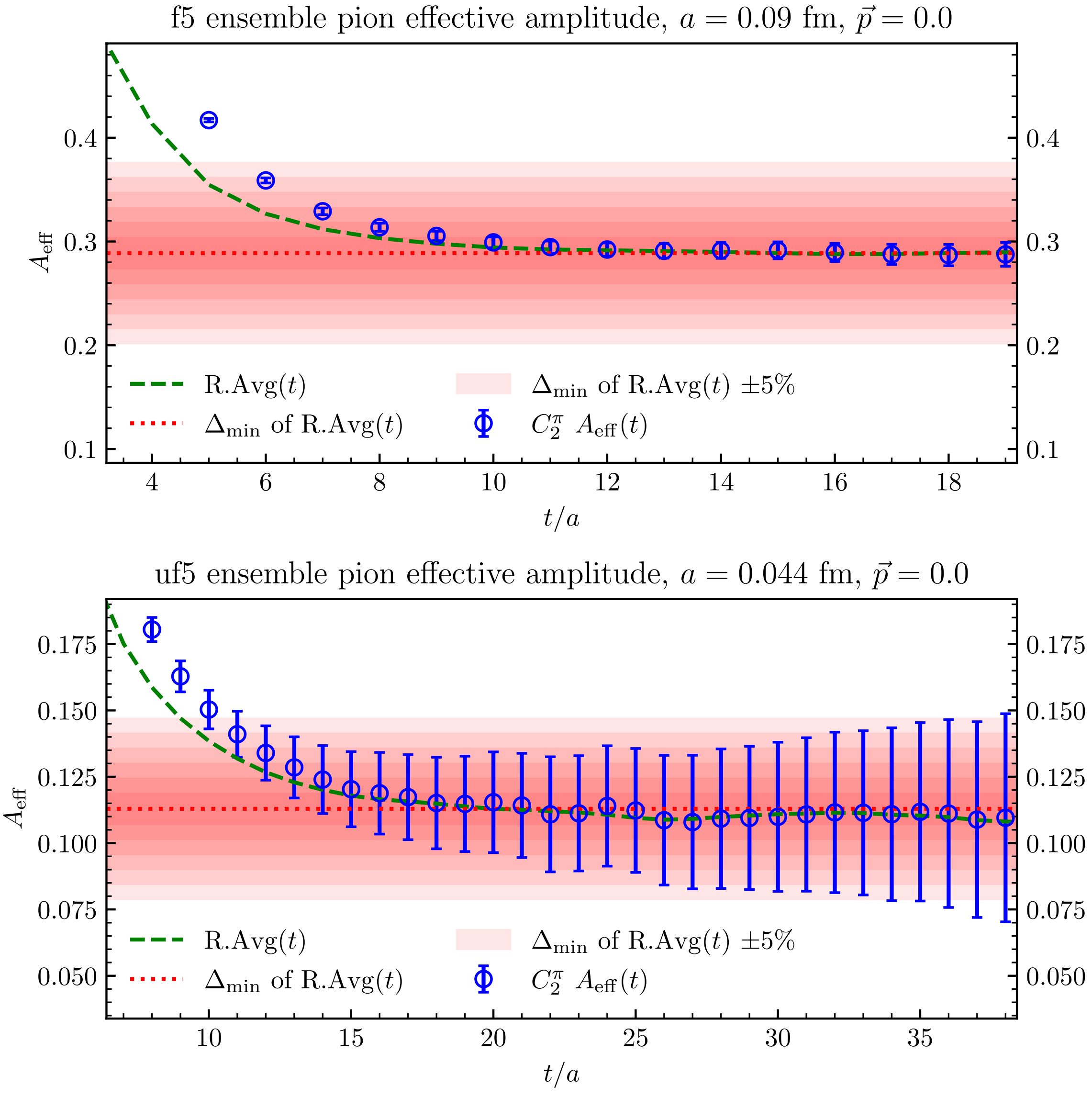

Figure 4.12: Sample pion effective amplitude plots on the f5 and uf5 ensembles. The effective amplitude $aM\mathrm{eff}(t)$, which is calculated from equation 4.15 and its respective two point correlation function C_2^{π}, is shown in blue. The rolling average of the effective mass R.Avg(t) is shown in dashed green. Where the change in this rolling average is minimized Δ_{min} of R.Avg(t) is shown in dotted red. Consecutive red bands show regions of $\pm 5\%$, out to $\pm 30\%$, of Δ_{min} of R.Avg(t).

4.4.6 Non-ground state and non-zero-twist meson amplitudes

Having discussed assigning priors to the amplitudes of zero-momentum, non-oscillating, exponential order $i = 0$ mesons, we can now go on to discuss how we assign priors to the rest of the amplitudes which appear in our two-point correlator fit function (equation 4.1). Let us begin with examining the amplitudes of non-oscillating $i = 0$ mesons with non-zero-momentum $P[A^M_{\vec{p}}]$. We can likewise employ a relativistic dispersion relation to assign these priors:

$$P[A^M_{\vec{p}}] = P[A^M_{\vec{0}}] \times \sqrt{\frac{P[E^M_{\vec{0}}]}{P[E^M_{\vec{p}}]}} \times \left[1 + P[\delta^M] \left(\frac{a\vec{p}}{\pi}\right)^2\right]. \tag{4.17}$$

Here we introduce another discretization parameter δ^M which performs the same function as ε^M in equation 4.12. We note that in this construction, $P[A^M_{\vec{p}}]$ becomes correlated with $P[E^M_{\vec{p}}]$. Across all ensembles and both decay channels we set $P[\delta^\pi]$, $P[\delta^K] = 0.0 \pm 1.0$. In test fitting we find that the fit posteriors for $A^M_{\vec{p}}$ and ε^M are consistent with their matching priors.

The remaining amplitude terms to account for are those with oscillating and or $i > 0$ components, which we can collectively refer to as A^*. To determine the priors for these amplitudes, we could in principle use equations of a form similar to equation 4.17. We find however that the corresponding non-ground state zero-twist energy and amplitude priors that would go into those equations already have large uncertainties. As a result, any uncertainty scaling which would come from a discretization parameter is insignificant. We therefore resort to a $\log(\mathrm{GBF})$ testing regime to set the priors for A^*. As a starting point, we set the central value of these priors equal to that of their non-oscillating $i = 0$ counterpart, with an initial fractional uncertainty of $\Delta(A^*) = 1.0$. We introduce this notation $\Delta(A^*)$ to indicate that we use one parameter to set the fractional uncertainty of all these amplitudes. We find that in $\log(\mathrm{GBF})$ testing, fractional uncertainties larger that 1.0 are preferred across all ensembles and both decay channels. The practical meaning of this finding aligns well with our expectations: we have little a priori knowledge on what values these amplitudes should be in our fit routine. Therefore having priors for these amplitudes with large fractional uncertainties permits the correlator data itself to maximally inform the fitter. The exact values of $\Delta(A^*)$ used in our final fit are given in tables 6.3 and 7.1.

4.5 Three-point correlation function priors

In the following subsections, we describe how we determine a full set of priors for the current insertion amplitudes $J \in \{S, V, T\}$, which include ground states, oscillating states, and higher order exponential states. These amplitudes we can colloquially refer to as the set of *three-point amplitudes*, the priors for which we can refer to as *three-point priors*. Again, these are slightly misleading labels; meson energies and amplitudes also appear in equation 4.18. The current insertion amplitudes J exclusively appear in the three-point function, and so "three-point" is not an unreasonable choice of shorthand. For a given three-point correlation function, its fit function is proportional to the summed permutations of the amplitude terms J_{ij}^{kl}, where $i, j \in [0, N_{\text{exp}})$, and $k, l \in \{n, o\}$. Here n denotes a non-oscillating state (rather than some order of exponential) and o denotes an oscillating state. Equation 4.18 gives the full fit equation for $H \to \pi$. A three point correlator for $H_s \to K$ is fit similarly.

$$
\begin{aligned}
C_3^{\pi,H}(t,T) = \sum_{i,j=0}^{N_{\text{exp}}-1} \Big[& A_i^{\pi,n} J_{ij}^{nn} A_j^{H,n} e^{-E_i^{\pi,n} t} e^{-E_j^{H,n}(T-t)} - (-1)^{(T-t)} A_i^{\pi,n} J_{ij}^{no} A_j^{H,o} e^{-E_i^{\pi,n} t} e^{-E_j^{H,o}(T-t)} \\
& - (-1)^t A_i^{\pi,o} J_{ij}^{on} A_j^{H,n} e^{-E_i^{\pi,o} t} e^{-E_j^{H,n}(T-t)} + (-1)^T A_i^{\pi,o} J_{ij}^{oo} A_j^{H,o} e^{-E_i^{\pi,o} t} e^{-E_j^{H,o}(T-t)} \Big]. \quad (4.18)
\end{aligned}
$$

The ground state three-point amplitudes J_{nn}^{00} in the equation above are the most important three-point amplitudes, as it is theses parameter that we use in form factor calculations. In our fitting approach however, the J_{nn}^{00} term receives no special treatment; parameters are fit simultaneously. It is for this reason we ensure that the priors for non-ground state three-point amplitudes are appropriately determined; they can have an effect on the fit posterior of the J_{00}^{nn} term. This follows the same rationale of wanting reasonable two-point priors, as discussed in the previous sections.

4.5.1 Determining ground state three-point amplitude priors

In a similar fashion to the determination of ground state two-point amplitudes, we can use effective three-point amplitude plots to determine widths and central values for their respective priors. To be more specific, effective three-point amplitude plots allow us to estimate the prior for the J_{00}^{nn} term in the equation 4.18. For a given three-point correlator, we can construct its effective amplitude from the following equation:

$$J_{\text{eff}}(t,T) = C_3(t,T)\frac{\exp\left[M_{\text{eff}}^{\pi(K)}t + M_{\text{eff}}^{B_{(s)}}(T-t)\right]}{A_{\text{eff}}^{\pi(K)} \times A_{\text{eff}}^{B_{(s)}}}. \tag{4.19}$$

For three-point amplitudes, we cannot use the same methods of prior determination that we used for determining two-point amplitudes, for reasons we will explain. There is also no expected dispersion relation we expect three-point amplitudes to follow. In fact, the q^2 dependence of these three-point amplitudes is a behavior we wish the data to have maximum influence in, rather than by any strict prior enforcement. Furthermore, as seen in equation 4.18, the value of a three-point correlation function for a given t,T has contributions from combinations of various oscillating and non-oscillating amplitudes, even in the case where $i,j=0$. Additionally, These oscillating amplitude components can have either positive or negative sign. The implication then is that even in cases where an effective three-point amplitude appears to achieve a steady plateau in some t range, it cannot be assumed that the J_{00}^{nn} amplitude is the only contributing state to that steady plateau. While in correlator fit testing it was often the case that the fit posterior for a given J_{00}^{nn} was consistent with some $J_{\text{eff}}(t,T)$ plateau, it was not universally true. For these reasons we cannot justify as narrow prior widths for well resolved ground state three-point amplitudes as for similarly well resolved two-point amplitudes.

With no dispersion relation on which to base non-zero-twist three-point amplitude priors, and a desire to not unduly influence the q^2 dependence of their corresponding fit posteriors, for much of this project we adopted a near-maximally conservative prior determination methodology. For a given current component $J \in \{S,V,T\}$, on a given ensemble, we opted to use a single prior central value and uncertainty for all heavy-quark mass and twist combinations. This central value and uncertainty was determined by visually looking at effective amplitude plots which included the effective amplitudes of all mass and twist combinations for a given current component. Such a plot might include twenty effective three-point amplitudes, from which a visual grouping of plateau behavior might be resolved with varying degrees of clarity. A central value would be determined from some apparent mean of these plateauing effective amplitudes, and the uncertainty would be determined such that both the upper and lower bounds of the plateau grouping were encompassed by the resultant prior bounds.

This prior determination methodology was utilized through most this research project and in many acceptable correlator fits. This methodology however is somewhat flawed when we consider a number of factors. First, this method of prior determination does not include *any* consideration of q^2 dependency for three-point amplitudes. While this choice is preferable to over-constraining any q^2 dependency, better fit results might be achieved by having *some* q^2 dependency built into our priors. Second, this method somewhat misconstrues the function of a prior's uncertainty as encoded in a `gvar`. By choosing to encode a prior's central value and uncertainty in a `gvar`, we encode that this central value is the mean of some normal distribution whose standard deviation is equal to the prior's uncertainty. This is no revelation, but it means that the interpretation of any value within a prior's uncertainty range being equally preferable and any value outside of it being discouraged is not coherent with the gaussian structure of the prior as encoded by a `gvar`.

This issue becomes more problematic when we saw how the average uncertainty and noise of high twist (low q^2) effective amplitudes were greater than those of low twist (high q^2) effective amplitudes. We also identified the general trend that effective amplitudes plateaus tend to decrease in value as twist increases. These effects combined mean that for a given current component and heavy-quark mass, effective amplitude plateaus are larger and more stable at low twists, but are smaller and less stable at high twists. Applying a gaussian prior, whose central value is a rough mean of this whole range of amplitudes, can create an undesirable fit outcome. In effect, the gaussian prior structure favors fit posteriors closer to the given mean or central value. The stable plateau of a zero or low-twist effective amplitude might be so well resolved that this pull towards the prior's central value has little effect in the fitter's calculation of that amplitude's fit posterior. Conversely, at the other end of the prior uncertainty bounds, the noisy and often unstable plateaus of the corresponding high twist amplitudes will be more influenced by this pull towards the mean. In other words, the more indeterminable a fit parameter is from the data alone, the more influence the matching parameter's prior has on the final fit posterior. This phenomena is intended by the constructed of our augmented χ^2 procedure. Considering these phenomena, we determined it was preferable to have different priors for the three-point amplitudes of different twist but matching current components. We do not differentiate priors by heavy quark mass here because, for a given current component, the effective amplitudes plots vary in plateau position and uncertainty much more as twist is varied rather than as heavy-quark mass is varied. This is shows explicitly in figure 4.13.

With the desire to have twist-specific priors for three-point amplitudes, we still do not want to venture into the territory of unfairly constraining the expected q^2 dependency. Therefore while we determine central values by visually identifying where an effective three-point amplitude plateaus, we assign a prior uncertainty equal to the associated central value as a minimum. In other words, all ground state three-point amplitude priors have a fractional uncertainty greater or equal to one. This method is consistent with not overly constraining the expected q^2 dependent behavior, and avoids the "pull towards the mean" problem of unstable high twist amplitudes given the same prior as stable low twist amplitudes. In some cases, an effective amplitude plot was so noisy or unstable that a fractional uncertainty of one could still be too constraining. Such cases are clearly indicated in tables 6.4 and 7.2.

4.5.2 Determining non-ground state three-point amplitude priors

Unfortunately, determining the magnitudes of non-ground state three-point amplitudes cannot be simply achieved by observing effective amplitude plots. Furthermore, for every one J_{00}^{nn} state, there are many more oscillating and higher order exponential states J_{ij}^{kl} where $\{i,j\} \neq \{0,0\}$ and or $k,l \neq n$. In fact, if $N_{\mathrm{exp}} = 4$, for every one J_{00}^{nn} state in a fit, there are up to 63 other states

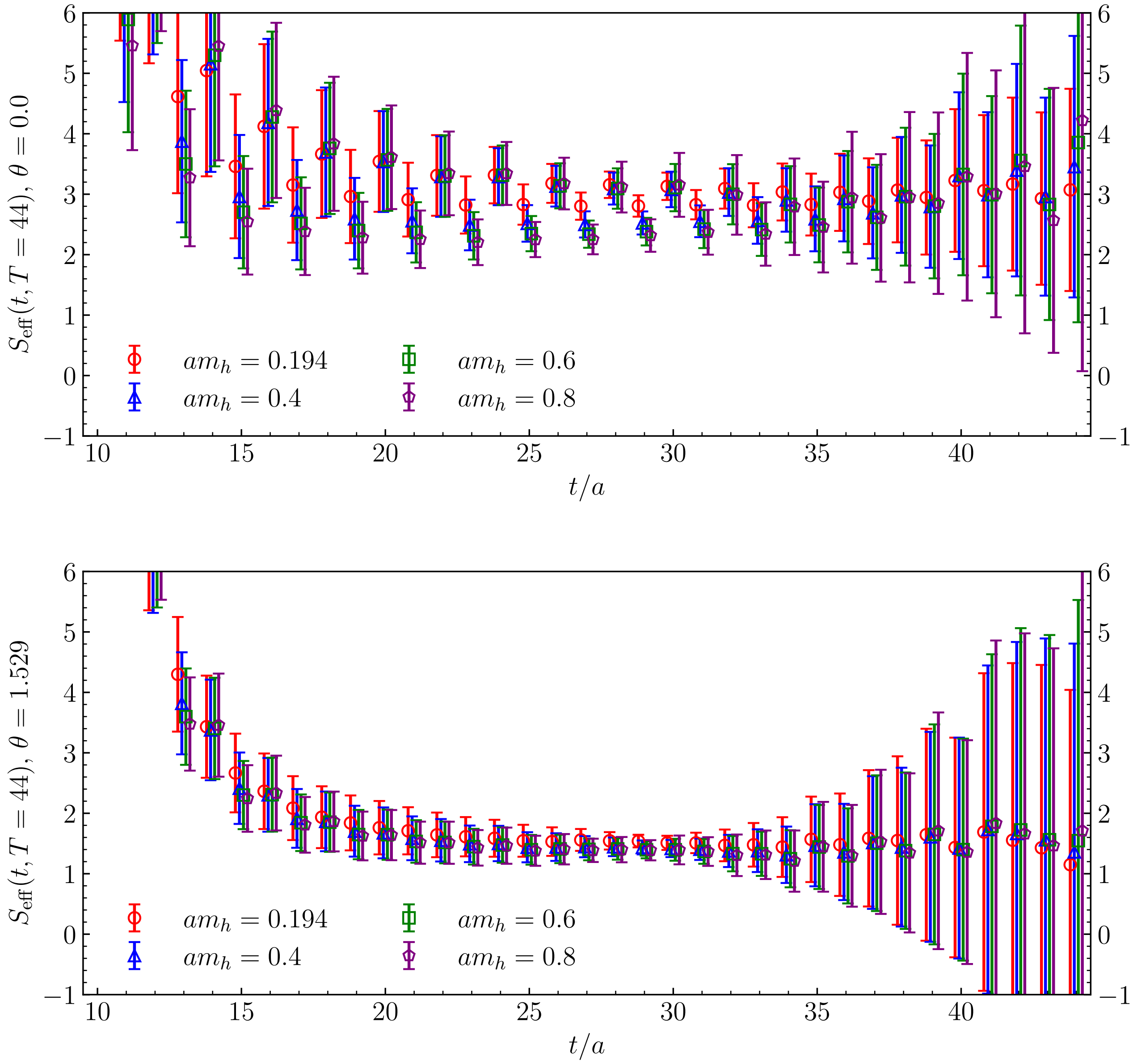

Figure 4.13: Sample effective amplitude plots of $H \to \pi$ scalar current insertion $S_{\rm eff}(t,T)$. The top plot shows data for which the light meson twist angle $\theta = 0.0$, and the bottom plot shows data for which $\theta = 1.529$. Both plots correspond to a source-sink separation $T = 44$ in lattice units, and four different heavy quark masses am_h. Some data is offset along t/a axis for visual clarity.

which contain oscillating and or higher order exponential components. This gives us 64 total fit parameters for every combination of current insertion, heavy quark mass, and daughter meson momentum each. Determining what the priors for these 63 non-ground state amplitudes ought to be then poses an obvious challenge. There is no algorithm or effective amplitude plot-based determination we can use; we have no *a priori* physics knowledge, other than knowing they can be positive or negative. Thankfully, that sign indifference allows us to simply assign a value of zero to the central value of all these non-ground state amplitude priors.

This still leaves us with the challenge of determining and assigning prior uncertainties for thousands of fit parameters. Following from the similar work of [17], we can first try grouping non-ground state priors into two categories. Per ensemble, for a given current component J, we can assign a single prior to all states which contain any higher order exponentials $J^{kl}_{ij\neq 00}$. What remains then are the lowest lying oscillating state amplitudes $J^{kl\neq nn}_{00}$, to which we can then assign a separate prior. We can refer to these two groupings as $J_{\neq 0}$ and J_{osc} as shorthand, the priors for which we can label $P[J_{\neq 0}]$ and $P[J_{\text{osc}}]$ respectively. With no prior physics knowledge to set the uncertainties of $P[J_{\neq 0}]$ and $P[J_{\text{osc}}]$, we used the highest uncertainty of a matching $P[J^{nn}_{00}]$ as an initial guess. We then utilized the same $\log(\text{GBF})$ optimization method discussed in section 4.3 to refine these guesses into final working values, which are listed in tables 6.5 and 7.3.

In test fitting, even after GBF optimizing the priors for oscillating and higher order three-point amplitudes, we found two consistent outlier cases where fit posteriors still differed from their respective priors by two or more standard deviations. These outlier cases occurred irrespective of mass, twist, or current component. The first of these cases were the J^{on}_{00} amplitudes. The second of these cases were the amplitudes J^{kl}_{10} for all $k,l \in \{n,o\}$. This suggested that our initial non-ground state prior grouping method could be improved. We therefore introduced an ensemble specific, but otherwise global, multiplicative factor σ_{ens} which effectively multiplies or *widens* the uncertainty of these special cases. We then underwent the same GBF optimization for this special prior widener for each ensemble, yielding values that varied approximately in the range of two to five across all ensembles. The exact values can also be found in tables 6.5 and 7.3. This entire process is somewhat "in the weeds" for standard correlator fitting prior selection, and while implementing these σ_{ens}

terms does not appear to have any measurable impact on the ground state amplitudes, their inclusion still improves the fit in two ways. First, their inclusion does make our correlator fitting routine slightly more conservative, that is to say, the affected priors are wider and less constraining to the fit. Second, fits which include these terms do meet the $\Delta\log(\text{GBF}) > 3$ threshold where we can state that the change is positive and significant.

4.6 Spurious states

To conclude this exhaustive discussion on setting priors, we ought to discuss the rare case in which the fitter incorrectly evaluates the data and identifies a *spurious state*. The *corrfitter* package documentation [82] goes more into depth on spurious states than we will here. For our purposes however, a spurious state is a nonphysical state identified by the fitter with some near-zero amplitude and incorrect energy splittings between it and its neighboring energy levels. Most importantly for our form factor calculation, a spurious state can significantly affect the ground state energy E_0 determined by the fitter. Thankfully, spurious states are artifacts of the fitting module, and are not a product of the data, and so identifying and removing them in our correlator fits is important and necessary.

In our correlator fitting we spotted that a spurious state appeared for the zero-twist pion energy (mass) while fitting the fphys ensemble. There, the energy splitting between the $i = 1$ and $i = 0$ states was orders of magnitude smaller than what would be expected by our physics informed prior would suggest. Curiously enough, this spurious state only appeared when we fit two and three-point correlator data simultaneously, as opposed to only fitting two-point correlators where no such spurious state appeared in the fit. Figure 4.14 gives a visualization of the discrepancy in expected versus resultant energy level splittings. In this example, the global fit gives an energy

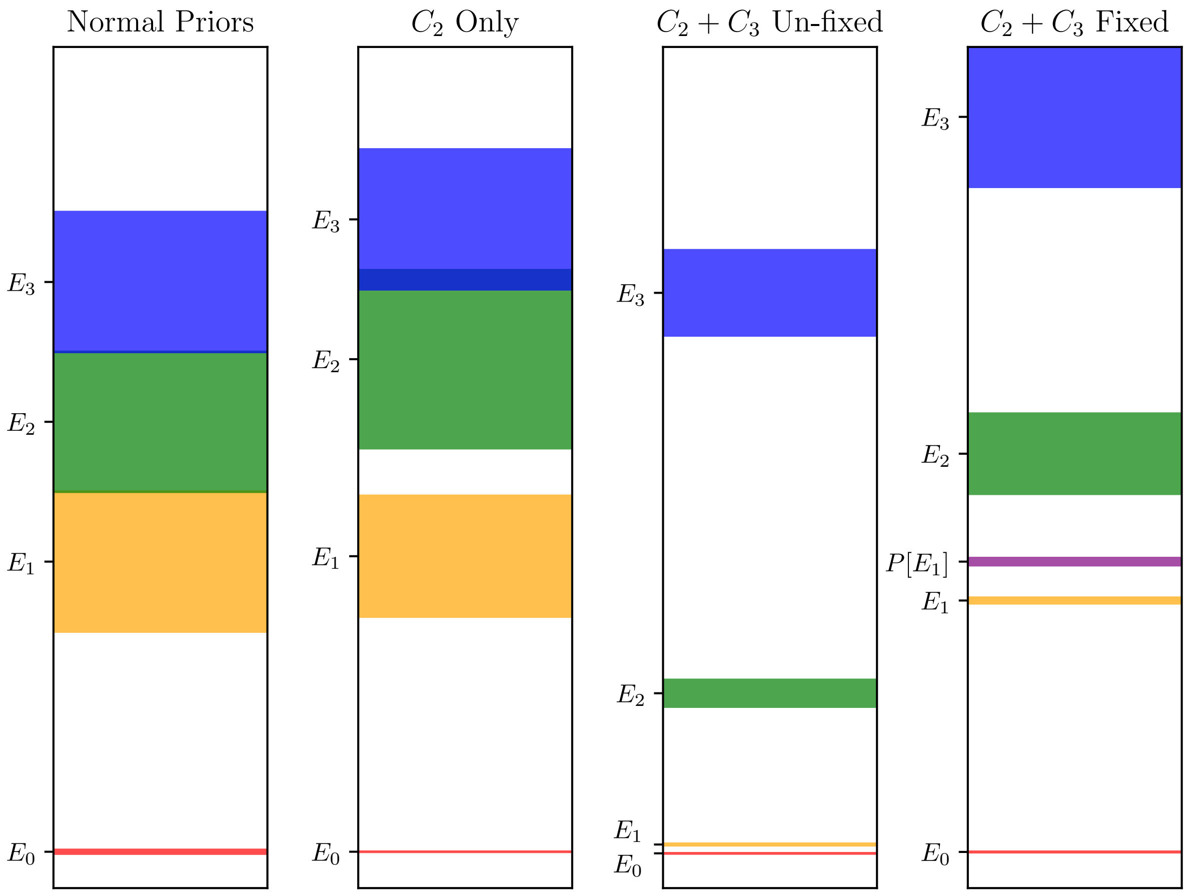

Figure 4.14: Test fit pion relative energy splitting plots. Results are shown for the $H \to \pi$ decay on the fphys ensemble for a pion of twist angle $\theta = 0.0$ (at rest in lattice frame). For each exponential energy state E_i, its shaded region covers $E_i \pm \sigma_{E_i}$, where relative energy increases upwards along the y-axis. The energies E_0, E_1, E_2, E_3 are shown in red, orange, green, and blue respectively. The Normal Priors subplot shows the $E_i \pm \sigma_{E_i}$ bounds of the zero-twist pion energy priors. The results of fitting only two-point correlators C_2 with normal priors is shown in the C_2 Only subplot. The results of fitting all two and three-point correlators with normal priors is shown in the $C_2 + C_3$ Un-fixed subplot, where it is clear the fitter has identified a spurious state as E_1. Finally, the results of fitting all two and three-point correlators with strict E_1 prior bounds (shown in purple as $P[E_1]$) are shown in the $C_2 + C_3$ fixed subplot.

splitting between E_1 and E_0 of less than 30 MeV. Furthermore, the ground state energy from the global fit differs from that of the two-point only fit by nearly 21 standard deviations, which is the only such case we have come across in our test fitting. This finding indicates that the $i = 1$ state in the global fit is a spurious state.

Among the techniques we have to remove this spurious state, the direct route we can take is to set a much more narrow prior for E_1. While we do not change the central value of $P[E_1]$, we find that assigning a fractional uncertainty of 0.05 is sufficient to effectively remove the spurious state from the fit. Though the now *fixed* global fit still produces values of E_1 which differ from the narrow prior by several standard deviations, the ground state energy E_0 is now consistent with the two-point fit and $P[E_0]$.

4.7 Testing auxiliary fit parameters

4.7.1 Testing N_{exp} and t_{min}

In addition to those discussed already, there are other parameters we can adjust to improve our fit results. The first we can discuss here are the total number of exponentials N_{exp} which we include in our fit forms (equations 4.1 and 4.2). These higher order exponential states have higher energies, and as a result decay quickly in our correlation functions. Therefore, after some minimum time t_{min}, only a few exponential states are likely contributing significantly to the correlation function. For this reason we tie together the study of N_{exp} and t_{min} in this research.

Adjusting these two auxiliary fit parameters presents trade-offs worth investigating. In considering the number of exponentials, too small of a value for N_{exp} might yield poor fit results, as there are not enough parameters (energies E_i and amplitudes A_i for example) to properly model the data. Meanwhile, increasing N_{exp} adds more parameters to the fit, whose contributions to the data might likely have decayed before a given t_{min}, or are otherwise indeterminable by the fitter. This can increase the fit computation time without improving the results. Ideally we wish to select a value of N_{exp} such that test fit results are stable, in that increasing or decreasing N_{exp} by one does not significantly affect ground state posteriors.

Meanwhile, adjusting t_{min} can have similar trade-off effects. Any correlator data of $t < t_{\text{min}}$ is not included in the correlator fit. By increasing t_{min}, we are effectively throwing out more and more data correlator data, which often can lead to larger uncertainties on fit posteriors. So while reducing t_{min} can in theory lead to smaller uncertainties, it also increases the likelihood of unwanted contributions to the data from higher order exponential states. Like testing values of N_{exp}, we wish to select values of t_{min} where adjusting by ± 1 does not significantly affect fit posteriors. Additionally, it is worth noting that we can set different values of t_{min} for different correlation functions, both two and three-point. This is also true across different ensembles and both meson decays. We tend to find however that a single value of t_{min} for all two-point correlators and another for all three-point correlators is sufficient for a given ensemble, for either meson decay.

Figures 4.15 and 4.16 show plots of various fit posteriors from different test fits, which have varying values of N_{exp} and t_{min}. From these plots we can see the general trend that, as t_{min} increases, the uncertainty of the fit posterior tends to increase. Meanwhile in figure 4.15, we can see that for a small $t_{\text{min}} = 5$, we might conclude that three exponentials are not sufficient to model the data; as that fit posterior differs significantly from those of the same $t_{\text{min}} = 5$ but larger N_{exp}. Aside from this case, These plots show that ground state fit results are mostly consistent across values of $N_{\text{exp}} \in \{3,4,5\}$. Not shown in these figures was our finding that a value of $N_{\text{exp}} = 2$ was not sufficient to model the data. We additionally find that values of $N_{\text{exp}} > 4$ do not have noticeable impacts on ground state fit posteriors. Across all fits we find that a value of $N_{\text{exp}} = 4$ is amenable to the various values of t_{min} we've selected for each ensemble, and vice versa.

4.7.2 Testing t_{max}

Like selecting an appropriate value of t_{min}, we can improve the results of two-point correlator fitting by selecting appropriate values of t_{max}. To recall, the construction of two-point correlation functions means that they are symmetrical about the midpoint of the lattice $t = N_t/2$. Our fitter takes advantage of this construction by effectively folding the two-point correlator data about its

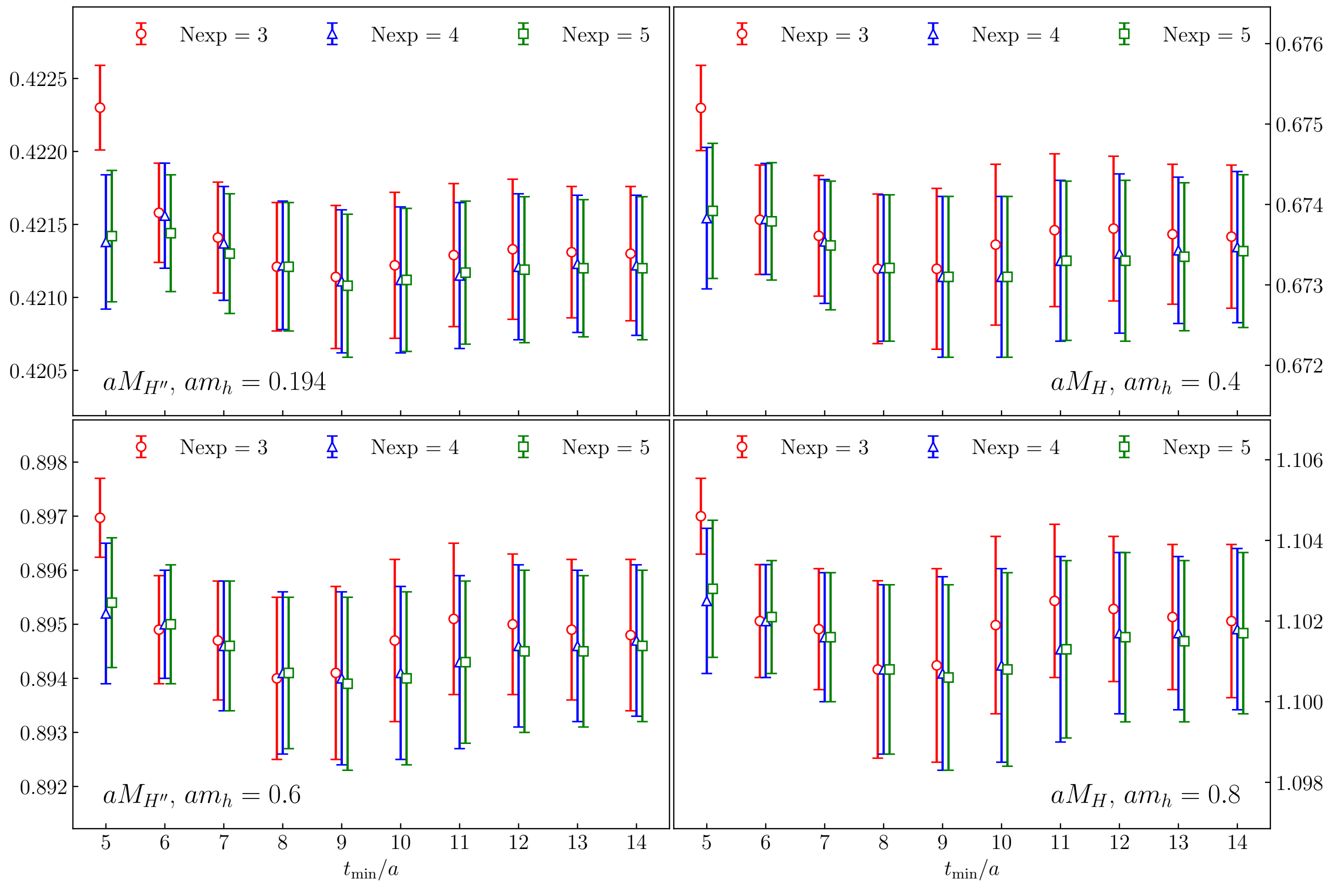

Figure 4.15: Sample N_{exp} and $t_{\min}$ testing plots. Results shown are test fit posteriors of the mass of the heavy meson $aM_{H''}$ of different heavy quark mass am_h on the uf5 ensemble. The fit posterior of each heavy meson mass is from separate test fits of varying N_{exp} and $t_{\min}$. Some data shown are slightly offset along the $t_{\min}/a$ axis for visual clarity.

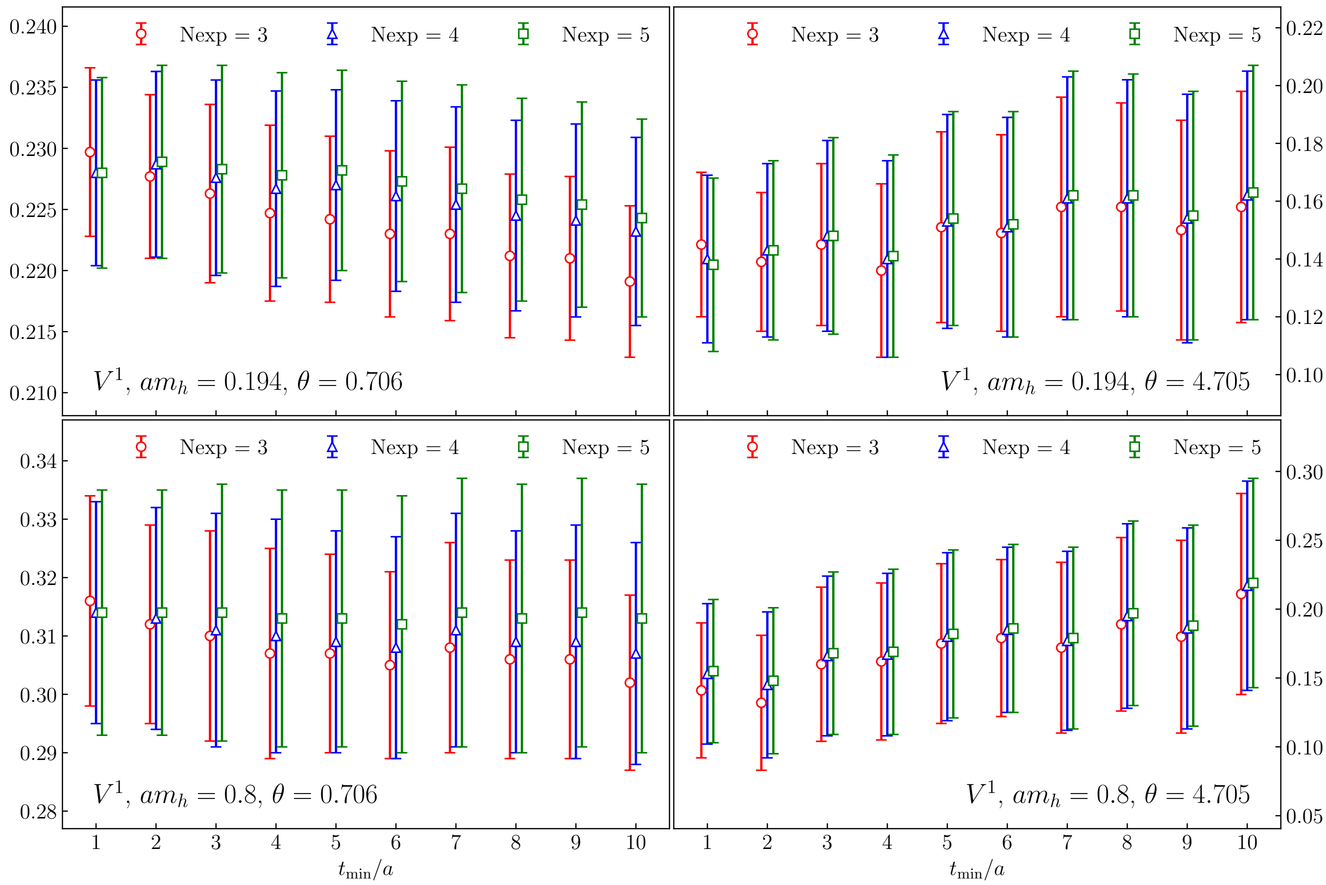

Figure 4.16: Sample N_{exp} and t_{min} testing plots. Results shown are test fit posteriors of the spatial current insertion amplitude V^1 of different heavy quark mass am_h and twist angle θ on the uf5 ensemble. The fit posterior of each current insertion amplitude is from separate test fits of varying N_{exp} and t_{min}. Some data shown are slightly offset along the t_{min}/a axis for visual clarity.

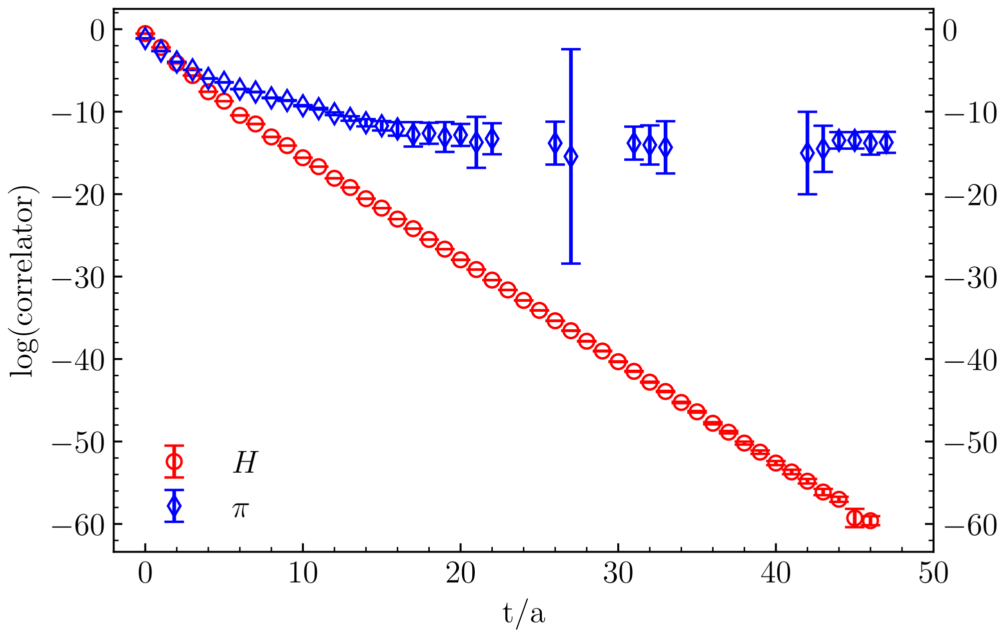

Figure 4.17: Sample H and π $\log(C_2^M)$ plot on the fphys ensemble. Data shown for $t/a \in [0, N_t/2]$ for $N_t/2 = 48$. Both the heavy meson H and light meson π have Goldstone pseudoscalar spin taste structure $\gamma_5 \otimes \xi_5$. The heavy quark in H has mass $am_h = 0.8$, and the light meson has twist $\theta = 5.311$, which is related to momentum via equation 4.10. Missing $\log(C_2^\pi)$ data correspond to values of C_2^π with negative sign.

midpoint. This does not double the statistics as both halves of the data are highly correlated, however it does slightly but meaningfully decrease uncertainties. Therefore if we establish that t_{min} and t_{max} define the domain of each two-point correlator which are evaluated by the fitter, then the maximum value of t_{max} we might set is $t_{\text{max}} = N_t/2$.

Unlike t_{min} however, t_{max} does not have the trade-off relationship with N_{exp} as described in the previous section. Instead, the purpose of setting a value of $t_{\text{max}} < N_t/2$ is to remove data from the fit that is too noisy as to be useful for the fit. This categorization mostly applies to two-point correlator values with negative sign. Because we fit two-point correlator data in log-space, negative sign correlator data cannot enter the fit. Figure 4.17 shows a $\log(C_2^M)$ plot where this phenomena is plainly apparent. This plot also shows the general trend of the uncertainty on correlator data increasing towards the temporal midpoint of the lattice. This effect is more pronounced for light meson correlators of higher twist angle.

After analyzing many $\log(C_2^M)$ plots, we find that setting $t_{\rm max} < N_t/2$ is only necessary in minority of cases. We find that for all heavy meson correlators a value of $t_{\rm max} = N_t/2$ is appropriate. For all ensembles and either meson decay, we find that only the two or three highest twist light meson correlators require values of $t_{\rm max} < N_t/2$.

4.7.3 Testing SVD cuts

Before we can finish our discussion on fitting correlator data we ought to discuss how we implement Singular Value Decomposition (SVD) cuts in our least squares fit equation. This discussion of SVD cuts mostly follows from appendix D of [109], from which we also adopt similar notation. First, let us illustrate the problem in our fit routine which the implementation of SVD cuts aims to solve. Recall that for a given fit (which is to say, for a ensemble and meson decay) we have N_s sample Monte Carlo correlation functions $\mathbf{G}^{(s)}$, where each correlation function can be represented as a vector of dimension N_G. For our least squares fit approach, we need to calculate the covariance matrix $\mathbf{M}_{\rm cov}$ given by

$$\mathbf{M}_{\rm cov} \approx \frac{1}{N_s(N_s-1)} \sum_s (\mathbf{G}^{(s)} - \overline{\mathbf{G}})(\mathbf{G}^{(s)} - \overline{\mathbf{G}})^T, \tag{4.20}$$

where $\overline{\mathbf{G}}$ is the sample average. We can then define the diagonal matrix of standard deviations $\mathbf{D}$ where $D_{ij} = \delta_{ij}\sigma_{\mathbf{G}_i}$. With this construction we can then write that $\mathbf{M}_{\rm cov} \equiv \mathbf{D}\mathbf{M}_{\rm corr}\mathbf{D}$, where $\mathbf{M}_{\rm corr}$ is the related *correlation matrix* (also known as the normalized covariance matrix we discuss in previous sections). This correlation matrix $\mathbf{M}_{\rm corr}$ has eigenvectors $\mathbf{v}_n$ and eigenvalues λ_n, such that $\mathbf{M}_{\rm corr}\mathbf{v}_n = \lambda_n \mathbf{v}_n$. For a vector fitting function $\mathbf{G}(\mathbf{p})$ of fit parameters $\mathbf{p}$, we can write our augmented χ^2 function as

$$\chi^2_{\rm aug}(\mathbf{p}) = \sum_{n=1}^{N_G} \frac{\left[\left(\overline{\mathbf{G}} - \mathbf{G}(\mathbf{p})\right)^T \mathbf{D}^{-1}\mathbf{v}_n\right]^2}{\lambda_n} + \chi^2_{\rm prior}. \tag{4.21}$$

If the number of sample correlation function N_s is sufficiently smaller than N_G, problems arise out of the approximation we make for $\mathbf{M}_{\text{cov}}$ in equation 4.20 [87, 89]. Under this approximation, if $N_s < N_G$ then we will be left with a number of zero-valued eigenvalues equal to $N_G - N_s$. Naturally, eigenvalues $\lambda_n = 0$ cause equation 4.21 to become undefined. Moreover, even in the case where N_s is greater than N_G by less 10-100 times, we end up underestimating eigenvalues, which can compromise/invalidate our least squares fit approach. The approximated eigenvalues λ_n which can negatively affect our χ^2 fit are those for which

$$\frac{\lambda_n}{\lambda_n^{\text{exact}}} < 1 - \sqrt{\frac{2}{N_G}}, \tag{4.22}$$

where λ_n^{exact} is theoretically exact eigenvalue. We unfortunately do not know the exact eigenvalues (hence the approximation), and so rely on bootstrapped copies of the correlator data to produce bootstrapped eigenvalues $\lambda_n^{\text{bootstrap}}$. The bootstrapped data is derived from the same ensembles, and likewise have the same number of samples N_S. We can therefore approximate the left-hand side of equation 4.22 as

$$\frac{\lambda_n}{\lambda_n^{\text{exact}}} \approx \frac{\lambda_n^{\text{bootstrap}}}{\lambda_n}. \tag{4.23}$$

Figure 16 in [109] demonstrates the validity of this approximation. With this established, we can now go on to establish the methodology of the SVD cut, which is shown in figure 4.18. If we plot $\lambda_n^{\text{bootstrap}}/\lambda_n$ against $\lambda_n/\lambda_{\text{max}}$, we can find the point along the y-axis where $\lambda_n^{\text{bootstrap}}/\lambda_n = 1 - \sqrt{2/N_G}$. The point along the x-axis where this intersection occurs is the SVD cut-off κ. Implementing this cut-off means that all eigenvalues λ_n smaller than $\kappa\lambda_{\text{max}}$ are replaced with $\kappa\lambda_{\text{max}}$.

Thankfully, the *gvar*, *lsqfit*, and *corrfitter* packages [80, 83, 82] have built-in functions which determine appropriate SVD cuts for our fits automatically. This is to say, SVD cuts are chosen such that eigenvalues below the cut-off are replaced by a value of $\kappa\lambda_n^{\text{max}}$. Utilizing SVD cuts ensures the validity of our least squares fitting routine. Additionally, implementing SVD cuts increases the uncertainty of our fit results. This choice is conservative in the same sense that increasing

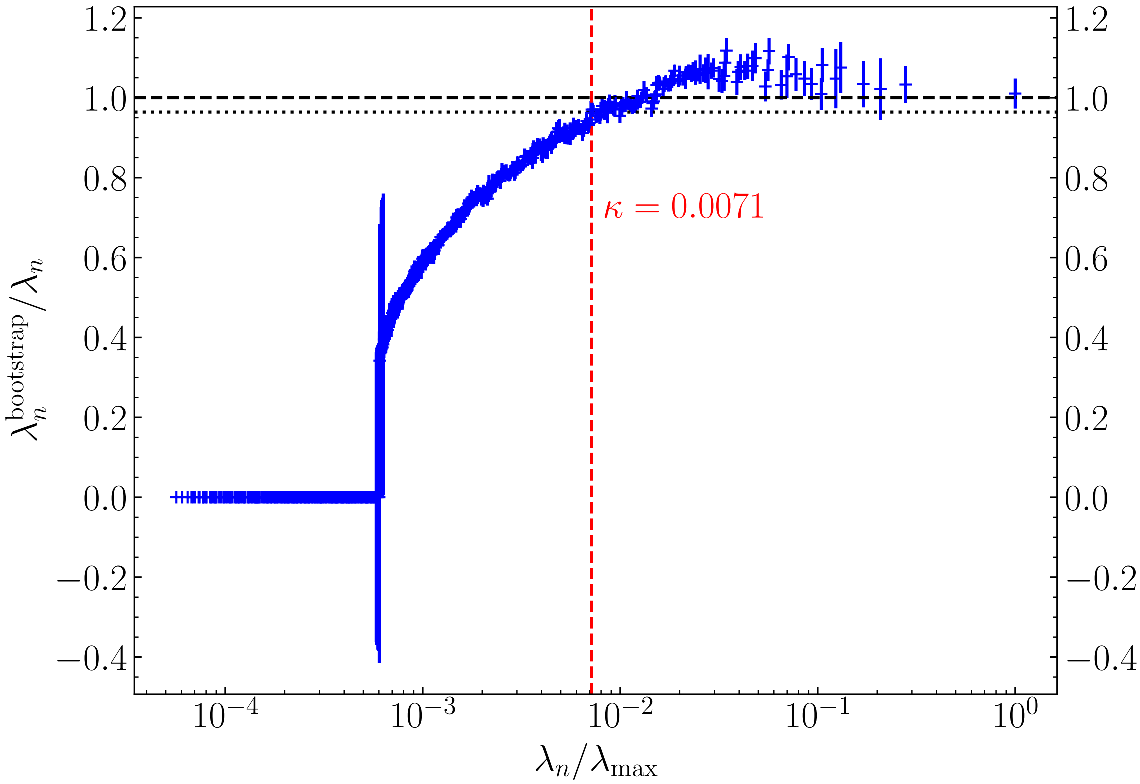

Figure 4.18: SVD diagnosis plot for a $D_s \to K$ fit on the f5 ensemble. Data shown (in blue) are the ratios of bootstrapped eigenvalues $\lambda_n^{\text{bootstrap}}$ to random sample eigenvalues λ_n, normalized along the x-axis by the maximum sample eigenvalue λ_{max}. The point along the y-axis where $\lambda_n^{\text{bootstrap}}/\lambda_n = 1 - \sqrt{2/N_G}$ is indicated by the dotted black line. Where the data crosses this line determines the SVD cut κ, indicated by the dashed red line. The point along the y-axis where $\lambda_n^{\text{bootstrap}}/\lambda_n = 1$ is indicated by the dashed black line.

prior uncertainties is a conservative choice for the fit. In testing we find that posterior fit results, are generally not sensitive to scaling the (automatically determined) SVD cut by an order of magnitude, nor are the quantities which determine goodness of fit (which we discuss in the next section).

4.8 Determining the quality of correlator fits

To conclude our lengthy chapter on fitting correlation functions, let us discuss explicitly the *holistic* means by which we judge the quality, or goodness of a correlator fit. We emphasize the word *holistic* here because these quantities do not necessarily alert us to problems with individual parameters (like spurious states which we discuss in section 4.6), but rather enable easy whole fit evaluation and comparison. These quantities are the χ^2 per degree of freedom ($\chi^2/\mathrm{d.o.f.}$), the fit quality Q (which is also known as the p-value), and the $\log(\mathrm{GBF})$ of a fit.

Naively, we might expect a good fit to have a $\chi^2/\mathrm{d.o.f.}$ nearly equal to one. This would imply that, per degree of freedom or fit parameter, the mean squared deviation of the correlator data from the line of best fit is nearly equal to the variance of the correlator data. However with our introduction of the augmented χ^2 (which appears in 4.3) we often are left with correlator fits with values of $\chi^2/\mathrm{d.o.f.}$ much less than one. This phenomenon is related to the uncertainties of priors we include in our fit; broader prior uncertainties will lower a fit's $\chi^2/\mathrm{d.o.f.}$. As discussed in the previous section, we assign reasonably broad priors wherever possible in our fits, and so this effect must be considered. SVD cuts can likewise artificially reduce the $\chi^2/\mathrm{d.o.f.}$ of a fit (see *lsqfit* documentation [83] and appendix D of [109]). Thankfully, the *lsqfit* package has built-in *noise* functions which address these problems. Enabling *prior noise* in a fit randomly increase or decreases the central values of the priors according to the gaussian distribution set by their uncertainties. Likewise enabling *SVD cut noise* affects the random sampling in the error distribution of our SVD cut. In theory then, enabling both prior and SVD cut noise will restore the $\chi^2/\mathrm{d.o.f.}$ of an otherwise good fit to be near equal to one. Due to the random nature of this added noise however, fits with prior and SVD cut noise enabled are not reproducible, and we therefore do not enable prior and SVD cut noise by default in our fit routine. Instead, before we accept any candidate final set of correlator fits, we rerun that same set of fits where the only change is that prior and SVD cut noise are enabled. Should this alternative set of noise enabled fits be otherwise of good quality, we can then accept that candidate set of noise disable correlator fits as the final set to carry forward into form factor calculation.

To be of good quality however, we also have to evaluate the quality factor Q of a fit. We can define Q as the probability that, if the null hypothesis H_0 is true, we could have a smaller value of χ^2 than what was calculated in the fit. This is to say that $Q = \Pr\left(\chi^2 \leq \mathrm{X}|\mathrm{H}_0\right)$ for some distribution X. The common standard which we adopt is that $Q \geq 0.05$ qualifies an acceptable fit. Like χ^2, our augmented least squares fit approach can likewise jeopardize the validity of the quality factor. Artificially broad prior uncertainties and prior central values taken from previous test fit results will minimize the contribution of χ^2_{prior} to χ^2_{aug} in equation 4.3. The quality factor of a fit is in part derived from the χ^2 of a fit, and so artificially narrow priors can likewise invalidate a strict interpretation of the meaning of Q. Enabling prior noise however has the same effect on the interpretation of Q as it does on χ^2. We therefore also ensure that noise enabled fits have acceptable fit posteriors of $\chi^2 \approx 1$ and $Q \geq 0.05$.

While enabling prior noise will validate the meaning of Q in the case of underfitting (artificially broad priors), it does not do the same for overfitting. If we implement priors with artificially or unjustifiably narrow priors, then the fitter would too strongly favor fit posteriors that match their respective priors, with little consideration of the data itself. To account for this overfitting, we utilize our final holistic measure of goodness of fit, which is the Gaussian Bayes Factor (GBF). We can define an effective definition of the GBF as the probability density that the final fit model would produce the original data through random gaussian sampling [110]. For some data D and model M, we can write that the GBF is equal to $\Pr(\mathrm{D}|\mathrm{M})$. This construction punishes a model (composed of priors that we set) that overfits the data. For two fits wich contain the same fit parameters but those parameters have different priors, whichever fit has a larger $\log(\mathrm{GBF})$ is generally preferred; a change of $\log(\mathrm{GBF})$ greater than three is significant [92] for the means of comparison. To summarize then, we evaluate the goodness of a fit by considering its χ^2/d.o.f, Q, and $\log(\mathrm{GBF})$. We select fits which minimize χ^2 and maximize $\log(\mathrm{GBF})$, so long as $Q \geq 0.05$. Conveniently for us, all three of these quantities are automatically calculated by the *lsqfit* package, the details of which are found in [83].

Chapter 5

Calculating Form Factors

In the previous chapter, we fully explored the topic of fitting two and three-point correlation functions. Here we first discuss how we transform the results of fitting correlation functions into a discrete set of lattice form factor data. We then go on to discuss how we utilize a modified z-expansion to fit that lattice form factor data to continuous fit forms, the final product being physical continuum form factors. The form factor discussion in this chapter applies for a general heavy to light meson decay $H \to L$, where H has either heavy-light or heavy-strange quark content, unless otherwise noted. The current status of form factor calculations for either $D, B \to \pi$ or $D_s, B_s \to K$ are found in chapters 6 and 7 respectively.

5.1 Lattice Form Factors

With a satisfactory set of correlator fit results, we can work towards calculating lattice form factor results. We emphasize the term *lattice* here because the form factors directly derived from our correlator fit results will still contain ensemble-specific lattice artifacts, namely those which come from non-zero lattice spacing and unphysical quark masses. Furthermore, these lattice form factors will be a discrete, non-continuous set of form factor values, rather than some function describing a continuous curve. In sections 5.2 and 5.3 we detail how we arrive at physical continuum form factors from these discrete form factors. For now however, let's examine the outputs of our correlator fitting.

The results of our correlator fitting include the energies and amplitudes of heavy and light mesons E_H, E_L, A_H, A_L. The results then also include a set of current insertion amplitudes $J \in \{S, V, T\}$. These energies and amplitudes correspond to different combinations of lattice spacings, quark masses, light meson momenta, and spin-taste construction. Many of these parameters correspond to higher order exponential and or oscillating states which appear in our correlation function fit forms (equations 4.1 and 4.18). However it is only the ground state heavy meson masses M_H, light meson energies E_L, and current insertion amplitudes J_{00}^{nn}, which we carry forward into form factor calculations[1].

5.1.1 Equations of lattice form factors

Before we can construct our lattice form factors f_0, f_+, and f_T, we must first calculate the corresponding lattice matrix element. Using equations 2.42 and 4.2, we can define the lattice matrix element as

$$\langle L| J_{\text{latt}} |\overset{(\wedge)}{H}\rangle = 2Z_{\text{disc}}\sqrt{M_H E_L} J_{00}^{nn}. \tag{5.1}$$

Here we use the same notation as the previous chapter for $J \in \{S, V, T\}$. Furthermore, we introduce the notation $^{(\wedge)}$ to denote that the heavy meson in the lattice matrix element must be of appropriate spin-taste construction for the accompanying lattice current J_{latt}. We write the Goldstone heavy meson as H, and any non-Goldstone heavy meson as $\hat{H} \in \{H', H'', H'''\}$. The spin-taste construction of these meson operators are given in equation 3.73. In the right hand side of equation 5.1 however we always use the Goldstone (spin-taste $\gamma_5 \otimes \xi_5$) heavy meson mass from our correlator

---

1. Considering that from this point onward we only care about the ground state meson masses and energies, we drop any $i = 0$ and non-oscillating indicating notation for the mesons.

fits. As discussed in chapter 3, the Goldstone heavy meson H only differs from its non-Goldstone counterparts $\hat{H}$ by discretization effects. Finally in equation 5.1 we also include a normalization term Z_{disc} which accounts for $\mathscr{O}(m_h)^4$ discretization effects [56]. We define Z_{disc} explicitly in the following section.

Having defined our lattice matrix elements in relation to correlator fit outputs, we can also define them in terms of scalar, vector, and tensor lattice form factors:

$$\langle L|\, S_{\text{latt}}\, |H\rangle = \frac{M_H^2 - M_L^2}{m_h - m_l} f_0(q^2), \tag{5.2}$$

$$Z_V\, \langle L|\, V^{\mu}_{\text{latt}}\, |H^{\prime(\prime\prime)}\rangle = f_+(q^2)\left(p_H^\mu + p_L^\mu - \frac{M_H^2 - M_L^2}{q^2} q^\mu\right) + f_0(q^2)\frac{M_H^2 - M_L^2}{q^2} q^\mu, \tag{5.3}$$

$$Z_T(\mu)\, \langle L|\, T^{k0}_{\text{latt}}\, |H^{\prime\prime\prime}\rangle = \frac{2iM_H p_L^k}{M_H + M_L} f_T(q^2, \mu). \tag{5.4}$$

Here we emphasize that the form factors are functions of the squared four-momentum transfer $q^2 = (p_H - p_L)^2$, where p_H and p_L are the heavy and light meson four-momenta. In equation 5.2 it is important to note that while the light meson mass M_L denotes either some pion or kaon mass, the term m_l always denotes the valence light quark mass on an ensemble, rather than the valence strange quark mass. In the equation for the vector lattice matrix element (equation 5.3) the index $\mu \in \{0, 1, 2, 3\}$ denotes the euclidean dimension (x_0, x_1, x_2, x_3), where x_0 is the temporal dimension of the lattice and x_1, x_2, x_3 are equivalent spatial dimensions. We use the non-Goldstone heavy meson H' (spin-taste $\gamma_5 \otimes \xi_5\xi_1$) with the temporal vector current V^0_{latt}, and we use the non-Goldstone heavy meson H'' (spin-taste $\gamma_5\gamma_0 \otimes \xi_5\xi_0$) with any spatial vector current $V^{1,2,3}_{\text{latt}}$. For the tensor matrix element the index k can denote any spatial euclidean dimension; we choose $k = 1$, and in the right hand side of equation 5.4 we have $i = \sqrt{-1}$. Unlike the scalar and vector form factors, the tensor form factor *is* dependent on some energy scale μ (not to be confused with the index μ in the vector current equation). Finally, Z_V and $Z_T(\mu)$ are renormalization terms which we discuss in the following section. We can also note that if we require matrix elements to be finite, then from equation 5.3 at $q^2 = 0$ we have $f_+(0) = f_0(0)$. This is a useful constraint that we can implement directly in our modified z-expansion fits, which we discuss in section 5.2.

5.1.2 Normalization and renormalization terms

In equation 5.1 we find the lattice discretization normalization term Z_{disc} [56], which we define as

$$Z_{\text{disc}} = \sqrt{\cosh(m_{\text{tree}})\left(1 - \frac{1+\varepsilon_{\text{tree}}}{2}\sinh^2(m_{\text{tree}})\right)}. \tag{5.5}$$

Here, m_{tree} is the tree level pole mass of a quark of bare mass m (in lattice units). We define m_{tree} and the Naik term $\varepsilon_{\text{tree}}$ in equations 3.38 and 3.39 in section 3.3.4. While these equations are true for any quark on the lattice, the m_{tree} and $\varepsilon_{\text{tree}}$ contributions from the light and strange quark masses are effectively zero, and so we only include the heavy quark mass contributions to Z_{disc}.

The next renormalization term we can discuss is Z_V, which we use to calculate vector form factors in 5.3. To determine Z_V, we first need to examine the continuum expression of the partially conserved vector current (PCVC) equation [111, 112], given by

$$q_\mu \langle L| V^\mu_{\text{local}} |H\rangle = (m_h - m_l) \langle L| S_{\text{local}} |H\rangle \,. \tag{5.6}$$

Here we emphasize that this relation only holds true for *local* current insertions, which is the case for all $J \in \{S, V, T\}$ in this work (see equation 3.73 for current insertion spin-taste construction). Luckily, this continuum expression remains valid on the lattice for the HISQ formalism [12], up to discretization effects. Taking this all into account, we can then also utilize the fact that the right hand side of equation 5.6 is fully normalized [111] to then define Z_V as

$$Z_V = \left.\frac{(m_h - m_l) \langle L| S |H\rangle}{(M_H - M_L) \langle L| V^0 |H'\rangle}\right|_{q^2 = q^2_{\text{max}}} . \tag{5.7}$$

We choose to calculate Z_V at the limit of $q^2 = q^2_{\text{max}}$, where both the heavy and light mesons are in the rest frame of the lattice. Adding three-momentum to mesons increases the noise of their correlation functions, and so evaluating Z_V at q^2_{max} ($\vec{p}_L = 0$) minimizes its uncertainty. Per ensemble and heavy quark mass, we can use the same value of Z_V for all V^μ and q^2 in equation 5.3 [14], which is valid up to discretization effects.

Table 5.1: Tensor renormalization factors $Z_T(\mu = 4.8 \text{ GeV})$ and their accompanying correlation matrix used in this work. Values are taken from tables VIII and IX in [3].

ensemble	Z_T	correlation matrix		
f5, fphys	1.0029(43)	1.0	0.99605	0.93562
sf5, sfphys	1.0342(43)	0.99605	1.0	0.93197
uf5	1.0476(42)	0.93562	0.93197	1.0

While Z_v is fully normalized, independent of energy scale, we cannot say the same for tensor form factor renormalization term Z_T. For some time, the determination of Z_T was only possible perturbatively and with large errors. The HPQCD collaboration in [3] however manages to calculate values of Z_T in the RI-SMOM scheme [113] which are then matched to the $\overline{\text{MS}}$ scheme [114, 115], correcting for non-perturbative artifacts and $\mathscr{O}(\alpha_s^4)$ errors. We present the values of Z_T and their accompanying correlation matrix we use in this work in table 5.1. The final values we use from table VIII in [3] are first calculated at an energy scale of $\mu = 2.0$ GeV in the RI-SMOM scheme. They are then converted to the $\overline{\text{MS}}$ scheme and run up the energy scale of the bottom quark pole mass. It is worth noting that we do not have separate values of Z_T for the fphys and sfphys ensembles. In our form factor calculations, they share the same value of Z_T as their f5 and sf5 counterparts. The energy scale $\mu = 4.8$ GeV is suitable for the physical $B \to \pi$ and $B_s \to K$ continuum extrapolations we perform. With the aims of producing $D \to \pi$ and $D_s \to K$ tensor form factors however, we need a way to run $Z_T(\mu)$ to a scale appropriate for a given M_H, which is $Z_T(\mu = 2.0 \text{ GeV})$ for the physical $D_{(s)}$ meson. Following from [3], we can derive a multiplicative factor Γ such that

$$f_T^{D_{(s)}\to\pi(K)}(q^2, \mu = 2.0 \text{ GeV}) = \Gamma \times f_T^{D_{(s)}\to\pi(K)}(q^2, \mu = 4.8 \text{ GeV}). \tag{5.8}$$

For an energy scale of $\mu = 2.0$ GeV, we arrive at a value of $\Gamma = 1.0773(17)$.

5.2 The modified z-expansion

In the previous section, we have described the necessary steps to translate correlator fit outputs into a discrete set of lattice form factors. In this section, we describe the necessary steps to fit that set of lattice form factor data into appropriate fit forms, which are continuous functions of q^2 in the range of $0 \leq q^2 \leq q^2_{\text{max}} = (M_H - M_L)^2$. The unphysical artifacts in our lattice form factor data are: unphysical and mistuned quark masses, lattice discretization effects, and non-zero lattice spacing. We address all of these issues simultaneously, fitting the lattice form factor data in accordance with *the modified z-expansion*, first introduced in [111].

5.2.1 Mapping to z

The core of this technique is the mapping of q^2 to some complex number z in the complex plane, and re-parameterizing $f_{0,+,T}$ as analytical functions of polynomials of z. To begin, we can first map $q^2 \to z$ by defining z as

$$z(q^2, t_0) = \frac{\sqrt{t_+ - q^2} - \sqrt{t_+ - t_0}}{\sqrt{t_+ - q^2} + \sqrt{t_+ - t_0}}. \tag{5.9}$$

Here we follow the notation of [116, 117, 118] where $t_+ = (M_H + M_L)^2$ is the beginning of a branch cut (which corresponds to the current insertion having enough energy for on-shell HL production), and t_0 is an arbitrary parameter that shifts $f_{0,+,T}$ along the Re$[z]$-axis. We choose to set $t_0 = 0$, such that $z(q^2 = 0,\ t_0 = 0) = 0$. This choice facilitates the enforcement of the kinematic constraint $f_0(0) = f_+(0)$, which is a consequence of equation 5.3. We note that this parameter t_0 is unrelated to the same notation which appears in chapters 3 and 4. In figure 5.1 we give an illustrative diagram which shows how we map $q^2 \to z$.

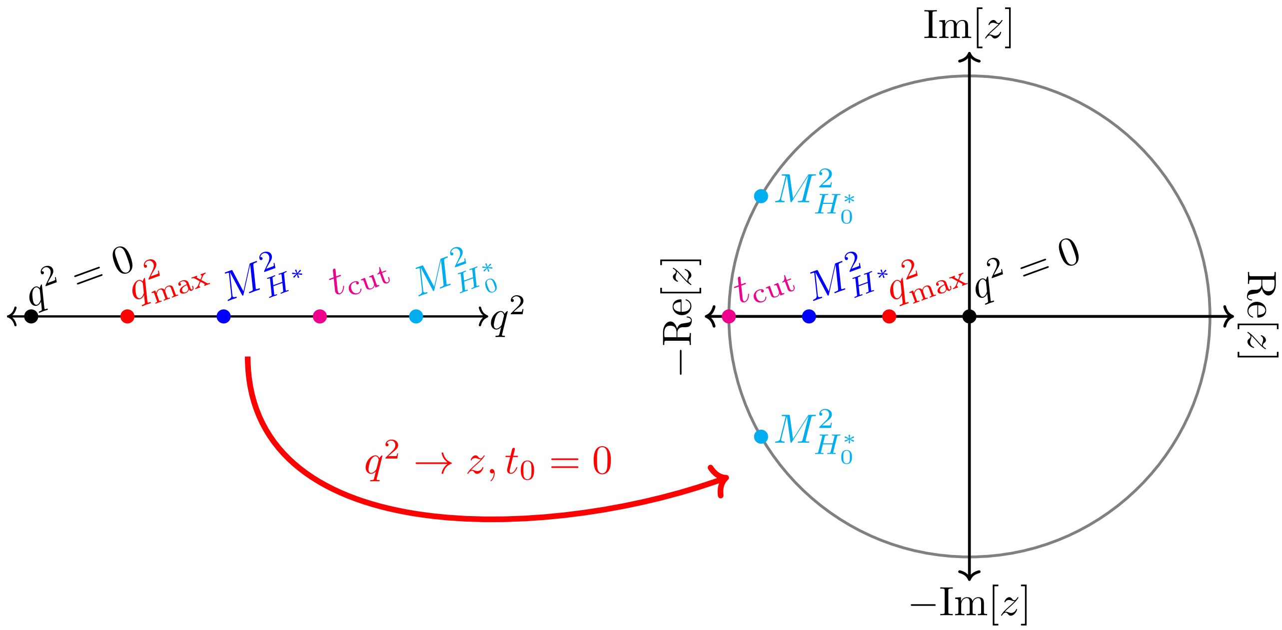

Figure 5.1: Diagram showing the mapping of $q^2 \to z$ for $t_0 = 0$, as defined in equation 5.9. We include a subthreshold pole mass M_{H^*} and a post threshold pole mass $M_{H_0^*}$, which appear in the pole mass terms defined by equations 5.24 and 5.26.

Having defined z, we can now parameterize the equations of $f_{0,+,T}$ in terms of polynomials of z. We use the Bourrely-Caprini-Lellouch (BCL) parameterization [117] as a basis to now define our form factor equations as

$$f_0(q^2) = \frac{\mathscr{L}}{P_0(q^2, M_H)} \sum_{n=0}^{N-1} a_n^0 z^n, \tag{5.10}$$

$$f_+(q^2) = \frac{\mathscr{L}}{P_+(q^2, M_H)} \sum_{n=0}^{N-1} a_n^+ \left(z^n - \frac{n}{N}(-1)^{n-N} z^N\right), \tag{5.11}$$

$$f_T(q^2, \mu) = \frac{\mathscr{L}}{P_T(q^2, M_H)} \sum_{n=0}^{N-1} a_n^T \left(z^n - \frac{n}{N}(-1)^{n-N} z^N\right). \tag{5.12}$$

This *modified* form of the BCL parameterization allows us to simultaneously extrapolate to zero lattice spacing and physical meson masses, across the physical range of q^2, while removing discretization effects and lattice artifacts. We can therefore characterize our modified z-expansion fit routine as using the results of correlator fitting as input data, while equations 5.10-5.12 are the fit forms. In these equations, $a_n^{0,+,T}$ are coefficients that multiply polynomials of z, which have a maximum order of $N-1$ for the scalar form factor, and a maximum order of N for the vector and tensor form factors. The inclusion of the z^N term models for the expected behavior of f_+ and f_T at large q^2. We also include a non-analytical $SU(2)$ logarithmic term $\mathscr{L}$, which accounts for light quark mass dependency using chiral perturbation theory (χpt). We account for possible pole terms in this parameterization by dividing by a pole-mass term $P_{0,+,T}(q^2, M_H)$. Doing so enforces that these functions be analytical in z. We explore the definitions of these parameters in the remainder of this section.

5.2.2 Coefficients of the z-expansion

The first terms we will discuss which appear in equations 5.10-5.12 are the coefficients $a_n^{0,+,T}$. We aim for these coefficients to capture the expected dependence on the heavy meson mass, quark mass mistuning, lattice discretization effects, and the (analytical) chiral extrapolation of the light quark mass. We therefore define $a_n^{0,+,T}$ as

$$\begin{aligned} a_n^{0,+,T} &= \left(\frac{M_D}{M_H}\right)^{\zeta_n} \left(1 + \rho_n^{0,+,T} \log\left(\frac{M_D}{M_H}\right)\right) \times (1 + \mathcal{N}_n^{0,+,T}) \\ &\times \sum_{i,j,k,l=0}^{N_{ijkl}-1} d_{ijkln}^{0,+,T} \left(\frac{\Lambda_{\mathrm{QCD}}}{M_H}\right)^i \left(\frac{am_h}{\pi}\right)^{2j} \left(\frac{a\Lambda_{\mathrm{QCD}}}{\pi}\right)^{2k} (x_\pi - x_\pi^{\mathrm{phys}})^l. \end{aligned} \tag{5.13}$$

We define the terms in equation 5.13 and prior selection in separate parts below.

Heavy meson mass dependency

We can first discuss the terms in equation 5.13 which are dependent on the mass of the heavy meson M_H. From Heavy Quark Effective Theory (HQET) we include an inverse power series of M_H in i, scaled by Λ_{QCD}. We also include a prefactor with fitted power ζ_n to account for the $M_H^{-3/2}$ behavior at low q^2 we expect from Large Energy Effective Theory (LEET) [119]. We have also seen this behavior modeled by a logarithmic term in [16]. We allow for this behavior by including a $\log(\frac{M_D}{M_H})$ term in equation 5.13, multiplied by the parameter $\rho_n^{0,+,T}$. We note that by setting $t_0 = 0$ in equation 5.9, the near-zero q^2 region of our form factors will be dominated by the z^0 terms in the z-expansion.

Quark mass mistuning

By the inclusion of the term $\mathcal{N}_n^{0,+,T}$ in equation 5.13, we account for possible sea and valence quark mass mistuning effects. This term does not account for the varying heavy quark masses. It also does not perform the χpt extrapolation of the unphysical light quark masses on the ensembles where $m_s/m_l \approx 5$. We address that functionality later in this section. For now, we can simply define the quark mass mistuning term $\mathcal{N}_n^{0,+,T}$ as

$$\mathcal{N}_n^{0,+,T} = c_{s,n}^{\mathrm{val},0,+,T}\delta_s^{\mathrm{val}} + c_{s,n}^{\mathrm{sea},0,+,T}\delta_s^{\mathrm{sea}} + 2c_{l,n}^{0,+,T}\delta_l + c_{c,n}^{\mathrm{sea},0,+,T}\delta_c^{\mathrm{sea}}. \tag{5.14}$$

The form of equation 5.14 is the sum of some fit parameters c times some known tuning term δ for each valence and sea quark. The mass of the light valence and light sea quarks are degenerate (hence the factor of 2 multiplying $c_{l,n}^{0,+,T}$), which is not true for the strange quark. For any valence or sea quark $q \in l,s$, we define δ_q as

$$\delta_q = \frac{m_q - m_q^{\mathrm{tuned}}}{10 m_s^{\mathrm{tuned}}}. \tag{5.15}$$

This form includes a factor of 10 in the denominator, which is a proxy that accounts for the expected expansion parameter $4\pi f_\pi$ from χpt. We can define m_s^{tuned} relative to the mass of the η_s meson[2]:

$$m_s^{\mathrm{tuned}} = m_s^{\mathrm{val}} \left(\frac{M_{\eta_s}^{\mathrm{phys}}}{M_{\eta_s}}\right)^2. \tag{5.16}$$

Though we do not calculate the values of M_{η_s}, $M_{\eta_s}^{\mathrm{phys}}$ in our correlator fits, we can rely on previous HPQCD results [16, 71] which are fit on the same gluon field ensembles. With m_s^{tuned} defined, we can use [67] to then define m_l^{tuned} using the ratio

$$\frac{m_s^{\mathrm{tuned}}}{m_l^{\mathrm{tuned}}} = 27.18(10). \tag{5.17}$$

2. While constructing a pseudo-scalar meson composed of a strange and anti-strange quark pair is unphysical, we are not prevented from construing such a meson on the lattice in pure QCD.

Finally for sea charm quark we can define δ_c^{sea} as

$$\delta_c^{\text{sea}} = \frac{m_c^{\text{sea}} - m_c^{\text{tuned}}}{m_c^{\text{tuned}}}, \tag{5.18}$$

where we again use previous HPQCD work which fixes m_c^{tuned} from the mass of η_c [120]. These values are used to guide our choice for the lightest heavy quark mass on each ensemble, which facilitates the calculation of $D \to \pi$ and $D_s \to K$ form factors.

Discretization effects

In equation 5.13, we also account for $\mathscr{O}(a^2)$ discretization effects. This includes effects which are dependent on the mass of the heavy quark $(am_h)^{2j}$, and those which are independent of any quark mass, for which we include $(a\Lambda_{\text{QCD}})^{2k}$. With this construction we allow for discretization effect dependencies that vary across ensembles with different heavy meson masses, and those which are constant for any given ensemble or heavy meson mass.

Light quark mass dependency

Finally, we include an analytical χpt term $(x_\pi - x_\pi^{\text{phys}})^l$ in equation 5.13 to account for any form factor dependence of the light quark (and therefore also light meson) mass. This term is especially useful in addressing the unphysically heavy light meson masses ($m_s/m_l \approx 5$) which appear in the f5, sf5, and uf5 ensembles. For any meson $\mathscr{M}$, physical or otherwise, we can define a unit-less mass parameter $x_{\mathscr{M}}$ as

$$x_{\mathscr{M}} = \frac{M_{\mathscr{M}}^2}{(4\pi f_\pi)^2}. \tag{5.19}$$

For x_π however, rather than using fit outputs M_π and f_π, we follow the method of [17] and construct a useful approximate form where

$$x_\pi^{\text{(phys)}} = 2\frac{m_l^{\text{(phys)}}}{5.63 m_s^{\text{phys}}}. \tag{5.20}$$

Here the notation which denotes physical masses is equivalent to the "tuned" notation describing valence quark masses discussed previously, and so we can use equations 5.16 and 5.17 to define m_s^{phys} and m_l^{phys}.

Coefficient prior choices

In the related Boyd-Grinstein-Lebed (BGL) parameterization [121, 122, 116], implementing the proper outer function imposes that the coefficients b_n which multiply the powers of z must be of order one or less. However for the BCL parameterization, we cannot explicitly enforce that the coefficients $a_n^{0,+,T}$ in equations 5.10-5.12 similarly lie within the bounds of 0 ± 1. In previous $B \to \pi$ and $B_s \to K$ lattice results which use the BCL parameterization, the coefficients of the z-expansion they calculate are often of order one or less [7]. We likewise expect (but do not strictly enforce) that our final values of $a_n^{0,+,T}$ are of order one or less. In our modified z-expansion however, the coefficients $a_n^{0,+,T}$ are constructed from the various terms in equation 5.13. Therefore the natural priors to assign to the many parameters in 5.13 are $0.0(1.0)$, unless there are physics informed reasons to do otherwise. For example, the coefficients $d_{ijkln}^{0,+,T}$ which multiply the terms which have powers i, j, k, l are mostly all given priors of $0.0(1.0)$ in our z-expansion fits. We know however the HISQ action is a^2-improved, in that $\mathscr{O}(a^2)$ HISQ errors are $\mathscr{O}(\alpha_s a^2)$ [12]. As such we can assign more strict priors to the terms which would be suppressed by the a^2 improvement. For example, we set $P[d_{i10ln}^{0,+,T}]$, $P[d_{i01ln}^{0,+,T}] = 0.0(3)$ to reflect the strong coupling constant $\alpha_s \approx 0.3$.

To match the expected $M_H^{-3/2}$ behavior at low q^2 [119], we assign the prior $P[\zeta_0] = 1.5(5)$, and directly set all other $\zeta_{n\neq 0} = 0$ in the z-expansion fit. With the aim of matching HQET to QCD, we follow from [13, 17] and assign priors $P[\rho_n^{0,+,T}] = 0(1)$ for all n. For $n = 0$, this choice permits different form factors to vary in ζ_0, and for $n \neq 0$ this choice allows for non-integer power M_H dependence.

For the quark mass mistuning term, we assign various priors to groups of the constants $c_n^{0,+,T}$ which appear in equation 5.14. For the valence strange quark, we assign a prior $P[c_{s,n}^{\mathrm{val},0,+,T}] = 0.0(1.0)$. We expect less contribution to $\mathscr{N}_n^{0,+,T}$ from the quarks in the sea, and so we arrive at priors $P[c_{s,n}^{\mathrm{sea},0,+,T}] = 0.0(5)$, $P[c_{l,n}^{0,+,T}] = 0.0(5)$, and $P[c_{c,n}^{\mathrm{sea},0,+,T}] = 0.0(1)$. In test fitting we ensure these priors are not overly constraining to the fit, using the same methods of $\log(\mathrm{GBF})$ testing discussed in chapter 4.

5.2.3 Chiral perturbation theory

In the prefactor which multiplies polynomial in equations 5.10-5.12, we include a non-analytical chiral logarithm term $\mathscr{L}$. The primary motivation for the inclusion of this term is to account for pion masses on three of our five gluon field ensembles which are unphysically heavy. Following from [123, 124], we can define separate $SU(2)$ chiral logarithm terms for either meson decay as

$$\mathscr{L}^{H\to\pi} = 1 - \Big(\frac{3}{8} + \frac{9g^2}{8}\Big)x_\pi\Big(\log x_\pi + \delta_{FV}\Big), \tag{5.21}$$

$$\mathscr{L}^{H_s\to K} = 1 - \frac{3}{8}x_\pi\Big(\log x_\pi + \delta_{FV}\Big). \tag{5.22}$$

Here we use the same definition for x_π as in equation 5.19, g is the coupling strength between between H, H^*, and π, and δ_{FV} is a small corrective term which accounts for finite volume effects. In our setup, the pion mass is effectively a light degree of freedom within the χpt expansion, as its mass varies significantly among the different ensembles. The kaons in our simulations however have masses which are more stable across ensembles; all our valence strange quark masses are nearly physical. Dependencies any mistuning in valence or sea strange quark mass are likely absorbed by the quark mass mistuning term $\mathscr{N}_n^{0,+,T}$. Furthermore, dependencies on the kaon mass are likely to be absorbed by the Λ_{QCD} terms in 5.13 as $M_K \approx \Lambda_{\mathrm{QCD}}$. For these reasons we choose to use $SU(2)$ chiral logarithm terms (with only x_π dependence) over their respective $SU(3)$ analogues (which have dependencies on x_K and x_η).

Table 5.2: Finite volume correction terms δ_{FV} used for each ensemble.

Ensemble	δ_{FV}
f5	0.0207875
fphys	0.0711225
sf5	0.019799
sfphys	0.0631322
uf5	0.0256137

It is worth remarking upon the presence of the coupling strength term g in equation 5.21 for $H \to \pi$ and its absence in equation 5.22 for $H_s \to K$. The coupling strength g arises out of one loop interactions, such as $H^* \leftrightarrow H\pi$, in the $H \to \pi$ decay, and is specifically related to the interaction of pions and heavy mesons with heavy-light quark content. In our $SU(2)$ treatment of the $H_s \to K$ decay however, there is no equivalent leading order $H_s^* \leftrightarrow H_s\pi$ contribution [125, 126].

If we now introduce the M_H argument for the coupling strength we can scale g with respect to heavy meson mass as

$$g(M_H) = g_\infty + C_1 \frac{\Lambda_{\text{QCD}}}{M_H} + C_2 \frac{\Lambda^2_{\text{QCD}}}{M_H^2}. \tag{5.23}$$

In this formulation, g_∞ is the coupling strength in the infinite mass limit, and $C_{1,2}$ are fitted constants. From [127] we have $g_\infty = 0.48(11)$. For the physical D and B masses we expect $g(M_D) = 0.570(6)$ [128] and, based on an average of [129, 130, 131] we expect $g(M_B) = 0.500(33)$. Based on trial fits using these values of $g(M_D)$ and $g(M_B)$, we assign broad priors to the fitted constants $P[C_1] = 0.5(1.0)$ and $P[C_2] = 0.0(3.0)$.

Finally to account for effects which depend on the finite volume of our lattices, we include the term δ_{FV} in our chiral logarithms functions. Table 5.2 gives the values of δ_{FV} we use, which are calculated from Equation (47) in [132]. These are first order values, and so to accommodate higher order effects we include an additional $(0.7\%)^2$ error for each δ_{FV} in our z-expansion fits.

5.2.4 Pole-mass terms

The final terms we can discuss which appear in equations 5.10-5.12 are the pole-mass terms $P_{0,+,T}(q^2, M_H)$. The motivation for including such terms is to account for potential subthreshold heavy-light production whose quantum numbers match the given current insertion. This is to say, we wish to account for the heavy mesons H_0^* ($J^P = 0^+$) and H^* ($J^P = 1^-$) who might have masses in the range between $q^2_{\text{max}} = (M_{H_{(s)}} - M_{\pi(K)})^2$ and $t_+ = (M_H + M_\pi)^2$. We wish to draw extra attention to the notation here, because the branch-cut at t_+ is always equal to the square of the sum of the two mesons masses whose quark content is heavy-light and light-light. This is true regardless of the spectator quark being a light quark or a strange quark. In previous sections we often use the notation for a generic heavy meson H whose quark content is either heavy-light or heavy-strange, but for the remainder of this section the notation H always denotes a heavy-light meson.

To begin, we can write the vector pole mass term $P_+(q^2, M_H)$ which appears in equation 5.11 as

$$P_+(q^2, M_H) = 1 - \frac{q^2}{M^2_{H^*}}. \tag{5.24}$$

Using experimental results for $M^{\text{phys}}_{D^*}$ and $M^{\text{phys}}_{B^*}$, we can construct an equation for M_{H^*} which interpolates between those two physical results. Using $M^{\text{phys}}_{D^*} = 2.00685(5)$ GeV and $M^{\text{phys}}_{B^*} = 5.32475(20)$ GeV [19], we can follow from [17, 13] and write

$$M_{H^*} = M_H + \frac{M_D^{\text{phys}}}{M_H}\Delta(D) + \frac{M_B^{\text{phys}}}{M_H}\left[\frac{M_H - M_D^{\text{phys}}}{M_B^{\text{phys}} - M_D^{\text{phys}}}\left(\Delta(B) - \frac{M_D^{\text{phys}}}{M_B^{\text{phys}}}\Delta(D)\right)\right], \tag{5.25}$$

where $\Delta(D) = M^{\text{phys}}_{D^*} - M^{\text{phys}}_D$ and $\Delta(B) = M^{\text{phys}}_{B^*} - M^{\text{phys}}_B$. We likewise define the tensor pole factor term $P_T(q^2, M_H) = P_+(q^2, M_H)$. This choice is motivated by the fact that, in the heavy quark limit and up to known kinematic factors, $f_T(q^2) = f_+(q^2)$ [133].

In the equation for the scalar form factor, we similarly define scalar pole mass term as

$$P_0(q^2, M_H) = 1 - \frac{q^2}{M^2_{H_0^*}}, \tag{5.26}$$

where H_0^* is a heavy meson with quantum numbers $J^P = 0^+$. Looking to the D meson end of the heavy quark mass spectrum, we have the PDG result that $D_0^* = 2.343(10)$ GeV [19]. While we do not have any experimental results for the mass of the B_0^* meson, we expect from HQET that the energy splitting $\Delta = M_{D_0^*} - M_D \approx 0.48$ GeV will be similar for the B system [134]. For the generic heavy-light meson H we can therefore define $M_{H_0^*} = M_H + \Delta$.

It is important to note that this definition places $(M_{H_0^*})^2$ above the branch cut threshold of $t_+ = (M_H + M_\pi)^2$, and so including this pole term in equation 5.10 is not strictly necessary. However in other work [135] and in our own test fitting, we find that the inclusion of this post-threshold pole mass term in the equation of the scalar form factor either has no effect, or somewhat improves fit results.

5.2.5 Testing z-expansion fits

In the previous sections we build the mathematical framework to perform a modified z-expansion fit, whose inputs are the outputs of some previous set of correlator fits. Before presenting the current status of our continuum $B, D \to \pi$ and $B_s, D_s \to K$ form factors in the following chapters, it is helpful to visually show the intermediate steps of the z-expansion fits. In figures 5.2 and 5.3, we show lattice form factor data from the uf5 ensemble correlator fit overlaid with continuous form factor curves, whose functions are built from the outputs of all-ensemble z-expansion test fits. These figures demonstrate that the z-expansion fit forms (equations 5.10-5.12) accommodate not only q^2 dependence, but heavy quark mass (and therefore heavy meson mass) dependency as well.

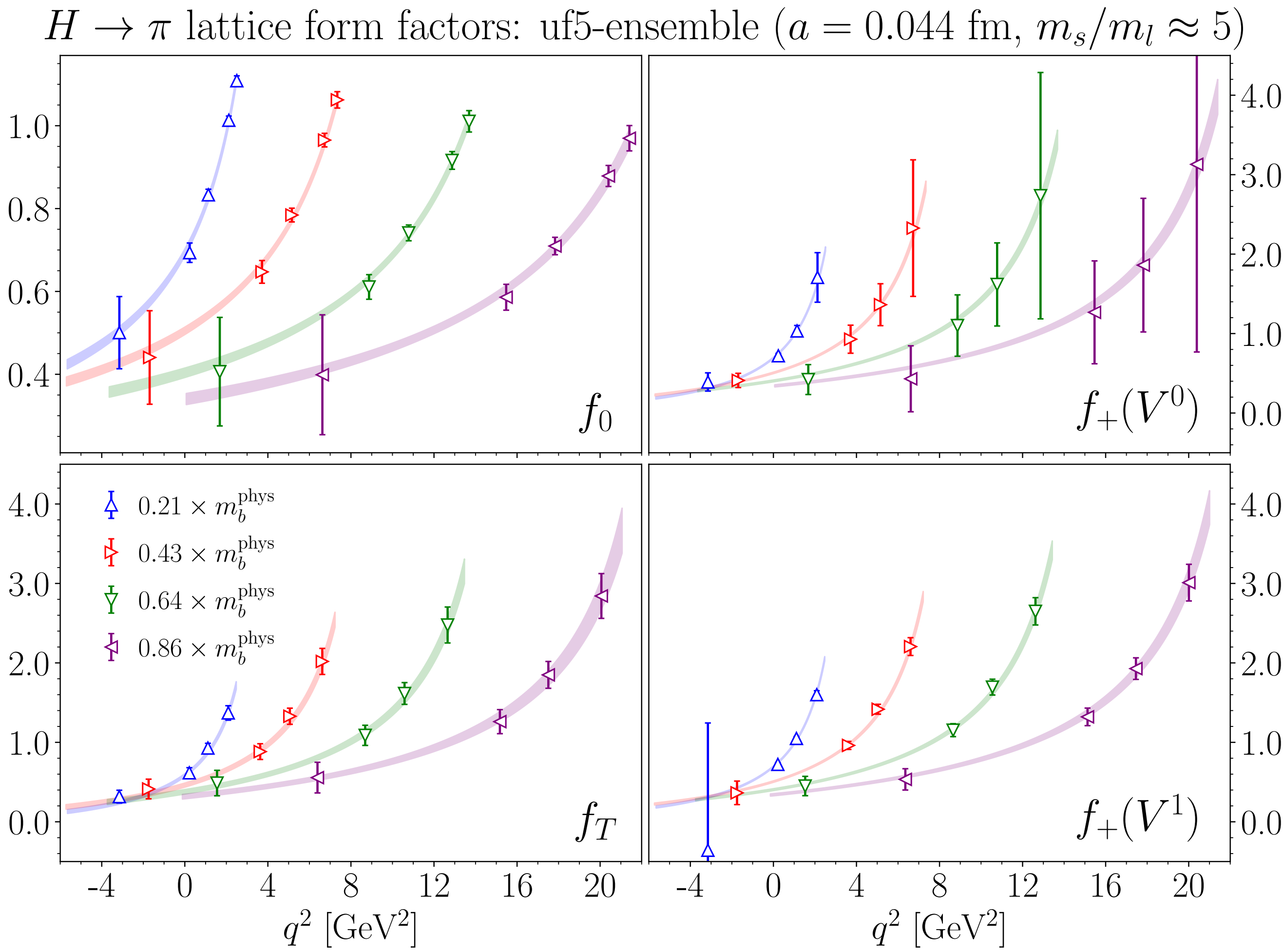

Figure 5.2: Plots show $H \to \pi$ lattice form factor data calculated from uf5 ensemble ($a = 0.044$ fm, $m_s/m_l \approx 5$) correlator fits, shown over large q^2 kinematic range. We show results for scalar (top left), temporal vector (top right), spatial vector (bottom right), and tensor (bottom left) form factors. Blue, red, green, and purple data corresponds to heavy quark masses equal to 0.21, 0.43, 0.64, and 0.86 times the physical b-quark mass respectively. The matching colored continuous curves are the functional form factor results constructed from the outputs of all-ensemble z-expansion test fits. The shaded region of each curve corresponds to the limits of the form factor results to ± 1 standard deviation.

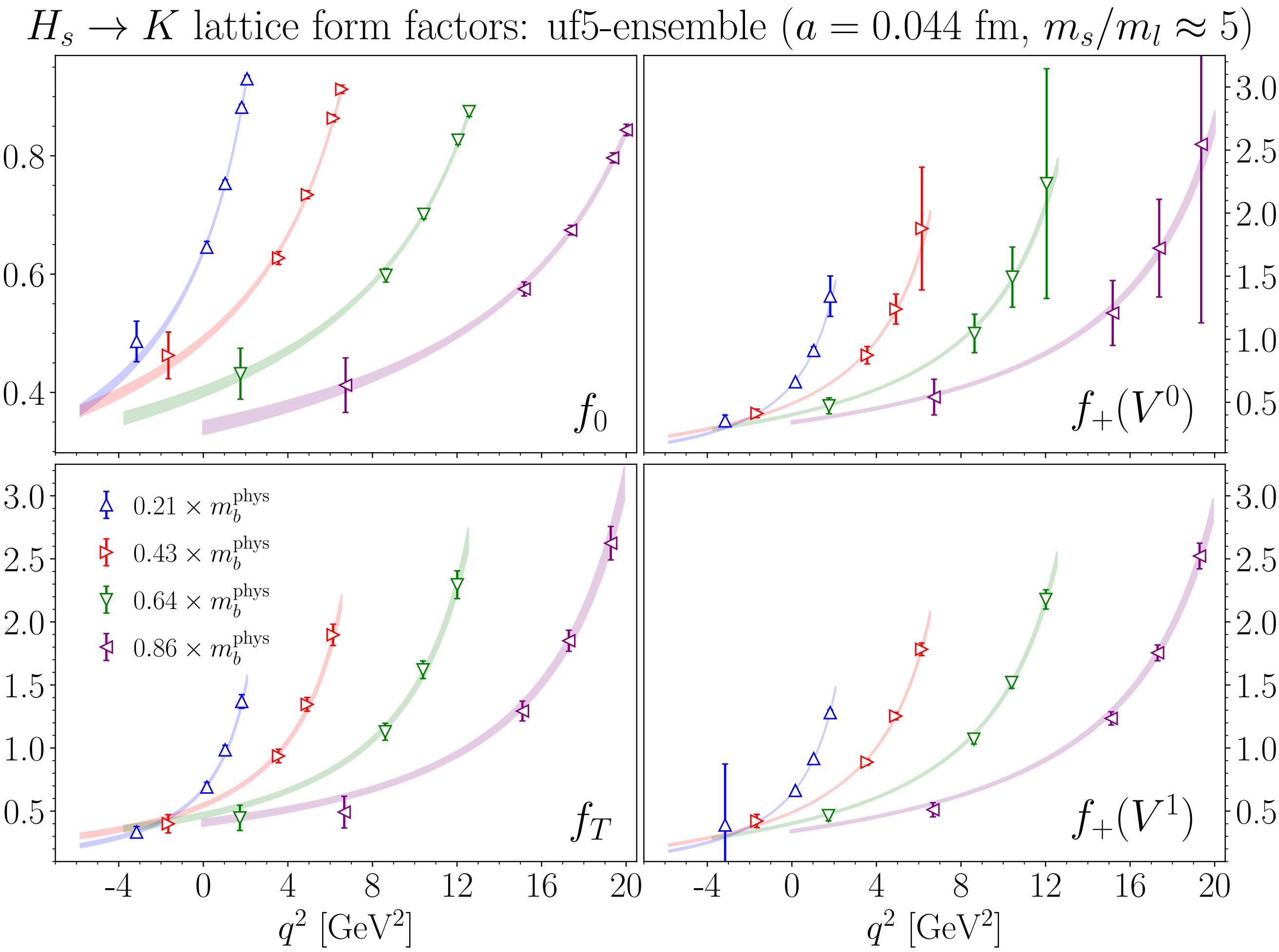

Figure 5.3: Plots show $H_s \to K$ lattice form factor data calculated from uf5 ensemble ($a = 0.044$ fm, $m_s/m_l \approx 5$) correlator fits, shown over large q^2 kinematic range. We show results for scalar (top left), temporal vector (top right), spatial vector (bottom right), and tensor (bottom left) form factors. Blue, red, green, and purple data corresponds to heavy quark masses equal to 0.21, 0.43, 0.64, and 0.86 times the physical b-quark mass respectively. The matching colored continuous curves are the functional form factor results constructed from the outputs of all-ensemble z-expansion test fits. The shaded region of each curve corresponds to the limits of the form factor results to ± 1 standard deviation.

5.3 Extrapolating to physical continuum form factors

In the previous section, we describe the fit equations for the scalar, vector, and tensor form factors which use the BCL parameterization as a basis. We modify this parameterization so that we can account for unphysical quark masses and meson mass dependencies, χPT, and discretization effects simultaneously in one fit. The result of this fit allows us to construct continuum limit versions of equations 5.10-5.12 which are valid for a generic heavy meson of mass M_H and the respective physical q^2 range where $0 \leq q^2 \leq q^2_{\text{max}} = (M_H - M_L)^2$.

We can define the continuum limit form factors $f^{\text{cont.}}_{0,+,T}(q^2, M_H)$ as

$$f_0^{\text{cont.}}(q^2, M_H) = \frac{\mathscr{L}^{\text{cont.}}(M_H)}{P_0(q^2, M_H)} \sum_{n=0}^{N-1} a_n^{0,(\text{cont.})}(M_H) z^n(M_H), \tag{5.27}$$

$$f_+^{\text{cont.}}(q^2, M_H) = \frac{\mathscr{L}^{\text{cont.}}(M_H)}{P_+(q^2, M_H)} \sum_{n=0}^{N-1} a_n^{+,(\text{cont.})}(M_H) \times \Big(z^n(M_H) - \frac{n}{N}(-1)^{n-N} z^N(M_H) \Big), \tag{5.28}$$

$$f_T^{\text{cont.}}(q^2, \mu, M_H) = \frac{\mathscr{L}^{\text{cont.}}(M_H)}{P_+(q^2, M_H)} \sum_{n=0}^{N-1} a_n^{T,(\text{cont.})}(M_H) \times \Big(z^n(M_H) - \frac{n}{N}(-1)^{n-N} z^N(M_H) \Big), \tag{5.29}$$

where we have made explicit all M_H arguments. The continuum chiral logarithm term $\mathscr{L}^{\text{cont.}}(M_H)$ differs from those describe in equations 5.21, 5.22 such that $\delta_{FV} = 0$, and $x_\pi \to x_\pi^{\text{phys}}$. We can define the continuum expansion coefficients $a_n^{0,+,T,(\text{cont.})}$ as

$$a_n^{0,+,T,(\text{cont.})}(M_H) = \Big(\frac{M_D^{\text{phys}}}{M_H} \Big)^{\zeta_n} \Big(1 + \rho_n^{0,+,T} \log\Big(\frac{M_H}{M_D^{\text{phys}}} \Big) \Big) \times \sum_{i=0}^{N_i - 1} d_{i000n}^{0,+,T} \Big(\frac{\Lambda_{\text{QCD}}}{M_H} \Big)^i, \tag{5.30}$$

where the only terms left in the summation are those for which $j, k, l = 0$ for $d_{ijkln}^{0,+,T}$ in equation 5.13. Such cases correspond to lattice spacing $a \to 0$ and $x_\pi \to x_\pi^{\text{phys}}$. Furthermore in the physical quark limit, the quark mass mistuning term $\mathscr{N}_n^{0,+,T} \to 0$. Therefore in this form $a_n^{0,+,T,(\text{cont.})}$ now only has functional dependence on the heavy meson mass M_H.

With this mathematical infrastructure, constructing physical continuum form factors is as simple as performing the appropriate z-expansion fit (either $H \to \pi$ or $H_s \to K$), plugging in the necessary fit outputs which appear in the continuum form factor equations, and then setting the desired physical heavy meson mass for either $D_{(s)}^{\text{phys}}$ or $B_{(s)}^{\text{phys}}$.

Chapter 6

$D \to \pi$ and $B \to \pi$ Form Factors

In this chapter, we present the current status of our $D \to \pi$ and $B \to \pi$ form factor calculations. Both these calculations are products of the same $H \to \pi$ correlator and z-expansion fits. Though we do have sets of acceptable fits which produce physical continuum form factor results (see section 6.4), we wish to highlight upfront that these results are not final. HPQCD plans to generate more $H \to \pi$ which will be incorporated into this line of research.

6.1 Calculation details

In chapter 3 we established the basis of our calculation details, but we shall summarize the key details here. Our calculations are carried out using MILC/HISQ $n_f = 2 + 1 + 1$ gluon field ensembles [72, 73, 74, 67], with HISQ valence quarks. The statistics of these ensembles is given in 6.1. In table 6.2 we give the ensemble-specific fit parameters which are most relevant to correlator fitting. These parameters include the correlator statistics, heavy quark masses, twist angles, and source-sink separations.

Table 6.1: Gluon field ensembles used in this work. The parameter $\beta = 6/g_s^2$ sets the strength of the strong coupling constant g_s^2. We discuss the ratio of the Wilson flow parameter w_0 divided by lattice spacing a in section 3.4.3. The dimensions of the lattice on each ensemble in lattice units are given in column 4, where we have three spatial dimension of length N_x and one temporal dimension of length N_t. Finally, the masses of the various sea and valence quarks in each ensemble are given in columns 5-9. These statistics apply to both our $H \to \pi$ and our $H_s \to K$ fits.

ensemble	β	w_0/a	$N_x^3 \times N_t$	$am_l^{\text{sea/val}}$	am_s^{sea}	am_c^{sea}	am_s^{val}	am_c^{val}
f5	6.3	1.9006(20)	$32^3 \times 96$	0.0074	0.037	0.440	0.0376	0.449
fphys	6.3	1.9518(7)	$64^3 \times 96$	0.00120	0.0363	0.432	0.036	0.433
sf5	6.72	2.896(6)	$48^3 \times 144$	0.0048	0.024	0.286	0.0234	0.274
sfphys	6.72	3.0170(23)	$96^3 \times 192$	0.0008	0.022	0.260	0.0219	0.2585
uf5	7.0	3.892(12)	$64^3 \times 192$	0.00316	0.0158	0.188	0.0165	0.194

Table 6.2: Parameters and statistics related to the correlation functions generated from the gluon field ensembles used in this work. Column 2 gives the number of configurations N_{cfg} times the number of sources N_{src} for a given ensemble. Column 3 gives the range of heavy quark masses (in lattice units), where the lightest option is chosen to be tuned to the physical charm quark mass. Column 4 gives the non-zero twist angles $\theta \neq 0.0$, which relate to three-momentum via equation 4.10; we note that all ensembles also have correlators with values of $\theta = 0$ as well. Finally, column 5 gives the range of source-sink separation values T. These parameters and statistics apply to both the $H \to \pi$ and $H_s \to K$ meson decays

ensemble	$N_{\text{cfg}} \times N_{\text{src}}$	am_h	$\theta \neq 0.0$	T
f5	500×16	0.450, 0.55, 0.675, 0.8	0.4281, 1.282, 2.1410, 2.570	15, 18, 21, 24
fphys	500×8	0.433, 0.555, 0.678, 0.8	0.58, 0.87, 1.13, 3.000	15, 18, 21, 24
sf5	500×8	0.274, 0.5, 0.65, 0.8	1.261, 2.108, 2.666, 5.059	22, 25, 28, 31
sfphys	100×4	0.2585, 0.5, 0.65, 0.8	2.522, 4.216, 7.94, 10.118	22, 25, 28, 31
uf5	375×4	0.194, 0.4, 0.6, 0.8	0.706, 1.529, 2.235, 4.705	29, 34, 39, 44

Table 6.3: Fractional uncertainties given to priors for ground state meson masses $\Delta(M)$ and amplitudes $\Delta(A)$. Heavy meson amplitude fractional uncertainties $\Delta(M_H)$ apply only to the lightest H meson option on each ensemble. The ratio $R(A_{m_3}/A_{m_0})$ is used in equation 4.16 to determine the fractional uncertainties of the heavier H meson amplitude priors. $\Delta(A^*)$ is the fractional uncertainty given to all non-ground state amplitude priors.

Ensemble	$\Delta(M_\pi)$	$\Delta(M_H)$	$\Delta(A_\pi)$	$\Delta(A_H)$	$R(A_{m_3}/A_{m_0})$	$\Delta(A^*)$
f5	0.05	0.05	0.05	0.11	2.0	5.0
fphys	0.10	0.05	0.05	0.22	2.0	6.1
sf5	0.10	0.05	0.10	0.10	4.0	2.6
sfphys	0.60	0.10	0.30	0.65	2.0	2.0
uf5	0.25	0.05	0.20	0.20	4.0	2.0

6.2 Correlator fits

In this section we present the specifications on our current set of $H \to \pi$ correlator fits, following the theory and methodology laid out in chapter 4. In our current correlator fits we model the data with $N_{\text{exp}} = 4$ exponentials, for both the oscillating and non-oscillating states. We follow the partitioned fit routine described in section 4.2 where we separate fitting three-point correlation functions into two separate parts based on the current insertion $J \in \{S, V^0\},\ \{V^1, T\}$.

6.2.1 Priors

Tables 6.3, 6.4, and 6.5 document the priors that go into our $H \to \pi$ correlator fits. These priors cover the uncertainties on meson energy and amplitude priors, and current insertion amplitude priors. As discussed in section 4.4, the central values of meson energy and amplitude priors are determined algorithmically, and the non-zero twist meson energy and amplitude priors are determined via dispersion relations. Priors not given here, such as the energy difference between radial excitations pion states, are discusses in chapter 4.

Table 6.4: $H \to \pi$ ground state three-point amplitude priors $P[J_{00}^{nn}]$ for all ensembles, twists θ, and current insertions $J \in \{S, V^0, V^1, T\}$. Twist is related to the pion's three-momentum $\vec{p}$ via equation 4.10. Methods for determining these priors are discussed in section 4.5.1.

Ensemble	θ	S	V^0	V^1	T
f5	0.0	2.6(2.6)	1.0(1.0)	-	-
	0.4281	2.4(2.4)	0.9(0.9)	0.15(0.15)	0.1(0.1)
	1.282	1.5(1.5)	0.6(0.6)	0.22(0.22)	0.15(0.15)
	2.1410	1.0(1.0)	0.5(0.5)	0.2(0.2)	0.12(0.12)
	2.570	0.8(0.8)	0.4(0.4)	0.2(0.2)	0.13(0.13)
fphys	0.0	4.75(4.75)	3.0(3.0)	-	-
	0.58	3.75(3.75)	2.5(2.5)	0.2(0.2)	0.15(0.15)
	0.87	3.25(3.25)	2.0(2.0)	0.25(0.25)	0.18(0.18)
	1.13	2.75(2.75)	1.5(1.5)	0.3(0.3)	0.15(0.15)
	3.000	1.50(1.50)	0.75(0.75)	0.25(0.25)	0.15(0.15)
	5.311	0.5(0.5)	0.25(0.25)	0.15(0.15)	0.1(0.1)
sf5	0.0	2.5(2.5)	2.0(2.0)	-	-
	1.261	1.75(1.75)	1.0(1.0)	0.3(0.3)	0.2(0.2)
	2.108	1.25(1.25)	0.65(0.65)	0.25(0.25)	0.2(0.2)
	2.666	1.0(1.0)	0.6(0.6)	0.25(0.25)	0.2(0.2)
	5.059	1.0(5.0)	1.0(4.0)	1.0(4.0)	0.2(3.0)
sfphys	0.0	4.75(4.75)	4.0(4.0)	-	-
	2.522	1.75(1.75)	1.25(1.25)	0.35(0.35)	0.2(0.2)
	4.216	1.5(1.5)	1.0(1.0)	0.35(0.35)	0.25(0.25)
	7.94	1.0(1.5)	0.5(1.0)	0.3(0.3)	0.2(0.2)
	10.118	1.0(3.0)	0.5(2.0)	0.3(1.0)	0.2(1.0)
uf5	0.0	2.75(2.75)	2.0(2.0)	-	-
	0.706	2.25(2.25)	1.5(1.5)	0.25(0.25)	0.2(0.2)
	1.529	1.5(1.5)	1.0(1.0)	0.3(0.3)	0.20(0.2)
	2.235	1.0(1.0)	0.75(0.75)	0.3(0.3)	0.20(0.2)
	4.705	1.0(1.0)	1.0(2.0)	0.3(1.0)	0.2(0.5)

Table 6.5: $H \to \pi$ prior absolute uncertainties for all ensembles, for all oscillating and or non-ground state fit parameters $J_{ij}^{kl} \neq J_{00}^{oo}$, for $J \in \{S, V^0, V^1, T\}$. The notation $J_{\neq 0}$ indicates the values used to assign priors to all higher order exponential states $J_{ij\neq 00}^{kl}$. The notation J_{osc} indicates the values used to assign priors to all lowest lying oscillating states $J_{00}^{kl\neq nn}$. Central values given to all associated priors are equal to 0.0. A special prior uncertainty scaling term σ_{ens} for each ensemble, which we discuss in section 4.5.2, is given in final column. The scaling term applies to select non-ground state three point amplitudes J_{00}^{on} and J_{10}^{kl} for all $k, l \in \{n, o\}$.

Ensemble	$S_{\neq 0}$	S_{osc}	$V^0_{\neq 0}$	V^0_{osc}	$V^1_{\neq 0}$	V^1_{osc}	$T_{\neq 0}$	T_{osc}	σ_{ens}
f5	0.5	1.75	0.7	3.5	0.1	0.22	0.07	0.12	1.8
fphys	1.43	4.4	1.0	10.0	0.21	0.06	0.08	0.12	2.2
sf5	0.32	1.4	0.46	3.0	0.10	0.23	0.05	0.25	4.0
sfphys	0.45	3.0	0.55	5.0	0.04	0.5	0.04	0.07	5.5
uf5	0.30	0.60	0.32	3.0	0.04	0.08	0.04	0.07	5.0

In later stages of this project we noticed that, on the fphys ensemble, the fit posterior for the discretization parameter ε^{π} consistently differed from its prior by one or several standard deviations. This prompted us to apply the standard $\log(\mathrm{GBF})$ testing routine discussed in 4.3 to $P[\varepsilon^{\pi}]$ uncertainties for all our ensembles, which before were universally set as $P[\varepsilon^{\pi}] = 0.0(1.0)$. In the case where this testing favored prior uncertainties smaller ± 1.0, we ended the testing routine and stuck with the more conservative $P[\varepsilon^{\pi}] = 0.0(1.0)$. This was the case for all other (not fphys) $P[\varepsilon^{\pi}]$ uncertainties, and so those discretization parameter priors remain as $P[\varepsilon^{\pi}] = 0 \pm 1$.

At the time, there was an additional twist angle $\theta = 5.311$ on the fphys ensemble, with corresponding two and three-point correlators which were included in our fit. With this additional twist option, the $\log(\mathrm{GBF})$ preferred uncertainty of $P[\varepsilon^{\pi}]$ was ± 36. The test fits with this prior gave posterior values of $\varepsilon^{\pi} = 6(13)$. We saw similar behavior in $H_s \to K$ correlator fits, where the $\log(\mathrm{GBF})$ preferred uncertainty of $P[\varepsilon^{K}]$ was ± 50. This nearly unbounded fit parameter coincided with $\theta = 5.311$ pion energy and amplitude posteriors with very large uncertainties, and central values which still differed from their priors by several standard deviations. Furthermore, in dispersion relation test plots like those in figure 6.1, the $\theta = 5.311$ pion energy and amplitude points consistently deviated from the expected range by several standard deviations. After numerous correlator test fits, the outputs of which we investigated thoroughly, we were unable to identify the origin of this discrepancy. This anomalous behavior was not in line with our expectations, even after considering lattice discretization effects. We experimented with removing $\theta = 5.311$ correlators from test fits, and after testing we found that the $\log(\mathrm{GBF})$ preferred uncertainty of ε^{π} was now ± 2.0, with posterior values of $\varepsilon^{\pi} = 1.31(90)$. For these reasons we decided to omit $\theta = 5.311$ correlators from our correlator fits. It is possible that there was a problem in the generation of correlator data with that twist option, though we do not completely rule out the possibility of there being some undiscovered problem in our fit routine. In the future we hope to address and resolve this anomaly, and for now we exclude those data from our fit.

6.2.2 Results

Here we can summarize the key results from our $H \to \pi$ correlator fits. In table 6.6 we present parameters which determine the quality of fit for our set of correlator fits, including each fit's χ^2/d.o.f. and log(GBF). Overall, we find that nearly all ground state fit posteriors are determined to be within their priors. We only see a minor disagreement of $> 1\sigma$ in three tensor current insertion amplitudes on the fphys ensemble. These tensor current insertion amplitudes correspond to a twist angle of $\theta = 1.13$, and heavy quark masses $am_h = 0.555$, 0.678, and 0.8. These parameters all have priors equal to $0.15(15)$, which were determined from visually assessing effective amplitude plots. Meanwhile their posteriors as determined by the fitter were $T^{\theta=1.13}_{am_h=0.555} = 0.3068(93)$, $T^{\theta=1.13}_{am_h=0.678} = 0.328(11)$, and $T^{\theta=1.13}_{am_h=0.8} = 0.345(13)$. All three of these offending parameters share the same twist angle, which is possibly indicative of their disagreement having a shared origin. The corresponding $\theta = 1.13$ ground state pion energy from this fit has a posterior which agrees with its prior, and so we do not believe that is where the problem lies. Instead, we find that these ground state amplitudes T^{nn}_{00} have comparable magnitudes to their corresponding excited state amplitudes T^{nn}_{10}. For example, in the $am_h = 0.8$ case we have $T^{nn}_{00} = 0.345(13)$ and $T^{nn}_{10} = -0.346(53)$. This large and well resolved excited state contribution likely obscured the true ground state signal in the corresponding effective amplitude plot, form which the ground state parameter's prior was determined. We therefore do not believe this disagreement jeopardizes the quality of our correlator fits.

For all but one of our ensembles, the value of χ^2/d.o.f. in one half of the fit is approximately equal to that of the other half. The outlier case is the fphys ensemble, where the χ^2/d.o.f. in the $\{S, V^0\}$ fit half is more than three times that of the $\{V^1, T\}$ half. Digging into those correlator fit results, we find that the two and three point correlators which contain a zero three-momentum pion are poorly modeled by the fit, at least in comparison to the other modeled correlation functions. Recall from section 4.6 that we identified spurious state behavior in the $E^{i=1}$ pion mass on this ensemble.

Table 6.6: Holistic fit quality parameters for our current set of $H \to \pi$ correlator fits. Per ensemble we partition our correlator fits into two halves based on which current insertions $J \in \{S, V^0, V^1, T\}$ are included. The degrees of freedom (d.o.f.), the χ^2/d.o.f., and the log(GBF) of each fit are given in columns 3, 4, and 5. We note this is the augmented χ^2 as defined in equation 4.3. All fits have a quality factor $Q = 1$. Section 4.8 discusses the significance of a fit's χ^2/d.o.f., quality factor, and log(GBF) in detail.

Ensemble	Current pair	d.o.f.	χ^2/d.o.f.	log(GBF)
f5	$\{S, V^0\}$	3518	0.155	75279
	$\{V^1, T\}$	2990	0.142	67885
fphys	$\{S, V^0\}$	3562	0.493	67741
	$\{V^1, T\}$	3034	0.159	64912
sf5	$\{S, V^0\}$	4686	0.082	119548
	$\{V^1, T\}$	3998	0.078	108046
sfphys	$\{S, V^0\}$	4975	0.023	112864
	$\{V^1, T\}$	4223	0.031	103046
uf5	$\{S, V^0\}$	7086	0.056	194028
	$\{V^1, T\}$	6014	0.067	174055

Though our treatment of removing that spurious state did improve fit results, it is possible that the poor correlator modeling is still reflective of some unresolved consequence of that spurious state. Like the issue of the $\theta = 5.311$ twist option on the fphys ensemble, we recognize this poor modeling as an item to address in the future.

One additional method of testing the quality of our correlator fits is to evaluate how well the pion energies and amplitudes as determined by the fitter follow their expected dispersion relations (equations 4.12 and 4.17). We carry out this test by analyzing dispersion relation plots, like those of figure 6.1. In these plots we compare fit posteriors to the dispersion relation expectations as a function of $|a\vec{p}|^2$. To account for discretization effects, we generally expect the plotted data to lie within the area bound by the functions $y = 1 \pm \left(\frac{a\vec{p}}{\pi}\right)^2$. We find that, overall, the non-zero twist pion energy and amplitudes follow the expected behavior well. One slight outlier case if that of the uf5 ensemble, where we see some data which differed from our expectation by two to three standard deviations.

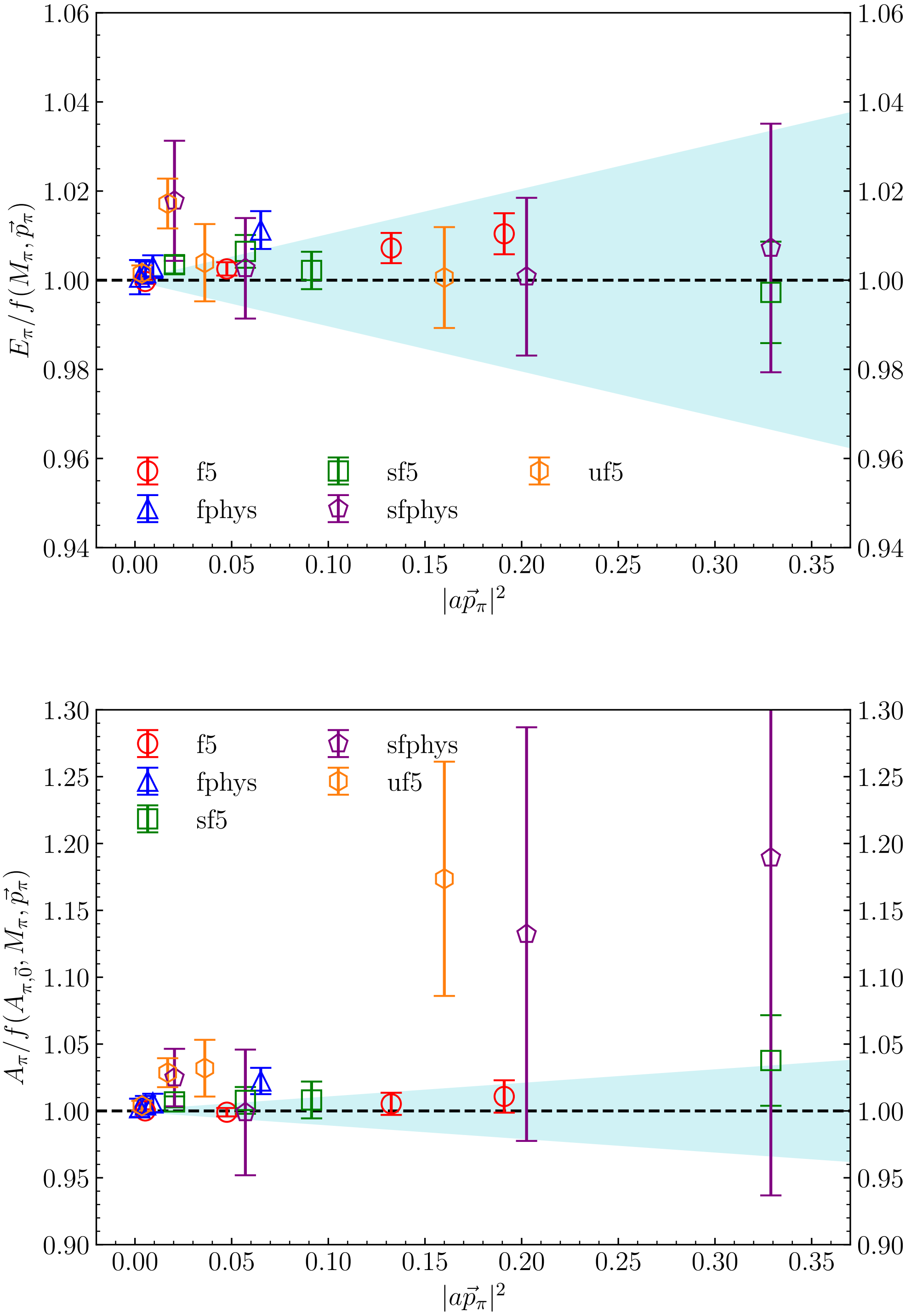

Figure 6.1: Energy (top) and amplitude (bottom) dispersion relation plots for current set of $H \to \pi$ correlator fits. Data shown are ground state, non-zero twist energy and amplitude fit posteriors divided by a function equal to the right hand side of either equation 4.12 (energy) or equation 4.17 (amplitude) without the discretization factor. The shaded cyan corresponds to the area bound by the functions $y = 1 \pm \left|\frac{a\vec{p}}{\pi}\right|^2$.

6.3 z-expansion fits

Having examined the current status of our correlator fits, we can carry forward the necessary fit parameters into our modified z-expansion, which is how we eventually arrive at $D \to \pi$ and $B \to \pi$ continuum form factors. We discuss the general methodology of calculating form factors this way in chapter 5. We perform our modified z-expansion under the BCL parameterization where $N = 3$, such that $N - 1 = 2$ is the maximum polynomial order of f_0, and $N = 3$ is the maximum polynomial order of f_+ and f_T.

6.3.1 Priors

Across sections and 5.2.2 and 5.2.3 we discuss how we assign priors to the coefficients and parameters which appear in our modified z-expansion, and we will summarize those prior assignments here. First, in equation 5.13 we see the parameter $N_{ijkl} \equiv (N_i, N_j, N_k, N_l)$, which determines the maximum order of associated terms that appear in the z-expansion coefficients. Among other things, this number determines the number of coefficients $d_{ijkln}^{0,+,T}$ which need priors in our fit. In testing, we find through $\log(\mathrm{GBF})$ testing that a value of $N_{ijkl} = (3, 2, 2, 3)$ is generally preferred, through the fits are not significantly sensitive to individual changes of ± 1 to j, k, or l. In table 6.7 we give the complete set of priors we assign to the parameters in our z-expansion fit.

In addition to these fit parameters, it is important to note that many correlator fit outputs serve as priors in our z-expansion fit. These parameters include the various heavy meson masses (with different heavy quark masses) and the energies of pions with varying momenta. These terms are required to define the physical q^2 range where $q^2 = (M_H^2 + M_\pi^2 - 2M_H E_\pi)$. We do not expect the z-expansion fit posteriors of these terms to vary from their priors; any such deviation would likely

Table 6.7: Priors assigned to z-expansion fit parameters. Many parameters have priors which share the same value as the priors of other parameters (e.g. $P[\rho_0^+]$, $P[\rho_0^T] = 0.0(1.0)$). In all cases, every prior is a separate gvar object which only corresponds to one parameter. These priors are applicable for both our $H \to \pi$ and $H_s \to K$ fits.

Parameter	Prior
g_∞	0.48(11)
C_1	0.5(1.0)
C_2	0.0(3.0)
$\rho_n^{0,+,T}$	0.0(1.0)
$d_{i10ln}^{0,+,T}$	0.0(3)
$d_{i01ln}^{0,+,T}$	0.0(3)
Other $d_{ijkln}^{0,+,T}$	0.0(1.0)
ζ_0	1.5(5)
$c_{s,n}^{\text{val},0,+,T}$	0.0(1.0)
$c_{s,n}^{\text{sea},0,+,T}$	0.0(5)
$c_{l,n}^{\text{sea},0,+,T}$	0.0(5)
$c_{c,n}^{\text{sea},0,+,T}$	0.0(1)

be indicative of some systematic problem in either fit. Similarly, there are also terms which enter the fit as `gvar` objects, such as physical meson masses. Because they are `gvar` objects, they are technically treated as priors in the fit, and we likewise do not expect the fit posteriors of these terms to vary in any significant way from their priors.

6.3.2 Results

In the next section we will present our current physical continuum form factors for both the $D \to \pi$ and $B \to \pi$ meson decays. Here we discuss the results of the z-expansion fit in the context of fitting the more general $H \to \pi$ decay, with lattice artifacts included.

We find the overall quality of our $H \to \pi$ fit to be good. With 340 degrees of freedom, the fit has a $\chi^2/\text{d.o.f.} = 0.306$, a Q value equal to one, and a $\log(\text{GBF}) = 574$. Like the case of correlator fitting, this χ^2 term is augmented by our Bayesian fitting approach. Nearly all fit posteriors fall within the ± 1 standard deviation bounds of their priors. The few instances where this is not the case include the parameters $d^{+}_{00002} = -1.51(38)$, and $d^{T}_{00002} = -1.60(46)$, whose priors are both $0.0(1.1)$. Though this discrepancy is less than only two standard deviations, these parameters do inform the shape of our form factor plots in a noticeable way. Of all the terms that compose the $a_n^{0,+,T}$ coefficients in equation 5.13, the coefficients $d^{0,+,T}_{ijkln}$ are the most deterministic contributors. Furthermore, from equation 5.30 we know that in the continuum limit, the only $d^{0,+,T}_{ijkln}$ coefficients which make up $a_n^{0,+,T,(\mathrm{cont.})}$ are those for which $(j,k,l) = (0,0,0)$, which is true for these disagreeing fit posteriors of interest: d^{+}_{00002} and d^{T}_{00002}. The corresponding a_2^{+} and a_2^{T} terms will likewise be negative and of order one rather than zero. When plotting form factors against $z(q^2)$, these coefficients multiply the z^2 terms, and so we would expect to see a negative quadratic shape in any function of z. In figures 6.2-6.5 we present scalar, vector, and tensor form factor plots as functions of z, with continuous best fit functions for lattice form factor data. In the vector and tensor plots, this anticipated negative curvature is clearly visible.

The other two fit posteriors which differ from their priors by more than one (but less than two) standard deviations are the energies of the fphys $\theta = 0.0$ pion energy and the uf5 $\theta = 1.529$ pion energy. The states of these two parameters do not immediately imply any behavior in our form factor plots, nor do they necessarily jeopardize the quality of the z-expansion fit. We already recognized that the zero twist pion energy corresponded to poor correlation function modeling in our correlator fit, so it is not unexpected to see that problem manifest in our z-expansion fit. We note these instances for completeness sake, and leave our analysis open to these posteriors changing with the addition of more data and corrections to our fit routines in the future.

In addition to plotting form factors against z or q^2, our z-expansion also allows us to see how form factors vary with the heavy meson mass M_H. In figure 6.6 we plot the continuum values of $f_{0,+,T}(q^2 = 0, M_H)$ and $f_{0,+,T}(q^2 = q^2_{\mathrm{max}}, M_H)$ as we vary M_H between the physical masses of the D and B mesons. As discussed in section 5.1.2, the tensor form factor has energy scale μ dependence, and we perform our z-expansion at the energy scale $\mu = 4.8$ GeV. For $D \to \pi$ we multiply $f_T(q^2, \mu = 4.8\ \mathrm{GeV})$ by the factor $\Gamma = 1.0773(17)$ so that our results are appropriate for the D meson energy scale of $\mu = 2.0$ GeV. In making figure 6.6 we linearly interpolate Γ, which multiplies $f_T(q^2, \mu = 4.8\ \mathrm{GeV}, M_H)$, from $1.0773(17) \to 1$ as we vary M_H from $M_D^{\mathrm{phys}} \to M_B^{\mathrm{phys}}$.

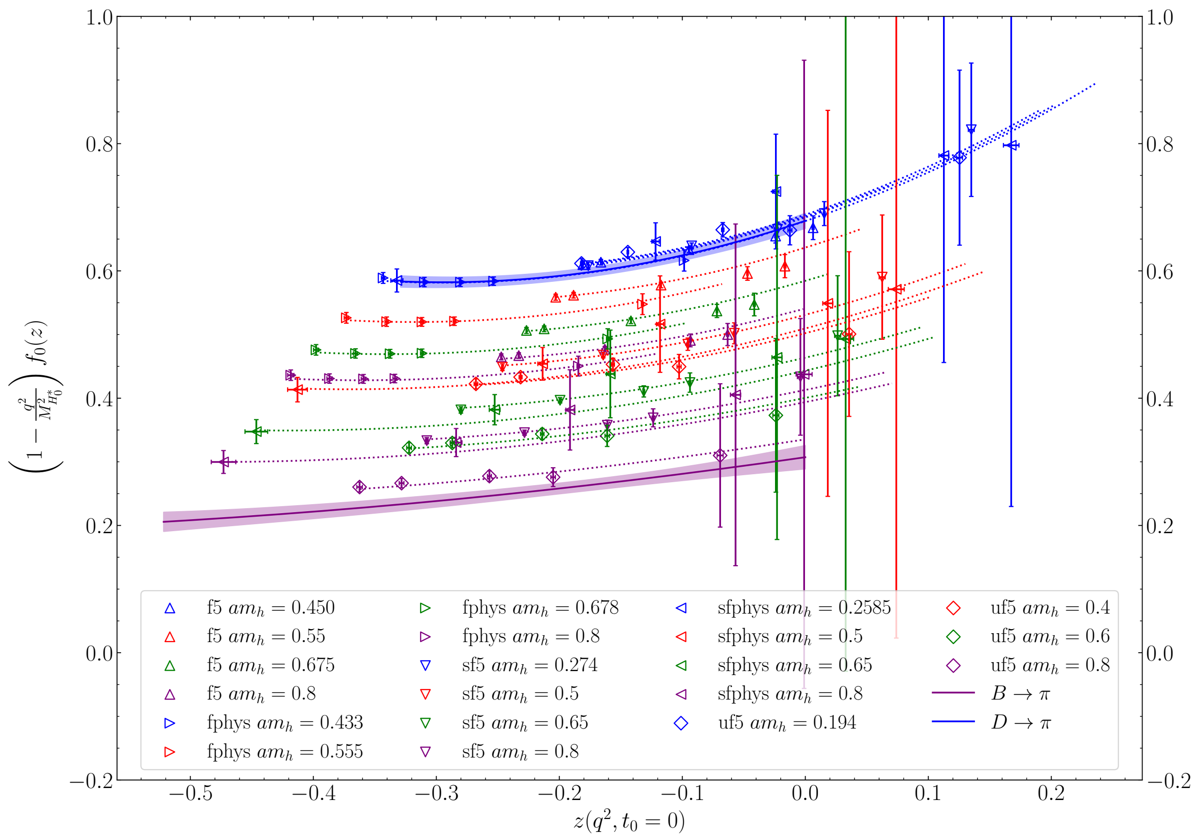

Figure 6.2: $H \to \pi$ modified z-expansion scalar form factor plot. Plotted data correspond to correlator fit results of varying heavy quark mass am_h on each ensemble. Continuous dotted lines represent the z-expansion line of best fit for a given heavy quark mass and ensemble, with all lattice artifacts still present. Continuous solid lines correspond to physical continuum fit of either $D \to \pi$ or $B \to \pi$ as a function of z.

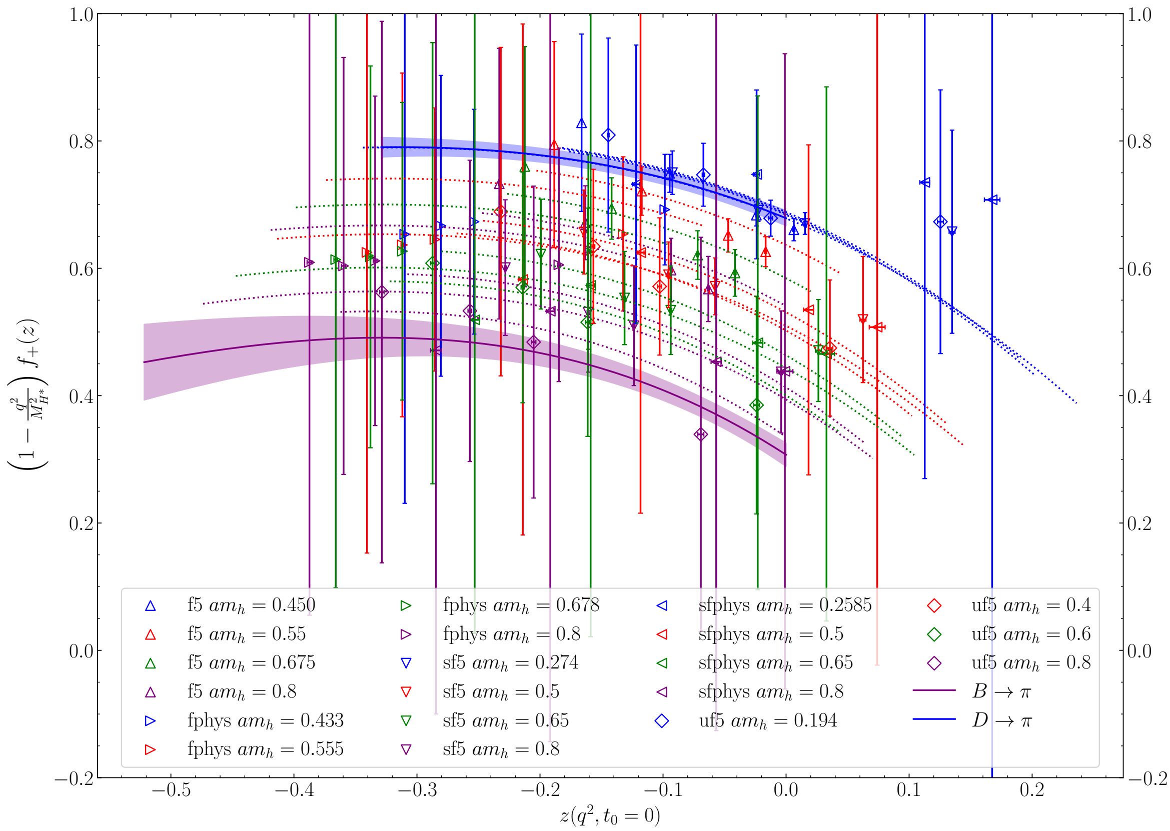

Figure 6.3: $H \to \pi$ modified z-expansion temporal vector form factor plot. Plotted data correspond to correlator fit results of varying heavy quark mass am_h on each ensemble. Continuous dotted lines represent the z-expansion line of best fit for a given heavy quark mass and ensemble, with all lattice artifacts still present. Continuous solid lines correspond to physical continuum fit of either $D \to \pi$ or $B \to \pi$ as a function of z. Continuous curves are informed by both temporal and spatial vector data, and are therefore the same curves present in figure 6.4.

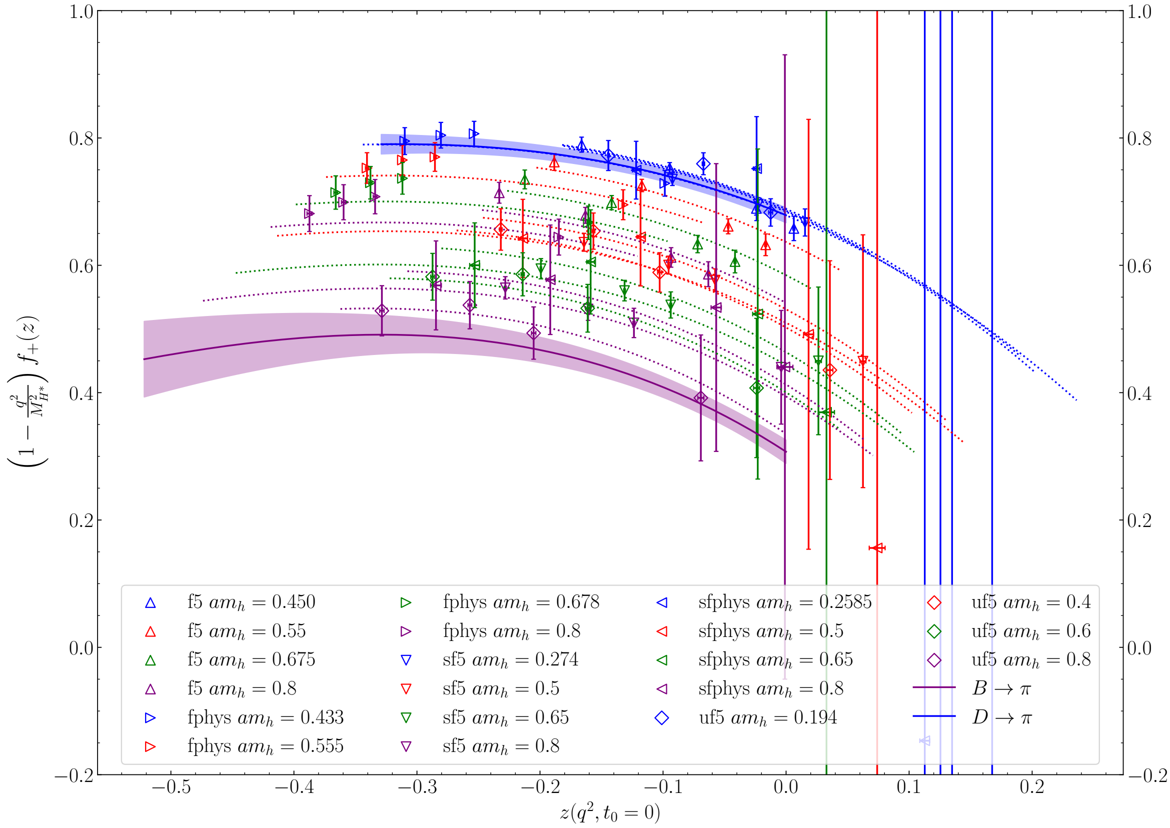

Figure 6.4: $H \to \pi$ modified z-expansion spatial vector form factor plot. Plotted data correspond to correlator fit results of varying heavy quark mass am_h on each ensemble. Continuous dotted lines represent the z-expansion line of best fit for a given heavy quark mass and ensemble, with all lattice artifacts still present. Continuous solid lines correspond to physical continuum fit of either $D \to \pi$ or $B \to \pi$ as a function of z. Continuous curves are informed by both temporal and spatial vector data, and are therefore the same curves present in figure 6.3.

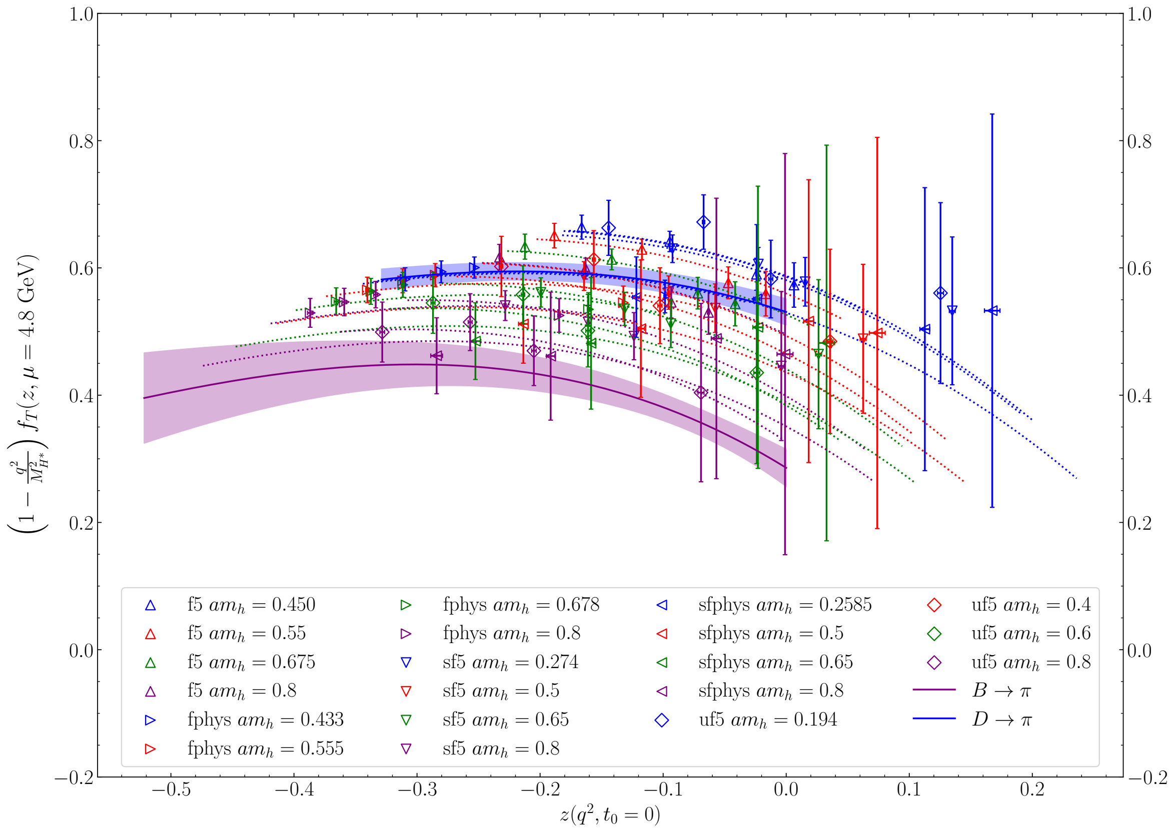

Figure 6.5: $\boldsymbol{H \to \pi}$ modified z-expansion tensor form factor plot. Plotted data correspond to correlator fit results of varying heavy quark mass $\boldsymbol{am_h}$ on each ensemble. Continuous dotted lines represent the z-expansion line of best fit for a given heavy quark mass and ensemble, with all lattice artifacts still present. Continuous solid lines correspond to physical continuum fit of either $\boldsymbol{D \to \pi}$ or $\boldsymbol{B \to \pi}$ as a function of z.

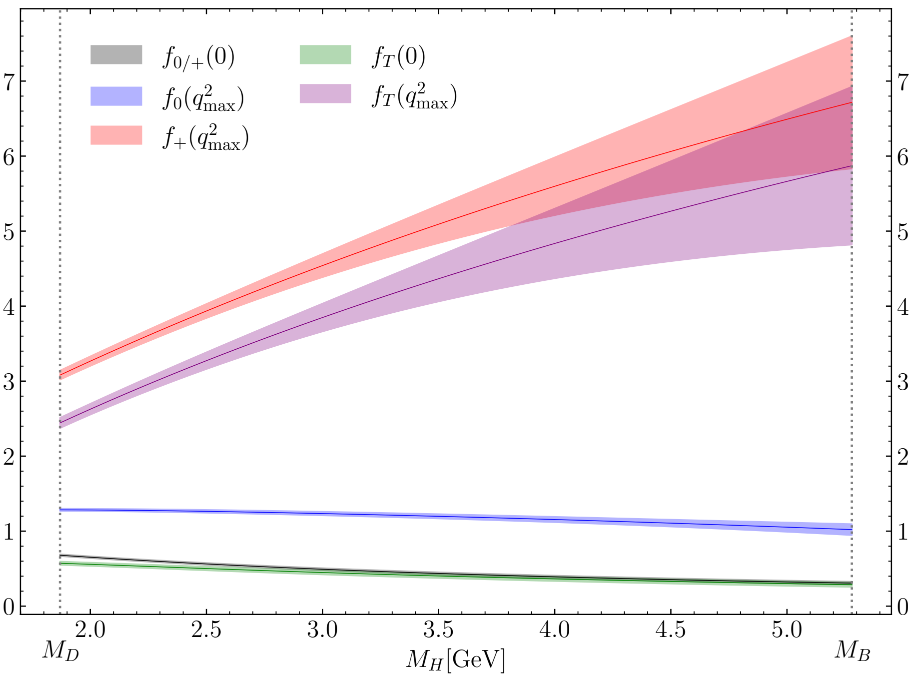

Figure 6.6: $H \to \pi$ continuum scalar, vector, and tensor form factors at $q^2 = 0$ and $q^2 = q^2_{\text{max}}$, where the heavy meson mass M_H varies between the mass of the D and B mesons. See text for how we scale $Z(\mu)$ for all M_H between M_D^{phys} and M_B^{phys}.

This linear interpolation is an approximation, and in the future we aim to implement the full functional dependence of $\mu(M_H)$ discussed in [3]. In this plot we can see how the vector and tensor form factors are consistent with each other at the M_B^{phys} end of the mass spectrum, while they decouple as $M_H \to M_D^{\text{phys}}$. This behavior is consistent with our standard model expectation that the tensor form factor becomes equivalent to the vector form factor in the heavy quark limit of $m_h \to \infty$.

6.4 Status of form factor calculations

Here we present the current status of both our $D \to \pi$ and $B \to \pi$ form factor calculations. This includes physical continuum form factor plots, general comparisons to other works, and discussion of where we expect improvements with the generation of more data over the next year by HPQCD.

Table 6.8: Physical continuum $D \to \pi$ z-expansion coefficients $a_n^{0,+,T}$, pole masses (in GeV), and chiral logarithm terms, presented alongside their corresponding correlation matrix. Using equations 5.27-5.29 these parameters can be used to reconstruct our current $D \to \pi$ form factor plots (figures 6.7 and 6.8).

$a_0^{0/+}$	a_1^0	a_2^0	a_1^+	a_2^+	a_0^T	a_1^T	a_2^T	$M^{\text{phys}}_{D_0^*}$	$M^{\text{phys}}_{D^*}$	$\mathscr{L}$
0.656(16)	0.632(73)	1.07(14)	-0.767(88)	-1.60(31)	0.515(21)	-0.61(14)	-1.71(41)	2.3430(99)	2.006850(50)	1.035(15)
1	0.67717	0.5507	0.12902	0.01262	0.31939	-0.06624	-0.0885	-0.02614	-0.00037	-0.68604
	1	0.89927	0.52392	0.29252	0.13505	0.02575	-0.00356	-0.23508	-0.00096	-0.15973
		1	0.5216	0.33013	0.10727	0.03467	0.01308	0.02504	-0.00051	-0.12391
			1	0.83202	-0.15224	0.05695	0.07633	-0.01964	-0.00182	0.3031
				1	-0.1468	0.01701	0.08564	-0.01106	0.00271	0.22852
					1	0.53111	0.27084	-0.00727	-0.00041	-0.38754
						1	0.87212	-0.00118	-0.0013	0.13011
							1	-9e-05	0.00116	0.13059
								1	0.00195	0.0122
									1	0.00014
										1

6.4.1 $D \to \pi$

Following from our modified z-expansion fit, we can recover physical continuum $D \to \pi$ form factors by setting $M_H = M_D^{\text{phys}}$ in equations 5.27-5.29. In doing so, we arrive at the coefficients, pole masses, and chiral logarithm term we provide in table 6.8. With these parameters we can finally construct physical continuum $D \to \pi$ form factors, which we plot as a function of z and of q^2 in figures 6.7 and 6.8 respectively.

Considering that this line of form factor calculations remains in progress, we do not make any rigorous comparisons to other similar $D \to \pi$ lattice form factor calculations. We will however make the general statement that the large negative curvature of the vector form factor as a functions of z (which is evidently on display in figure 6.7), is not found in the Fermilab Lattice and MILC Collaborations' related $D \to \pi$ calculation [4]. Similarly, our current values of the coefficients $a_0^{0,+}$ do not align well with those found in the same work.[1] In table 6.9 we compare our $D \to \pi$ form factor results at $q^2 = 0$ and $q^2 = q^2_{\text{max}}$ to those of Fermilab/MILC. The FLAG average takes into account $D \to \pi$ results from multiple lattice groups, including those of Fermilab/MILC however the Ferm-

1. The direct comparison of the coefficients $a_n^{0,+}$ is enabled by the fact that Fermilab/MILC also use $t_0 = 0$ in their z-expansion.

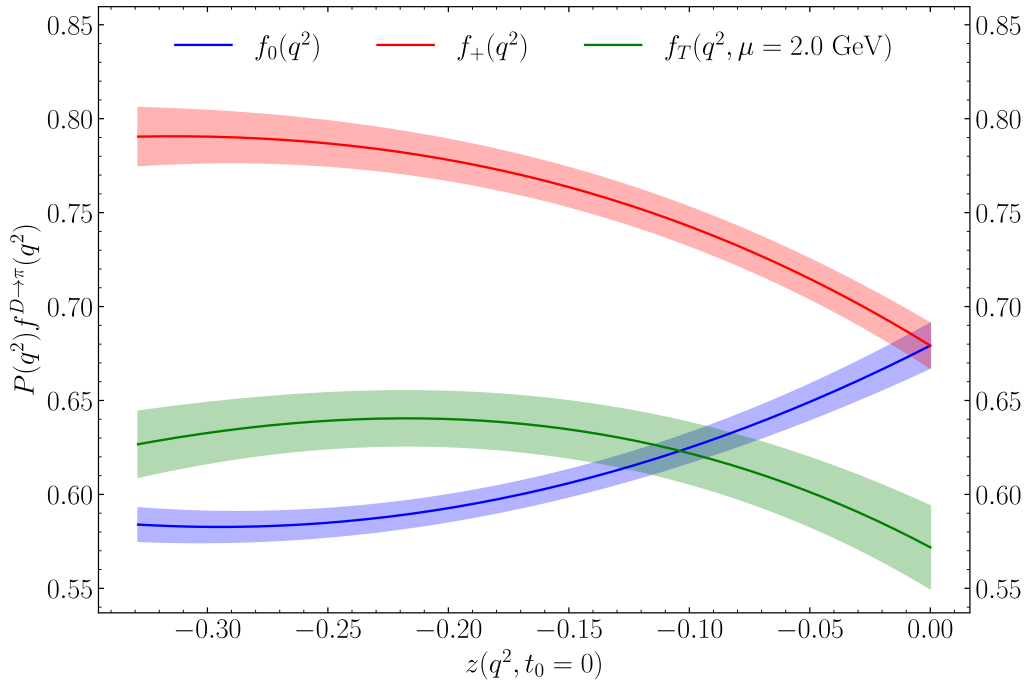

Figure 6.7: Current continuum $D \to \pi$ scalar, vector, and tensor form factors, multiplied by the appropriate pole term $P(q^2)$ (defined in equations 5.24 and 5.26). Results span the entire physical q^2 range.

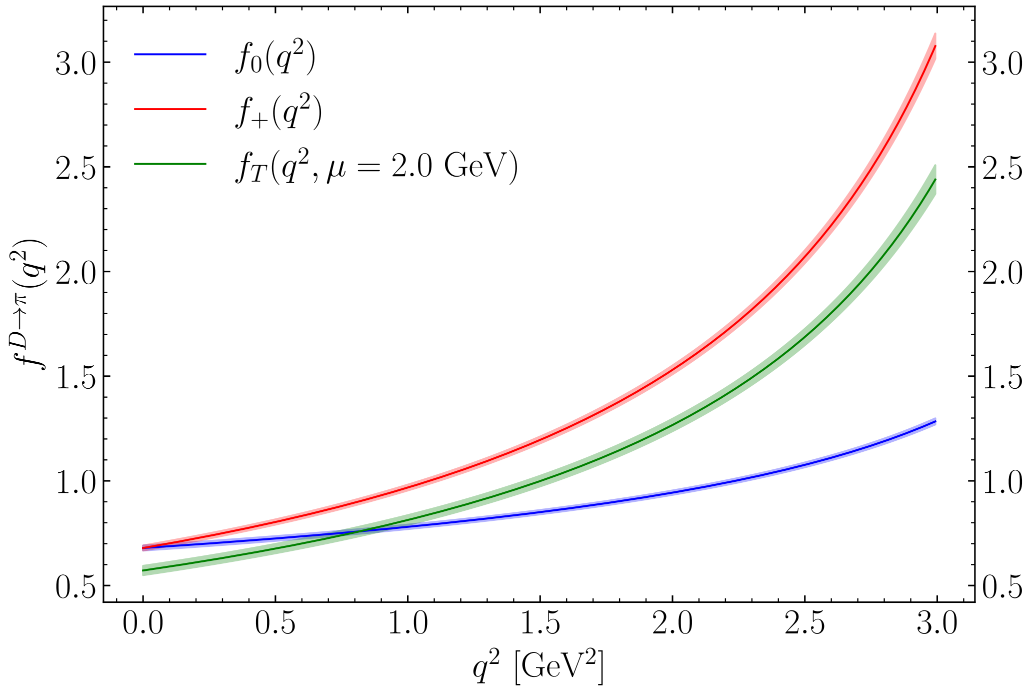

Figure 6.8: Current continuum $D \to \pi$ scalar, vector, and tensor form factors. Results span the entire physical q^2 range.

Table 6.9: Comparison of our current $D \to \pi$ form factor results to those of Fermilab/MILC [4] at $q^2 = 0$ and $q^2 = q^2_{\mathrm{max}}$. Fermilab/MILC does not calculate tensor form factors. The difference in standard deviations σ between our results and those of Fermilab/MILC is given in row 3, while the ratio of errors is given in row 4.

Form factor	$f_{0/+}(0)$	$f_T(0)$	$f_0(q^2_{\mathrm{max}})$	$f_+(q^2_{\mathrm{max}})$	$f_T(q^2_{\mathrm{max}})$
This work [a]	0.679(12)	0.572(22)	1.284(15)	3.077(60)	2.440(68)
Fermilab/MILC [b]	0.6300(51)	-	1.2783(61)	3.119(57)	-
$\lvert \mathrm{Mean}(a-b)/\sigma(a-b)\rvert$	3.758	-	0.352	0.507	-
$\sigma(a)/\sigma(b)$	2.353	-	2.459	1.052	-

ilab/MILC data which contributes to the FLAG average have smaller uncertainties than the other contributing data, and so we choose to compare our current results to those of Fermilab/MILC directly. We find that our $f_{0,+}(q^2_{\mathrm{max}})$ results are consistent with those of Fermilab/MILC, however there is a difference of $\approx 3.8\sigma$ between our results and theirs for $f_{0/+}(0)$.

Having now called attention to the Fermilab/MILC $D \to \pi$ results, we wish to reiterate to the reader that this line of lattice calculations, up until its current status and into the future, is carried out independently of the Fermilab/MILC collaborations calculation. At no point have we altered or corrected out lattice calculations such that their results are more in line with those in [4]. Our line of calculations is still ongoing, a handful of problems, detailed in this chapter, remain in either our correlator and z-expansion fits, and so we do not make any significant comparisons beyond general observations.

One such general observation we can make is to notice the difference between the vector and tensor form factors in figure 6.8. As mentioned in the previous section, we expect the vector and tensor form factors to decouple away from the heavy mass limit, and so the difference between the two we find here is expected. We can also see that $f_T < f_+$ across the entire range of q^2, which is not the case for our $D_s \to K$ results (which we discuss in the next chapter).

As a final check to our $D \to \pi$ form factors results, we performed a series of $H \to \pi$ fits with a subset of the available data. In these fits, we only included two and three-point correlator data which corresponded to values of $am_h \approx am_c$. we did this with the aim of ruling out the possibility that fitting $am_h > am_c$ data could unduly influence our determination of $D \to \pi$ form factors. After conducting this check, we found that excluding $am_h > am_c$ data from our correlator and z-expansion fits had no significant effect on $D \to \pi$ form factor results. In particular, the values of $f_{0,+,T}$ at $q^2 = 0$ and $q^2 = q^2_{\mathrm{max}}$ determined from this smaller fit were consistent with those of our global fit (which are given in the first row of table 6.9).

In the future continuation of this work, we intend to perform a separate z-expansion fit using the BGL parameterization. Under this parameterization and the appropriate outer function, we can directly enforce that the coefficients analogous to $a_n^{0,+,T}$ in the BCL parameterization are of order one or less. This is powerful constraint that we cannot directly enforce under the BCL parameterization. Seeing as all $|a_2^{0,+,T}| \geq 1$ in table 6.8, we anticipate that a BGL parameterization of the z-expansion will yield interesting results for comparison. The necessary outer functions in the BGL parametrization require the calculation of *susceptibilities* as inputs, and we are actively working on that calculation.

6.4.2 $B \to \pi$

Let us now move on to discuss our current $B \to \pi$ results, which can be constructed by the parameters given in table 6.10. Like the case of $D \to \pi$, we can observe that the magnitude of our $a_2^{+,T}$ coefficients are greater than two, which manifests as the pronounced negative curvature of the vector and tensor form factors (as function of z) found in figure 6.9. Unlike our $D \to \pi$ results, we can see that the coefficients a_n^+ and a_n^T are largely consistent with each other, the consequences of which manifest as overlapping continuous functions of f_+ and f_T across the entire q^2 range in figures 6.9 and 6.10.

Table 6.10: Physical continuum $B \to \pi$ z-expansion coefficients $a_n^{0,+,T}$, pole masses (in GeV), and chiral logarithm terms, presented alongside their corresponding correlation matrix. Using equations 5.27-5.29 these parameters can be used to reconstruct our current $B \to \pi$ form factor plots (figures 6.9 and 6.10).

$a_0^{0/+}$	a_1^0	a_2^0	a_1^+	a_2^+	a_0^T	a_1^T	a_2^T	$M_{B_0^*}^{\text{phys}}$	$M_{B^*}^{\text{phys}}$	$\mathscr{L}$
0.297(18)	0.27(12)	0.15(18)	-1.21(18)	-2.45(58)	0.277(28)	-1.15(32)	-2.46(90)	5.7553(99)	5.32475(20)	1.0357(78)
1	0.86414	0.73745	0.48484	0.24895	0.39804	0.1726	0.10758	-0.00967	-0.00112	-0.04264
	1	0.94155	0.53328	0.28059	0.37896	0.17659	0.11258	-0.0156	-0.00144	0.03553
		1	0.49763	0.27863	0.31972	0.15338	0.09784	0.04263	-0.00112	0.04447
			1	0.81564	0.09954	0.09536	0.08105	-0.0162	-5e-05	0.12869
				1	0.02328	0.04555	0.05776	-0.01335	0.00551	0.10747
					1	0.67375	0.48202	-0.00075	-0.00048	-0.00633
						1	0.8887	-0.00059	0.00034	0.07907
							1	-0.00059	0.00356	0.06093
								1	-6e-05	0.00637
									1	0.00036
										1

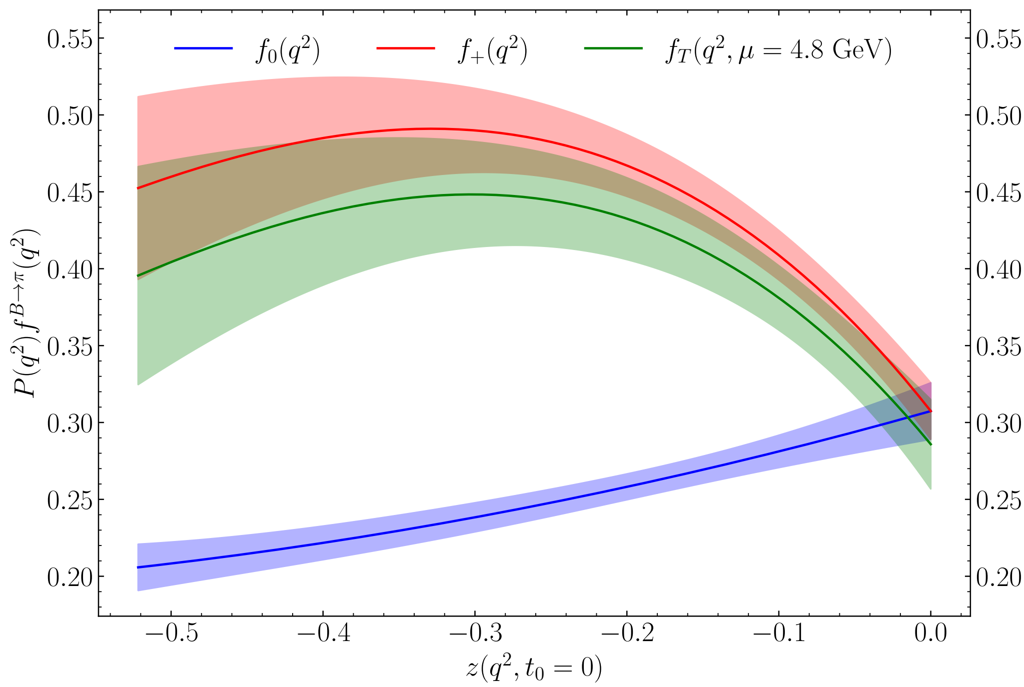

Figure 6.9: Current continuum $B \to \ \pi$ scalar, vector, and tensor form factors, multiplied by the appropriate pole term $P(q^2)$ (defined in equations 5.24 and 5.26). Results span the entire physical q^2 range.

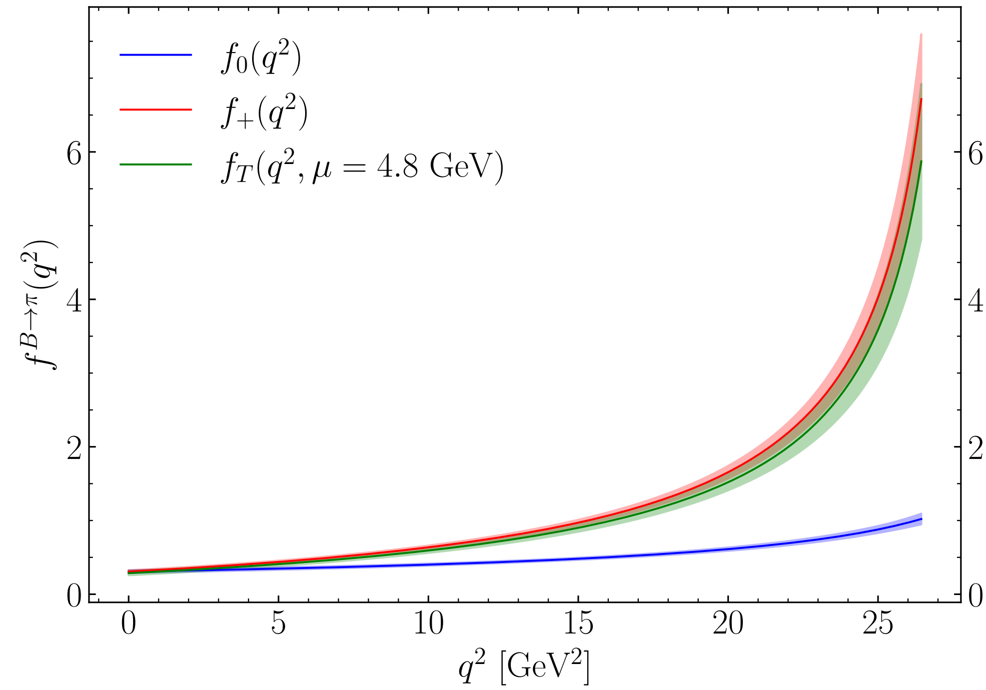

Figure 6.10: Current continuum $B \to \pi$ scalar, vector, and tensor form factors. Results span the entire physical q^2 range.

FLAG provides their current average of $B \to \pi$ form factors results in [7]. This average incorporates lattice calculations which follow different methodologies, such as separating continuum and chiral extrapolations into different fits. They also differ in gluon field ensembles specifications, such as the number of quark flavors in the sea or choice of quark/gluon action. Again, we do not wish to jeopardize the independence of our own results, but we note that the FLAG average of $f_+^{B\to\pi}(z(q^2))$ does not exhibit the relatively large negative curvature on display in figure 6.9. Independent of observing the FLAG average, we already recognize that the current values of a_n^+ and a_n^T might be indicative of a systemic problem in our fits, and we plan to address that problem moving forward. Like in our $D \to \pi$ results, we expect the forthcoming BGL parameterization to make improvements to our current form factors in this regard.

Table 6.11: Comparison of our current $B \to \pi$ form factor results to those of Fermilab/MILC [5, 6] at $q^2 = 0$ and $q^2 = q^2_{\text{max}}$. The difference in standard deviations σ between our results and those of Fermilab/MILC is given in row 3, while the ratio of errors is given in row 4.

Form factor	$f_{0/+}(0)$	$f_T(0)$	$f_0(q^2_{\text{max}})$	$f_+(q^2_{\text{max}})$	$f_T(q^2_{\text{max}})$
This work [a]	0.307(18)	0.286(29)	1.020(73)	6.72(88)	5.9(1.1)
Fermilab/MILC [b]	0.334(44)	0.315(53)	1.174(55)	8.76(66)	8.44(64)
$\lvert \text{Mean}(a-b)/\sigma(a-b) \rvert$	0.561	0.471	1.681	1.859	1.998
$\sigma(a)/\sigma(b)$	0.409	0.547	1.327	1.333	1.719

In table 6.11 we compare our current $B \to \pi$ form factor results at $q^2 = 0$ and $q^2 = q^2_{\text{max}}$ to those of Fermilab/MILC [5, 6]. Like the case for $D \to \pi$, the Fermilab/MILC data which contributes to the FLAG average of $B \to \pi$ have smaller uncertainties than the other contributing data, and so we choose to compare our current results to those of Fermilab/MILC directly. We find that our current result agree with theirs at $q^2 = 0$, though their uncertainties are larger than ours by about a factor of 2. However at $q^2 = q^2_{\text{max}}$ we see a difference of $\approx 1.6\sigma - 2.0\sigma$, with comparable uncertainties.

We generate lattice data on five different gluon field ensembles in this work, and are in the process of generating four more. These ensembles are the *course-five*, *course-physical*, *very course-five*, and *very course-physical* ensembles, which follow the same notation patterns as those on this work. We are also in the process of generating more data on the sfphys ensemble which contains heavy quark masses approximately equal to the physical bottom quark mass. We expect this new data improve our current results and reduce uncertainties, especially in the extrapolation to zero lattice spacing and physical quark masses.

Chapter 7

$D_s \to K$ and $B_s \to K$ Form Factors

In this chapter, we present the current status of our $D_s \to K$ and $B_s \to K$ form factor calculations. Both of these calculations are products of the same $H_s \to K$ correlator fit and z-expansion fit. These calculations do have dependency on the pion and heavy-light meson masses from our $H \to \pi$ correlator fits, which we discussed in the previous chapter. We again wish to emphasize that these lattice calculations are works in progress; the results we present in this chapter are likely to change as we generate more lattice data and refine our fit routines.

7.1 Calculation details

In chapter 3 we established the basis of our calculation details, but we shall summarize the key details here. Our calculations are carried out using MILC/HISQ $n_f = 2+1+1$ gluon field ensembles [72, 73, 74, 67], with HISQ valence quarks. These calculations share the same statistics as our $H \to \pi$ fits, and so those presented in table 6.1 apply to $H_s \to K$ as well. This is also true for the ensemble-specific fit parameters given in table 6.2. These parameters include the correlator statistics, heavy quark masses, twist angles, and source-sink separations.

Table 7.1: Fractional uncertainties given to priors for ground state meson masses $\Delta(M)$ and amplitudes $\Delta(A)$. Heavy-strange meson amplitude fractional uncertainties $\Delta(M_{H_s})$ apply only to the lightest H_s meson option on each ensemble. The ratio $R(A_{m_3}/A_{m_0})$ is used in equation 4.16 to determine the fractional uncertainties of the heavier H_s meson amplitude priors. $\Delta(A^*)$ is the fractional uncertainty given to all non-ground state amplitude priors.

Ensemble	$\Delta(M_K)$	$\Delta(M_{H_s})$	$\Delta(A_K)$	$\Delta(A_{H_s})$	$R(A_{m_3}/A_{m_0})$	$\Delta(A^*)$
f5	0.02	0.05	0.03	0.11	2.0	5.0
fphys	0.02	0.05	0.03	0.22	2.0	6.1
sf5	0.05	0.05	0.08	0.10	4.0	2.6
sfphys	0.05	0.10	0.15	0.65	2.0	2.0
uf5	0.10	0.05	0.15	0.20	4.0	2.0

7.2 Correlator fits

In this section we present the results of our current set of $H_s \to K$ correlator fits. These fits follow the theory and methodology laid out in chapter 4. Like our $H \to \pi$ fits, we model the data with $N_{\text{exp}} = 4$ exponentials, for both the oscillating and non-oscillating states. We follow the partitioned fit routine described in section 4.2 where we separate fitting three-point correlation functions into two separate fits based on the current insertion $J \in \{S, V^0\},\ \{V^1, T\}$.

7.2.1 Priors

As mentioned in section 6.2.1, in later stages of this work we applied $\log(\text{GBF})$ testing to the uncertainties of the discretization parameter's prior $P[\varepsilon^{\pi}]$. Here we can discuss the results of doing the same for $P[\varepsilon^{K}]$ in our $H_s \to K$ fits. In doing so, the $\log(\text{GBF})$ preferred uncertainties of ε^K were ± 50.0, ± 5.0, and ± 3.0 on the fphys, sf5, and sfphys ensembles respectively, while the f5 and uf5 ensemble uncertainties were smaller than ± 1.0. Like in our $H \to \pi$ fits, the behavior of the $\theta = 5.311$ correlators on the fphys ensemble exhibited the same anomalous behavior. After removing those correlators from the fit routine we found that the $\log(\text{GBF})$ preferred uncertainty of ε^K was now less than ± 1.0. For all these reasons we likewise exclude $\theta = 5.311$ correlators from our $H_s \to K$ fits, and we aim to resolve this anomaly in the future.

Table 7.2: $Hs \to K$ ground state three-point amplitude priors $P[J_{00}^{nn}]$ for all ensembles, twists θ, and currents $J \in \{S, V^0, V^1, T\}$. Twist is related to the kaon's three-momentum $\vec{p}$ via equation 4.10. Methods for determining these priors are discussed in section 4.5.1.

Ensemble	θ	S	V^0	V^1	T
f5	0.0	1.8(1.8)	0.8(0.8)	-	-
	0.4281	1.75(1.75)	0.75(0.75)	0.1(0.1)	0.07(0.07)
	1.282	1.35(1.35)	0.6(0.6)	0.2(0.2)	0.12(0.12)
	2.1410	1.0(1.0)	0.5(0.5)	0.22(0.22)	0.14(0.14)
	2.570	0.85(0.85)	0.5(0.5)	0.3(0.3)	0.15(0.15)
fphys	0.0	1.90(1.90)	1.0(1.0)	-	-
	0.58	1.75(1.75)	0.9(0.9)	0.1(0.1)	0.05(0.05)
	0.87	1.75(1.75)	0.85(0.85)	0.12(0.12)	0.08(0.08)
	1.13	1.75(1.75)	0.8(0.8)	0.15(0.15)	0.1(0.1)
	3.000	1.25(1.25)	0.6(0.6)	0.2(0.2)	0.15(0.15)
	5.311	0.5(0.5)	0.3(0.3)	0.15(0.15)	0.1(0.1)
sf5	0.0	2.0(2.0)	1.0(1.0)	-	-
	1.261	1.5(1.5)	0.75(0.75)	0.25(0.25)	0.2(0.2)
	2.108	1.2(1.2)	0.6(0.6)	0.3(0.3)	0.2(0.2)
	2.666	1.0(1.0)	0.6(0.6)	0.3(0.3)	0.2(0.2)
	5.059	1.0(1.0)	0.75(0.75)	0.25(0.50)	0.2(0.2)
sfphys	0.0	2.0(2.0)	1.25(1.25)	-	-
	2.522	1.5(1.5)	0.9(0.9)	0.25(0.25)	0.15(0.15)
	4.216	1.25(1.25)	0.75(0.75)	0.3(0.3)	0.2(0.2)
	7.94	1.0(1.0)	0.5(0.5)	0.25(0.25)	0.2(0.2)
	10.118	1.0(1.0)	0.5(1.0)	0.2(0.4)	0.2(0.3)
uf5	0.0	2.0(2.0)	1.25(1.25)	-	-
	0.706	1.75(1.75)	1.0(1.0)	0.2(0.2)	0.15(0.15)
	1.529	1.5(1.5)	0.75(0.75)	0.3(0.3)	0.20(0.2)
	2.235	1.0(1.0)	0.6(0.6)	0.3(0.3)	0.20(0.2)
	4.705	1.0(1.0)	0.5(1.0)	0.3(1.0)	0.2(0.5)

Table 7.3: $H_s \to K$ prior absolute uncertainties for all ensembles, for all non-ground state fit parameters $J_{ij}^{kl} \neq J_{00}^{oo}$, for $J \in \{S, V^0, V^1, T\}$. The notation $J_{\neq 0}$ indicates the values used to assign priors to all higher order exponential states $J_{ij \neq 00}^{kl}$. The notation $J_{\rm osc}$ indicates the values used to assign priors to all lowest lying oscillating states $J_{00}^{kl \neq nn}$. Central values given to all associated priors are equal to 0.0. A special prior uncertainty scaling term $\sigma_{\rm ens}$ for each ensemble, which we discuss in section 4.5.2, is given in final column. The scaling term applies to select non-ground state three point amplitudes J_{00}^{on} and J_{10}^{kl} for all $k, l \in \{n, o\}$.

Ensemble	$S_{\neq 0}$	$S_{\rm osc}$	$V^0_{\neq 0}$	$V^0_{\rm osc}$	$V^1_{\neq 0}$	$V^1_{\rm osc}$	$T_{\neq 0}$	$T_{\rm osc}$	$\sigma_{\rm ens}$
f5	0.43	1.1	0.75	2.0	0.12	1.0	0.8	1.0	1.8
fphys	0.42	1.52	1.0	3.3	0.11	0.2	0.06	0.22	2.2
sf5	0.24	0.55	0.26	0.86	0.1	0.25	0.01	0.3	4.0
sfphys	0.2	0.4	0.25	2.0	0.07	0.14	0.08	0.16	5.5
uf5	0.16	0.4	0.25	0.20	0.07	0.21	0.06	0.15	5.0

Table 7.4: Wholistic fit quality parameters for our current set of $H_s \to K$ correlator fits. Per ensemble we partition our correlator fits into two halves based on which current insertions $J \in \{S, V^0, V^1, T\}$ are included. The degrees of freedom (d.o.f.), the χ^2/d.o.f., and the log(GBF) of each fit are given in columns 3, 4, and 5. We note this is the augmented χ^2 as defined in equation 4.3. All fits have a quality factor $Q = 1$. Section 4.8 discusses the significance of a fit's d.o.f., quality factor, and log(GBF) in detail.

Ensemble	Current pair	d.o.f.	χ^2/d.o.f.	log(GBF)
f5	$\{S, V^0\}$	3549	0.121	81458
	$\{V^1, T\}$	3021	0.071	73493
fphys	$\{S, V^0\}$	3577	0.152	80751
	$\{V^1, T\}$	3049	0.130	73332
sf5	$\{S, V^0\}$	4718	0.118	127936
	$\{V^1, T\}$	4030	0.184	115586
sfphys	$\{S, V^0\}$	5022	0.054	127977
	$\{V^1, T\}$	4270	0.052	114808
uf5	$\{S, V^0\}$	7112	0.116	207806
	$\{V^1, T\}$	6040	0.064	185691

7.2.2 Results

Here we can summarize the key results from our $H_s \to K$ correlator fits. In table 7.4 we present parameters which determine the wholistic quality of the current set of correlator fits, including each fit's χ^2/d.o.f. and log(GBF). We find that these fits are of acceptable quality, and all ground state fit posteriors are consistent with their priors.

Like in the case of $H \to \pi$, we can use dispersion relation plots to evaluate how well the fit-determined kaon energy and amplitudes compare to our expectations. Figure 7.1 gives these plots for our current $H_s \to K$ correlator fits. For the energy dispersion relation, we find that the fit posteriors generally follow our expectation, though in the $|ap_K|^2 < 0.10$ region of the plot the sf5, sfphys, and uf5 kaon energies consistently lie outside and above the region in which we expect them. This pattern is somewhat more pronounced in the corresponding amplitude plot, where the behavior even extends into the high $|ap_K|^2$ range. Though these data fall outside our expectations by only a few standard deviations, the somewhat consistent behavior could be indicative of some problem in our correlator fits we have yet to address.

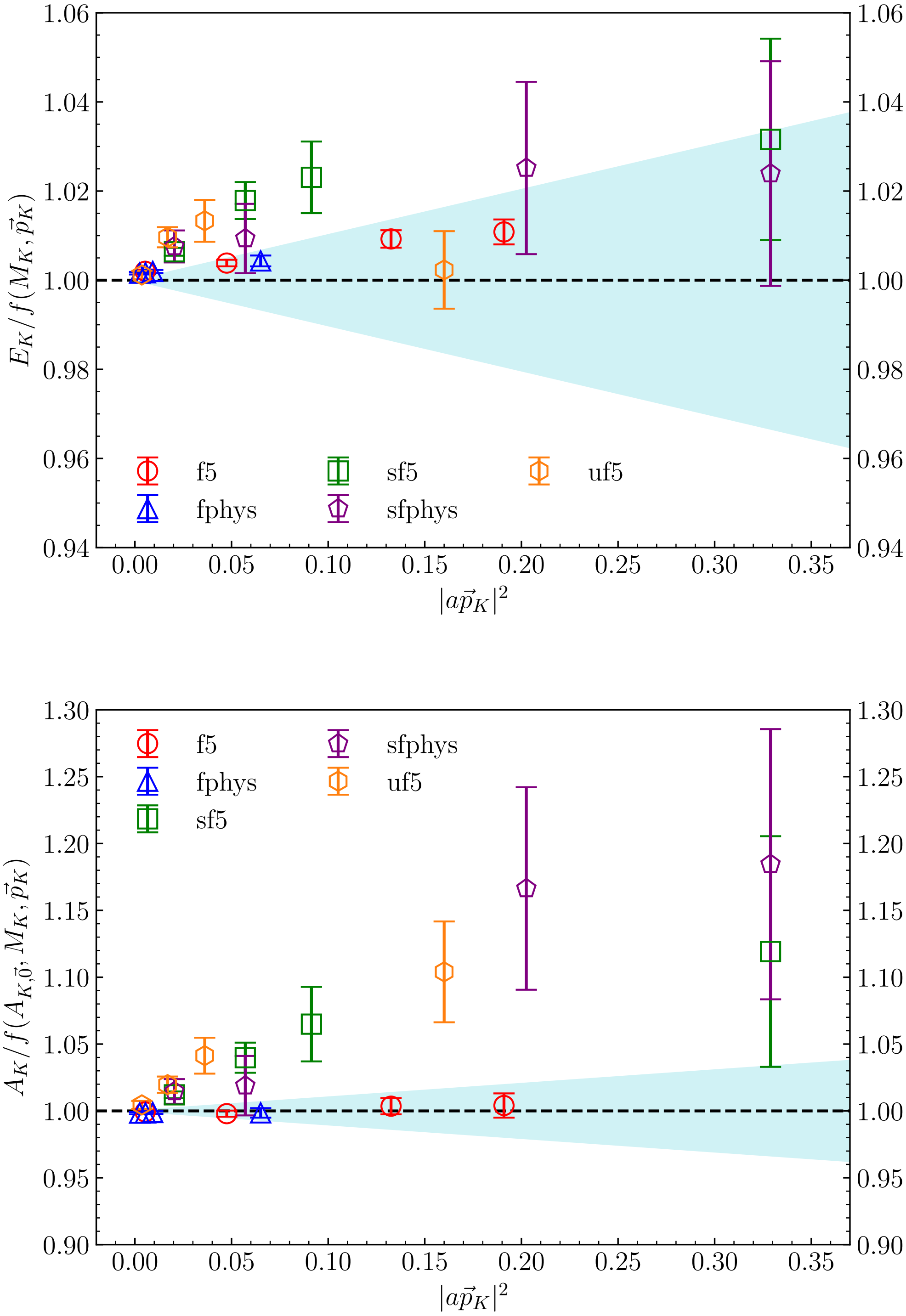

Figure 7.1: Energy (top) and amplitude (bottom) dispersion relation plots for current set of $H_s \to K$ correlator fits. Data shown are ground state, non-zero twist energy and amplitude fit posteriors divided by a function equal to the right hand side of either equation 4.12 (energy) or equation 4.17 (amplitude) without the discretization factor. The shaded cyan corresponds to the area bound by the functions $y = 1 \pm \left|\frac{a\vec{p}}{\pi}\right|^2$.

7.3 z-expansion fits

As discussed in chapter 5, the modified z-expansion is how we transform correlator fit results into $D_s \to K$ and $B_s \to K$ continuum form factors. In this section we discuss that process generally in the context of $H_s \to K$. Like our $H \to \pi$ fits we perform our modified z-expansion under the BCL parameterization where $N = 3$, such that $N - 1 = 2$ is the maximum polynomial order of f_0 and $N = 3$ is the maximum polynomial order for f_+ and f_T.

7.3.1 Priors

The priors in this $H_s \to K$ z-expansion fit share the same assignments as in the $H \to \pi$ case, which are given in table 6.7. These prior assignments correspond to $N_{ijkl} \equiv (N_i, N_j, N_k, N_l) = (3,2,2,3)$. We similarly find in test fits that the results are insensitive to individual changes of ± 1 to j, k, or l. Our discussion of priors for our z-expansion fit of $H \to \pi$ largely applies to the $H_s \to K$ case as well, with a few extra caveats. We assign priors to the parameters in table 6.7 similarly for $H_s \to K$, although because the coupling term $g(M_H)$ does not appear in the this fit (see equation 5.22), the parameters g_∞, C_1, and C_2 do not contribute to this fit. Meanwhile, we do need the M_H and M_π results from our $H \to \pi$ correlator fit in our z-expansion fit of $H_s \to K$. As discussed in chapter 5, the branch cut threshold of $H_s \to K$ occurs at $t_+ \equiv (M_H + M_\pi)^2$, and the pole terms which appear in the prefactor still correspond to the excited heavy-light states H_0^* and H^*.

7.3.2 Results

Here we will discuss the quality of our current $H_s \to K$ z-expansion fit, saving our discussion of our physical continuum $D_s \to K$ and $B_s \to K$ form factors for the next section. We find the overall quality of our $H_s \to K$ fit to be fair, which is to say, not as good as our $H \to \pi$ fit. Our $H_s \to K$ fit has 340 degrees of freedom, a $\chi^2/\text{d.o.f.} = 0.527$, a quality factor $Q = 1$, and a $\log(\text{GBF}) = 841$. The $\log(\text{GBF})$ of both fits are not comparable, as the $H_s \to K$ fit has more degrees of freedom. The $\chi^2/\text{d.o.f.}$ is higher however, which manifests as a higher number of fit parameters whose posteriors differ from their priors by more than one standard deviation. Furthermore, many of these offending parameters are likely deterministic to the shape of our form factor plots. To begin, we find that the high twist kaon energies from the f5, fphys, and sf5 ensembles have posteriors which differ from their priors by one to two standard deviations. Seeing that this is a consistent behavior across three of our five ensembles, this finding is likely indicative of a systemic problem at the low q^2 range in either or both of our correlator and z-expansion fits.

Unlike in our $H \to \pi$ fit, we do not see fit posteriors of the coefficients $|d^{+,T}_{00002}| > 1.0$ in our $H_s \to K$ fit, and we therefore do not expect to find large curvature in our $f_{+,T}(z)$ plots. We do however find in our fit that the posterior value of $d^0_{00002} = 1.03(25)$, which would imply some degree of positive curvature to the $f_0(z)$.

In figures 7.2-7.5 we present scalar, vector, and tensor form factor plots as functions of z, with continuous best fit functions for lattice form factor data. As anticipated, there is a slight positive curvature to the scalar form factor functions, and less so for the vector and tensor functions.

The equations to build physical continuum form factors (equations 5.27-5.29) still have heavy meson mass dependency. In figure 7.6, we vary M_{H_s} between the physical D and B masses to see the effect which that variation has on $f_{0,+,T}(q^2, M_H)$ at $q^2 = 0$ and $q^2 = q^2_{\text{max}}$. In section 6.3.2 we describe our approximate method of linearly interpolating the scaling factor Γ, which multiplies

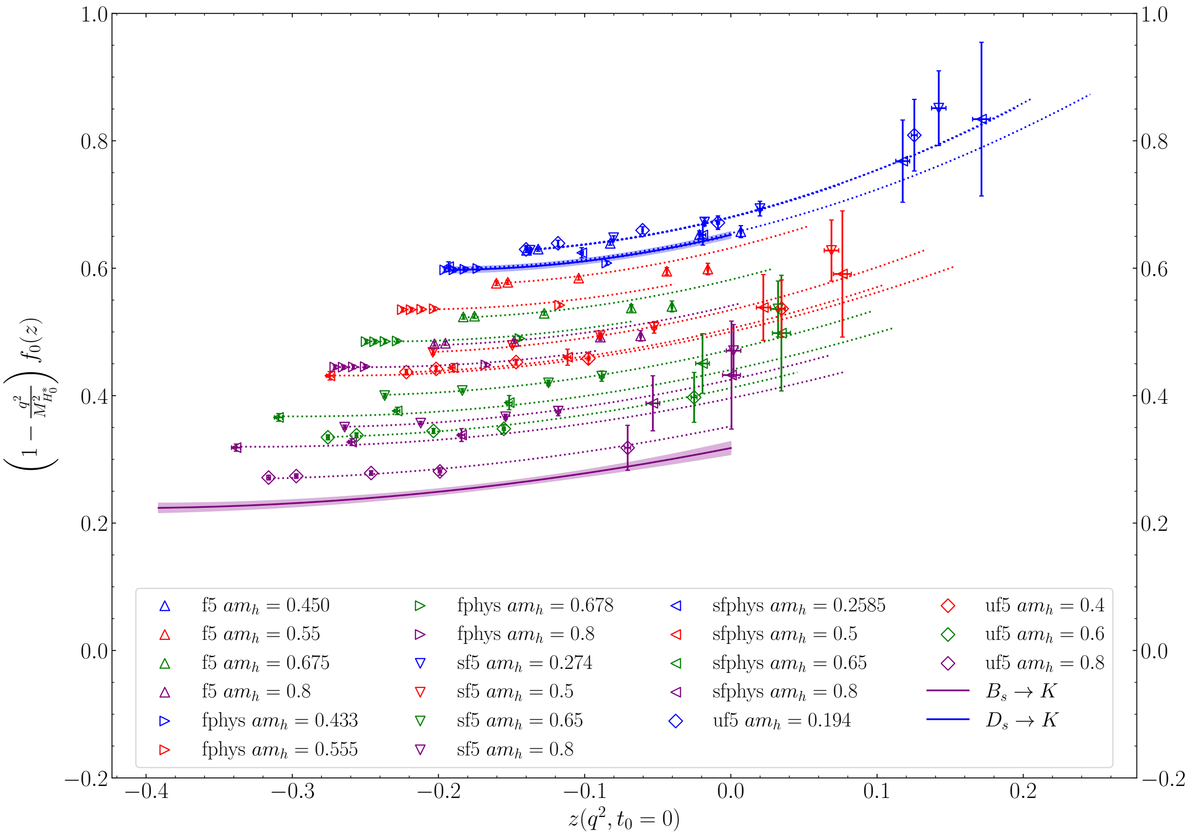

Figure 7.2: $H_s \to K$ modified z-expansion scalar form factor plot for $H_s \to K$. Plotted data correspond to correlator fit results of varying heavy quark mass am_h on each ensemble. Continuous dotted lines represent the z-expansion line of best fit for a given heavy quark mass and ensemble, with all lattice artifacts still present. Continuous solid lines correspond to physical continuum fit of either $D_s \to K$ or $B_s \to K$ as a function of z.

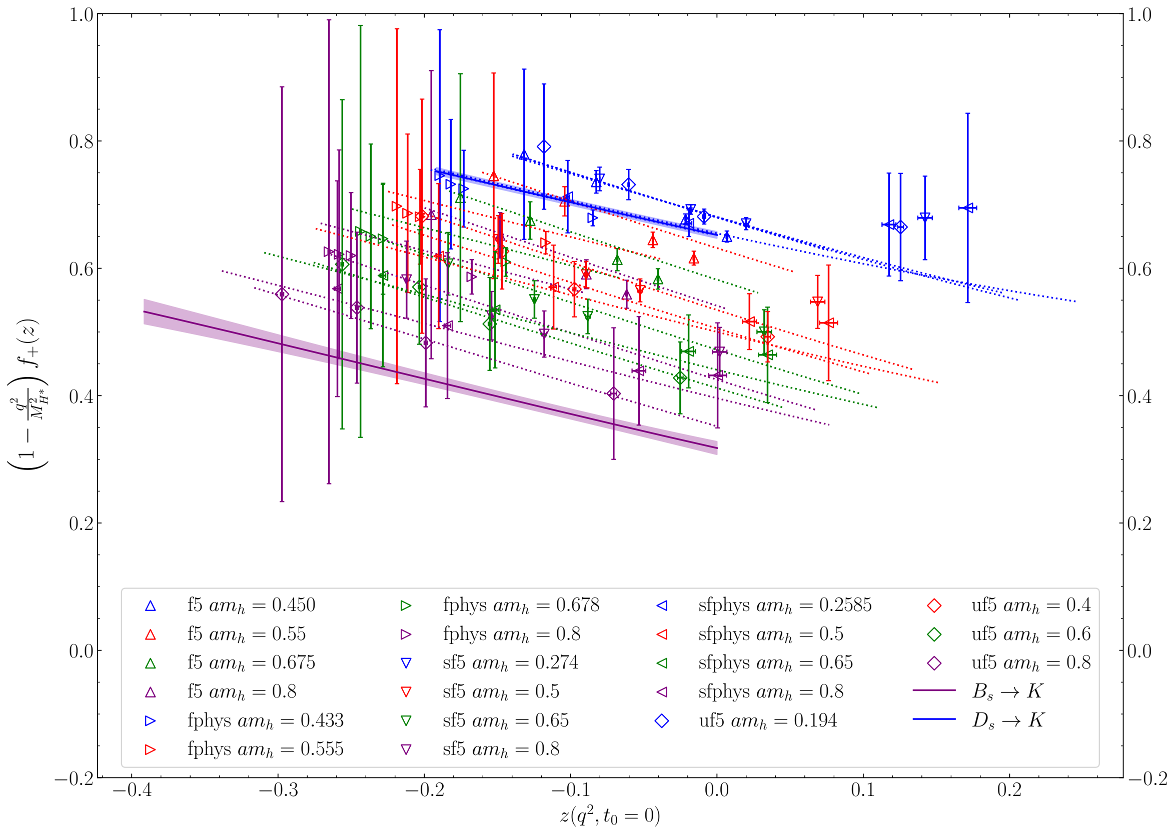

Figure 7.3: $H_s \to K$ modified z-expansion temporal vector form factor plot for $H_s \to K$. Plotted data correspond to correlator fit results of varying heavy quark mass am_h on each ensemble. Continuous dotted lines represent the z-expansion line of best fit for a given heavy quark mass and ensemble, with all lattice artifacts still present. Continuous solid lines correspond to physical continuum fit of either $D_s \to K$ or $B_s \to K$ as a function of z. Continuous curves are informed by both temporal and spatial vector data, and are therefore the same curves present in figure 7.4.

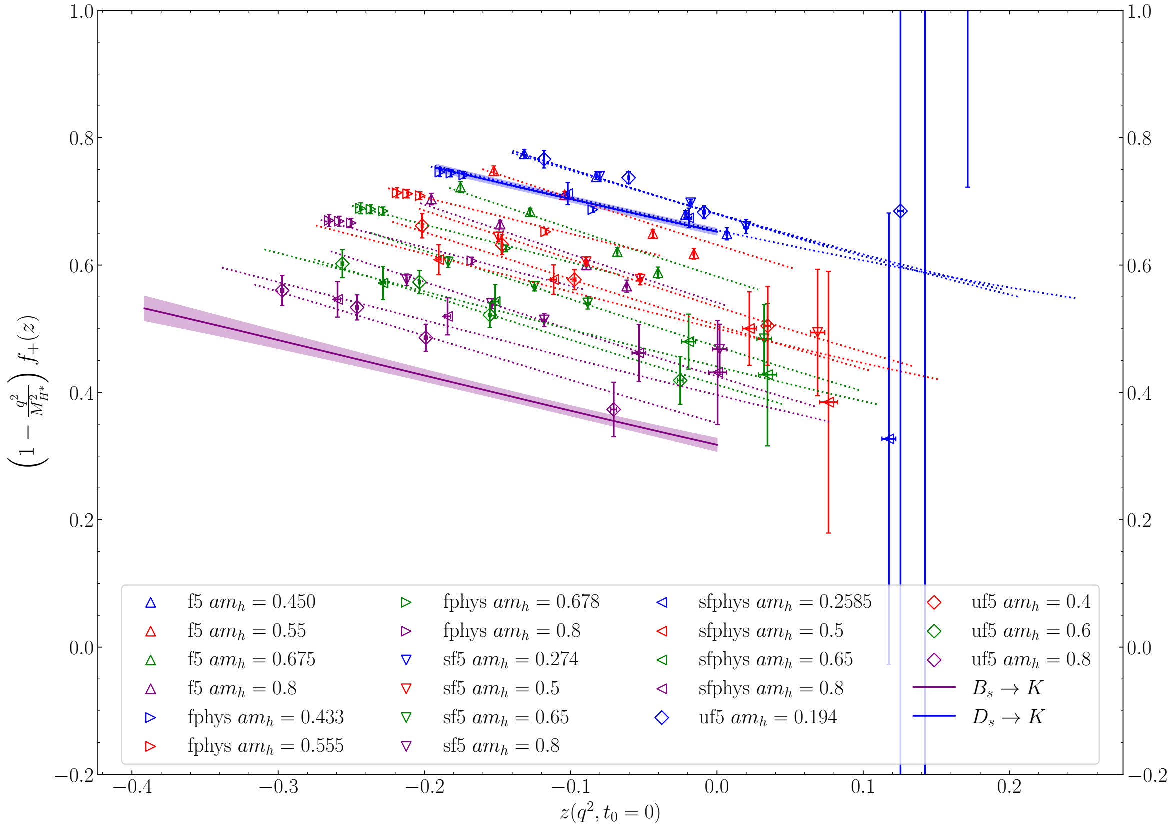

Figure 7.4: $H_s \to K$ modified z-expansion spatial vector form factor plot for $H_s \to K$. Plotted data correspond to correlator fit results of varying heavy quark mass am_h on each ensemble. Continuous dotted lines represent the z-expansion line of best fit for a given heavy quark mass and ensemble, with all lattice artifacts still present. Continuous solid lines correspond to physical continuum fit of either $D_s \to K$ or $B_s \to K$ as a function of z. Continuous curves are informed by both temporal and spatial vector data, and are therefore the same curves present in figure 7.3.

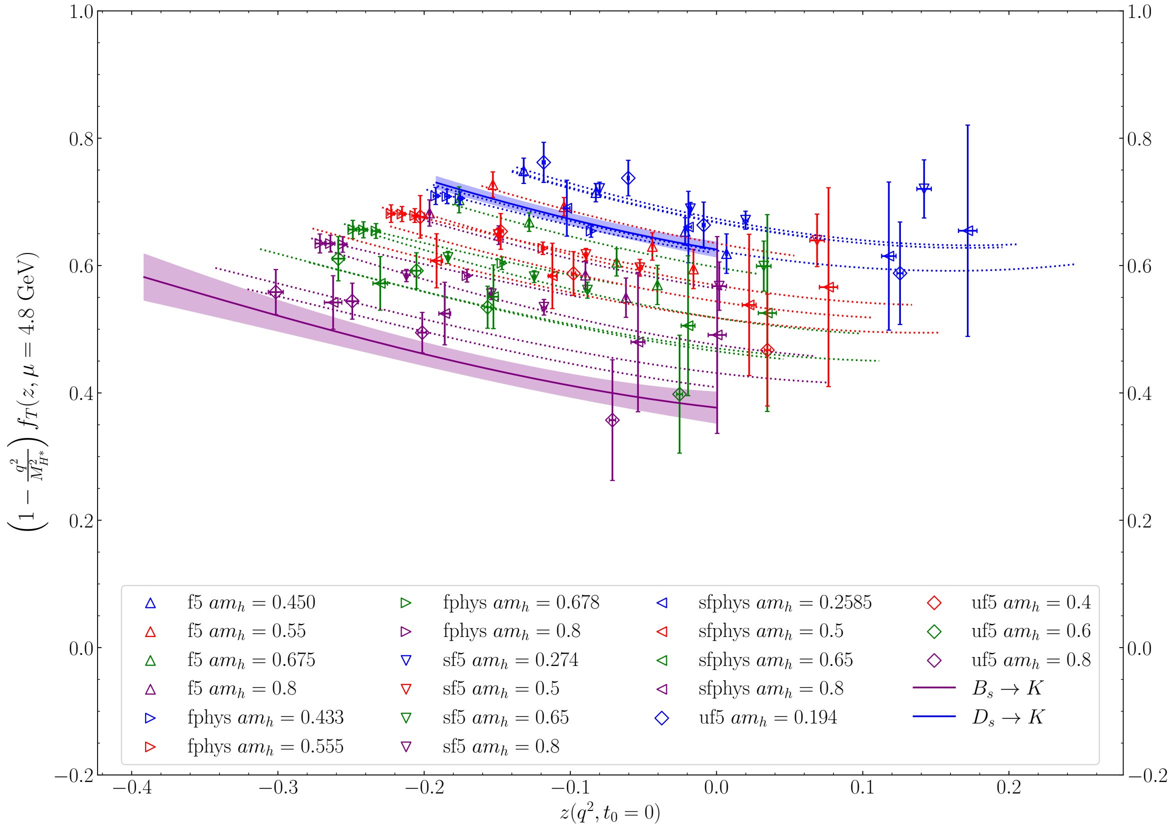

Figure 7.5: $H_s \to K$ modified z-expansion tensor form factor plot for $H_s \to K$. Plotted data correspond to correlator fit results of varying heavy quark mass am_h on each ensemble. Continuous dotted lines represent the z-expansion line of best fit for a given heavy quark mass and ensemble, with all lattice artifacts still present. Continuous solid lines correspond to physical continuum fit of either $D_s \to K$ or $B_s \to K$ as a function of z.

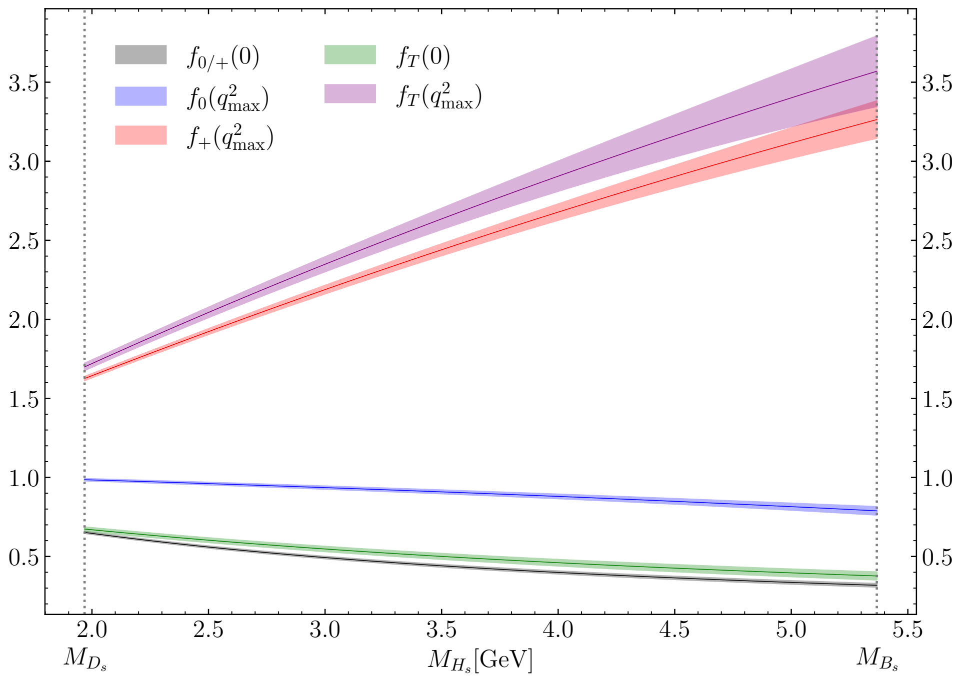

Figure 7.6: $H_s \to K$ continuum scalar, vector, and tensor form factors at $q^2 = 0$ and $q^2 = q^2_{\text{max}}$, where the heavy meson mass M_{H_s} varies between the mass of the D_s and B_s mesons. See text for how we scale $Z(\mu)$ for all M_{H_s} between $M_{D_s}^{\text{phys}}$ and $M_{B_s}^{\text{phys}}$

$f_T(q^2, \mu = 4.8 \text{ GeV}, M_H)$ for any M_H. We use that same method here. In the case of $H \to \pi$, we observed the phenomenon of $f_+ \approx f_T$ as $M_H \to M_B^{\text{phys}}$. Figure 7.6 however does not show that same behavior as strongly for $H_s \to K$. In the case where $q^2 = 0$, at no point are the vector and tensor form factors ever consistent with each other within one standard deviation[1]. In the case of $q^2 = q^2_{\text{max}}$, the regions which span ± 1 standard deviations of of either function only barely overlap towards the M_{B_s} end. Because we have to extrapolate to the physical B_s mass, we expect uncertainties to grow as $M_{H_s} \to M_{B_s}^{\text{phys}}$, and so this overlap is possibly the result of growing uncertainties rather than the behavior we expect from approaching the heavy mass limit. Regardless, the $M_{B_s}^{\text{phys}}$ mass scale is not equivalent to he heavy quark limit where we expect $f_T = f_+$, and so this finding is not necessarily unexpected.

1. While on this plot it looks like the $f_{0/+}(0)$ and $f_T(0)$ curves overlap at the M_{D_s} end, figure 7.7 shows that they differ by just over one standard deviation.

Table 7.5: Physical continuum $D_s \to K$ z-expansion coefficients $a_n^{0,+,T}$, pole masses (in GeV), and chiral logarithm term, presented alongside their corresponding correlation matrix. Using equations 5.27-5.29 these parameters can be used to reconstruct our current $D_s \to K$ form factor plots (figures 7.7 and 7.8). Correlations whose magnitudes are less than 10^{-5} are listed as <1e-05.

$a_0^{0/+}$	a_1^0	a_2^0	a_1^+	a_2^+	a_0^T	a_1^T	a_2^T	$M^{\text{phys}}_{D_0^*}$	$M^{\text{phys}}_{D^*}$	$\mathscr{L}$
0.6388(51)	0.540(43)	1.35(14)	-0.489(47)	0.17(24)	0.612(11)	-0.365(95)	0.71(42)	2.3430(99)	2.006850(50)	1.021259(60)
1	0.54829	0.33965	0.41148	0.13967	0.04485	-0.00858	-0.04983	-0.03394	-0.00016	-0.0014
	1	0.80979	0.63345	0.31861	0.03173	-0.02427	-0.07128	-0.37908	-0.00105	0.00017
		1	0.58873	0.37999	0.00288	-0.02995	-0.06057	0.04696	-0.0003	0.00045
			1	0.78567	-0.08738	-0.05722	0.00258	-0.02346	-0.0036	-0.00246
				1	-0.13072	-0.07521	0.07889	-0.01077	0.00222	<1e-05
					1	0.5535	0.17559	-0.00179	-0.00019	0.00115
						1	0.75821	-0.00065	-0.00211	-0.00051
							1	0.00195	0.0007	3e-05
								1	0.00195	<1e-05
									1	<1e-05
										1

7.4 Status of form factor calculations

Here we present the current status of both our $D_s \to K$ and $B_s \to K$ form factor calculations. This entails physical continuum form factor plots, and discussion of where we expect the forthcoming generation of more data to improve these current results.

7.4.1 $D_s \to K$

In table 7.5 we give the coefficients, pole masses, and chiral logarithm terms which, when input into equations 5.27, 5.28 and 5.29, generate our current physical continuum $D_s \to K$ form factors. Figures 7.7 and 7.8 give the current scalar, vector, and tensor form factors as functions of z and q^2. As we might expect from the z-expansion fit, the only coefficient with a magnitude greater than one is $a_2^0 = 1.35(14)$, while a_2^+ is consistent with zero and $a_2^T = 0.71(42)$. The curvatures of the functions in 7.7 reflect these findings.

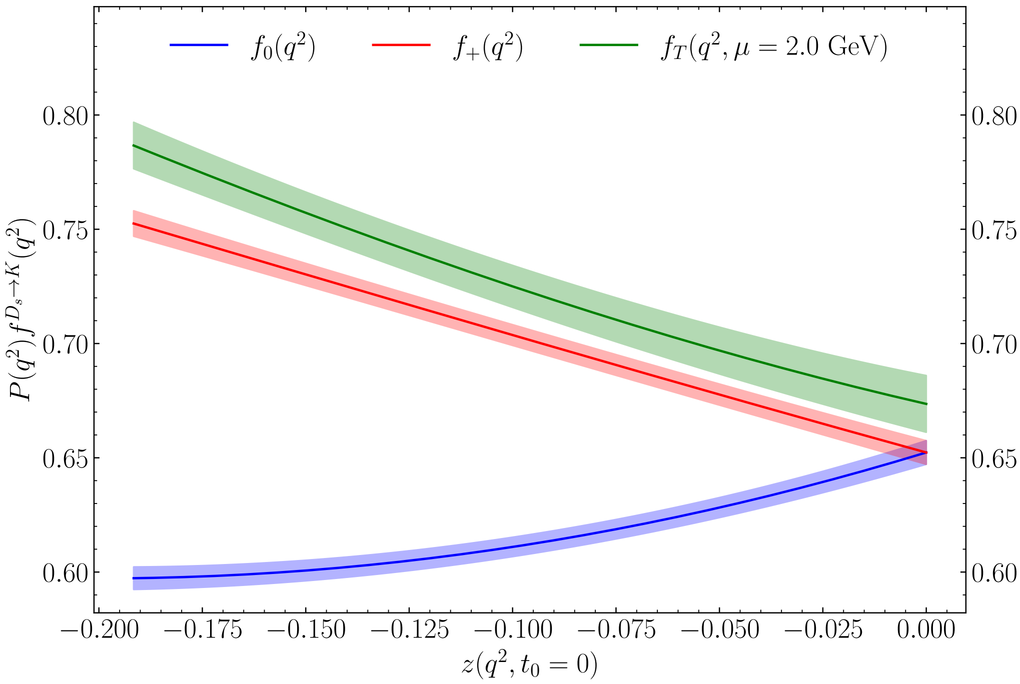

Figure 7.7: Current continuum $D_s \to K$ scalar, vector, and tensor form factors, multiplied by the appropriate pole term $P(q^2)$ (defined in equations 5.24 and 5.26). Results span the entire physical q^2 range.

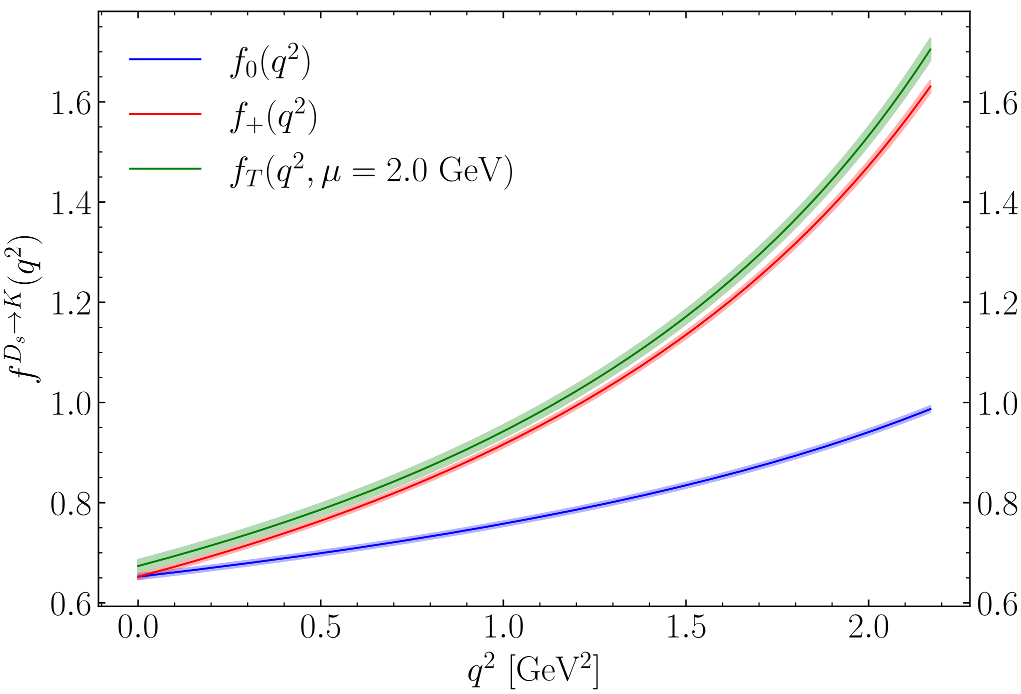

Figure 7.8: Current continuum $D_s \to K$ scalar, vector, and tensor form factors. Results span the entire physical q^2 range.

Table 7.6: Comparison of our current $D_s \to K$ form factor results to those of Fermilab/MILC [4] at $q^2 = 0$ and $q^2 = q^2_{\text{max}}$. Fermilab/MILC does not calculate tensor form factors. The difference in standard deviations σ between our results and those of Fermilab/MILC is given in row 3, while the ratio of errors is given in row 4.

Form factor	$f_{0/+}(0)$	$f_T(0)$	$f_0(q^2_{\text{max}})$	$f_+(q^2_{\text{max}})$	$f_T(q^2_{\text{max}})$
This work [a]	0.6523(52)	0.674(12)	0.9869(61)	1.631(12)	1.705(22)
Fermilab/MILC [b]	0.6307(20)	-	0.9843(18)	1.576(13)	-
$\lvert\text{Mean}(a-b)/\sigma(a-b)\rvert$	3.877	-	0.409	3.109	-
$\sigma(a)/\sigma(b)$	2.600	-	3.388	0.923	-

While the functions f_+ and f_T do not align in both our $D \to \pi$ and $D_s \to K$ results, the separation in our $D_s \to K$ results is much smaller. Furthermore, we can observe that while $f_+ > f_T$ for the entire q^2 range in $D \to \pi$, the opposite appears to be true for $D_s \to K$. To our knowledge, there are no published, lattice-determined tensor form factor results for either of these meson decays, and so we have no point of comparison to make on whether or not this behavior is expected.

We refrain from making any rigorous comparison to other $D_s \to K$ scalar or vector form factor calculations, though we can once again point the reader towards the Fermilab/MILC $D_s \to K$ results in [4]. In table 7.6 we compare our $D_s \to K$ form factor results at $q^2 = 0$ and $q^2 = q^2_{\text{max}}$ to those of Fermilab/MILC (FLAG does not present any $D_s \to K$ averages). We find that our results at $f_0(q^2_{\text{max}})$ are consistent with those of Fermilab/MILC, however our $f_+(q^2_{\text{max}})$ and $f_{0/+}(0)$ results differ from those of Fermilab/MILC by $\approx 3.1\sigma$ and $\approx 3.9\sigma$ respectively. As discussed in chapter 6, we do not change our methodology in response to any of these comparisons.

In a similar fashion to our $D \to \pi$ fits, we also performed a series of $H_s \to K$ fits which only considered $am_h \approx am_c$ correlator data. We did so with the aim of ruling out the possibility that fitting $am_h > am_c$ data could have an unexpected and significant impact on our final $D_s \to K$ form factor results. After conducting this test, we find that resultant $D_s \to K$ form factors are largely consistent with those from our global fit. Comparing the results of $f_{0,+,T}$ at $q^2 = 0$ and $q^2 = q^2_{\text{max}}$ specifically, we find consistency to within one standard deviation of our global fit results (which are given in the first row of table 7.6), with one exception. In the *charm-only* fit, we calculate $f_{0/+}(0) = 0.6387(62)$, which differs from the global fit result of $f_{0/+}(0) = 0.6523(52)$ by 1.681σ.

In the context of the overall consistency between the charm-only and global fit results for both $D \to \pi$ and $D_s \to K$, this discrepancy is not statistically significant. We would however like to acknowledge that this minor disagreement occurs in the low q^2 (high kaon momentum) kinematic range: the same range where we observed other minor issues in our correlator fitting. We believe that continued work on this line of correlator fits ought to investigate these phenomena more thoroughly.

Our line of calculations is ongoing, and there are likely changes/fixes to our fitting in the future which might change our current results. As mentioned in the previous section, there is possibly some issue on our fit related to the high-twist kaon energies that go into it. We expect that the new lattice data being generated on coarser ensembles and the alternate BGL parameterization will make general improvements to our fit.

7.4.2 $B_s \to K$

Having discussed our $D_s \to K$ results, let us move on to our final meson decay of interest: $B_s \to K$. We give the necessary coefficients, pole masses, and chiral logarithm term to construct physical continuum $B_s \to K$ form factors via equations 5.27-5.29 in table 7.7. Our current scalar, vector, and tensor form factor plots are presented in figures 7.9 and 7.10 as functions of z and q^2 respectively. Unlike all our other meson decays, none of the $a_2^{0,+,T}$ coefficients in table 7.7 have magnitudes greater than one, which manifests as their being little curvature in any of the functions over the entire physical q^2 range. This behavior lies in stark contrast to the significant negative curvature of the vector and tensor $B \to \pi$ form factors shown in figure 6.9.

As alluded to in section 7.3.2, we see little overlap between the vector and tensor functions. Though we expect $f_T = f_+$ in the heavy quark limit of $m_b \to \infty$, it is not necessarily unexpected to find $f_T \neq f_+$ at the mass scale of $M_{B_s}^{\text{phys}}$. We are curious to see if this behavior might change with the introduction of new lattice data, especially the forthcoming $am_h \approx m_b^{\text{phys}}$ data on the sfphys

Table 7.7: Physical continuum $B_s \to K$ z-expansion coefficients $a_n^{0,+,T}$, pole masses (in GeV), and chiral logarithm term, presented alongside their corresponding correlation matrix. Using equations 5.27-5.29 these parameters can be used to reconstruct our current $B_s \to K$ form factor plots (figures 7.9 and 7.10). Correlations whose magnitudes are less than 10^{-5} are listed as <1e-05.

$a_0^{0/+}$	a_1^0	a_2^0	a_1^+	a_2^+	a_0^T	a_1^T	a_2^T	$M_{B_0^*}^{\text{phys}}$	$M_{B^*}^{\text{phys}}$	$\mathscr{L}$
0.311(10)	0.444(79)	0.53(15)	-0.511(82)	0.18(26)	0.368(24)	-0.31(18)	0.63(57)	5.7563(99)	5.32475(20)	1.021259(60)
1	0.86769	0.70364	0.59657	0.27739	0.24015	0.12834	0.05879	0.00621	-0.00163	-0.00021
	1	0.92648	0.63522	0.28227	0.20998	0.12218	0.05845	0.00093	-0.0019	3e-05
		1	0.57483	0.26126	0.16523	0.10688	0.05307	0.07078	-0.00174	0.0002
			1	0.75182	0.05626	0.07888	0.06093	-0.01433	-0.00225	-0.00092
				1	-0.00973	0.02864	0.05167	-0.01536	0.00506	<1e-05
					1	0.62399	0.374	0.0009	-0.00172	0.00034
						1	0.82758	0.00058	-0.00174	-0.00026
							1	0.001	0.00248	2e-05
								1	-4e-05	<1e-05
									1	<1e-05
										1

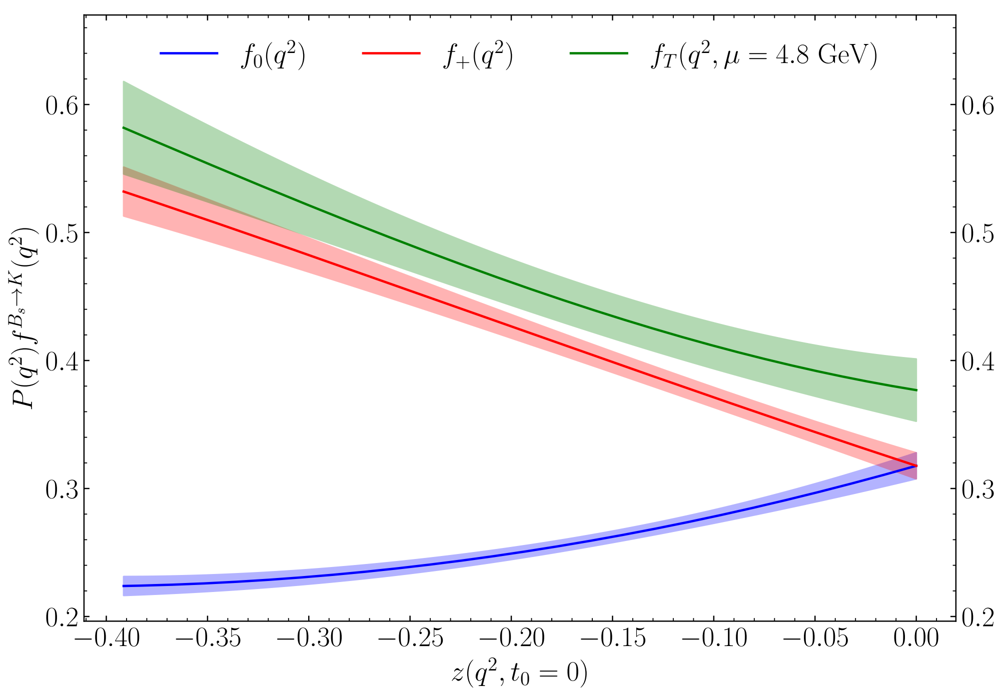

Figure 7.9: Current continuum $B_s \to K$ scalar, vector, and tensor form factors, multiplied by the appropriate pole term $P(q^2)$ (defined in equations 5.24 and 5.26). Results span the entire physical q^2 range.

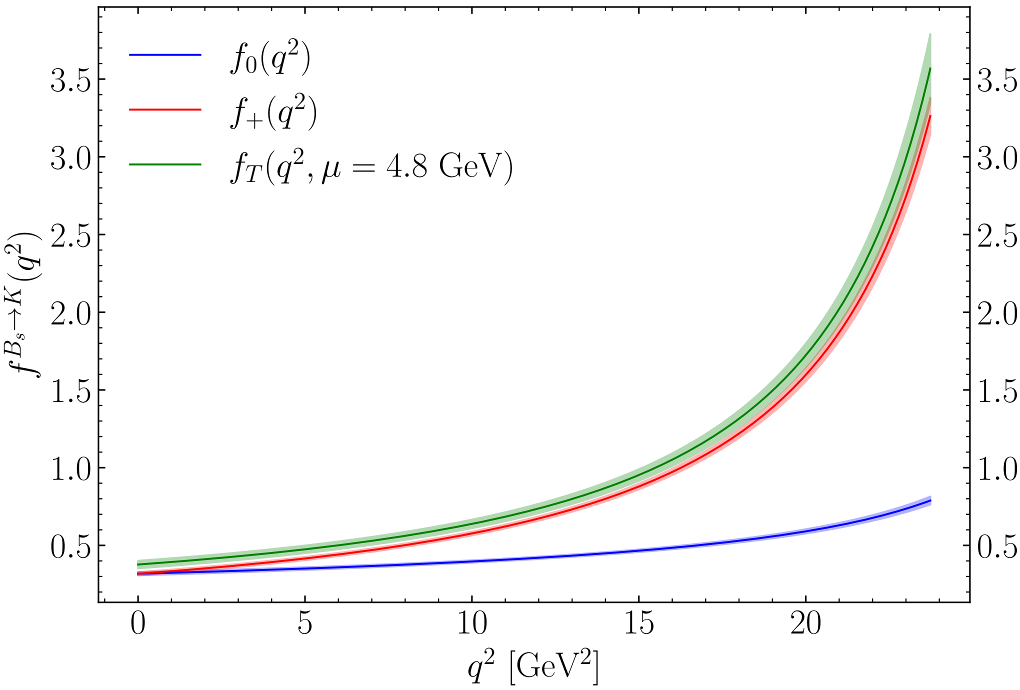

Figure 7.10: Current continuum $B_s \to K$ scalar, vector, and tensor form factors. Results span the entire physical q^2 range.

ensemble. We maintain the possibility however that peculiarities such as these may still originate from unresolved problems in our fit routines. Like the other meson decays in this work, we expect that the addition of new data at coarser lattice spacings, and an alternate z-expansion fit under the BGL parameterization will make general improvements to these results.

In table 7.8 we compare our $B_s \to K$ form factor results to those of the FLAG average in [7] at $q^2 = 0$ and $q^2 = q^2_{\max}$. Unlike the FLAG average for $B \to \pi$ form factors, the lattice calculations [8, 9, 10, 11] which contribute to the the FLAG average of $B_s \to K$ form factor results all have comparable uncertainties. We find that our current results for $f_{0,+}(q^2_{\max})$ are consistent with the FLAG average, while the results for $f_{0/+}(0)$ only differ by $\approx 1.2\sigma$. We can also see that our results have equal or smaller uncertainties to those of the FLAG average.

Table 7.8: Comparison of our current $B_s \to K$ form factor results to those of the FLAG average [7](FLAG average results are calculated from [8, 9, 10, 11]) at $q^2 = 0$ and $q^2 = q^2_{\text{max}}$. FLAG does not calculate tensor form factors. The difference in standard deviations σ between our results and those of the FLAG average is given in row 3, while the ratio of errors is given in row 4.

Form factor	$f_{0/+}(0)$	$f_T(0)$	$f_0(q^2_{\text{max}})$	$f_+(q^2_{\text{max}})$	$f_T(q^2_{\text{max}})$
This work [a]	0.318(10)	0.377(24)	0.789(25)	3.26(12)	3.57(22)
FLAG average [b]	0.270(39)	-	0.814(29)	3.18(12)	-
$\lvert\text{Mean}(a-b)/\sigma(a-b)\rvert$	1.199	-	0.64	0.486	-
$\sigma(a)/\sigma(b)$	0.256	-	0.862	1.000	-

Chapter 8

Conclusions

Let us now summarize the key principles of this work. Under the constraints of the Standard Model, we have used the techniques of lattice QCD to calculate scalar, vector, and tensor form factors across the entire kinematic range for the following semileptonic heavy meson decays: $D \to \pi$, $B \to \pi$, $D_s \to K$, and $B_s \to K$. This line of lattice calculations is characterized by the HISQ action and the heavy-HISQ method, using MILC $N_f = 2+1+1$ gluon field ensembles. In chapter 4 we discussed our complete methodology for fitting correlation functions to the appropriate fit forms, with a focus on our exact implementation of a Bayesian fitting approach. In chapter 5 we detailed how we transform correlator fit results into continuum form factor functions via the modified z-expansion. These two chapters provide the methodological framework for how we have arrived at our current form factor results, presented in chapters 6 and 7.

Concerning all four meson decays of interest to this work, we have made substantial progress in having calculated their scalar, vector, and tensor form factors using lattice QCD. Table 8.1 summarizes the values of our form factor results at $q^2 = 0$ and $q^2 = q^2_{\text{max}}$ for all four meson decays. These results are not final, and we have identified where problems remain in this line of lattice calculations. Furthermore, as discussed in chapters 6 and 7, we are still actively generating more correlator data which we intend to incorporate into our lattice calculations. We expect corrections to our methodology and the inclusion of new data to improve our current results, which, when in a finalized state, we intend to publish.

Table 8.1: Summary of our current form factor results at $q^2 = 0$ and $q^2 = q^2_{\mathrm{max}}$.

Decay	$f_{0/+}(0)$	$f_T(0)$	$f_0(q^2_{\mathrm{max}})$	$f_+(q^2_{\mathrm{max}})$	$f_T(q^2_{\mathrm{max}})$
$D \to \pi$	0.679(12)	0.572(22)	1.284(15)	3.077(60)	2.440(68)
$D_s \to K$	0.6523(52)	0.674(12)	0.9869(61)	1.631(12)	1.705(22)
$B \to \pi$	0.307(18)	0.286(29)	1.020(73)	6.72(88)	5.9(1.1)
$B_s \to K$	0.318(10)	0.377(24)	0.789(25)	3.26(12)	3.57(22)

Upon finalization, the scalar and vector form factor results will be used, among other things, to calculate the values of the CKM matrix elements V_{cd} and V_{ub}. These matrix elements carry substantial implications to Standard Model (and potentially beyond Standard Model) flavor physics, and so more precise determinations of these matrix elements are incredibly valuable. Though other lattice determinations of the scalar and vector form factors of these meson decays do exist, we anticipate that our finalized results will make substantial improvements upon those calculations. We uphold this expectation largely on account of our use of the HISQ action and heavy-HISQ method across a broad kinematic range. Furthermore, we maintain the aim for this line of lattice calculations to be the first to publish $D \to \pi$, $D_s \to K$, and $B_s \to K$ tensor form factor results from lattice QCD. We also aim to publish tensor form factor results for $B \to \pi$, which will improve upon those in other works for the same reasons discussed above. In these regards we have made substantial progress.

Bibliography

[1] Logan Sean Roberts, Chris Bouchard, Olmo Francesconi, and Will Parrott. Towards more accurate $B_{(s)} \to \pi(K)$ and $D_{(s)} \to \pi(K)$ form factors. *PoS*, LATTICE2024:262, 2025.

[2] J. Charles, A. Hocker, H. Lacker, S. Laplace, F. R. Le Diberder, J. Malcles, J. Ocariz, M. Pivk, and L. Roos. CP violation and the CKM matrix: assessing the impact of the asymmetric b factories. *The European Physical Journal C*, 41(1):1–131, 2005.

[3] D. Hatton, C. T. H. Davies, G. P. Lepage, and A. T. Lytle. Renormalization of the tensor current in lattice QCD and the J/ψ tensor decay constant. *Physical Review D*, 102:094509, 2020.

[4] Alexei Bazavov et al. D-meson semileptonic decays to pseudoscalars from four-flavor lattice QCD. *Phys. Rev. D*, 107:094516, 2023.

[5] Jon. A. Bailey et al. $|V_{ub}|$ from $B \to \pi\ell\nu$ decays and $(2+1)$-flavor lattice QCD. *Phys. Rev. D*, 92:014024, 2015.

[6] Jon A. Bailey et al. $B \to \pi\ell\ell$ form factors for new-physics searches from lattice QCD. *Phys. Rev. Lett.*, 115(15):152002, 2015.

[7] Y. Aoki et al. Flag review 2024. *Phys. Rev. D*, 113:014508, 2026.

[8] C. M. Bouchard, G. Peter Lepage, Christopher Monahan, Heechang Na, and Junko Shigemitsu. $B_s \to K\ell\nu$ form factors from lattice QCD. *Phys. Rev.*, D90:054506, 2014.

[9] J. M. Flynn, T. Izubuchi, T. Kawanai, C. Lehner, A. Soni, R. S. Van de Water, and O. Witzel. $B \to \pi\ell\nu$ and $B_s \to K\ell\nu$ form factors and $|V_{ub}|$ from 2+1-flavor lattice QCD with domain-wall light quarks and relativistic heavy quarks. *Phys. Rev.*, D91(7):074510, 2015.

[10] Alexei Bazavov et al. $B_s \to K\ell\nu$ decay from lattice QCD. *Phys. Rev. D*, 100(3):034501, 2019.

[11] J. M. Flynn, R. C. Hill, A. Jüttner, A. Soni, J. T. Tsang, and O. Witzel. Exclusive semileptonic $B_s \to K\ell\nu$ decays on the lattice. *Phys. Rev. D*, 107(11):114512, 2023.

[12] E. Follana et al. Highly improved staggered quarks on the lattice with applications to charm physics. *Phys. Rev. D*, 75:054502, 2007.

[13] E. McLean, C. T. H. Davies, J. Koponen, and A. T. Lytle and. $B_s \to D_s\ell\nu$ form factors for the full q^2 range from lattice QCD with non-perturbatively normalized currents. *Physical Review D*, 101(7), 2020.

[14] Laurence J. Cooper, Christine T. H. Davies, Judd Harrison, Javad Komijani, and Matthew Wingate. $B_c \to B_{s(d)}$ form factors from lattice QCD. *Physical Review D*, 102:014513, 2020.

[15] Judd Harrison, Christine T. H. Davies, and Andrew Lytle. $B_c \to J/\psi$ form factors for the full q^2 range from lattice QCD. *Physical Review D*, 102:094518, 2020.

[16] W. G. Parrott, C. Bouchard, C. T. H. Davies, and D. Hatton. Toward accurate form factors for B-to-light meson decay from lattice QCD. *Physical Review D*, 103:094506, 2021.

[17] W. G. Parrott, C. Bouchard, and C. T. H. Davies. $B \to K$ and $D \to K$ form factors from fully relativistic lattice QCD. *Physical Review D*, 107:014510, 2023.

[18] Judd Harrison and Christine T. H. Davies. $B \to D^*$ vector, axial-vector and tensor form factors for the full q^2 range from lattice QCD, 2024. arXiv:2304.03137 [hep-lat].

[19] S. Navas et al. Review of particle physics. *Phys. Rev. D*, 110:030001, 2024.

[20] R. Aaij et al. First evidence of the decay $B^+ \to \pi^+e^+e^-$, 2026. arXiv:2604.26784 [hep-ex].

[21] Michael E. Peskin and Daniel V. Schroeder. *An Introduction to Quantum Field Theory.* Addison-Wesley, Reading, Massachusetts, 1995.

[22] Steven Weinberg. *The Quantum Theory of Fields, Volume 1: Foundations.* Cambridge University Press, Cambridge, UK, 1995.

[23] Matthew D. Schwartz. *Quantum Field Theory and the Standard Model.* Cambridge University Press, Cambridge, UK, 2014.

[24] M. Gell-Mann. A schematic model of baryons and mesons. *Physics Letters*, 8(3):214–215, 1964.

[25] H. Fritzsch, M. Gell-Mann, and H. Leutwyler. Advantages of the color octet gluon picture. *Physics Letters B*, 47(4):365–368, 1973.

[26] A. Salam and J.C. Ward. Electromagnetic and weak interactions. *Physics Letters*, 13(2):168–171, 1964.

[27] Steven Weinberg. A model of leptons. *Phys. Rev. Lett.*, 19:1264–1266, 1967.

[28] Peter W. Higgs. Broken symmetries and the masses of gauge bosons. *Phys. Rev. Lett.*, 13:508–509, 1964.

[29] Abdus Salam. Weak and electromagnetic interactions. *Proceedings of the Nobel Symposium No. 8*, 1968.

[30] Hideki Yukawa. On the interaction of elementary particles. I. *Progress of Theoretical Physics Supplement*, 1:1–10, 1955.

[31] Nicola Cabibbo. Unitary symmetry and leptonic decays. *Phys. Rev. Lett.*, 10:531–533, 1963.

[32] Makoto Kobayashi and Toshihide Maskawa. CP-Violation in the renormalizable theory of weak interaction. *Progress of Theoretical Physics*, 49(2):652–657, 1973.

[33] Lincoln Wolfenstein. Parametrization of the kobayashi-maskawa matrix. *Phys. Rev. Lett.*, 51:1945–1947, 1983.

[34] S. L. Glashow, J. Iliopoulos, and L. Maiani. Weak interactions with lepton-hadron symmetry. *Phys. Rev. D*, 2:1285–1292, 1970.

[35] R. L. Workman and Others. Review of Particle Physics. *PTEP*, 2022:083C01, 2022.

[36] G. C. Wick. Properties of Bethe-Salpeter wave functions. *Phys. Rev.*, 96:1124–1134, 1954.

[37] Kenneth G. Wilson. Confinement of quarks. *Phys. Rev. D*, 10:2445–2459, 1974.

[38] G. Peter Lepage. Lattice QCD for Novices, 2005. arXiv:hep-lat/0506036.

[39] Nicholas Metropolis, A. W. Rosenbluth, M. N. Rosenbluth, A. H. Teller, and Edward Teller. Equation of state calculations by fast computing machines. *The Journal of Chemical Physics*, 21(6):1087–1092, 1953.

[40] W. K. Hastings. Monte carlo sampling methods using Markov chains and their applications. *Biometrika*, 57(1):97–109, 1970.

[41] Michael Creutz. Monte carlo study of quantized SU(2) gauge theory. *Physical Review D*, 21:2308–2315, 1980.

[42] Simon Duane, A. D. Kennedy, B. J. Pendleton, and Duncan Roweth. Hybrid monte carlo. *Physics Letters B*, 195:216–222, 1987.

[43] Kenneth G. Wilson. *Monte-Carlo Calculations for the Lattice Gauge Theory*, pages 363–402. Springer US, Boston, MA, 1980.

[44] K. Symanzik. Continuum limit and improved action in lattice theories: (i). principles and 4 theory. *Nuclear Physics B*, 226(1):187–204, 1983.

[45] M. Lüscher and P. Weisz. On-shell improved lattice gauge theories. *Communications in Mathematical Physics*, 97(1):59–77, 1985.

[46] G. Peter Lepage and Paul B. Mackenzie. Viability of lattice perturbation theory. *Phys. Rev. D*, 48:2250–2264, 1993.

[47] Magnus R. Hestenes and Eduard Stiefel. Methods of conjugate gradients for solving linear systems. *Journal of Research of the National Bureau of Standards*, 49(6):409–436, 1952.

[48] Steven Gottlieb, W. Liu, D. Toussaint, R. L. Renken, and R. L. Sugar. Hybrid-molecular-dynamics algorithms for the numerical simulation of quantum chromodynamics. *Phys. Rev. D*, 35:2531–2542, 1987.

[49] Thomas Appelquist and J. Carazzone. Infrared singularities and massive fields. *Phys. Rev. D*, 11:2856–2861, 1975.

[50] Luuk H. Karsten and Jan Smith. Lattice fermions: Species doubling, chiral invariance and the triangle anomaly. *Nuclear Physics B*, 183(1):103–140, 1981.

[51] N. Kawamoto and J. Smit. Effective lagrangian and dynamical symmetry breaking in strongly coupled lattice QCD. *Nuclear Physics B*, 192(1):100–124, 1981.

[52] B. Sheikholeslami and R. Wohlert. Improved continuum limit lattice action for QCD with wilson fermions. *Nuclear Physics B*, 259(4):572–596, 1985.

[53] John Kogut and Leonard Susskind. Hamiltonian formulation of wilson's lattice gauge theories. *Phys. Rev. D*, 11:395–408, 1975.

[54] G. Peter Lepage. Flavor-symmetry restoration and symanzik improvement for staggered quarks. *Phys. Rev. D*, 59:074502, 1999.

[55] Satchidananda Naik. On-shell improved action for QCD with susskind fermions and the asymptotic freedom scale. *Nuclear Physics B*, 316(1):238–268, 1989.

[56] Christopher Monahan, Junko Shigemitsu, and Ron Horgan. Matching lattice and continuum axial-vector and vector currents with nonrelativistic QCD and highly improved staggered quarks. *Physical Review D*, 87:034017, 2013.

[57] C.T. Sachrajda and G. Villadoro. Twisted boundary conditions in lattice simulations. *Physics Letters B*, 609(1):73–85, 2005.

[58] Paulo F. Bedaque. Aharonov–bohm effect and nucleon–nucleon phase shifts on the lattice. *Physics Letters B*, 593(1–4):82–88, 2004.

[59] G.M. de Divitiis, R. Petronzio, and N. Tantalo. On the discretization of physical momenta in lattice QCD. *Physics Letters B*, 595(1):408–413, 2004.

[60] D. Guadagnoli, F. Mescia, and S. Simula. Lattice study of semileptonic form factors with twisted boundary conditions. *Physical Review D*, 73(11), 2006.

[61] J.M. Flynn, A. Jüttner, and C.T. Sachrajda. A numerical study of partially twisted boundary conditions. *Physics Letters B*, 632(2):313–318, 2006.

[62] Brian Colquhoun, Christine T. H. Davies, Daniel Hatton, and G. Peter Lepage. New high-precision b, c, and s masses from pseudoscalar-pseudoscalar correlators in nf=4 lattice QCD. *Phys. Rev. D*, 113(7):074522, 2026.

[63] Howard Georgi. An effective field theory for heavy quarks at low energies. *Physics Letters B*, 240(3):447–450, 1990.

[64] Estia Eichten and Brian Hill. An effective field theory for the calculation of matrix elements involving heavy quarks. *Physics Letters B*, 234(4):511–516, 1990.

[65] Matthias Neubert. Heavy-quark effective theory, 1996. arXiv:hep-ph/9610266.

[66] Matthias Neubert. Effective field theory and heavy quark physics. In *Physics In $D \geq 4$ Tasi 2004*, page 149–194. World Scientific, 2006.

[67] A. Bazavov et al. $\boldsymbol{B}$- and $\boldsymbol{D}$-meson leptonic decay constants from four-flavor lattice QCD. *Phys. Rev. D*, 98:074512, 2018.

[68] Szabolcs Borsányi et al. High-precision scale setting in lattice QCD. *Journal of High Energy Physics*, 2012(9):10, 2012.

[69] Martin Lüscher. Properties and uses of the wilson flow in lattice QCD. *Journal of High Energy Physics*, 2010(8):71, 2010.

[70] S. Dürr et al. Lattice QCD at the physical point: simulation and analysis details. *Journal of High Energy Physics*, 2011(8):148, 2011.

[71] R. J. Dowdall, C. T. H. Davies, G. P. Lepage, and C. McNeile. V_{us} from π and K decay constants in full lattice QCD with physical u, d, s, and c quarks. *Phys. Rev. D*, 88:074504, 2013.

[72] A. Bazavov, C. Bernard, C. DeTar, W. Freeman, Steven Gottlieb, U. M. Heller, J. E. Hetrick, J. Laiho, L. Levkova, M. Oktay, J. Osborn, R. L. Sugar, D. Toussaint, and R. S. Van de Water. Scaling studies of QCD with the dynamical highly improved staggered quark action. *Physical Review D*, 82:074501, 2010.

[73] A. Bazavov, C. Bernard, J. Komijani, C. DeTar, L. Levkova, W. Freeman, Steven Gottlieb, Ran Zhou, U. M. Heller, J. E. Hetrick, J. Laiho, J. Osborn, R. L. Sugar, D. Toussaint, and R. S. Van de Water. Lattice QCD ensembles with four flavors of highly improved staggered quarks. *Physical Review D*, 87:054505, 2013.

[74] A. Bazavov, C. Bernard, N. Brown, J. Komijani, C. DeTar, J. Foley, L. Levkova, Steven Gottlieb, U. M. Heller, J. Laiho, R. L. Sugar, D. Toussaint, and R. S. Van de Water. Gradient flow and scale setting on MILC HISQ ensembles. *Phys. Rev. D*, 93:094510, 2016.

[75] Bipasha Chakraborty, C. T. H. Davies, B. Galloway, P. Knecht, J. Koponen, G. C. Donald, R. J. Dowdall, G. P. Lepage, and C. McNeile. High-precision quark masses and QCD coupling from $n_f = 4$ lattice QCD. *Phys. Rev. D*, 91:054508, 2015.

[76] M. Foster and C. Michael. Quark mass dependence of hadron masses from lattice QCD. *Phys. Rev. D*, 59:074503, 1999.

[77] C. McNeile and C. Michael. Decay width of light quark hybrid meson from the lattice. *Phys. Rev. D*, 73:074506, 2006.

[78] Matthew Wingate, Junko Shigemitsu, Christine T. H. Davies, G. Peter Lepage, and Howard D. Trottier. Heavy-light mesons with staggered light quarks. *Phys. Rev. D*, 67:054505, 2003.

[79] Bradley P. Carlin and Thomas A. Louis. Bayes and empirical bayes methods for data analysis. *Statistics and Computing*, 7(2):153–154, 1997.

[80] Peter Lepage, Christoph Gohlke, and Daniel Hackett. gplepage/gvar: gvar version 13.0.2, 2024.

[81] G.P. Lepage, B. Clark, C.T.H. Davies, K. Hornbostel, P.B. Mackenzie, C. Morningstar, and H. Trottier. Constrained curve fitting. *Nuclear Physics B - Proceedings Supplements*, 106-107:12, 2002.

[82] Peter Lepage. gplepage/corrfitter: corrfitter version 8.2, 2021.

[83] Peter Lepage and Christoph Gohlke. gplepage/lsqfit: lsqfit version 13.2.3, 2024.

[84] B. A. Thacker and G. Peter Lepage. Heavy-quark bound states in lattice QCD. *Phys. Rev. D*, 43:196–208, 1991.

[85] I.T. Drummond and R.R. Horgan. Improved langevin methods for spin systems. *Physics Letters B*, 302(2):271–278, 1993.

[86] Gregory Kilcup. Quenched staggered spectrum at $\beta = 6.0$, 6.2 and 6.4. *Nuclear Physics B - Proceedings Supplements*, 34:350–353, 1994. Proceedings of the International Symposium on Lattice Field Theory.

[87] C. Michael and A. McKerrell. Fitting correlated hadron mass spectrum data. *Phys. Rev. D*, 51:3745–3750, 1995.

[88] Boram Yoon, Yong-Chull Jang, Chulwoo Jung, and Weonjong Lee. Covariance fitting of highly-correlated data in lattice QCD. *Journal of the Korean Physical Society*, 63:145–162, 2013.

[89] C. Michael. Fitting correlated data. *Phys. Rev. D*, 49:2616–2619, 1994.

[90] D. Sivia and J. Skilling. *Data Analysis: A Bayesian Tutorial*. Oxford science publications. OUP Oxford, 2006.

[91] B.P. Carlin and T.A. Louis. *Bayes and Empirical Bayes Methods for Data Analysis, Second Edition*. Chapman & Hall/CRC Texts in Statistical Science. Taylor & Francis, 2010.

[92] Robert E. Kass and Adrian E. Raftery. Bayes factors. *Journal of the American Statistical Association*, 90:773, 1995.

[93] C. Aubin, C. Bernard, C. DeTar, J. Osborn, Steven Gottlieb, E. B. Gregory, D. Toussaint, U. M. Heller, J. E. Hetrick, and R. Sugar. Light hadrons with improved staggered quarks: Approaching the continuum limit. *Phys. Rev. D*, 70:094505, 2004.

[94] C. Bernard. Staggered chiral perturbation theory and the fourth-root trick. *Phys. Rev. D*, 73:114503, 2006.

[95] Claude Bernard, Maarten Golterman, and Yigal Shamir. Effective field theories for QCD with rooted staggered fermions. *Phys. Rev. D*, 77:074505, 2008.

[96] Willem E. A. Verplanke, Zoltan Fodor, Antoine Gérardin, Jana N. Guenther, Laurent Lellouch, Kalman K. Szabo, Balint C. Toth, and Lukas Varnhorst. Lattice QCD calculation of the η and η' meson masses at the physical point using rooted staggered fermions. *Phys. Rev. D*, 111:094506, 2025.

[97] C. W. Bernard, Carleton E. DeTar, Ziwen Fu, and Sasa Prelovsek. Taste breaking effects in scalar meson correlators. *PoS*, LAT2006:173, 2006.

[98] Jozef J. Dudek, Robert G. Edwards, and David J. Wilson. An a_0 resonance in strongly coupled $\pi\eta$, $k\overline{K}$ scattering from lattice QCD. *Phys. Rev. D*, 93:094506, 2016.

[99] David J. Wilson, Jozef J. Dudek, Robert G. Edwards, and Christopher E. Thomas. Resonances in coupled $\pi k, \eta k$ scattering from lattice QCD. *Phys. Rev. D*, 91:054008, 2015.

[100] Gumaro Rendon, Luka Leskovec, Stefan Meinel, John Negele, Srijit Paul, Marcus Petschlies, Andrew Pochinsky, Giorgio Silvi, and Sergey Syritsyn. $i = 1/2$ s-wave and p-wave $k\pi$ scattering and the κ and K^* resonances from lattice QCD. *Phys. Rev. D*, 102:114520, 2020.

[101] M. Neubert. Heavy-quark symmetry. *Phys. Rept.*, 245:259–396, 1994.

[102] Keval Gandhi and Ajay Kumar Rai. Study of B, B_s mesons using heavy quark effective theory. *Eur. Phys. J. C*, 82:777, 2022.

[103] C.B. Lang, Daniel Mohler, Sasa Prelovsek, and R.M. Woloshyn. Predicting positive parity B_s mesons from lattice QCD. *Physics Letters B*, 750:17–21, 2015.

[104] C. McNeile, C. Michael, and G. Thompson. Hadronic decay of a scalar b meson from the lattice. *Phys. Rev. D*, 70:054501, 2004.

[105] Chris Bouchard, G. Peter Lepage, Christopher Monahan, Heechang Na, and Junko Shigemitsu. Rare decay $B \to K\ell^+\ell^-$ form factors from lattice QCD. *Physical Review D*, 88(5), 2013.

[106] Bipasha Chakraborty, W. G. Parrott, C. Bouchard, C. T. H. Davies, J. Koponen, and G. P. Lepage. Improved V_{cb} determination using precise lattice QCD form factors for $D \to K\ell\nu$. *Physical Review D*, 104(3), 2021.

[107] Jan Smit. *Introduction to Quantum Fields on a Lattice*. Cambridge Lecture Notes in Physics. Cambridge University Press, 2002.

[108] D. Ebert, R. N. Faustov, and V. O. Galkin. Heavy-light meson spectroscopy and Regge trajectories in the relativistic quark model. *Eur. Phys. J. C*, 66:197–206, 2010.

[109] R. J. Dowdall, C. T. H. Davies, R. R. Horgan, G. P. Lepage, C. J. Monahan, J. Shigemitsu, and M. Wingate. Neutral B-meson mixing from full lattice QCD at the physical point. *Physical Review D*, 100(9), 2019.

[110] Richard D. Morey, Jan-Willem Romeijn, and Jeffrey N. Rouder. The philosophy of Bayes factors and the quantification of statistical evidence. *Journal of Mathematical Psychology*, 72:6–18, 2016. Bayes Factors for Testing Hypotheses in Psychological Research: Practical Relevance and New Developments.

[111] Heechang Na, Christine T. H. Davies, Eduardo Follana, G. Peter Lepage, and Junko Shigemitsu. $D \to K, l\nu$ semileptonic decay scalar form factor and V_{cs} from lattice QCD. *Physical Review D*, 82:114506, 2010.

[112] J. Koponen, C. T. H. Davies, G. C. Donald, E. Follana, G. P. Lepage, H. Na, and J. Shigemitsu. The shape of the $D \to K$ semileptonic form factor from full lattice QCD and V_{cs}. 2013.

[113] G. Martinelli, C. Pittori, C.T. Sachrajda, M. Testa, and A. Vladikas. A general method for non-perturbative renormalization of lattice operators. *Nuclear Physics B*, 445(1):81–105, 1995.

[114] G. 't Hooft. Dimensional regularization and the renormalization group. *Nuclear Physics B*, 61:455–468, 1973.

[115] Steven Weinberg. New approach to the renormalization group. *Phys. Rev. D*, 8:3497–3509, 1973.

[116] C. Glenn Boyd, Benjamín Grinstein, and Richard F. Lebed. Model-independent determinations of $B \to Dl\nu$, $D^*l\nu$ form factors. *Nuclear Physics B*, 461(3):493–511, 1996.

[117] Claude Bourrely, Laurent Lellouch, and Irinel Caprini. Model-independent description of $B \to \pi l\nu$ decays and a determination of $|V_{ub}|$. *Phys. Rev. D*, 79:013008, 2009.

[118] Christian M. Arnesen, Benjamin Grinstein, Ira Z. Rothstein, and Iain W. Stewart. Precision model independent determination of $|V_{\mathrm{ub}}|$ from $B \to \pi l\nu$. *Phys. Rev. Lett.*, 95:071802, 2005.

[119] J. Charles, A. Le Yaouanc, L. Oliver, O. Pène, and J.-C. Raynal. Heavy-to-light form factors in the final hadron large energy limit of QCD. *Physical Review D*, 60(1), 1999.

[120] D. Hatton, C. T. H. Davies, B. Galloway, J. Koponen, G. P. Lepage, and A. T. Lytle. Charmonium properties from lattice $\mathrm{QCD}+\mathrm{QED}$: Hyperfine splitting, J/ψ leptonic width, charm quark mass, and a_μ^c. *Phys. Rev. D*, 102:054511, 2020.

[121] C. Glenn Boyd, Benjamín Grinstein, and Richard F. Lebed. Constraints on form factors for exclusive semileptonic heavy to light meson decays. *Phys. Rev. Lett.*, 74:4603–4606, 1995.

[122] C. Glenn Boyd, Benjamín Grinstein, and Richard F. Lebed. Precision corrections to dispersive bounds on form factors. *Phys. Rev. D*, 56:6895–6911, 1997.

[123] Johan Bijnens and Ilaria Jemos. Hard pion chiral perturbation theory for $B \to \pi$ and $D \to \pi$ formfactors. *Nuclear Physics B*, 840(1):54–66, 2010.

[124] Johan Bijnens and Ilaria Jemos. Vector formfactors in hard pion chiral perturbation theory. *Nuclear Physics B*, 846(2):145–166, 2011.

[125] A. Bazavov et al. B- and D-meson decay constants from three-flavor lattice QCD. *Phys. Rev. D*, 85:114506, 2012.

[126] C. Aubin and C. Bernard. Heavy-light semileptonic decays in staggered chiral perturbation theory. *Phys. Rev. D*, 76:014002, 2007.

[127] Asmaa Abada, Damir Bećirević, Philippe Boucaud, Gregorio Herdoiza, Jean Pierre Leroy, Alain Le Yaouanc, and Olivier Pène. Lattice measurement of the couplings $\hat{g}_\infty$ and $g_{B^*B\pi}$. *Journal of High Energy Physics*, 2004(02):016, 2004.

[128] J. P. Lees et al. Measurement of the $D^*(2010)^+$ natural linewidth and the $D^*(2010)^+$–D^0 mass difference. *Phys. Rev. D*, 88:052003, 2013.

[129] J. M. Flynn, P. Fritzsch, T. Kawanai, C. Lehner, C. T. Sachrajda, B. Samways, R. S. Van de Water, and O. Witzel. $B^*B\pi$ coupling using relativistic heavy quarks. *Phys. Rev. D*, 93:014510, 2016.

[130] William Detmold, C.-J. David Lin, and Stefan Meinel. Axial couplings and strong decay widths of heavy hadrons. *Phys. Rev. Lett.*, 108:172003, 2012.

[131] Fabio Bernardoni, John Bulava, Michael Donnellan, and Rainer Sommer. Precision lattice QCD computation of the $B^*B\pi$ coupling. *Physics Letters B*, 740:278–284, 2015.

[132] C. Bernard. Chiral logs in the presence of staggered flavor symmetry breaking. *Phys. Rev. D*, 65:054031, 2002.

[133] Richard J. Hill. Heavy-to-light meson form factors at large recoil. *Phys. Rev. D*, 73:014012, 2006.

[134] Ritu Garg, Preeti Bhall, K K Vishwakarma, and Alka Upadhyay. Radially excited bottom mesons in heavy quark effective theory. *Progress of Theoretical and Experimental Physics*, 2025(12):123B06, 2025.

[135] Benjamín Grinstein and Richard F. Lebed. Above-threshold poles in model-independent form factor parametrizations. *Phys. Rev. D*, 92:116001, 2015.